Experimental Characterisation and Forming Analysis of Pure Unidirectional Stitched Glass Fibre Non-Crimp Fabric

by

Himanthi Nimrekha Kahavita Kahavitage Dona

James Watt School of Engineering

College of Science and Engineering

University of Glasgow

Submitted in fulfilment of the requirements for the degree of

Doctor of Philosophy in Mechanical Engineering

December 2024

Abstract

This research focuses on the experimental characterisation and forming analysis of pure-unidirectional non-crimp fabric (pure-UDNCF). This fabric consists of low-stiffness polyamide stitches with a tricot-chain stitching pattern where the chain stitches run along the front of the fabric, perpendicular to the glass tow direction. Notably, there are no stabilising tows oriented transverse to the main tow direction in this fabric, a common feature in many 'quasi-UDNCF', this allows extension of the stitch in the transverse direction under certain loading conditions. The lack of stabilising tows introduces a possible low-energy deformation mode to the pure-UDNCF, which is absent in biaxial fabrics and primarily in quasi-UDNCF. Thus, compared to biaxial fabrics, the in-plane deformation modes of pure-UDNCF are complex and dominated by transverse extension and shear. Therefore, characterisation tests typically developed to characterise woven fabrics are unsuitable for pure-UDNCF, because more than one low-energy deformation may occur, and the deformations can be coupled during deformation experiments. This was evident following the initial evaluation of pure-UDNCF with two principal shear tests, namely the Uniaxial Bias Extension test (UBE test is a tensile test performed on a rectangular-shaped fabric with the warp and weft rows oriented ±45° to the direction of applied tensile force) and the Picture Frame (PF) test (all four sides are clamped orthogonal to the tows). The results revealed a significant difference in shear stiffness, with the PF test being significantly higher than the UBE test. This unique observation encourages further investigation to determine the cause of the difference. The intent is to understand whether the different behaviour of the two tests is real, or a problem related to using the tests for this fabric.

The experimental error of the PF test was investigated using two modifications: the pre-displaced PF test and the G-clamped PF test. The pre-displaced PF test was used to investigate the misalignment error and involved two pre-displacements (4mm and 6mm). The existing tight clamps (nut and bolts) were replaced with G-clamps of two different pressures (high and low) to determine how the clamping condition affected the measured shear force. The resulting combined (high and low) G-clamped PF test curve was close to the 6mm pre-displaced PF test curve, and both curves were significantly reduced than the initial PF test results. Furthermore, the friction in the bearing of the PF rig was eliminated to improve the accuracy of the PF test, however, even after these modifications, the standard UBE test results showed less axial force than the PF test curve. Moreover, in addition to shear, an in-plane bending contribution was identified at high shear angles in the PF test. As a result, the axial force measured in the PF test of the pure-UDNCFs was considered to be a combination of shear and in-plane bending. In the UBE test, the in-plane contribution was not significant, however, stretching in the stitch direction was observed and assumed to help minimise the contribution from in-plane bending of the tows. Therefore, during the UBE test, was considered to be a coupling between shear stiffness-tensile strain in the stitch direction, and

between tensile stiffness in the stitch direction-shear strain. Experiments were further performed to isolate the contribution of each deformation mode i.e., shear, in-plane bending and tensile strain in the stitch direction. New characterisation tests namely cruciform bias extension (CBE) test, parallelogram shear-stretch (PSS) test and simple shear (SS) test have been designed to explore a wider deformation space i.e., different combinations of shear and tensile strain in the stitch direction. In addition to these new shear tests, the PF test was performed with pure-UDNCF samples at different stitch pre-stretched levels to provide insights into unexplored areas of the (shear angle) - (tensile stretch) parameter space. The plotted results in the (shear angle) - (tensile stretch) parameter space revealed that the pure-UDNCF was sensitive to pre-stretching in the stitch direction during sample preparation. A new method for determining the amount of pre-stretch in each test was introduced, and the results were adjusted to be more realistic and accurate.

Except for the tensile test performed in the stitch direction, all the tests generated more than one contribution from the three low-stiffness deformation modes to the axial force i.e., shear, in-plane bending and tensile strain in the stitch direction. An iterative approach was developed to isolate the three stiffnesses of the pure-UDNCF by considering the combined experimental results of the PSS, SS, tensile, PF test, and pre-stretched PF tests. This has led to a new method of determining in-plane bending stiffness using experimental data. The separate contributions from shear, in-plane bending and tensile strain in the stitch direction, provided good predictions of the measured axial force of each of the experiments. In addition to the shear tests, a cantilever bending test was performed on pure-UDNCF to measure the out-of-plane bending stiffness of the fabric. Furthermore, a new experiment was developed to measure the in-plane bending of pure-UDNCF qualitatively. This test could be further developed to quantify in-plane bending stiffness and is flagged as future work. Appropriate data obtained by these experimental methods can be used as input parameters to constitutive models to predict the material behaviour.

Following the shear and bending characterisation tests, hemispherical forming experiments were performed. Two fixation methods, i.e., acetone/epoxy solution and adhesive spray, were used to maintain the desired shape and facilitate the handling of formed specimens during post-analysis. Fabrics with different tow-stitch orientations were used to form the mono and bilayer hemispherical specimens. A combination of a 3D laser scanner (Escan H) and 3D modelling software (Autodesk 3ds Max) was successfully used to determine the shear angles and stretching in the stitch direction at selected locations on the formed hemispheres. Post-analysis of the formed bilayer hemispheres revealed that both fixation procedures provided long-term stability; however, the acetone/epoxy method caused fewer defects than the adhesive spray method due to facilitating inter-ply sliding and reducing the internal stresses between the two plies. The adhesive spray method worked well in modifying the fabric forming behaviour, offering improved control over fibre orientation, and helping to reduce gaps or inconsistencies in the fabric. Therefore, the fast and simple adhesive spray method can optimise the forming behaviour and be used locally to modify the behaviour in specific locations. These experimental forming results provide a solid foundation for validating numerical models that predict the forming behaviour of pure-UDNCF.

Acknowledgements

This thesis reflects the end of a remarkable journey, and I am grateful to many individuals and organisations for their essential support throughout this endeavour.

First and foremost, I want to express my heartfelt gratitude to my supervisor, Dr Philip Harrison, for his constant guidance, constructive criticism, and unending encouragement. Your insight, experience, and dedication have been the foundation of my academic growth. I am also grateful to my academic co-supervisor, Dr Eddie McCarthy (University of Edinburgh), and industrial supervisor, Dr Mingfu Zhang (Johns Manville, USA), for their thoughtful feedback and support, which substantially enhanced this research. In addition, I would like to thank the former industrial supervisor Dr Klaus Gleich (Johns Manville, Germany) and Professor Conchúr Ó Brádaigh (University of Edinburgh), for their invaluable mentorship and for shaping the initial direction of this research.

This project is a joint effort between the University of Glasgow and the University of Edinburgh, and I am thankful for the resources and collaborative environment provided by both institutions. I am particularly grateful to the industrial partner of the project, Johns Manville, for generously providing the materials that served as a key foundation for this research. Your contribution enhanced the quality of this work and strengthened the link between academia and industry.

I would like to thank the National Manufacturing Institute Scotland (NMIS) and the Scottish Research Partnership in Engineering (SRPe) for their invaluable support and funding, which made this research possible. Their commitment to advancing engineering and manufacturing innovation has been a source of inspiration throughout my doctoral journey.

A special thanks to my colleagues at the School of Engineering, University of Glasgow, especially Dr Iain Campbell and technical staff at Materials Laboratory and Mechanical Workshop, Mr John Davidson, Mr Charlie Patterson, Mr Wilson MacDougall and Mr Alistair MacFarlane for their assistance in troubleshooting technical issues and ensuring the smooth execution of experiments.

This achievement would not have been possible without the unconditional love and guidance of my family, who stood by me through every hardship. Words cannot express my gratitude to my parents for their unwavering faith in me and constant encouragement, which have been my greatest source of motivation. To my brother and sister-in-law, thank you for always lifting me up and inspiring me to reach new heights. To my spouse and my eight-year-old son, thank you for being my constant source of strength and understanding, especially during the most challenging moments of this journey.

Finally, I am very thankful to the citizens of Sri Lanka for funding the free education and to the citizens of Scotland for supporting the scholarships through their taxes. Your generosity has shaped my journey and inspired me to give it back to society.

This thesis is as much a product of your support as it is of my efforts. Thank you all for being part of this journey.

දිරියෙන් ලද මාආදර පවුලෙන්
නුවණින් ලද ගුරු දෙගුරුන්ගෙන්
සවියෙන් ලද ඔබෙ බදු මුදලින්
උගතෙමි නිදහසේ සිප්සත මනාලෙසින්
පුදනෙමි පබැඳුම ඔබවෙත හද බැතියෙන්

Author Declaration

I hereby declare that this thesis entitled '***Experimental Characterisation and Forming Analysis of Pure Unidirectional Stitched Glass Fibre Non-Crimp Fabric***' is the result of my independent work and has not been submitted for any other degree or professional qualification at the University of Glasgow or any other institution. Any work done in collaboration with others has been clearly indicated, and all sources of information have been properly acknowledged and referenced.

Himanthi Nimrekha Kahavita Kahavitage Dona

December 2024

List of Publications and Awards

Journal paper

- Kahavita, K. D. H. N., McCarthy, E. D., Zhang, M., Brádaigh, C. Ó., & Harrison, P. (2023). Characterising the shear resistance of a unidirectional non-crimp glass fabric using modified picture frame and uniaxial bias extension test methods. International Journal of Material Forming, 16(5), 49. https://doi.org/10.1007/s12289-023-01765-0
- Kahavita, K. D. H. N., McCarthy, E. D., Zhang, M., Brádaigh, C. Ó., & Harrison, P. Characterising the Shear-Stretch Response of a Pure Unidirectional Non-Crimp Fabric: Measuring In-Plane Bending Stiffness. In preparation for submission to the International Journal of Material Forming (2025).

Conference papers

- Kahavita, K. D. H. N., McCarthy, E. D., Zhang, M., Brádaigh, C. Ó., & Harrison, P. (2022). Investigation of the In-Plane Deformation Kinematics of a Unidirectional Non-Crimp Glass Fabric. International Conference on Manufacturing of Advanced Composites. Sheffield, UK.
- Kahavita, K. D. H. N., Harrison, P., McCarthy, E. D., Zhang, M., & Brádaigh, C. Ó. (2023). Characterization of the In-Plane Shear Behaviour of a Unidirectional Non-Crimp Glass Fabric. 20th International Conference on Experimental Mechanics (ICEM20) (pp. 283-284). Porto, Portugal: European Society for Experimental Mechanics.
- Kahavita, K. D. H. N., Harrison, P., McCarthy, E. D., Zhang, M., & Brádaigh, C. Ó. (2023). Characterising the In-plane Deformation Behaviour of a Unidirectional Non-Crimp Glass Fabric. 17th International Conference on Advances in Experimental Mechanics. Glasgow, UK: British Society for Strain Measurement.

Protocol (www.protocols.io)

- Kahavita, N., & Harrison, P. (2024). Uniaxial Bias Extension Test on Woven Engineering Fabrics. dx.doi.org/10.17504/protocols.io.81wgbyy93vpk/v1

Awards

- First runner-up in the Industry Doctorate Programme Poster Competition (SRPe Annual Conference 2023).
- Student attendance award at the 20th International Conference on Experimental Mechanics (ICEM20) (Department of Engineering, University of Porto).

Table of Contents

List of Figures

List of Tables

Nomenclature and Abbreviations

Abbreviations

Pure-UDNCF - Pure Unidirectional Non-Crimp Fabrics

UBE - Uniaxial bias extension

PF - Picture frame

CBE - Cruciform Bias Extension

SS - Simple Shear

PSS - Parallelogram Shear-Stretch

PSPF - Pre-Stretched Picture Frame

3D - Three Dimensional

FRCs - Fibre-reinforced Composites

UD - Unidirectional

FEM - Finite Element Method

NCF - Non-Crimp Fabrics

PAN - Poly-acrylonitrile

PMMA - Polymethyl methacrylate

UV - Ultra Violet

FL - Float Length

ISO - International Standard Organization

ASTM - American Society for Testing and Materials

BS - British Standard

KES - Kawabata's Evaluation System

DIC - Digital image correlation

DVC - Digital Volume Correlation

PJN - Pin-jointed net

XCT - X-ray computer tomography

MPM - Material point method

DOF - Degrees of Freedom

Al - aluminium

AWPs - anti-wrinkle plates

WOA - wrinkle onset angle

SD - Standard Deviation

SLS - Structured Light Scanning

PVA - Polyvinyl alcohol

AE - Acetone/epoxy

Ad - Adhesive spray

Nomenclature

C - Bending length of the fabric (m)

G - Flexural rigidity (Nm)

l - Overhanging length of the fabric (m)

w - Weight per unit area of the fabric (kg)

$\phi_{s(i)}$ - Initial inter-fibre angle of the UBE test (˚)

ϕ_s - Change in the inter-fibre angle in UBE test (˚)

d_s - Extended length during UBE test (m)

λ - Aspect ratio of the specimen

L_A - Side length of Region A of the UBE specimen (m)

θ - Shear angle (˚)

d_{pf} - Crosshead displacement during the PF test (m)

L_{pf} - Side length of the PF rig (m)

$\emptyset$ - Frame angle at a given displacement of the PF rig (˚)

F_s - Normalised shear force per unit length in PF test (N/m)

F_{af} - Total axial force of the PF test (N)

ε_p - Engineering strain of the positive pre-displaced PF rig

δ_p - Theoretical tow shear angle in the positive pre-displaced PF rig (˚)

ε_n - Engineering strain in the negative pre-displaced PF rig

δ_n - Theoretical tow shear angle in the negative pre-displaced PF rig (˚)

θ_1 - Initial frame angle in positive pre-displaced PF test (˚)

θ_2 - Frame angle at a given displacement in positive pre-displaced PF test (˚)

θ_1' - Initial frame angle in negative pre-displaced PF (˚)

θ_2' - Frame angle at a given displacement in negative pre-displaced PF (˚)

d_1, d_1' - Constants depend on the pre-displacement of the PF test

D, D' - Displacements of the machine crosshead in PF test (m)

ε_T - Engineering strain in the stitch direction during the tensile test

D_T - Crosshead displacement in the tensile test (m)

W_T - Initial width of the tensile test specimen (m)

L_T - Initial length of the tensile test specimen (m)

Φ_A - Angle between tows and axial displacement in the PSS test (˚)

ω_A - Angle between stitches and axial displacement in the PSS test (˚)

L_0 - Initial length of Region A in the PSS specimen (m)

D_A - Displacement of the machine crosshead during the PSS test (m)

α_A - Theoretical engineering strain in the stitch direction during the PSS test

β_A - Experimental engineering strain in the stitch direction during the PSS test

L_1 - Stitch length at a given displacement in the PSS test (m)

θ_s - Theoretical shear angle of the SS test (˚)

D_B - Machine displacement in the SS test (m)

L_0' - Initial length of the SS test specimen (m)

α_s - Theoretical engineering strain in the stitch direction during the SS test

β_s - Experimental engineering strain in the stitch direction during the SS test

L'_0 - Initial length of Region A of the SS specimen (m)

L'_1 - Stitch length at a given displacement of the SS specimen (m)

$\dot{D}_s$ - Displacement rate in the stitch direction in the PSS and SS tests (ms^{-1})

$\dot{D}$ - Displacement rate of the machine crosshead in the PSS and SS tests (ms^{-1})

$F_{at\theta}$ - Axial force per unit length due to tension along the stitch direction in the SS test (Nm^{-1})

$F_{t\theta}$ - Tensile force per unit length measured in the stitch direction from the tensile test (Nm^{-1})

$F_{as\theta}$ - Axial machine force attributable to fabric shear in the SS test (Nm^{-1})

F_s - Material shear force per unit length acting along the tow direction in the SS test (Nm^{-1})

$f_{at\theta}$ - Force due to tension in the stitch direction in the PSS test (Nm^{-1})

$f_{as\theta}$ - Axial machine force attributable to fabric shear in the PSS test (Nm^{-1})

f_s - Material shear force per unit length acting along the tow direction in the PSS test (Nm^{-1})

F_{MS} - Normalised shear force in the machine system of each PF test (Nm^{-1})

F_{IS} - Normalised material shear force in the tow direction in the PF test (Nm^{-1})

F_I - In-plane bending surface in the machine system in the PF test (Nm^{-1})

F_{II} - Normalised inherent in-plane bending force (Nm^{-1})

M_f - Weight of the in-plane bending test specimen (m)

w_f - Width of the specimen in the in-plane bending test (m)

l_f - Length of the specimen in the in-plane bending test (m)

Chapter 1 Introduction

As technology advances, producing a wide range of composite materials has become popular to achieve properties superior to those of the individual constituents. The increasing demand for lightweight, high-performance composites has driven innovation in fabric reinforcements. In collaboration with the University of Edinburgh and Johns Manville, this research investigated a novel unidirectional stitched glass fibre non-crimp fabric called pure-UDNCF which contains only polyamide stitching to stabilise the fabric in the transverse direction to the main tows and has no additional stabilising fibres. The pure-UDNCF provided by the company is designed to serve as an alternative to unidirectional (UD) tapes but with higher thickness. Such materials are receiving increasing attention because of their potential to enable the production of thermoplastic composites with high mechanical properties and directional strength, providing versatility for advanced structural applications. However, the unique structure of pure-UDNCF, stabilised solely by stitching and the absence of additional stabilising fibres, has caused significant challenges during the composite forming.

Beyond the structural role in composite manufacturing for aerospace and automotive components, the unique mechanical properties of the pure-UDNCF open possibilities for innovative applications in various industries. The significant stretching in the stitch direction of the fabric could be used in the field of energy storage, i.e., supercapacitors and flexible battery casings. In addition, the ability to control deformation precisely could lead to the development of smart textiles with embedded sensors for structural health monitoring or physiological data capture. Moreover, the flexibility and deformation behaviour of pure-UDNCF could be explored in biomedical applications, such as reinforcement in prosthetic devices or wearable exoskeletons. To identify specific applications, further investigations are needed, and the ability to manipulate the deformation characteristics of the material offers exciting prospects beyond traditional composite manufacturing, paving the way for the next generation of multifunctional materials.

The collaboration with Jones Manville provided access to pure-UDNCF materials and industrial expertise, ensuring that the research aligns with real-world applications and challenges. The liaison with the University of Edinburgh enriches the project with professional guidance in composite materials and manufacturing. Previous studies at the University of Glasgow have focused on the characterisation and modelling of textile composites, providing a strong foundation for this investigation into the unique forming behaviour of the pure-UDNCF. This project further expands its significance by delving deeper into the specific deformation mechanisms of a material with significant industrial potential. Due to the high anisotropy nature of the fabric and excessive stretching in the stitch direction, the standard mechanical experiments are ineffective for investigation. Consequently, the research required the development of novel experimental methods and extensive effort to understand the mechanical properties and behaviour of the material during forming. This thesis presents the findings from these investigations, the fundamental mechanical properties, and the forming analysis of pure-UDNCF.

The structure of the rest of this chapter is as follows: Section 1.1 provides research background including an overview of fibre-reinforced composites, non-crimp fabrics, the mechanical characterisation tests and the forming of pure-UDNCF. The aim and objectives of the research are discussed in Section 1.2, and Section 1.3 covers the framework of this research project. The thesis structure is provided in Section 1.4.

1.1. Research Background

1.1.1. Fibre-Reinforced Composites

Among the various types of composites, fibre-reinforced polymer (FRP) composites have gained significant popularity in various fields such as automotive, wind energy, and aeronautics engineering where high strength and stiffness with lightweight are required (see Figure 1.1). FRP composites consist of two or more constituents, typically a stiff, brittle fibre surrounded by a matrix. Based on the matrix phase, FRP composites are classified into two main categories, namely thermoset and thermoplastic. When heat is applied, thermoplastics become soft (and eventually liquefied) and harden once cooled. This process is reversible and can be repeated several times without affecting the mechanical properties of the material. At the molecular level, the secondary bonding forces are reduced as the temperature rises due to the increase in molecular motion. The relative movement of adjacent chains is therefore facilitated when stress is applied. In contrast, thermosetting polymers cannot be reshaped or melted once cured because they are network polymers with covalent cross-links between adjacent molecular chains. Thermosetting composites are still the predominant type of advanced composite because of their strong mechanical properties. However, thermoplastic composites are gaining an increasing market share due to advantages including enhanced ductility, improved impact resistance, faster processing rates and better recyclability [1].

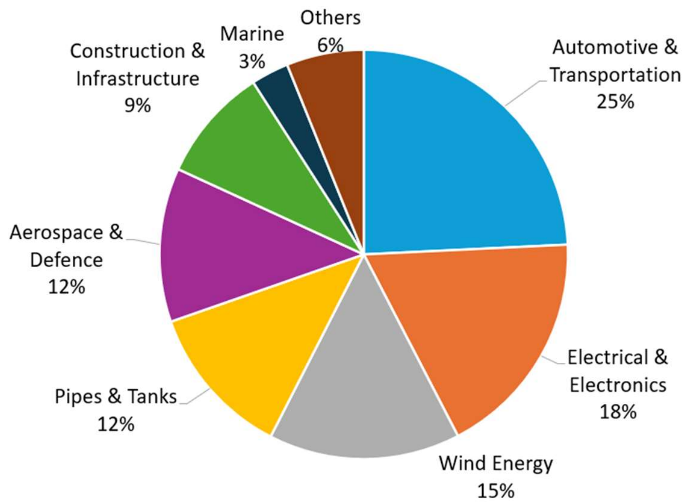

Figure 1.1: Market share distribution of fibre-reinforced polymer composites [2]

1.1.2. Non-Crimp Fabrics

At present, thermoplastic composites reinforced with continuous fibres are gaining popularity in high-performance applications due to the improvement of mechanical properties achieved through control of fibre distribution and direction, as well as recyclability and lightweight. Among engineering fabrics, glass fabrics offer several distinct advantages as reinforcement materials including cost-effectiveness, high tensile strength, electrical insulation properties, compatibility with various resin systems and versatility in fabric forms (such as woven and non-crimp fabrics) [3] [4]. The behaviour of the reinforcement during the forming process is significant because the presence of defects such as wrinkles, tearing, and fibre waviness that are potentially induced during forming will influence the mechanical properties of the final product. Therefore, a deep understanding of the reinforcement material and its forming behaviour is required for efficient manufacturing. Finite Element Simulations (FEM) are important in manufacturing as they predict how reinforcements deform during forming processes, allowing for parameter optimisation, defect reduction, and improving product quality. Accurate simulations begin by characterising the mechanical and forming behaviour of the material, including shear, tensile, bending stiffness, and frictional characteristics. Experimental data from these characterisations provide essential inputs to develop and validate the FEM models, ensuring reliable predictions and efficient manufacturing processes.

Among the broad category of fabric reinforcements, non-crimp fabrics (NCF) have gained significant attention due to their unique characteristics, which provide an optimal balance between mechanical performance (e.g. strength and stiffness) and manufacturability [5]. NCFs are generally multiaxial, stitched reinforcements that eliminate the crimp occurring in woven fabrics and allow fibres to align in predetermined directions. Unidirectional non-crimp fabrics (UDNCF) are a specialised form of NCFs where all fibres are aligned in a single direction, optimising load bearing in the main fibre direction. A unidirectional orientation is particularly useful for applications that require high strength along a specific axis, such as wind turbine blades. There are two types of UDNCF namely quasi-UDNCF and pure-UDNCF. The main difference between these two reinforcements is that in quasi-UDNCF, stitches are perpendicular to the main tows and the fabric also contains a small weight fraction of additional glass fibre tows, orientated transverse to the main fibre direction to stabilise the fabric during handling and forming. The fabric structure of pure-UDNCF consists only of tows and stitches that are perpendicular to each other, here there are no additional stabilising fibres. These differences between the two fabrics lead to very different mechanical forming behaviours. This thesis focuses on pure-UDNCF, a less explored variant of non-crimp fabrics.

1.1.3. Mechanical Characterisation Tests of Pure-Unidirectional Non-Crimp Fabrics

In this thesis, the forming mechanics of various engineering fabrics are investigated using several experimental methods, though the focus is on pure-UDNCFs. The cantilever bending test, the uniaxial bias extension (UBE) test and the picture frame (PF) test are commonly used methods for characterising the forming behaviour of engineering fabrics. The cantilever bending test measures the out-of-plane bending stiffness of warp, weft, and bias directions of the fabric. The latter also allows the torsional stiffness of unsheared fabric to be measured using inverse modelling. One of the main deformation mechanisms during draping in most engineering fabrics is shearing. The shear stiffness of the fabric is directly determined by the UBE test and the PF test. In addition, the in-plane bending, and torsion stiffness of the fabric can be indirectly determined via inverse modelling through the development of an accurate model of the system [6]. Shear deformation of woven fabrics occurs due to in-plane rotation of the tows at interlacing points and sliding of these tows relative to each other [7]. The shear deformation of pure-UDNCF involves the relative sliding of unidirectional tows, which differs from woven fabrics due to the presence of stitches. During the draping of pure-UDNCF, large transverse strains can be reached due to the presence of low-stiffness stitches perpendicular to the main load-bearing tows and the absence of stabilising fibres. Thus, compared with other biaxial fabrics, the in-plane deformation of pure-UDNCF is complex and dominated by transverse stretching and shear deformations. Figure 1.2 shows the UBE test specimens of plain-woven fabric (Figure 1.2a) and pure-UDNCF (Figure 1.2b&c) at the same shear angle. The pure-UDNCF specimen experiences an additional type of deformation during the UBE test, i.e., stretching in the stitch direction (see the yellow arrow in Figure 1.2b; Figure 1.2c shows a zoomed-in view of Figure 1.2b). This can be observed by comparing the side lengths of the central region, L_A and L'_A in the specimen. Due to this complex deformation, the pure-UDNCF cannot be fully characterised by the common experiments i.e., tensile, UBE and PF tests and remains challenging due to their complex structural properties and anisotropic nature.

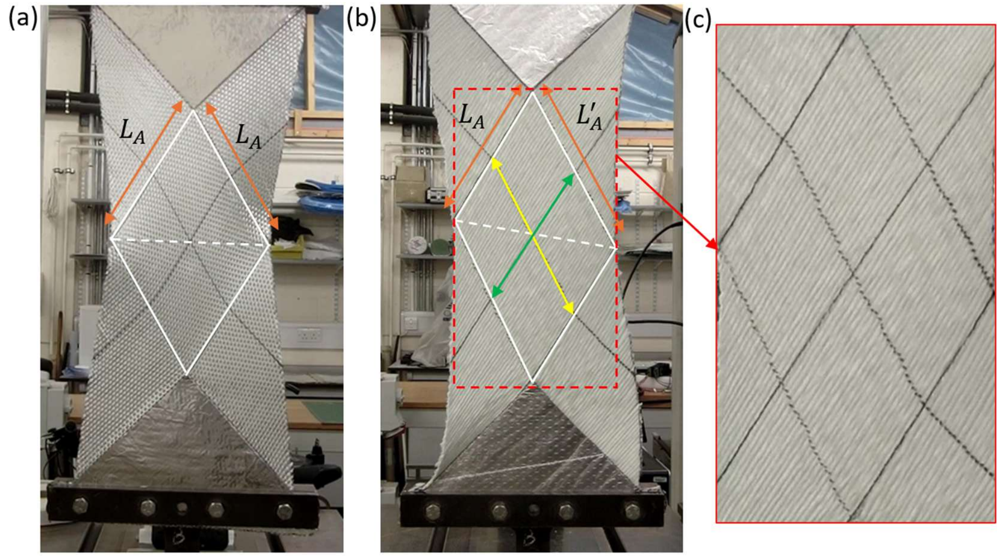

Figure 1.2: Deformed uniaxial bias extension specimens at 30˚ shear angle (a) plain-woven (b) pure-UDNCF, the yellow and green arrows indicate the initial chain-stitch direction and the tow direction, respectively. (c) a magnified image of (b). The white dashed line marked in the figures indicates that the deformation within the central region of the pure-UDNCF is not pure shear

1.1.4. Forming of Pure-Unidirectional Non-Crimp Fabrics

The deformation mechanics of a material significantly influence the success of the forming process over a given geometry. Unlike woven fabrics, NCFs do not have inherent crimp, which alters their response during forming. Pure-UDNCF provides better formability than other NCFs because the absence of stabilising fibres reduces restrictions on fibre movement during forming, allowing the material to conform more easily to complex geometries. However, if pure-UDNCF fabrics are not carefully managed, they are more prone to defects for the same reason, i.e., lack of stabilising fibres. The formability of pure-UDNCF is influenced by factors such as stitch patterns, anisotropic mechanical behaviour, boundary conditions, and the complex interactions between these factors. In addition, the orientation between the plies is important to control the mechanical properties and optimise the product for its intended use. When forming the NCF, it is necessary to achieve optimal re-orientation of tows and stitches to allow defect-free products with desired mechanical properties. Hemispherical forming by punch and die is a common method to form a flat 2D fabric into a complex 3D shape. The forming experimental data, such as shear angles and stretching in the stitch direction at selected locations of the hemisphere, can be used to validate the output of the numerical forming models (created by inputting the results of characterisation tests of engineering fabrics, such as tensile, shear, and bending tests).

1.2. Aim and Objectives of the Research

This doctoral thesis focuses on the experimental characterisation and forming analysis of pure-UDNCFs. Characterisation tests are focused on capturing the material behaviour specific to pure-UDNCF, including anisotropic and nonlinear responses. Appropriate data obtained by these experimental methods can be used to develop constitutive models to predict the behaviour of the material. Furthermore, the hemispherical forming of pure-UDNCF is performed using the punch-and-die method, where different deformation modes are observed. Once a constitutive model is developed with appropriate input parameters, it can be incorporated into a numerical simulation to predict the behaviour of the material during forming. The experimental forming results can then be used to validate the numerical forming simulations.

The objectives of this research are as follows:

- **Develop appropriate new characterisation tests and modify the standard tests** to measure the mechanical properties of pure-UDNCFs required by the forming models, which cannot be accurately assessed through existing testing techniques.
- **Proposing methods to decouple the forces** acting on the pure-UDNCF using selected experiments. The presence of more than one low-energy deformation mode for pure-UDNCF and the coupling between those deformations is possible due to the unique fabric structure including low-stiffness stitches. The challenge is to isolate the separate contributions to the measured force and from this, to estimate the various stiffnesses.
- **Perform hemispherical forming experiments** on pure-UDNCF to observe material behaviour under complex forming conditions including forming defects such as wrinkles, gaps and fibre waviness.
- **Explore methods to obtain experimental forming data**, specifically measuring shear angles and stitch stretching at selected points on the hemisphere to understand localised fabric deformation (this data can then be compared with the forming simulations).

1.3. Research Area

Figure 1.3 shows the framework of this research project that focuses on experimental analysis of the forming behaviour of pure-UDNCFs. It consists of two main sections and Figure 1.3 shows the various phases involved in the research.

- **Characterisation Tests:** The research begins by applying conventional mechanical characterisation techniques to the fabric as an initial attempt to understand its baseline properties. However, since pure-UDNCFs lack stabilising fibres, these tests are insufficient for full characterisation. To address constraints in conventional procedures, new experimental tests are developed. These tests aim to accurately capture the unique mechanical properties of pure-UDNCF, focusing on shear, tensile strain in the stitch direction, and bending behaviours under different conditions. It is difficult to capture the accurate properties when coupling occurs between different deformation modes. To further refine the characterisation, a method is implemented to isolate specific contributions from different experiments.

- **Forming Tests:** This section focuses on the behaviour of the fabric during complex forming conditions. Hemispherical forming is selected to observe the fabric deformation under complex shapes and a detailed analysis is performed after forming. Data such as shear angles and stretching in the stitch direction at selection locations on the formed hemispheres is collected, this data can ultimately be used to validate any future computational models that predict the forming behaviour of pure-UDNCFs.

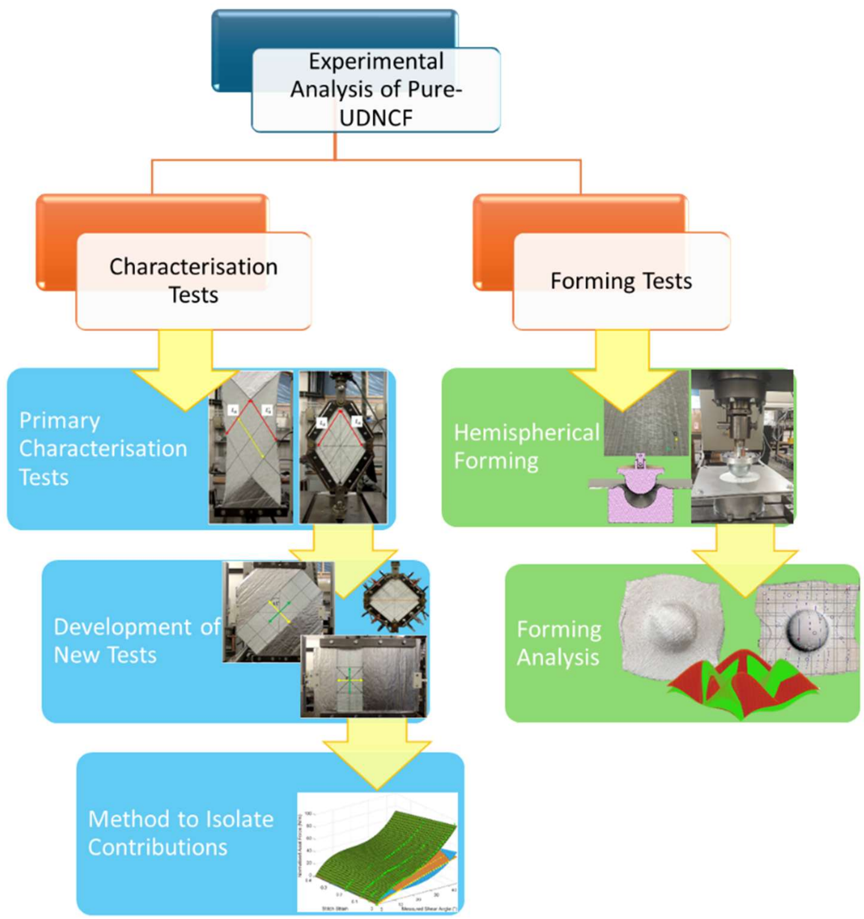

Figure 1.3: The structural framework of the thesis

1.4. Thesis Structure

Each chapter contains outputs that align with the objectives stated in Section 1.2 and the structure of the thesis is as follows:

- **Chapter 2** provides a comprehensive literature review on fibre-reinforced composites, fabric reinforcements, fabric architecture, fabric characterisation tests, full-field measurement method for fabric deformation, dry fabric forming and computation framework of fabric reinforcements. This chapter will also identify research gaps that underline the need for the current study.
- **Chapter 3** details the shear and tensile experiments using standard tests. This chapter discusses the two principal shear tests on pure-UDNCF, namely the uniaxial bias extension test and the tightly-clamped picture frame test, and compares the results of these two tests. Furthermore, the chapter proposes a few modifications to the tightly-clamped picture frame test to address misalignment and clamping condition errors and a way to adjust friction in the PF rig bearings. In addition, the standard tensile test along the stitch direction of the fabric is explained in the chapter.
- **Chapter 4** presents new shear experiments on the pure-UDNCF, i.e., cruciform bias extension test, parallelogram shear-stretch test, and simple shear test to obtain different combinations of shear and tensile strain in the stitch direction with a better control of in-plane bending. In addition to these new shear tests, another new picture frame test method i.e., the pre-stretched PF test is proposed to achieve insights into unexplored areas of the deformation space. Except for the tensile test in the stitch direction, all other tests performed on Pure-UDNCF show multiple deformation contributions. Therefore, a new interactive method is proposed to isolate different stiffnesses (shear, in-plane bending and tensile) of the pure-UDNCF.
- **Chapter 5** discusses the bending characterisation of the pure-UDNCF. The cantilever bending test is performed to obtain the out-of-plane bending stiffness of the fabric. Furthermore, this chapter proposes a new test method to qualitatively measure the in-plane bending of engineering fabrics.
- **Chapter 6** describes the hemispherical forming experiment and analysis. This chapter covers the experimental forming setup, procedures, and fixing methods applied to maintain the desired shape after forming. Furthermore, a novel approach to gathering data from formed hemispheres i.e., measuring shear angles and stretching in the stitch direction at selected locations is discussed.
- **Chapter 7** summarises the findings, evaluates the contributions of the research, and suggests potential directions for future studies on pure-UDNCF characterisation and forming.

Chapter 2 Literature Review

2.1. Introduction

Fibre-reinforced composites (FRCs) have emerged as advanced materials with exceptional strength-to-weight ratios, superior design flexibility and tailorable properties. This chapter explores the existing knowledge of these materials, with a particular emphasis on how fibre reinforcement and its architecture influence the performance of FRCs. The review begins by exploring the concept of fibre reinforcement, examining various types of fibres and their influence on the mechanical behaviour of composites. It then investigates the critical aspect of fibre architecture, discussing how woven (crimp fabric), and non-crimp fabric significantly impact the final properties of the material. The literature review then examines various fabric characterisation tests to assess the mechanical properties and behaviour of textile reinforcements used in FRCs. These tests provide essential data to develop constitutive models that simulate the forming processes.

The chapter further explores full-field measurement methods for fabric deformation. These advanced techniques offer a comprehensive understanding of how fabrics deform under external force, aiding in the optimisation of forming processes and predicting component behaviour. Afterwards, the review explores various dry fabric-forming methods, which encompass the fixation method of fabrics used to create the desired shape of the preforms. Finally, the chapter examines the role of numerical modelling in fabric mechanics. Computational tools allow researchers to simulate the behaviour of fabrics under various conditions, providing valuable insights into their performance and aiding in the design of optimised composite structures. Understanding the modelling approaches is important for selecting the most suitable method to accurately simulate the forming process. This literature review aims to establish a strong foundation for the research presented later in this thesis by comprehensively analysing these key aspects. The concluding section of the literature review emphasises the gaps in knowledge that this research aims to address.

2.2. Fibre-Reinforced Composites

In recent years, fibre-reinforced composites have gained considerable attention in various fields including aerospace, automotive, and structural engineering where light-weighting is desirable with high strength. FRCs can be categorised into two main groups based on the matrix phase, namely thermosets and thermoplastics. Thermosetting composites are the most widely used type of advanced composite. Nevertheless, continuous fibre-reinforced thermoplastic composites are capturing an increasing share of the market due to improved impact resistance, damage tolerance, and flexible manufacturing process (i.e., can be reheated and reshaped multiple times) compared to thermosetting composites [1]. In addition, the recyclability of the thermoplastic matrix offers potential for sustainable manufacturing practices that align with growing environmental concerns. However, the high-temperature processing conditions and higher viscosity during the melting states typically required for these materials are challenging [8].

FRCs can be again categorised into two classes based on the length of the reinforcing fibres, namely continuous (i.e., fibres with a very high aspect ratio or length-to-diameter ratio) and discontinuous [9] [10]. The high aspect ratio of continuous fibres allows efficient and uniform load transfer throughout the composite. Also, continuous FRCs show high stiffness, damage tolerance and fatigue due to their stable and well-organized structure. Therefore, continuous FRCs are categorised under high-performance composites [11] [3]. The preferred alignment of fibres depends on the type of loading applied to the composite. Continuous FRCs can be further classified into unidirectional (i.e., fibres oriented in a single direction) and bi- or multi-directional (i.e., fibres oriented in two or more directions). Studies comparing the mechanical properties of unidirectional and bidirectional glass FRCs [12] [13] imply that composites with unidirectional fibres exhibit better properties, including higher tensile, and compressive strengths, than bidirectional composites (stitched or woven) because the continuous unidirectional fibres are aligned in the direction of axial loading, and provides maximum benefits for the mechanical properties of the composite (i.e., predominantly oriented fibres allow for efficient load transfer along the fibre direction). However, the choice between unidirectional and bidirectional composites depends on the application: unidirectional composites excel under uniaxial loading, while bidirectional or multi-directional composites are better suited for multi-axial loading conditions.

When compared to continuous FRCs, discontinuous or short FRCs provide excellent low-cost productivity and formability in complex shapes [14]. The random orientation of short fibres leads to isotropic properties by distributing loads in multiple directions, whereas aligned short fibres provide high stiffness and strength in the direction of alignment. The properties of the discontinuous FRCs depend on the percentage of fibre alignment [15] and researchers have used different methods to align the short fibres. Gan et al. [16] achieved 54% and 81% of the fibre alignment in the range of ±5˚ and ±10˚, respectively using the vibration-assisted dry alignment method. Yu et al. [17] proposed another method to align the short fibres by changing the momentum of the fibre suspension i.e., subjecting the suspension to a high-velocity flow field. This study further emphasises that aligning 65–67% fibres within ±3° range can achieve competitive mechanical properties with continuous FRCs. To improve the performance of FRCs, scientists are motivated to develop composite laminates by combining continuous and short fibre-reinforced materials [16] [18] [19] [20]. The presence of continuous fibres in multiple directions provides good strength and stiffness while the presence of short fibres provides better fracture toughness and impact resistance. Hence, these composite laminates offer versatile solutions for various engineering applications. All classifications of FRCs discussed in this section are summarised in Figure 2.1.

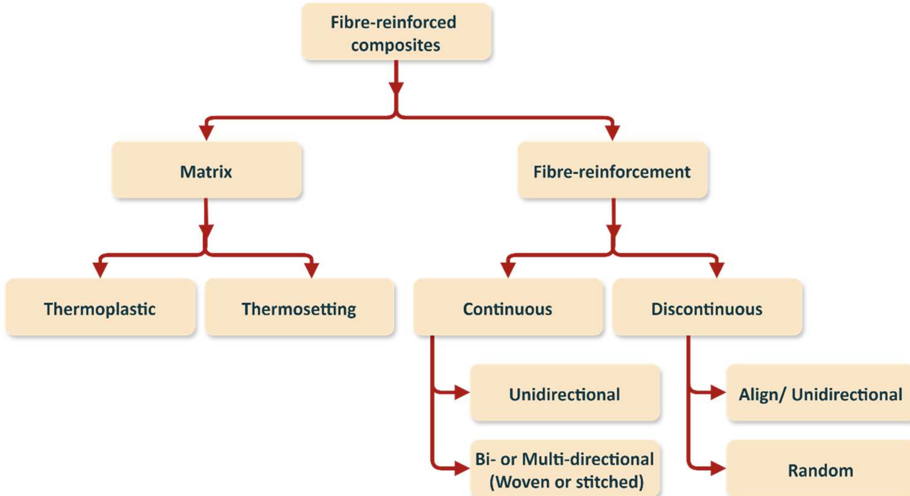

Figure 2.1: Classification of fibre-reinforced composites

2.3. Fabric Reinforcements

Depending on the nature, fabrics can be categorised into two, natural and synthetic fabrics. Natural fibres were popular in the early nineties due to their high abundance and cost-effectiveness. Recently synthetic fibres have increased in popularity compared to natural fibres due to their superior mechanical properties [11]. Table 2.1 compares the mechanical properties of selected synthetic and natural fibres. Researchers primarily concerned with mechanical properties of products, i.e., strength (tensile, compressive, flexural, shear), toughness and impact resistance, are motivated to develop synthetic fibre-reinforced composites. They are also interested in developing hybrids (i.e., a combination of both natural and synthetic fibres) to maintain better mechanical properties of the products with environmental friendliness and cost-effectiveness [21].

Table 2.1: Comparison of the mechanical properties of selected synthetic and natural fibres *[22]*

	Fiber	Diameter (μm)	Tensile Strength (MPa)	Tensile Modulus (GPa)	Density (g/cm^3)
Synthetic	Carbon	5–10	2000–5000	200–600	1.8
	E-glass	7–25	1950–3500	70–80	2.55
	S-glass	8–12	4500–4700	75–90	2.5
	Kevlar	12	3000–3150	63–67	1.4
Natural	Basalt	10–20	2800–3100	80–90	2.6–2.7
	Flax	12–20	400–600	12–25	1.2–1.5
	Hemp	25–500	300–700	20–70	1.3–1.5
	Sisal	11–22	350–700	7–22	1.4–1.5
	Kenaf	30–40	150–250	10–20	1.1–1.2
	Jute	17–20	350–780	20–30	1.3
	Coir	10–24	550–650	4–6	1.2

Among the many types of synthetic fibres, glass, carbon, and aramid (Kevlar) are commonly used to produce fibre-reinforced composites. Carbon and glass are further sub-classified under inorganic synthetic fibres and aramid is classified under organic (see Figure 2.2). Among all reinforcing fibres, carbon fibres exhibit significantly higher tensile strength and modulus due to the presence of crystalline graphite [23]. Most carbon fibres are made using PAN (Poly-acrylonitrile) as the precursors, while the rest are extracted from pitch (i.e., byproduct of the petroleum distillation process) or rayon (i.e., regenerated cellulose) [24] [25]. The precursor used to produce carbon fibre has a significant impact on the carbon content and the crystalline structure of the final product (i.e., the physical and mechanical properties of the fibre vary depending on the selected precursor) [24]. Newcomb and Chae [24] compared the mechanical properties of commercially available carbon fibres produced using three different precursors (i.e., PAN, pitch, and rayon-based carbon fibres). Among the carbon fibres of approximately the same diameter (7µm), PAN-based carbon fibres show higher tensile strength than pitch-based carbon fibres, while rayon-based carbon fibres show the lowest tensile strength (see Table 21.1 in Newcomb and Chae [24]). However, the greater tensile modulus of pitch-based carbon fibres implies that they are stiffer than PAN-based carbon fibres. In addition to the tensile properties, commercially available PAN- and pitch-based carbon fibres have variable electrical and thermal conductivity ranges. Carbon fibre-reinforced composites are more sensitive to fibre misalignment than glass fibres, and even a little misalignment results in a significant loss in compressive and fatigue strength. The crystal alignment strengthens the carbon fibre. However, on the other hand, fibres are brittle and can break more easily under impact loads than glass fibres [26].

Aramid fibres, known for their excellent mechanical properties including higher impact and abrasion resistance than ordinary inorganic fibres due to highly oriented molecular structure with a high strength-to-weight ratio, play an important role in fibre-reinforced composite materials (i.e., especially in the manufacture of ballistic protection products) [27] [28]. Aramid fibres can be classified into two groups, namely para-aramid, and meta-aramid, depending on the relative position of the amide bonds (CO–NH) in the fibre structure. In terms of mechanical properties, especially in tensile strength, para-aramid fibres (such as Kevlar®) offer higher strength compared to meta-aramid fibres (such as Nomex®) due to the alignment of strong covalent bonds along the fibre axis [29]. Meta-aramid fibres, on the other hand, are commonly used in the production of fire-retardant fabrics because of their high chemical and thermal resistance [27]. Nevertheless, aramid fibres often present low compression strength due to the poor interactions between adjacent polymer chains (i.e., hydrogen and van der Waals bonds) [30]. In addition, aramid fibres are less resistant to UV and moisture. Therefore, the use of aramid fibres for applications with higher environmental impacts is minimised [31].

Glass fabrics are commonly used as an engineering fabric due to their advanced characteristics such as high tensile strength, wear and impact resistance, chemical and water resistance, and excellent thermal insulation properties including cost-effectiveness [10]. Among glass fibres of various chemical compositions, the highest percentage of continuous fibre-reinforced composites are made of E-glass fibres (Electrical grade glass fibres) due to better mechanical properties with cost-effectiveness [29]. Glass fibres with improved strength are called S-glass fibres (high Strength glass fibres). Compared to E-glass, S-glass fibres have 40% improved tensile and flexural strength with a maximum of 20% higher compression strength [26]. The other types of glass fibres are A-glass (alkali glass), AR-glass (alkali-resistant glass), C-glass (chemical-resistant glass), D-glass (dielectric constant glass), R-glass (high strength glass), ECR-glass (E-glass with chemical resistance), S-2 glass (high-strength glass fibre with a slightly different composition than S-glass), M-glass (fibre with additional flexibility) and Z-glass (resistance to various environmental factors including UV, acid, salt and alkali) [23] [32] [33]. Since different types of glass fibres are available, it is important to select the most suitable type of glass fibre to achieve the desired performance with a price target for glass fibre-reinforced composite production. Based on the fabrication method, glass fabrics are available in braided, knitted, stitched, woven and non-woven forms and the selection may vary depending on the final requirement. Also, two-dimensional, or three-dimensional architectures can be woven using glass fabrics [34].

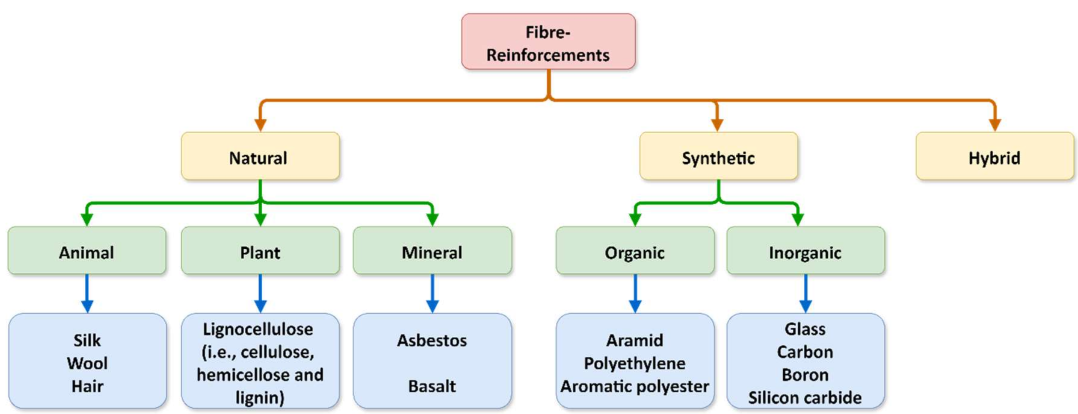

Figure 2.2: Classification of fibre-reinforcement based on the nature of the fibres

2.4. Fabric Architecture

Based on the fibre architecture, engineering fabrics can be classified as unidirectional (1D), planar (2D) or three-directional (3D) structures. Compared to unidirectional fabrics, textile fabrics are preferred due to the advantages of handling, draping, thickness, and strength of the composite materials produced [35]. Forming textiles allows the development of complicated geometries. 2D textiles are available in woven, braided, knitted and random forms and this report focuses on two-dimensional woven fabrics and non-crimp fabrics. In the classification of 3D textiles, Mouritz [36] did not consider non-crimp fabric as a 3D structural textile due to the presence of non-structural secondary fibres in the direction of thickness. Therefore, non-crimp fabrics are classified here as another type of textile fabric.

2.4.1. 2D Woven Fabrics

2D woven engineering fabrics are manufactured by interlacing two sets of tows into 0° (warp) and 90° (weft or fill). There are three basic types of 2D woven fabric, namely, plain, twill and satin. The float length (FL) is the number of tows in the vertical direction, bound by a tow in a horizontal direction) is a weave parameter and plays a significant role in the geometry of the fabric [37]. The simplest structure is a plain weave fabric. It is manufactured by interlacing a regular combination pattern of tows (Figure 2.3a), woven one warp yarn over and under one weft yarn (FL = 1). In the twill structure (Figure 2.3b), one warp yarn is woven over two and under one weft yarn (FL = 2) and in the structure of the satin fabric, one warp yarn is woven over more than two weft yarns and under one weft yarn (Figure 2.3c) [38] [39].

Compared to the twill and satin weaves, a plain weave possesses excellent stability due to the symmetrical weave structure. Plain fabrics can absorb higher energy and withstand deformation due to high friction between the tows. On the other hand, satin weave fabrics are more drapable and have a lower crimp (the yarn waviness due to interlacing) than plain and twill types. The forming properties of the fabric are strongly dependent on the weave parameters, including architecture, tow size, and the gap between tows (open-weave or closed-weave) [38] [40].

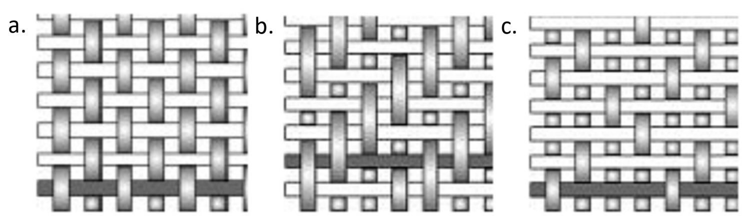

Figure 2.3: Schematic representation of conventional 2D woven fabric types (a) Plain (b) Twill (c) Satin [37]

2.4.2. Non-crimp Fabrics (Stitched Fabrics)

Non-crimp fabric (NCF) is a type of engineering textile consisting of one (uniaxial), two (biaxial) or many (multiaxial) aligned layers of differently oriented unidirectional layers of tows held together with a non-structural secondary thread [37] [41] (see Figure 2.4). Compared to woven fabrics, NCFs have an advantage in terms of mechanical properties such as improved strength and stiffness due to the absence of crimping. Besides, the presence of secondary thread or stitching fibres improves the properties in the direction of thickness by bonding the unidirectional layers of tows together. When designing an NCF, significant attention should be paid to its structure to improve the mechanical properties, and drapability over moulds of various shapes. The stitching in the NCF plays an important role in the drapability of the fabrics. Stitches are typically made of polyester due to its excellent knitting properties (such as better tensile strength, flexibility, and tear resistance, which help to improve the properties in the direction of thickness by binding the unidirectional layers of tows together) and cost-effectiveness [42]. However, weak bonding between polyester yarns and matrix may cause failure in the composite [43]. In some studies, polyester stitches are replaced with polyethylene [44] [45] stitches or structural fibres such as E-glass [46] [47] [48] to improve fabric properties. Using matrix-soluble stitching materials with low melting points, such as polyamide and phenoxy, rather than polyester yarns, can improve the mechanical properties of composites [49].

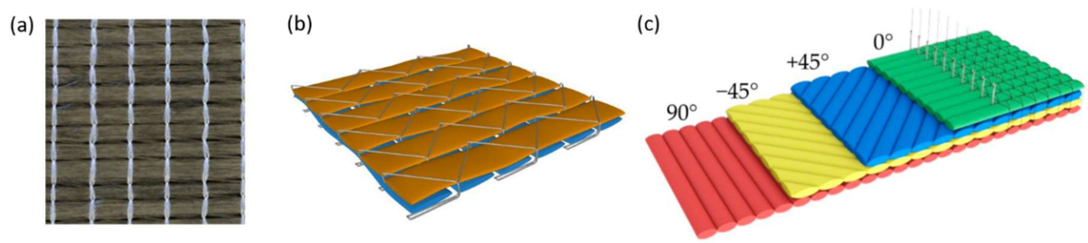

Figure 2.4: (a) uniaxial (b) biaxial (c) multiaxial non-crimp fabrics with stitches [50] [51] [52]

The stitching parameters (i.e. stitch gauge, length, and pattern) are essential in developing a suitable NCF based on the final application. The stitching gauge reflects the number of stitches over the width of the fabric; a higher number improves the stability but reduces the drapability. The gap between two stitches is known as the stitching length, and the drapability increases with shorter stitch length, however, the cost of the production increases as the fabric production rate decreases. There are different types of stitching patterns (ex: chain, tricot, tricot-chain, etc.) that can be used to control the formability of the NCF. Generally, chain stitching can improve the drape quality, while tricot stitching enhances the stability (or reduces the pre-shear) of the fabric. The optimal combination of these two patterns can balance the drape and stability properties [43].

The experimental and numerical analysis of the forming behaviour of unidirectional NCFs (UDNCFs) is limited when compared to biaxial engineering fabrics (i.e., woven, and biaxial NCFs). Most previous experimental investigations into the formability of UDNCFs, e.g. [10] [44] [46] [53] [54] [55] [56] [57] [58] have considered fabrics that are not purely unidirectional and do in fact, contain a small weight fraction of glass fibre tows, orientated transverse to the main fibre direction, incorporated to stabilise the fabric during forming (referred to as 'quasi-UD-NCFs' by Vallons et al. [59], a terminology adopted throughout this thesis). Despite their relatively minor influence on the final mechanical properties of a composite part, the relatively high stiffness of these stabilising tows (compared to the stitch stiffness) means that they can play a significant role in the forming behaviour of the fabrics [44]. The in-plane shear and out-of-plane bending of quasi-UD-NCFs were experimentally investigated by several authors [10] [44] [46] [54] [55] [56] [57] [58]. The in-plane shear behaviour is often found to be asymmetrical with respect to the shear direction, because of the position and orientation of the stitching. The influence of the stabilising tows on formability depends on several factors, including the degree of attachment of the stabilising tows to the rest of the fabric; a looser coupling allows for more intraply-slip, potentially leading to 'ambiguous' mechanical behaviour [44]. Despite the interest in quasi-UD-NCFs, the forming mechanics of purely UD-NCFs, i.e. those that use only stitching to stabilise the fabric and have no additional stabilising transverse glass-fibre tows stitched to the back of the fabric have received relatively little attention [60] [61]**.**

2.5. Fabric Characterisation

A finite element simulation is an effective tool for determining the effect of the forming condition on deformation. The input parameters for the macroscale constitutive models for the forming behaviour can be predicted using multiscale modelling approaches [62] [63] [64], however, the constitutive behaviour of a material is usually determined via experimental analysis [6] [65] [66]. Harrison P. [67] emphasises six key mechanical properties that primarily influenced the deformation of engineering fabrics and advanced composites during forming:

- Tensile properties along two fibre directions - the ability of the material to resist stretching.
- Shear resistance – the ability to resist in-plane deformation caused by shear forces.
- Out-of-plane flexural modulus - stiffness when bending out of the plane.
- In-plane flexural modulus - resistance to bending within the plane.
- Transverse compressive modulus - how the material resists compression across its thickness.
- Integrity/cohesion of the sheet - the structural consistency of the material and ability to hold together during forming.

In addition to these properties, friction and boundary conditions of the forming process are critical in controlling the behaviour of the fabrics and composites under stress during forming and preventing the formation of unwanted defects. The interaction of these mechanical properties can result in various deformation modes in the engineering fabrics (see Figure 2.5). The deformation of engineering fabrics during forming can be classified into in-plane and out-of-plane deformations based on the direction of the applied forces and the resulting fabric response. In-plane deformations refer to forces applied on the fabric within its plane, without causing it to deviate from its original surface, such as tension, compression, and shear. Out-of-plane deformations, on the other hand, involve forces that cause the fabric to bend or twist perpendicular to its original plane, resulting in three-dimensional distortions [68] [69]. One of the main modes of deformation that enables fabric to drape over curved surfaces is in-plane shear. Inter-tow slippage and cross-over point slippage influence fibre movement and shear compliance. In stitched fabrics, tow-to-stitch slippage is the movement of yarns relative to the stitching that influences shear and tensile behaviour [70]. In addition, in-plane bending influences fibre waviness, while out-of-plane bending determines the ability of a material to conform to double-curved surfaces without excessive stiffness or wrinkling [71]. Therefore, understanding these deformation modes is essential for optimising forming processes and predicting the mechanical response of engineering fabrics. This section will describe different characterisation test methods used for engineering fabrics, the principles behind each test, and the modifications stated in the literature to improve results.

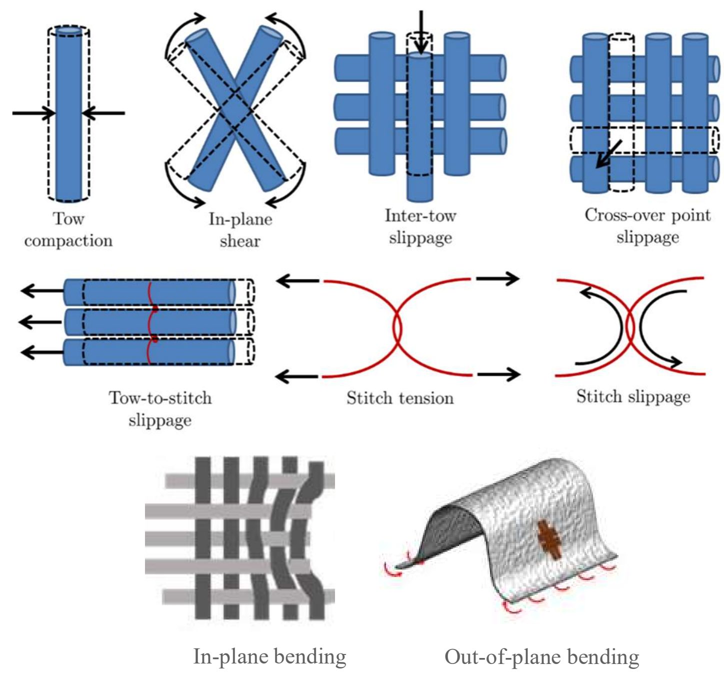

Figure 2.5: Deformation modes of engineering fabrics [70] [72] [73]

2.5.1. Bending Tests

Bending tests provide essential insight into material stiffness, drape, and overall performance in applications where bending is a factor. Various test methods are available to determine the bending stiffness of fabric reinforcements, and those methods can be divided into two groups, namely methods that provide basic stiffness and methods that provide advanced bending behaviour of materials. Peirce bending test (or cantilever bending test) [74] and Kawabata bending test (or KES-FB2 bending test) [75] are the most common bending tests used to evaluate the bending properties of fabric reinforcements. Among these two tests, the cantilever bending test is categorised under the first group where it provides a simple method of determining the bending stiffness of the fabric by linear deformation theory. The Kawabata method belongs to the second category and can capture the complex non-linear behaviour (i.e., moment-curve response) of fabrics [76]. The following sections discuss these two common bending tests used to characterise textile reinforcements in more detail.

2.5.1.1. Cantilever Bending Test

Peirce's cantilever test [74] is a common test method used to determine the out-of-plane bending stiffness of textile materials in the warp, weft, and bias directions. In addition, the torsional stiffness of unsheared fabric can be estimated via the development of an accurate model of the system (i.e., inverse modelling) [6]. The American Society for Testing and Materials (ASTM), the International Organization for Standardization (ISO), and British Standard (BS) are nationally and globally recognised organisations that developed and published many materials testing standards. Peirce's cantilever test is the basis for the ASTM D1388 [77], ISO 4604 [78], and BS 3356 [79] standards as well as for the FAST (Fabric Assurance by Simple Testing) method [80]. According to the cantilever bending test with fixed angle bending meters/flexometers method, the fabric bends under its weight and the overhanging length of the fabric (l) is measured at a predetermined angle (see Figure 2.6). The cantilever bending test adheres to the principles of beam theory and assumes that the fabric is linear elasticity [74].

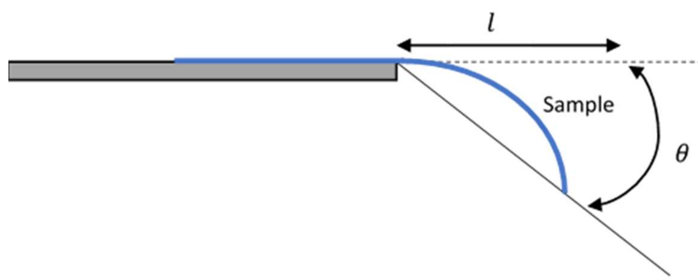

Figure 2.6: Schematic diagram of the cantilever bending test

By utilising elasticity theory and empirical data, Peirce derived two equations to calculate the bending length of the fabric, C, and the flexural rigidity, G, in relation to the overhanging length, l, the angular deflection, θ (see Figure 2.6), and the weight per unit area of the fabric, w;

$$C = l.f_1(\theta) \tag{2.1}$$

where, $f_1 = \left[\frac{\cos\frac{\theta}{2}}{8\ \tan}\right]^{1/3}$

$$G = wC^3 \tag{2.2}$$

All the standard methods, including the British standard (BS 3356 [79]), require the use of a flexometer platform with a 41.5° slope (i.e., predetermined angle). This angle simplifies Eq. 2.1 and makes it easy to calculate the bending length,

i.e., if $\theta = 41.5°$ then, $\left[\frac{\cos\theta/2}{8\tan\theta}\right]$ = 0.5

and

$$C = \frac{l}{2} \tag{2.3}$$

Substituting Eq. 2.3 in Eq. 2.2, the flexural rigidity of the fabric can be calculated as,

$$G = \frac{wl^3}{8} \tag{2.4}$$

Forming simulations were conducted to study the reliability of the cantilever bending test [67]. The numerical simulations introduced a correction factor $[f(\theta)]$ to Peirce's equation of flexural rigidity, resulting in a corrected value that closely corresponded (≈0.3%) with the British Standard. This suggests that no considerable adjustment is required for the British standard, as errors in Peirce's power series solution and the assumptions in the British Standard effectively cancel out at an angular deflection of 41.5°.

Modifications of the Cantilever Bending Test by Other Researchers

Most of the literature on determining the flexural rigidity of composite reinforcements is based on Peirce's principle of cantilever theory. The bending device invented by Peirce allowed to measure the angle for a selected overhanging length (see Figure 2.7a). Chu et al. [81] simplified Peirce's method by measuring the overhang length of the fabric for a specific inclined angle (see Figure 2.7b), and the slope of the flexometer was estimated $C/l = 0.5$ at 43° using Peirce's data. According to Bickley's more accurate data [82], Abbott N.J. [83] found that $C/l = 0.5$ when using a 41˚ slope. The angle of 41.5˚ was eventually accepted and all the standard methods (i.e., ASTM D1388 [77], ISO 4604 [78], BS 3356 [79] and FAST [80]) are based on the latter method of measuring the overhang length of the fabric for a specific inclined angle of 41.5˚. Nowadays, commercial bending meters/flexometers (ex: the Shirley stiffness tester (see Figure 2.7c) [84] and the FAST-2 bending testers (see Figure 2.7d) [85]) are designed with a predetermined angle of 41.5˚.

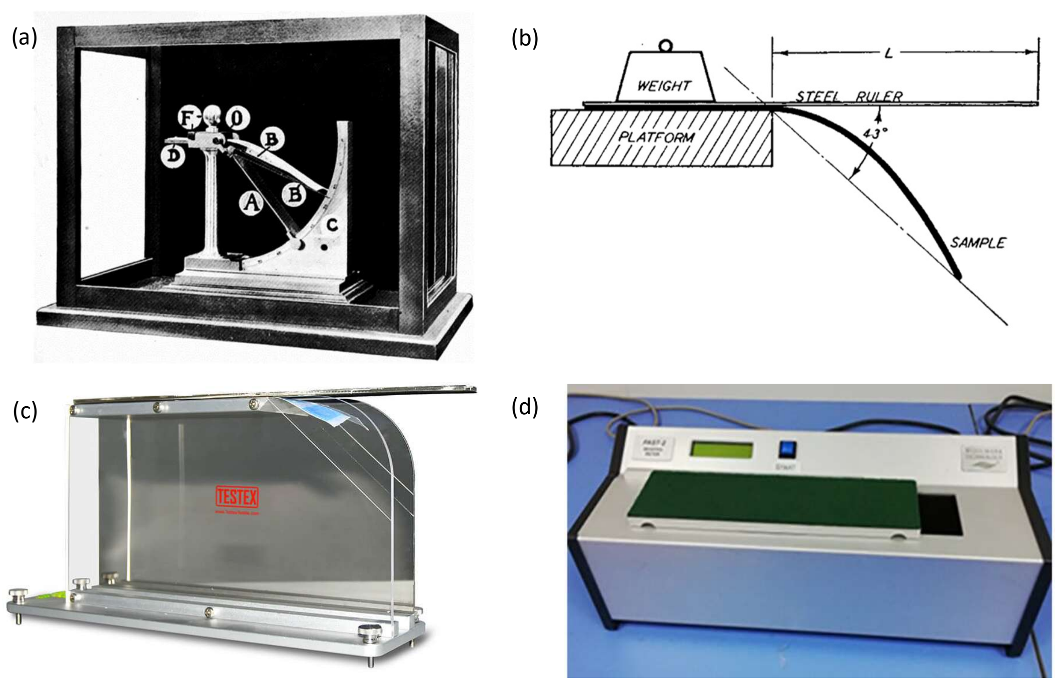

Figure 2.7: (a) Peirce's bending device [74] (b) Chu et al. [81] strip bending tester (c) commercially available Shirley stiffness tester [84] (d) FAST-2 bending tester [85]

In the cantilever test, the specimen and the ruler are manually extended (with a uniform force) along the top horizontal plane of the flexometer and the overhang length of the specimen is measured after the specimen touches the 41.5° slope. The test may contain errors because the technique is manual and requires adequate training. Therefore, researchers have used automated cantilever bending testing machines to avoid human errors [86] [87] [88]. Human error is also possible in determining whether the sample touches the slope. To overcome this, Lammens et al. [89] introduced a cantilever bending setup with an aligned laser plane (see Figure 2.8). This allows better determination of the overhanging length while maintaining the desired angle of 41.5˚.

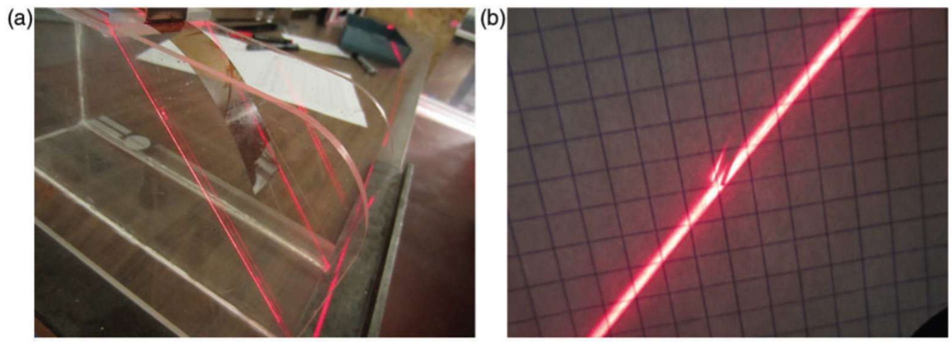

Figure 2.8: (a) A cantilever bending setup with an aligned laser plane (b) Projection onto a sheet of paper of the edge of the sample crossing the laser plane

Apart from the modifications of the typical cantilever bending test setup, some researchers have tried advanced cantilever bending tests to determine the nonlinear bending behaviours of stiff reinforcements. de Bilbao et al. [90] introduced a new device to perform cantilever bending tests under various loads. The new device consists of two units: mechanical and optical. The mechanical unit allows the specimen to deform under its weight and allows larger curves to be reached by adding weight to the free end of the specimen. The optical unit allows taking pictures of deformed specimens (i.e., the Cartesian coordinates of the deformed sample can be obtained for each bending length). This setup allowed nonlinear bending stiffness of engineering fabrics i.e. as a function of curvature and the results implied that bending stiffness decreases dramatically with increasing curvature. de Bilbao et al. [90] further stated that this device can be used to test for yarns or reinforcement with single or multiple layers. Liang et al. [91] used a method similar to de Bilbao et al. [90] and their setup includes an environmental chamber. This allowed further extended testing of composite samples under various temperatures.

Soteropoulos et al. [92] performed the cantilever bending test on a biaxial NCF (0˚/90˚) where the specimen was fixed vertically to avoid nonlinear bending behaviour due to rotation or twisting of the free end of the specimen. In this setup, the specimen deformed only by applying controlled loads to its free end. Dangora et al. [93] used a similar setup to Soteropoulos et al. [92] with an addition of a heating element. This setup allows for characterising the bending behaviour of a thermoplastic cross-ply lamina under high-temperature conditions. Alshahrani and Hojjati [94] further improved this setup by adding a linear actuator to control the sample deflection and applied rate, and a mini-load cell to measure the required load to obtain the relevant deflection (see Figure 2.9). According to the research results, the proposed bending test allowed for precise control of bending shape, processing rate, and temperature, and these parameters were within the optimal range for the tested thermosetting resins. Compared to these methods, the de Bilbao et al. [90] method is more general, with less emphasis on precision and material specificity. Harrison et al. [95] proposed another simple modification to the cantilever bending test to operate under high-temperature conditions using a lightweight aluminium ramp inside a Zwick environmental chamber. This setup enabled simultaneous testing of multiple specimens and faster data collection.

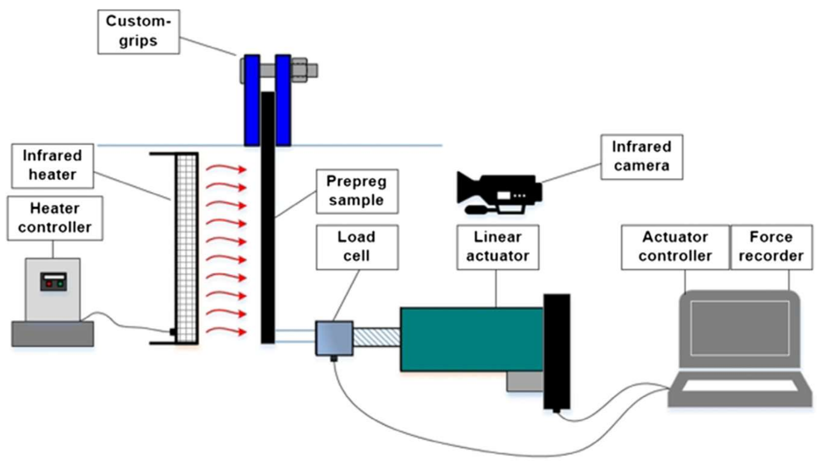

Figure 2.9: Schematic diagram of the vertical bending test setup [94]

2.5.1.2. Kawabata Bending Test

Kawabata's Evaluation System (KES) provides an alternative method for determining the non-linear bending moment-curvature relationship of fabrics during a load-unload cycle (KES-FB2 bending test – see Figure 2.10a). The test specimen is mounted vertically to avoid the influence of gravity on the experiment. One sample end is secured to a fixed clamp and the other to a moving clamp (see Figure 2.10b). The bending moment during the test is measured as the fabric specimen is bent via a range of curvatures (i.e., as the moving clamp bends the sample in a circular path, it captures detailed information about its bending behaviour, including how stiffness changes with curvature) [90]. Although the Kawabata bending test device is expensive and limited in availability, researchers are focusing on this method for accurate modelling of fabric materials because the physical and mechanical properties emphasised by this method are more detailed and accurate [96] [97] [98]. Unlike the Bilbao et al. method [90], the Kawabata system is highly automated and provides precise measurements of bending stiffness along with other fabric properties such as shear, tensile, and surface properties, making it suitable for in-depth textile analysis.

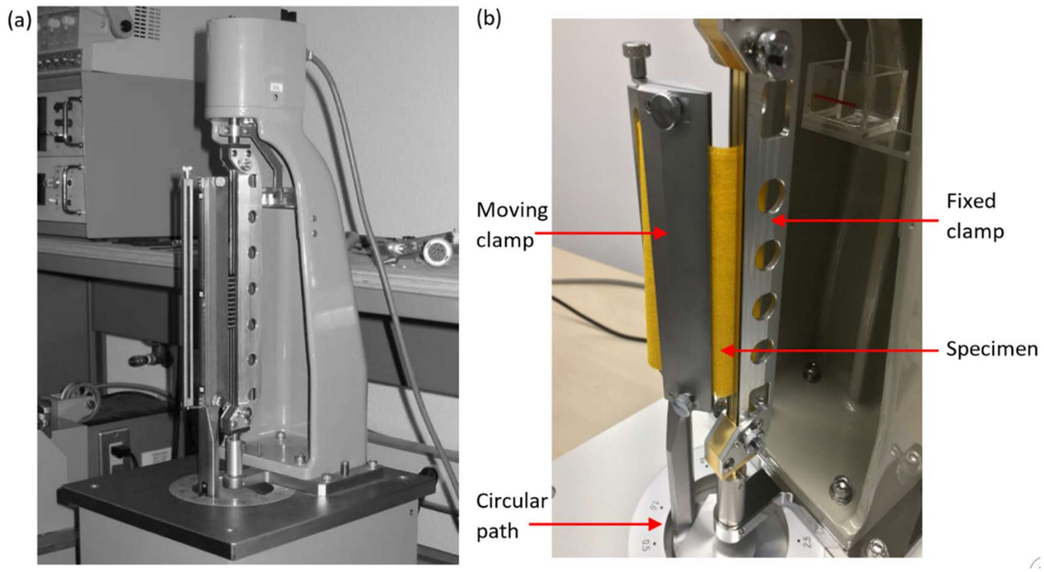

Figure 2.10: (a) Kawabata bending tester [90] (b) Closeup image of the fixed and moving clamps [99]

2.5.2. Shear Characterisation Tests

Shear is a common deformation that occurs during the forming of fibre-reinforced composites. The formation of complex 3D shapes from 2D fabric preforms includes the application of significant shear deformations due to fibre reorientation (i.e., slipping and rotating along and away from the orthogonal axes) [100]. When combined with a suitable analysis, the shear stiffness of the fabric can be directly determined by the uniaxial bias extension (UBE) test [6] [101]. In addition, the in-plane bending, and torsion stiffness of the fabric can be indirectly determined through the development of an accurate model of the system [6]. The picture frame (PF) test is also used to determine the in-plane shear behaviour of dry fabric reinforcements and pre-impregnated composites and has played an important role in studies on the characterisation of woven fabrics. A few studies have reported the PF test to determine the shear behaviour of unidirectional stitched fabrics [44] [46] [102]. According to some studies, the PF test is not recommended for UD fabric prepregs because tow misalignments can increase the occurrence of defects such as ply splitting [102] [103].

Both UBE and PF tests appear to be the same when simply considering the macro scale behaviour of the reinforcement. However, detailed examinations of the two test techniques revealed some substantial differences, particularly in the shear force, locking angle, and the onset of wrinkling [104]. Most of the comparative studies of these two shear test methods show that the resultant shear stiffness of the fabric measured in the PF test is significantly higher than that of the bias extension test [105] [106] [107] [108] [109]. The reason behind this is the fibre tension during the PF test. Fabric misalignment and yarn crimping were determined to be the sources of changing tension during the picture frame test of woven fabrics [66]. The PF test produces nearly uniform kinematics in the test specimen (though the clamped boundary does lead to significant in-plane bending of the tows [110] [111]), however, preventing misalignment of fibres during clamping is crucial to the reliability of picture frame tests since even a slight change in fibre orientation can result in a significant difference in shear force. Therefore, for some fabrics such as NCFs (less so for woven fabrics), the repeatability of the test results is low in the PF test. The UBE test is relatively unaffected by specimen misalignment; however, it does cause non-homogeneous kinematics across the test specimen and a tendency for intra-ply slippage at high shear angles [112]. Furthermore, the results of the UBE test may also be unreliable due to poor sample preparation and careless machine installation [113].

2.5.2.1. Uniaxial Bias Extension Test

The UBE test specimens are clamped where the direction of the warp and weft tows are positioned ±45° to the direction of applied tensile force. The specimen is divided into three areas namely, Region A, B and C (see Figure 2.11). The aspect ratio (hight-to-width ratio, λ) of the specimen is usually considered as at least two because it ensures that the pure shear is formed in the centre of the specimen or Region A. The shear of Region B is considered as half of the shear of Region A if the tows are assumed to be inextensible and no inter-tow slip throughout the test.

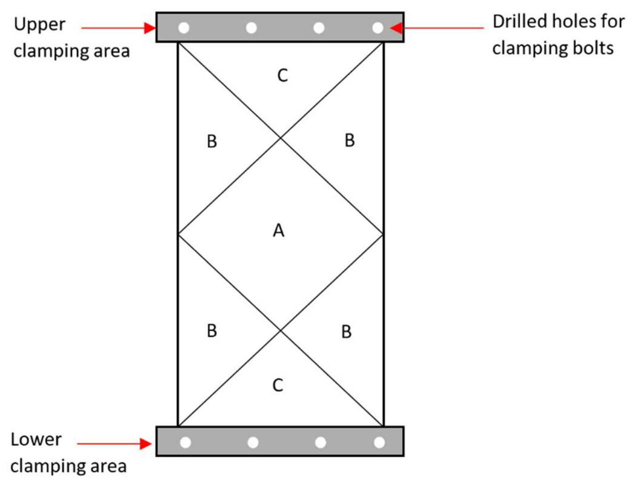

Figure 2.11: Diagram of undeformed UBE test specimen

If warp and weft tows are present in exactly ±45° directions within the specimen (perpendicular to each other) the initial inter-fibre angle ($\phi_{s(i)}$) is 90°. The upper and lower ends of the sample are clamped to the machine using clamping bolts (see Figure 2.11). The lower clamp is fixed on the machine bed and only the upper clamp moves upwards when the force is applied. As a result of this vertical movement of the specimen, the shape of Region A shifts from square (blue) to diamond (green) as shown in Figure 2.12. The change in the inter-fibre angle (ϕ_s) due to the tension, can then be determined by the dimensional changes in the geometry of the specimen.

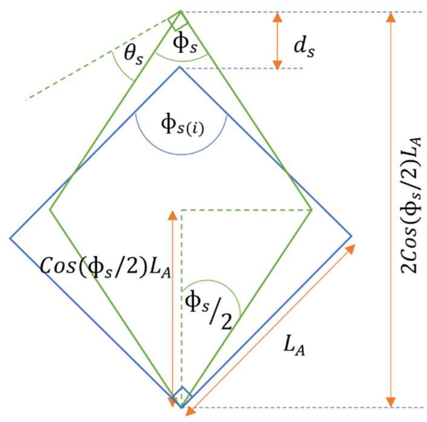

Figure 2.12: Shear deformation of Region A

If the aspect ratio of the specimen (λ) is greater than 2 [114], the extended length, d_s, can be derived as,

$$d_s = 2(\lambda - 1)L_A \left[\cos\left(\frac{\Phi_s}{2}\right) - \cos\left(\frac{\Phi_{s(i)}}{2}\right)\right] \tag{2.5}$$

where, L_A is the side length of Region A. The inter-fibre angle at a given displacement (Φ_s) can be calculated using the rearrangement of Eq. 2.5 as,

$$\Phi_s = 2acos\left[\frac{d_s}{2(\lambda-1)L_A} + \cos\left(\frac{\Phi_{s(i)}}{2}\right)\right] \tag{2.6}$$

The shear angle (θ) can then be simply determined by the difference between the initial inter-fibre angle ($\Phi_{s(i)} = 90°$) and inter-fibre angle at a given displacement (Φ_s).

$$\theta = 90 - \Phi_s \tag{2.7}$$

Source of Errors in the UBE Test

Reliable estimation of the mechanical test results of fabrics is required to predict the correct forming behaviour using accurate numerical simulations. The accuracy of the test results is primarily influenced by inadequate specimen preparation, analysis techniques and the formation of wrinkles [113]. The main two sources of errors, namely, specimen pre-shear and out-of-plain wrinkling are discussed below hence minimising these errors can improve the accuracy of data.

Specimen Pre-Shear

As stated in Section 2.5.2.1, the initial inter-fibre angle ($\Phi_{s(i)}$) is used as 90° for the calculation by considering that the pre-shearing error is zero. However, it is technically impossible to preserve the $\Phi_{s(i)}$ at precisely 90°. Past experimental research shows that accurate results can be observed by maintaining a pre-shear angle below ~0.5° and a standard deviation of the $\Phi_{s(i)}$ measurements within ~2° [113]. Therefore, to minimise the pre-shear error, the $\Phi_{s(i)}$ should be measured multiple times at the beginning of each test and the angle should ideally be maintained within the specified range by simply adjusting the dimensions of the specimen after installation to the machine. In addition, careful handling of the specimen at each stage of the test (from cutting the piece of fabric from the roll to the installation of the specimen to the machine) is essential to mitigate the pre-shearing error.

Out-of-plain Wrinkling

The out-of-plane wrinkle error source occurs in the later phases of the UBE test. Early studies explained the occurrence of wrinkles based on the locking angle (see section 2.8.1.1). However, current thinking is that wrinkles appear if in-plane compressive force induced during forming is high enough to overcome wrinkle resistance due to out-of-plane bending and torsional stiffness of the fabric [115]. It has been found that wrinkling induces a substantial overestimation of up to 20% of the measured shear angle when using manual image analysis to interpret the test results [113]. Although the occurrence of wrinkling is considered a source of the UBE test error, the wrinkling onset angle can also be used to infer the mechanical properties (i.e., torsional rigidity) of a sheared fabric via inverse modelling. The wrinkles are usually formed in the centre of the specimens (Region A, see Figure 2.11) where the measurements are taken for the fabric shear stiffness analysis. As the wrinkles develop, the flat smooth surface of the specimen becomes a wavy structure, reducing the reliability of the measurements; for example, large specimens tend to develop wrinkles at low shear angles and have a significant impact on the test results [6]. Harrison et al. [101] implemented a wrinkle mitigation technique using two parallel Perspex plates (Anti-wrinkle plates) which is discussed in detail in the following section.

Normalization Method of UBE Test

As mentioned in Section 2.5.2, both UBE and PF tests are used as standard methods to characterise the shear behaviour of fabrics in composite forming. Both tests should be independent of the test method and the size of the test specimen to compare shear resistance. The shear resistance of the PF test can be easily estimated using Eq.2.12 since the kinematics are reasonably uniform throughout the test specimen (neglecting the effects of in-plane bending stiffness near the clamped edges of the specimen [116]). However, the inhomogeneous deformation of the UBE test makes the normalisation process more complicated. Two rate-independent normalisation theories have been suggested by Harrison et al. [117] and Hivet and Duong [105] to calculate the shear force from the axial force using stress power-based analysis with different arguments (Eq. 2.8 [117] and Eq. 2.9 [105], respectively). After analysing the two theories, it was discovered that the separately developed two theories produce identical results [117]. The ultimate resultant shear force at angle θ [$F_{sh}(\theta)$] is a function of its own value at $\theta/2$ [$F_{sh}(\theta/2)$]. Therefore, iterative scheme needs to solve the equation.

$$F_{be}(\theta) = \frac{\sqrt{2}.W}{(\lambda-1)}\left\{F_{sh}(\theta).(2\lambda-3).\cos\left(\frac{\pi}{4}-\frac{\theta}{2}\right) + F_{sh}(\theta/2)\frac{\left[\sin\left(\frac{\pi}{4}-\frac{\theta}{4}\right)\right]}{\left[\sin\left(\frac{\pi}{4}-\frac{\theta}{2}\right)\right]}.cos\left(\frac{\pi}{4}-\frac{\theta}{4}\right)\right\} \quad (2.8)$$

$$F_{be} = \frac{F_{sh}(\theta)\;.\;(2H-3W)\;cos\;(\theta)}{\left(\frac{H}{W}-1\right).[cos(\theta/2)-sin(\theta/2)]} + F_{sh}(\theta/2)\;.\;\frac{W\;.\;cos\;(\theta/2)}{\left(\frac{H}{W}-1\right).[cos(\theta/2)-sin(\theta/2)]} \quad (2.9)$$

where, λ, H, and W represent aspect ratio ($\lambda = H/W$), height, and width of the specimen, respectively.

Past Modifications of the Uniaxial Bias Extension Test by Other Researchers

<u>Sample Modification</u>

A modified version of the UBE test includes bonding aluminium foil on both sides of Region C using epoxy resin (see Figure 2.13). As a result, Region C remains undeformed, mitigating intra-ply slippage. Consequently, an 'encastre' boundary condition exists between Region B and Region C [67]. Harrison et al. [6] further experimented on the effect of adhering aluminium sheets to the specimen as a function of sample size, and the findings highlighted that sticking the aluminium foil does not affect the wrinkle onset angle or the maximum normalised axial force. The results further implied that the aluminium bonding significantly reduced the normalised displacement related to the maximum axial force for all selected specimen sizes and was unaffected by specimen size. Therefore, this method is extremely effective in reducing intra-ply slippage in Region C.

Figure 2.13: A modified version of the UBE test specimen includes sticking an aluminium foil on both sides of the Region C [67]

<u>Testing Procedure Modifications</u>

Understanding the development of wrinkles is important as it can dramatically reduce the apparent shear stiffness of the specimen and the reliability of the test results. Harrison et al. [101] implemented a wrinkle mitigation technique using two parallel Perspex plates (anti-wrinkle plates) as shown in Figure 2.14. Both numerical and experimental analyses evidenced the benefit of incorporating transparent anti-wrinkle plates to mitigate wrinkle formation. According to the numerical predictions, the introduction of Anti-wrinkle plates could provide more accurate kinematic measurements, i.e., reduce the shear angle error by up to 20%. This method extends the ability to obtain accurate measurements at high shear angles and forces. Krogh et al. [55] also applied this wrinkle mitigation technique on quasi-UDNCF fabric (see Figure 2.15) and successfully improved the accuracy of measurements up to high shear angles.

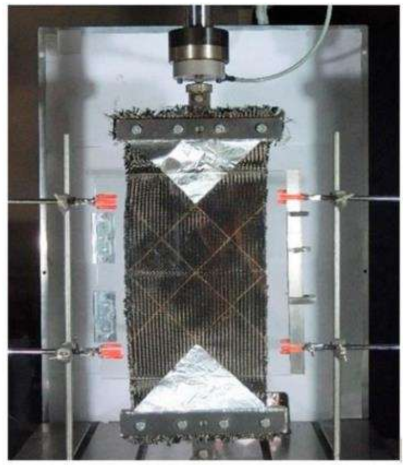

Figure 2.14: The front view of the carbon fabric UBE test specimen positioned between the anti-wrinkle plates [101]

Size and Shape Modifications

The aspect ratio ($\lambda = H/W$) of a UBE specimen is considered to be at least two because it ensures that the pure shear is formed in the centre of the specimen or the Region A. Harrison et al. [6] performed UBE tests on different sizes of 2×2 twill-weave carbon fabric specimens with the aspect ratio of two: 100 ×200, 150 ×300 and 200 ×400 mm^2. According to the findings, large specimens conform more closely to ideal shear kinetics. Furthermore, larger specimens tend to develop wrinkles at lower shear angles, which shows a significant impact on the test results. Pourtier et al. [118] investigated the kinematics of the UBE test with different sizes of biaxial NCF samples with aspect ratios greater than two: 80 ×200, 150 ×375 and 200 ×500 mm^2. The results were similar, and large specimens were sensitive to deformations (i.e., at low shear angles (up to 10) slippage is the main deformation, and beyond that tow rotation becomes prominent). Therefore, larger samples improve UBE test reliability for NCF material. Krogh et al. [55] modified the conventional rectangular shape of the UBE specimen into a diamond shape of a quasi-UD glass fabric (see Figure 2.15). The results implied that the quasi-UDNCF deforms in pure shear for up to moderate shear angle and then converts to simple shear. This transition can be extended to high shear angles on a diamond-shaped UBE specimen (cut near the gauge area) tested with anti-wrinkle plates.

Figure 2.15: Diamond-shaped UBE specimen with anti-wrinkle plates at 40 mm displacement [55]

2.5.2.2. Picture Frame Test

The picture frame consists of four identical bars hinged on each other by bearings (see Figure 2.16a). The way the specimens are clamped differs significantly between the UBE and the PF experiments. In the UBE test, two of the four sides of the specimen are clamped, while in the PF test, all four sides are clamped. Therefore, the PF test minimises the rotation of fibres compared to the UBE test. Figure 2.16b shows the dimensions of the PF test specimen.

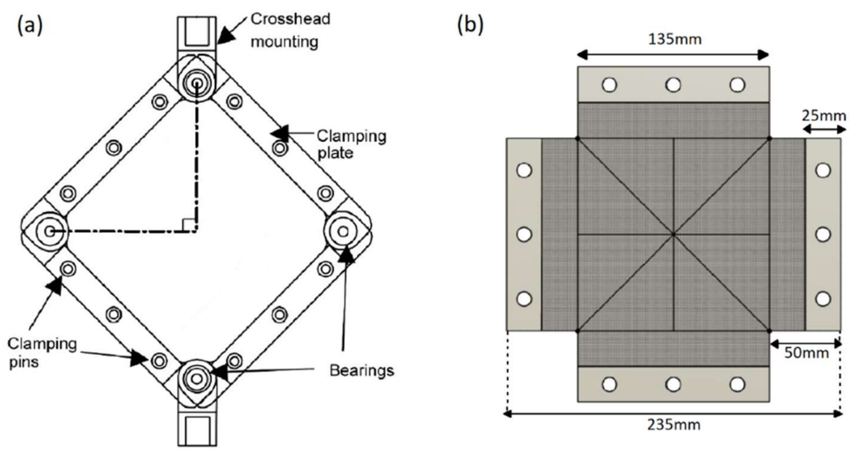

Figure 2.16: (a) Schematic of a picture frame shear rig [119] (b) Diagram of undeformed picture frame test specimen

When pulling the frame diagonally in one direction, the square shape of the frame transforms into a rhomboid shape due to the axial force (see Figure 2.17). Based on the test geometry change, the shear angle θ, in fabric can be directly related to the displacement of the crosshead, d_{pf}, using the Eq. 2.10,

$$\theta = \frac{\pi}{2} - 2acos\left[\frac{1}{\sqrt{2}} + \frac{d_{pf}}{2L_{pf}}\right] \tag{2.10}$$

where, L_{pf} is the side length of the picture frame rig [109]. The shear angle (θ) can be simply determined by the difference between the initial frame angle (90°) and the frame angle at a given displacement ($\emptyset$).

$$\theta = \frac{\pi}{2} - \emptyset \tag{2.11}$$

For the picture frame test, the shear resistance of the fabric is expressed as

$$F_s = \frac{F_{af}}{2L_{pf}cos\frac{\emptyset}{2}} \tag{2.12}$$

where, F_s and F_{af} represent the normalised shear force per unit length and the total axial force, respectively. Ideally, the force applied to the empty frame should be zero. However, in practice, some frictional forces may exist; if so, the net force should be calculated by subtracting the frictional force from the total axial force.

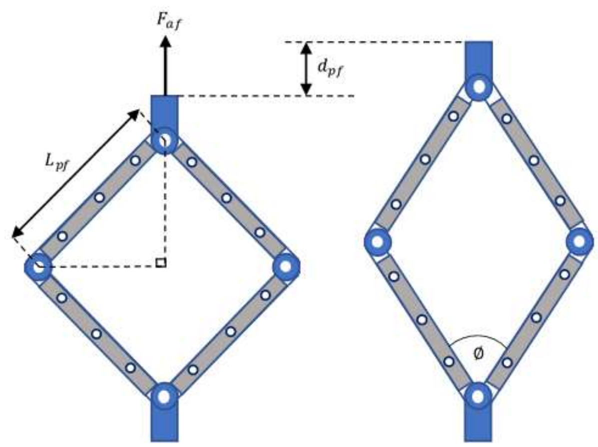

Figure 2.17: Arms rotation of the picture frame rig

Source of Error in the Picture Frame Test

Misalignment of the Picture Frame Test

When loading the specimen to the rig during the experiment, it is critical to keep the tows aligned with the side of the rig. Depending on the type of misalignment, the fabric tows may be subjected to tensile or compressive strain (see Figure 2.18). Tensile strain prevents the specimen from wrinkling; however, it can lead to significant force overestimations. In contrast, compressive strains induce wrinkles at low shear angles, resulting in considerable force underestimation [114]. So far, no standard tool, sample size, or procedure has been developed to measure the shear behaviour of fabrics. The benchmark study of the PF test [120] compared the shear properties of three fabric samples with six different frame designs and sample sizes. The results show a wide variation in the shear measurements of the PF test for the same fabric. This result is not surprising because, to achieve better results, the yarns must be aligned with the frame arms; however, achieving 100% alignment is unrealistic. Therefore, the benchmark study emphasised that best practices and procedures can lead to more accurate results. Various modifications to the standard PF test have been made by researchers to mitigate the drawbacks of the PF test, particularly fabric tension caused by misalignment and clamping, some of which are discussed in the following section.

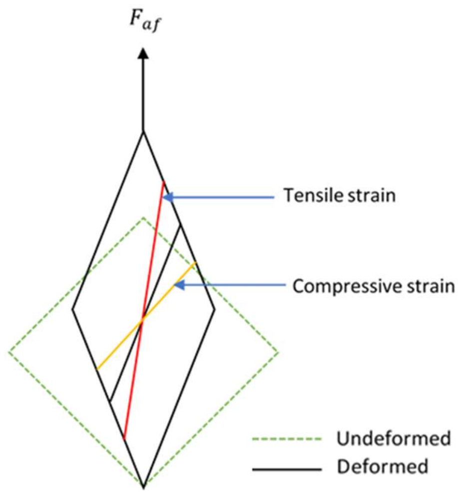

Figure 2.18: Types of misalignments of the tows in the PF test [121]

Past Modifications of the Picture Frame Test by Other Researchers

<u>Frame Modifications</u>

In certain investigations, in addition to conventional picture frames with plate-bolt clamping (see Figure 2.19a), lever systems were used (see Figure 2.19b). The lever system consists of a sliding link to connect the amplifier frame to the crosshead of the tensile tester and an amplifier. When determining accurate shear force, the amplitude factor, or the ratio between the picture frame length and the amplifier frame length, must be considered. The strain rate of the test can be enhanced by increasing the amplitude factor. Therefore, an amplifier can help if the crosshead velocity of the machine is limited [120] [57]. However, the tension of the fibres is not considerably affected by this form of picture frame. Launay et al. [122] conducted an instrumented PF test in which the clamping system of the specimen was connected to the picture frame via two load sensors in both the warp and weft directions. As a result, during the test, the tension of the yarns can be measured and adjusted. The results indicated that the normalised force of the PF specimens tested with zero tension was similar to the standard UBE test results of two commercial fabrics. Hosseini et al. [104] also used a modified PF test with four servomotors with a load cell placed perpendicular to the frame bars to provide tension/compression to the warp and weft yarns to overcome yarn tension caused by misalignment (see Figure 2.19c). Furthermore, the PF test has been modified to perform a frameless PF test with the inclusion of a sensor [123]. In this study, a heat gun was used to consolidate the outer frame of the sample (commingled polypropylene/glass fabric), and a sensor was attached to the fabric next to the middle yarn to record the relative deformation of the yarns during the test. The strain induced in the yarns is proportional to the change in sensor resistance. The results showed that the needle-integrated frameless PF test provided greater shearing characterisation with the absence of the misalignment effect than the conventional PF test.

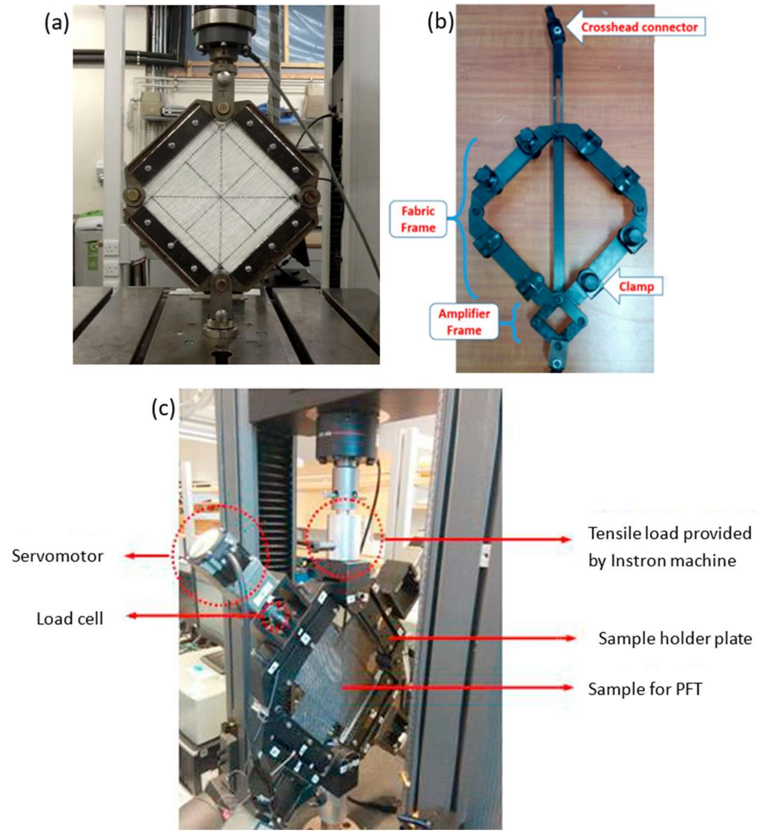

Figure 2.19: Different kinds of PF tests (a) conventional (b) with amplifier [57] (c) with four load cells [104]

Clamping Modifications

Besides the misalignment of yarns, rigid clamping can also cause tension in the yarns by reducing the free rotation [105]. Therefore, some researchers used different clamping techniques instead of plate-bolt clamping to improve the uniform deformation of the sample, such as the application of thin rubber strips below and above the sample clamping area [44], and needle gripping of the folded ends of the sample (see Figure 2.20) [104]. Besides that, Milani et al. [107] proposed using a reduced clamping area by only pinning the samples in the corners (see Figure 2.21). A balanced twill woven fabric was tested, and the resulting boundary conditions were kind of similar to the bias extension test. The comparison of normalised force vs strain curves from the UBE and PF studies revealed that both curves are close to each other up to strain 0.15, after which the deviation occurs due to the failure to completely omit fibre stretching during the test. However, the PF test with a smaller clamping area resulted in a significant reduction in normalised force compared to the standard PF test.

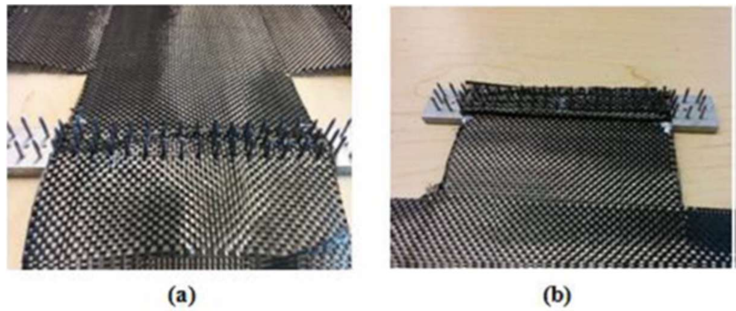

Figure 2.20: (a) Using needles in the PF test boundary conditions (b) a folded sample in the grips to increase the interaction between the fabric ends and the needles [104]

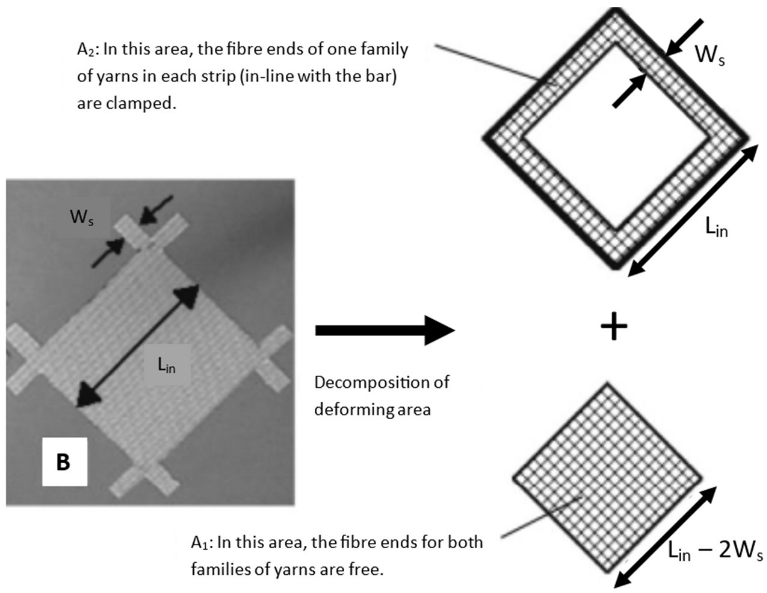

Figure 2.21: Decomposition of the deforming area in the modified picture frame test specimen [107]

Testing Procedure Modifications

To eliminate tension caused by fabric orientation, some researchers attempted to mechanically pre-condition the PF specimens by shearing the sample several times up to a moderate shear angle. This also aids in the elimination of the edge effect, the improvement of test repeatability, and the enhancement of uniform deformation throughout the specimen [120] [124]. However, in practice, this form of preconditioning is not feasible because the change in the meso-structure of the specimen caused by preconditioning is not representative of the unconditioned specimen. Besides that, Krishnappa et al. [125] used a PF setup with a pre-tensioning apparatus to overcome alignment and clamping issues in the PF test (see Figure 2.22). The optimum tension range for the unidirectional non-crimp fabric is selected as 2N–4N. This method can also be used to remove crimping from textile reinforcement.

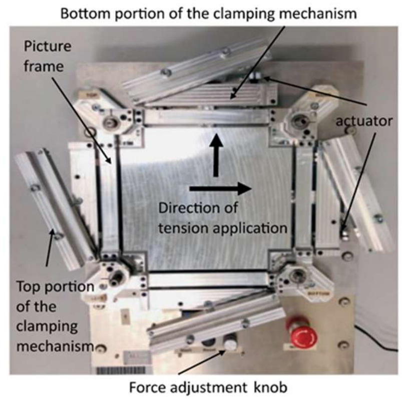

Figure 2.22: Pre-tension apparatus [125]

Sample Modification

Sample preparations of the PF test sometimes differ from one research to the next. Some researchers proposed removing the transverse yarns in the arm region to avoid the potential force caused by the yarns on the edge of the specimen due to shearing [105] [120]. As a result, wrinkling will begin within the region of interest rather than the arm of the specimen. Furthermore, by allowing free rotation of yarns, this form of modification can reduce fibre tension. Figure 2.23 shows the two distinct methods of transverse yarn removal in the arm region.

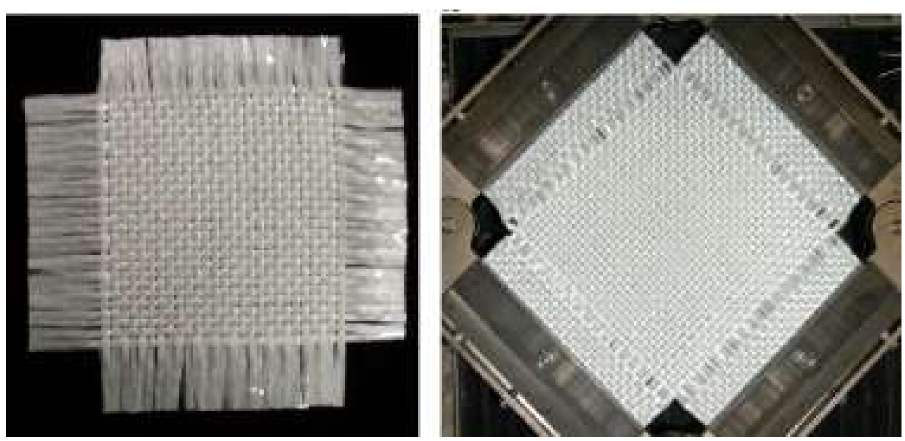

Figure 2.23: Two different methods of transverse yarn removal in the arm region of the PF test [120]

2.5.3. Tensile Test

The tensile test is a basic characterisation method that determines the strength, stiffness, and elongation of fabrics, prepregs, or composite materials before they break under tension. Tensile testing on individual fibres, fibre groups (tows) [126] [127], or stitches [127] helps in determining the inherent strength and elongation of the reinforcement. Tensile tests on prepregs are used to determine the initial bonding strength between the matrix and the reinforcement by observing the failure modes (such as fibre pull-out and debonding between matrix and fibres), as well as how interfacial debonding causes defects in the composite [128] [129]. The final tensile test results of the cured prepregs or the finished composite material indicate the overall performance of the fibres, matrix, and fibre-matrix interface [130].

Researchers use different standard methods to perform the tensile test during the various stages of composite production. The ASTM D885 [131] standard has been used on various types of textile yarns (tows) including glass [126], aramid [132], quartz [133] and basalt [126], to produce the input data for mesoscale constitutive models of fabrics. Yue et al. [134] performed the tensile test on a single fibre of Kevlar using the ASTM D3379 [135] method and calculated Young’s modulus of tow compared with Young’s modulus calculated by the ASTM D885 method. The results imply that Young's modulus of fibres measured in the ASTM D3379 method is lower than the ASTM D885 due to the complex structure of tows (i.e., twist, interactions between fibres) compared to a single fibre. In January 2023, ASTM announced the withdrawal of standard D885, which is no longer considered applicable for use [136]. Some studies employed ASTM D2256-02 [137] to determine the tensile properties of engineering fabric tows [138] [139]. However, the ASTM D2256-02 is not widely used for engineering fabrics since it requires special clamping adaptors for the yarns with high Young’s modulus.

The tensile test has also been performed on the stitching threads of non-crimp fabrics to evaluate the overall performance of the reinforcement. Quenzel et al. [127] performed the tensile test on the individual components, i.e., glass tows and polyester stitches of five different biaxial non-crimp fabrics using ISO 3341 [140] and ISO 2062 [141] standards, respectively. The polyester stitches show a significant elongation compared to glass tows and the Young’s modulus of the stitches is 50 times less than the Young’s modulus calculated for glass tows at 0-5% stitch elongation. Apart from the individual components of the fabric, some studies have focused on performing tensile testing on the fabric itself. Manins et al. [142] and Ahmad et al. [126] characterised hybrid woven fabrics using the ISO 13934-1 [143] standard (see Figure 2.24). This standard is mainly specified for woven fabrics. However, the ISO 13934-1 standard has also been used to characterise non-crimp glass fabrics by Quenzel et al. [127] and Khiêm et al. [144] as there are no specific methods given in the literature to characterise non-crimp fabrics. Both studies conclude that the ±45° biaxial NCFs show a noticeable tension in the stitches, which has a significant effect on the tensile strength of the NCF. Quenzel et al. [127] evaluated tensile strengths of ±45° and 0/90° biaxial NCFs. Compared with the ±45° biaxial NCFs, 0/90° NCF shows the lowest and highest tensile strength in the direction of stitches and the direction perpendicular to the stitches, respectively. The reason for the difference in tensile strength of the 0/90° biaxial NCF is attributed to the low packing density of fibres along the 0° direction (i.e., stitch direction).

Figure 2.24: Tensile test setup for woven fabric following ISO 13934-1 [126]

2.6. Full-Field Measurement Methods for Fabric Deformation

Shear test data are often analysed using shear or axial force versus shear angle graphs and measured shear angle versus ideal (assumes pin-jointed net kinematics) shear angle graphs. The shear stiffness of the fabric is derived from the axial force versus measured shear angle curves (i.e., assuming that the fabric response is rate-independent, and the shear stiffness is purely a function of the shear angle [45]) while the average measured shear angle vs the ideal shear angle curves are important to estimate the in-plane bending stiffness of the fabric [6] and the onset of intra-ply slip [45] [114]. Therefore, the shear angle is a more fundamental measure of the internal deformation within the material. Apart from the shear angle, measuring localised strains within the fabric helps assess its stress distribution and potential failure points. Therefore, a complete understanding of fabric deformation can be obtained by measuring the full-field fabric strain while measuring the shear angle [116]. Boundary conditions (i.e., how the fabric interacts with the clamps or grips used during testing) can significantly affect the strain distribution within the fabric, and the effect can vary between different test setups. Various methods used to measure fibre angles and strains in a mechanical characterisation test are reported in the literature. The following section aims to discuss some common methods such as manual image analysis, algorithmic analysis, and optical measurement methods used to obtain full-field measurement for fabric deformation.

2.6.1. Manual Image Analysis

Manual image analysis is a simple and cost-effective method used to gather data to characterise the forming mechanics of fabrics using high-resolution cameras and an image processing tool. Prodromou and Chen [145] proposed this method to determine the relationship between the fabric architecture and locking angle (i.e., the shear angle corresponding to the observation of wrinkling, discussed in Section 2.8.1.1 in detail). Later, for better observations of fibre angles, the selected fibres or tows are marked using a marker pen (see Figure 2.25) and then manually measured the inter-fibre angle by tracing the marked lines using an image processing tool [6] [113] (i.e., ImageJ [146]). The shear angle of the respective displacements is then calculated by subtracting the inter-fibre angles at specified intervals from the initial inter-fibre angle. This method has certain drawbacks. This technique is a time-consuming visual analysis and may include processing errors (i.e., selection of the distance between camera and specimen, camera angle etc.) and human errors (i.e., finding the correct starting point of the test, accurately measuring inter-fibre angles during post-test analysis etc.). Therefore, adequate training is required before using this technique.

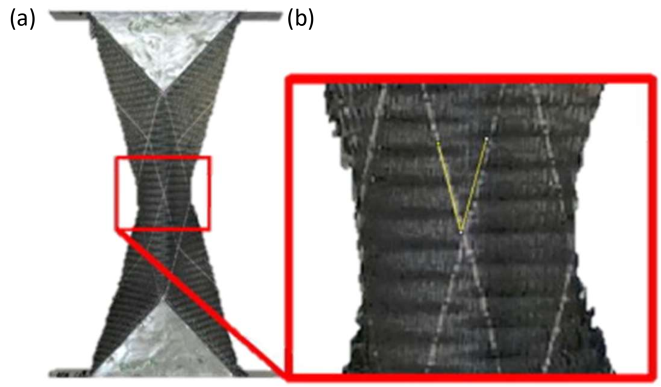

Figure 2.25: (a) Manually measuring the fibre angles of the UBE specimen using ImageJ software (b) close-up view of the tracking lines [113]

2.6.2. Algorithmic Analysis

Using line tracking algorithms to map the fibre angle and displacement at any particular point on the surface of a fabric specimen represents an advanced step forward from the manual image analysis method. This is a fast and easy semi-automated method that also minimises human error during post-analysis. Different studies show the effectiveness of tools like MATLAB, and Python using the Hough transform to determine the shear angles [147] [111] of the specimen. Figure 2.26a shows how the Hough transform is applied to determine the shear angle using the image analysis technique. The Hough transform is a computer vision tool used to detect marked lines in captured images of specimens. In this method, first, the points are selected on a reference image (i.e., the x and y coordinates of the selected points are determined in pixels). The difference in the x and y coordinates of each preselected point between the reference image and the image selected for analysis represents the displacements in those directions. This information is used to determine the shear angle of the specimen at a given displacement [147]. Figure 2.26b shows the detected lines of the specimen at a different level of displacement. Furthermore, the studies have used MATLAB-based line-tracking algorithms to determine the strain [148] [149] measurements of engineering fabrics.

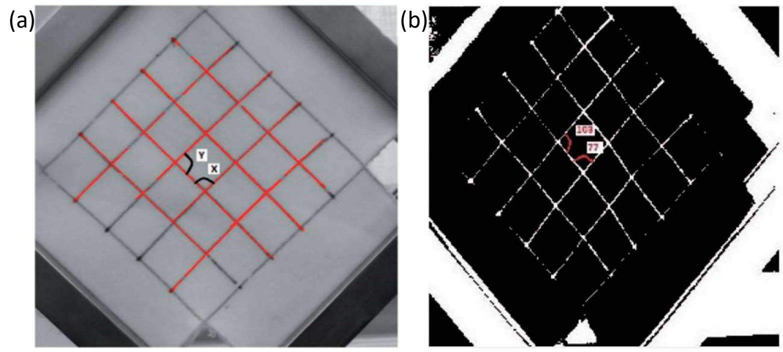

Figure 2.26: (a) The Hough transform method for detecting lines in a specimen (undeformed reference image) (b) Using grayscale images to identify lines in the deformed specimen [147]

2.6.3. Optical Measurement Methods

While no optical instrument has been specifically designed to measure inter-fibre angles in engineered fabrics, various studies have adapted existing optical methods to determine fibre orientation. The most common non-destructive optical method is the digital image correlation (DIC) method, which can be used to capture local elongations of sheared specimens to determine the shear angle. The DIC method usually involves applying a speckle pattern as a distinct marker on the sample surface to track the deformation, however, for some materials, the speckle pattern can be the natural texture due to the inherent surface properties [150]. The DIC technique acquires multiple images during the deformation of the sample and presents qualitative and quantitative measurements of the sample relative to the reference image. DIC can be classified into three: 2D-DIC (i.e., limited to in-plane deformation of planar specimens due to the use of a single fixed camera), 3D-DIC (since two cameras are used, it is capable of capturing deformation on both flat and curved surfaces) and DVC (or Digital Volume Correlation is a volumetric imaging device ideal for determining the internal deformation of opaque solid objects) [151]. The deformation of engineering fabrics is usually measured using the 3D-DIC method to capture the full-field measurement and to determine the fabric deformation under various stress conditions (i.e., quantify the parameters such as strain distribution, displacement gradient, and failure modes across the specimen). The software used to perform the DIC analysis (such as ARAMIS, LIMESS, and VIC-Snap) monitors the position of the points throughout the deformation process and determines the local shear angle of the fabric by calculating the strain field (see Figure 2.27) [152].

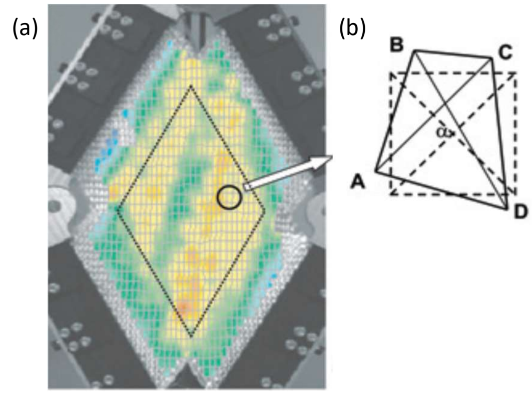

Figure 2.27: (a) Shear angle field of a picture frame test obtained using DIC (b) the position of the diagonals drawn across the selected points in the sample in both undeformed (dashed line) and deformed (solid line) scenarios [152]

Most of the DIC analysis of engineering fabrics requires an additional step of application of speckle pattern on the surface. Therefore, the selection and application of the proper pattern is a critical and time-consuming step. In addition, there is a debate that this speckle pattern paint may affect the properties of the fabrics. Krogh et al. [111] obtained the shear angles from both the image processing method using the Hough transform (algorithm analysis) and the DIC method for the same fabric. Although the application of speckle patterns can affect fabric properties, the results show that the spatial resolution of Hough transforms is lower compared to DIC due to the high noise level, and the Hough transform method needs to be further developed. Krieger [153] and Gibbs [154] examined NCF specimens using a novel commercial system called the Apodius vision system. According to Gibbs [154], the system consists of two parts: laser scanning to map a point cloud of the specimen and optical imaging to produce a surface map of the fibre architecture (i.e., a high-resolution optical sensor captures multiple images of the surface of the specimen). The output of the Apodius software does not provide information such as shear angle calculation and standard deviation of the average fibre angle. Therefore, a customised MATLAB script is used to analyse the output from Apodius. This method enables gathering fibre angle data without the application of any sample coating and can be exported to Abaqus CAE for direct comparison with the simulation results.

2.7. Dry Fabric Forming

Forming a dry fabric into a desired shape is a critical step in discovering the inherent properties of the fabric. By analysing the behaviour of dry fabrics under controlled forming conditions (such as tool loads, forming rate, blank-holder pressures, and processing temperature), researchers can identify areas prone to wrinkling, buckling, fibre fracture, tearing or inconsistencies, and identify potential problem areas before they become detrimental in the final applications. In addition, comparing the experimental results of fabric forming with numerical simulations is an important step in validating the accuracy of the model [155]. This functional approach leads to the optimization of forming processes and ultimately to the manufacture of high-performance engineered fabric structures.

The shape of the preform is generally obtained by the punch and die draping process (i.e., such as stamp forming and deep drawing). Many studies have been conducted on the forming of textile reinforcement in hemispherical [156] [157] [158], double-dome [159] [160] [153], tetrahedral [155] [160] [161] and square box shapes [161] [162] [163]. To increase the accuracy of the dry fabric forming process, the forming conditions (i.e., process parameters such as temperature, pressure and forming rate), as well as the design of the punch and die are critical. This is because proper design tools ensure that the fabric maintains the optimum tension and alignment throughout the forming process, minimising deformation defects. In this process, fabric reinforcement is placed between the die and the blank holder. The punch pushes the reinforcement into the shape of the bottom mould, thereby giving the reinforcement the desired form (see Figure 2.28). The gap between punch and die is important to maintain the fabric integrity during forming (i.e., small gaps cause excessive compression while large gaps cause inconsistent thickness) [159]. Yu [164] experimented with two biaxial fabrics (balanced twill woven and pillar stitched NCF) to examine the dependence of the wrinkling behaviour on the mesoscale architecture of the fabric by introducing a gap between the blank holder and the die (i.e., enable the fabric to wrinkle out-of-plane in a controlled manner during the forming). A symmetric wrinkle pattern has been observed in balanced woven fabric while NCF has shown an asymmetric wrinkle pattern due to asymmetric shear resistance caused by pillar stitching.

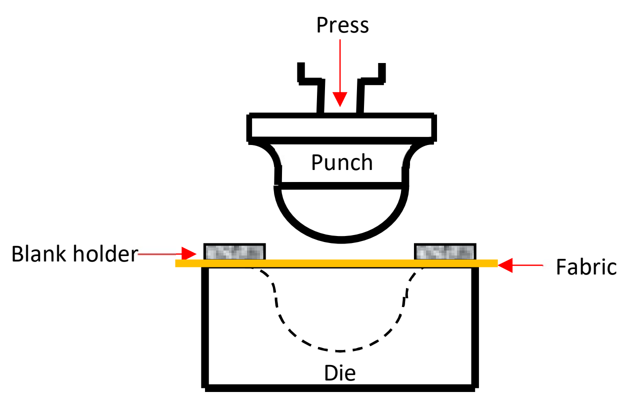

Figure 2.28: Schematic diagram of the punch and die draping process

2.7.1. Fixation Methods of Fabrics

After the dry fabric is formed, the fabric may try to return to its original shape after the pressure is released from the punch. Therefore, fixing methods help to lock the fabric to ensure that the desired shape is maintained. In addition, fixing methods can help solidify the fabric structure, making it easier to handle during post-analysis. Allaoui et al. [161] fixed the dry preform by spraying resin on the fabric surface at the end of the forming. In contrast, Khan et al. [159] applied the resin to the fabric surface before forming the fabric. Applying resin prior to forming may significantly affect the forming behaviour of the fabric and make it challenging to remove the fabric from the die without damaging the fabric, even with a release agent. Gibbs [154] applied a thin layer of epoxy binder instead of liquid lubricant between two layers of fabric before deformation to reduce the friction of yarns. The study assumes that the binder could help to stabilise the fabric and minimise the amount of lubricant required to be applied between the ply and the tool surface. Ackerman [165] attempted to fix each layer of steered-fibre fabric in the respective configuration using a methylated spirit solution with the epoxy (0.5%) resin. This method can also be used as a post-fabric fixing method and helps in easier removal and better handling of the fabric without damaging the shape (see Figure 2.29). In addition, Ackermann [165] and Xiao [166] applied a thin layer of adhesive spray as a method of fixing the steered pattern. However, with both methods, Ackermann [165] recommended the use of methylated spirit solution with the epoxy resin because the presence of adhesive spray may result in different material properties of the final composite.

Figure 2.29: After the application of methylated spirit solution with the epoxy (0.5%) resin to the plain-woven fabric [165]

2.7.2. Full-field Measurement Methods for Fabric Forming

After fixing the formed textile reinforcement, the next step is the post-analysis of the formed fabric specimens. Measuring the full-field fibre angle and strain of formed components is a crucial step. As an easy and simple method, the researchers manually measured the inter-fibre angles using a universal protractor [157] or goniometer [158] along the selected tows to calculate the shear angles. Li et al. [157] further used a digital camera with a MATLAB script to analyse the changes in the central area of a fabric when it was formed into a hemispherical shape. As discussed in Section 2.6, some studies [116] [153] performed full-field 3D-deformation analysis on formed fabric using the 3D-DIC technique with draping algorithms developed via MATLAB. Further, Gibbs [154] used a combination of the Apodius vision system and the MATLAB script to evaluate the local shear angles on both sides of the formed hemisphere.

The use of fixation methods for dry fabric analysis can sometimes be bypassed with the help of advanced tools and enable the analysis of unfixed fabrics during the forming process. Pazmino et al. [160] applied DIC technology while forming the fabrics using open dies (see Figure 2.30). This method requires a specialised setup with a two-camera stereo vision system and careful surface preparation. It is assumed that applying a very thin layer of paint (speckle pattern) does not change the deformation behaviour of the fabric. The study used MatchID3D image correlation software for the post-analysis process. This method allows researchers to directly observe the behaviour of the fabric under forming pressure, revealing real-time strain distribution and potential areas of instability.

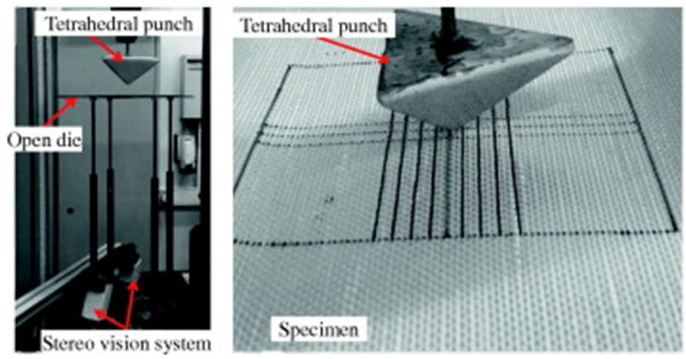

Figure 2.30: The forming setup that includes an open die [160]

2.8. Computational Framework of Fabric Reinforcements

Experimental analysis is very important for validating material properties. However, determining the corresponding process parameters using only experimental approaches experiences high processing time and cost. Therefore, researchers use computational modelling to simplify the development process by significantly reducing the number of experimental trials and minimising the need for the design and manufacture of expensive mould tooling. The choice of method in fabric forming simulations depends on the level of detail considered in the fabric structure and the accuracy requirements of the forming predictions. Depending on the discretisation level, three main modelling scales are used to describe fabric: macroscale, mesoscale and microscale (see Figure 2.31). Fabric is considered a multi-scale material. Changes at the microscale level affect the mesoscale interactions, which in turn control the macroscopic properties of the fabric.

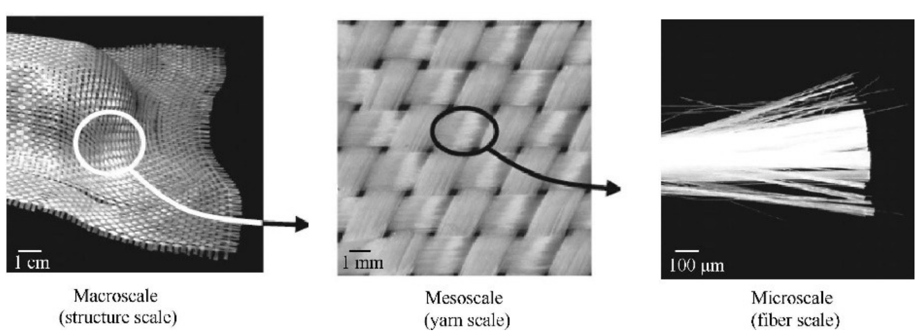

Figure 2.31: Multiscale analysis for textile reinforcement [167]

At the macroscale level, the fabric is treated as a continuous material, thus providing a fast and efficient way to predict large-scale behaviour. This level focuses on the overall shape and deformation of the fabric under external influences such as gravity or tension. At this stage, fabric properties such as stiffness, strength and drapability can be determined. Experimental data are used to calibrate the parameters of the selected macroscale model. These models often rely on mathematical equations that describe the relationship between stress, strain, and other properties [168]. By adjusting the parameters of these equations based on the experimental results, the model can be adjusted to represent the specific fabric being analysed.

In mesoscale modelling, fabrics are considered interlaced or interconnected networks and analyse the behaviour of individual tows. The mesoscale is more accurate than the macroscale because it predicts fabric behaviour under stress by considering yarn interactions. There are two commonly used textile geometry modelling tools, namely, TexGen [169] and WiseTex [170] to generate realistic mesoscopic structures of textile reinforcements. TexGen is an open-source software primarily designed for modelling woven textiles. To generate complex fabric structures such as NCFs, TexGen users need to write scripts because the model requires several parameters to create both the stitching yarns and the fibrous structures (tows). The commercially available WiseTex tool provides features designed for modelling NCFs and is able to generate unit cells using the parameters of the fibrous structure, stitching pattern and experimental data [171] [172]. WiseTex eliminates the need for complex scripting, however, generating proper unit cells in NCFs requires proper training and experience.

While macroscale and mesoscale modelling provide a valuable overview of fabric reinforcement, microscale modelling can be used to understand the complex details of fibre-level interactions i.e., microscale modelling is a filament-based approach. For example, microscale modelling of NCFs considers the interaction of the individual filaments within the yarn and the interaction between the stitches. Numerical models produced with microscale data provide exceptionally detailed information about materials, however, the models are computationally expensive and time-consuming. Computational limitations make microscale forming simulations of textiles difficult to implement, thus researchers have focused more on macroscale and mesoscale forming simulations that offer a better balance between accuracy, efficiency, and cost-effectiveness.

2.8.1. Fabric Forming Simulations

Forming simulations made by an appropriate modelling tool can be used to predict both fibre directions after forming and defects such as wrinkles. The deformation mechanics of a material significantly influence the success of the forming process over a given geometry. Therefore, modelling the forming mechanics is an important topic to improve the manufacturing process and the final mechanical properties of resulting advanced composite parts. The deformation of engineering textiles and advanced composites during the forming process is driven by several important mechanical properties of the fabric (shear resistance, in-plane and out-of-plane stiffness, torsional stiffness, transverse compressive stiffness, the integrity of the fabric and tensile properties of warp and weft fibre directions) along with friction and boundary conditions [67]. The development of appropriate computational models is essential for achieving accurate simulation results. There are two aspects to computational modelling, the constitutive modelling (e.g. hypo-elastic, hyper-elastic, second-order gradient etc.) and the numerical methods (e.g. kinematic mapping, finite element analysis, material point method). Constitutive models provide information on material behaviour under deformation, i.e., mathematically represent the behaviour of fabrics under different deformation conditions using experimental parameters, while numerical methods provide the computational framework for solving the governing equations. Over the past few decades, researchers have developed a range of powerful simulation techniques to model the fabric-forming (or draping) process. Sections 2.8.1.1 and 2.8.1.2 discuss these two aspects in more detail.

2.8.1.1. Numerical Methods

Kinematic Mapping Method

Numerical analysis of fabric is derived from methods based on kinematic mapping techniques. The kinematic mapping assumes the fabric is a 'pin-jointed net' (PJN) of rigid bars (i.e., fibres are inextensible and pinned at the cross-over points with no relative slip, uniform surface contact is achieved, and fibre layers are assumed to be infinitely thin [173]) and all the deformation is based on trellis shear (i.e., rotation of the warp and weft yarns). The limitations of the kinetic drape simulation are related to the method of setting the constraints. There are two methods used to define the constraints, namely, conventional, and inverse. In the conventional method, draping is usually achieved by selecting an initiation point and the initial fibre directions. The complete local fibre mapping is then obtained using trigonometric strategies. The selection of the initial point and fibre direction makes the conventional drape modelling solution very sensitive to the experience of the operator [174]. In the inverse method, draping begins with a unique draping pattern that corresponds to a unique geometry (i.e., two yarn paths are chosen across the surface, and the final shape is evaluated for practical application) [175]. In practice, inverse modelling is not a design tool because usually component designs are driven by specific shapes. However, Hancock and Potter [176] identified a specific set of shapes with advantageous properties for manufacturing. More importantly, the research revealed that relatively minor geometric changes to these shapes can lead to significant improvements in their conformability.

By simulating forming behaviour and analysing stress and strain distributions, researchers can gain critical insight into potential problem areas. One of the first studies to use macroscale kinematic analysis, Tam and Gutowski [177] revealed the importance of the in-plane shear in the fabric to the ideal mapping of complex shapes and described a method to identify the forming deformation by characterising the magnitude of the critical shear angle in highly curved areas. In subsequent studies of kinematic analysis, a locking angle has been defined, and attempts have been made to predict defects such as wrinkling occurrence by comparing local shear angles with the locking angle [178]. As shown in Figure 2.32, without any external force (before deformation begins), the contact angle between warp and weft is approximately 90^o. When an external force acts, shear forces induce relative rotation of the yarns. The idea was that the space between the yarns is reduced during shear and the adjacent yarns reach the minimum angle (or angle of locking) that can no longer be rotated. If the shear force continues further, the material becomes deformed, and wrinkles appear in the fabric due to the formation of inner compression forces. This concept provides insight into how woven patterns and fibre orientations affect forming behaviour. Fabrics with a high locking angle (tows oriented more perpendicular to the forming direction) are more resistant to wrinkling than fabrics with a low locking angle. However, this hypothesis does not consider the internal stress and strain distribution in the fabric. In addition, material properties such as tow stiffness and friction are neglected, which play a critical role in wrinkle formation.

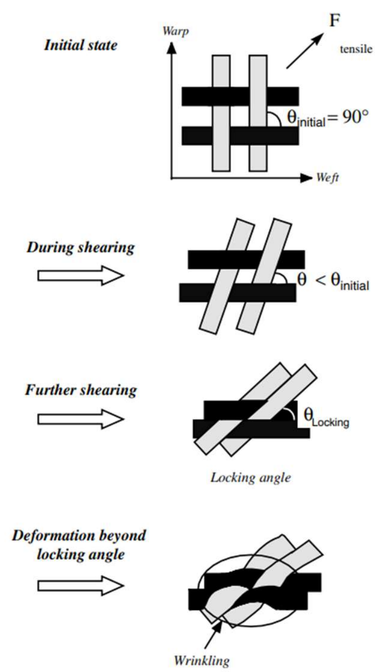

Figure 2.32: Wrinkling formation during the shearing of fabric [178]

Kinematic analysis helps understand some aspects of wrinkle formation, however, it has limitations. Although the kinematic analysis describes the wrinkling process using the above concept, the occurrence of all other defects (such as fibre misalignment, fibre splitting and stretching in the stitch direction) in fabric forming cannot be predicted. The simplifications used in kinematic mapping algorithms enable rapid fibre direction predictions after forming and provide simulation results in less than a minute [179]. However, these approximations lead to reduced accuracy. In addition, this method cannot be applied to multi-layered fabrics to obtain accurate predictions due to the inconsideration of the forces acting on the object such as frictional forces between the layers. Moreover, kinematic draping algorithms do not consider process boundary conditions. Therefore, these algorithms are more suitable for manual processing (hand-layup) rather than automated forming [180].

Finite Element Method

The finite element method (FEM) is a powerful tool for solving partial differential equations and is widely used to simulate complex fabric-forming processes. It allows for predicting fabric deformation under different forming conditions and ultimately achieves its final 3D shape with a realistic representation of the manufacturing process. FEM subdivides a large domain into small and simple components called finite elements. The deformation and motion of these elements are modelled using momentum balance equations and after combining these equations, they form a matrix that models the whole system. The most interesting characteristic of FEM is its capacity to manage complex geometries, materials behaviours, and boundary conditions (interaction with the tools and other components, such as grippers and blank holders) that are simplified or ignored in kinematic mapping [181]. There are three mechanical modelling approaches depending on the scale at which the analysis is made, namely, continuous (macro-modelling), discrete (meso-modelling), and semi-discrete (an intermediate method between macro- and meso-modelling) [182]. Researchers have recently developed many complex models, such as semi-discrete models, to understand how textiles behave during forming. However, the simplest, macro-scale models are practical for designing and testing the forming process of real-world parts.

Material Point Method

FEM has been widely used in the investigation of fabric reinforcements. However, complex meso-structures can pose challenges in generating high-quality mesh when materials undergo extensive deformation including high stretching and compression. The material point method (MPM), i.e. the meshless particle method, has attracted much attention because it offers many advantages over FEM, including the ability to handle large deformations and be efficient for complex geometries [183]. Lv et al. [184] used the MPM to improve the computational efficiency of textile animations and the models discussed in this study incorporate complex fabric behaviours such as bending, wrinkling, and large-scale deformation. A recent study by Nazemi and Milani [185] evaluated the effectiveness of the MPM and FEM in simulating a hemispherical forming of woven fabric reinforcement and validated the two numerical methods with experimental data. The study revealed that MPM was approximately 20 times faster than FEM models and that both models showed the same acceptable reliability in experimentally validated predictions. The study suggests that MPM is a promising method for simulating the forming of textile reinforcements, however, further research is needed to address its limitations, such as the effect of the model on the mould with sharp edges/corners and how to observe major wrinkles in formed fabric.

2.8.1.2. Constitutive Modelling

Continuous Approach

The textile reinforcement is treated as a continuous medium in this approach, and macroscopic modelling with standard finite elements is commonly used. The early FEMs are based on the linear elastic behaviour of materials [39] [186]. Hyper-elastic and hypo-elastic models (i.e., non-orthogonal material models) developed later as researchers were required to model fabric with more complex behaviour. Hypo-elastic models (a simplified approach to modelling material behaviour) are used in finite element analysis at large strains and the rate constitutive equations are indeed based on the current configuration (i.e., the relationship between stress and strain rates in the material, considering the current deformation state) [159]. Hypo-elastic approaches are easy to implement in nonlinear finite element approaches, however, sufficient small-time steps are required for good accuracy. Yu et al. [187] implemented a 2D non-orthogonal constitutive model, consisting of two primary components (i.e., tensile and shear stress contributions). The model represented the two different derivations of incremental stress/ incremental strain and shear force/ shear angle in the same reference system. The only requirement in this model to simulate a rate-independent shear behaviour is the shear force-shear angle configured with a polynomial function. However, during installation, this model eventually fell across numerical issues. Harrison et al. [188] have introduced a multi-scale energy model using truss and shell elements to simulate the thermoforming process of viscous textile composites. The tensile component of the previous model [187] (Figure 2.33a) was replaced by the truss elements to overcome the difficulties. This model contains unit cells with hybrid elements of truss and membrane elements (Figure 2.33b) which represent the tensile properties of individual fibres and the shear properties of woven fabric material, respectively [188].

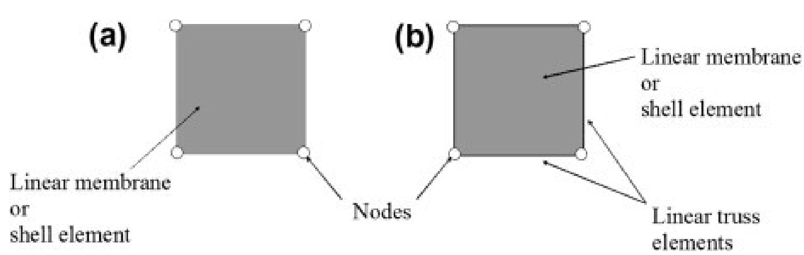

Figure 2.33: Unit cell representation of fabric structure in FEM (a) 2D non-orthogonal constitutive model in Yu et al. [187] (b) non-orthogonal constitutive model in Harrison et al. [188]

Khan [159] used a hypo-elastic approach for woven fabric to simulate the forming of a double-dome shape and the results imply a good agreement between the measured and numerical geometries. Figure 2.34 compares numerical simulations with experimental forming results for fabric reinforcement. For quantitative analysis of the tests, shear angles were measured along a selected path in selected regions of the deformed fabric. As noted by the researchers, the comparison of experimental and numerical results has generated satisfactory results. Khan et al. [189] further analysed the influence of some parameters like binder force, friction coefficient and forming speed using the hypo-elastic computational model to improve the pre-forming simulation.

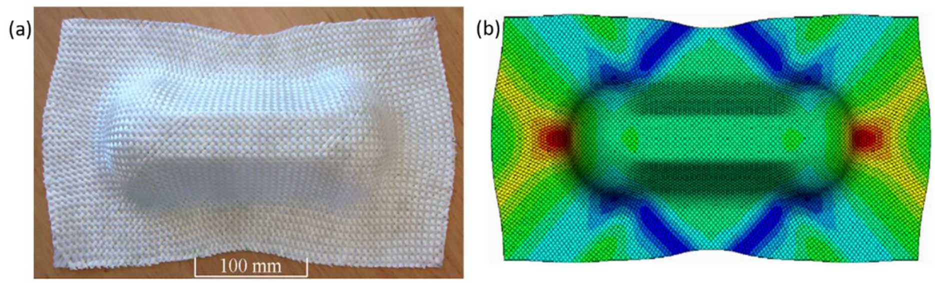

Figure 2.34: Double dome forming tests (a) Experimental (b) Numerical [159]

Unlike hypo-elastic models, hyper-elastic models are often related to the initial configuration of the material and describe the stress-strain relationship in a way that avoids needing small time steps in calculations (i.e., integral representation). The stress-strain relationship is based on the energy stored within the material due to deformation (strain energy density) and how this energy changes with respect to strain measures [190]. Therefore, hyper-elastic models can be appropriate for modelling textile draping when considering one-way deformation (without unloading). They may become less accurate under conditions of large strains if unloading or bidirectional deformation occurs. However, hyper-elastic models can be properly adapted for materials with history-dependent behaviour such as elasto-plasticity [191]. On the other hand, hyper-elastic models can exhibit rate-dependent behaviour such as visco-hyperelastic models. Kulkarni et al. [192] recently published a paper describing the viscoelastic compaction behaviour of a 3D woven fabric using a visco-hyperelastic modelling approach with a modified Maxwell-Weichert rheological model. Therefore, it is important to consider material characteristics before selecting whether the model is rate-dependent or independent.

The deformation behaviour of textile reinforcements is significantly different from other materials and mainly depends on the fibre orientation (fabric architecture). Textiles exhibit high tensile stiffness along the fibre direction and relatively low shear or bending stiffness in the same direction. Therefore, before applying conventional constitutive models for textile reinforcement to explain the fabric behaviour during the forming process, it is necessary to decouple the deformation mechanisms [193]. Various studies have been performed at the macroscopic scales using commercially available FE software (i.e., ABAQUS, LS-DYNA, and ANSYS), and among them, some papers discuss the forming behaviour of complex textiles such as NCFs discussed in Section 2.8.2.2 in detail. When considering hypo-elastic and hyper-elastic models, both offer a valuable initiation for material modelling in FEM due to their simplicity and applicability to a wide range of materials including textile reinforcements. However, there are some limitations in these models including fully accounting for the influence of the fibre orientation and its evolution during the forming process of textile reinforcements [194]. Some models incorporate the relationship between stress, strain, and strain gradient to enhance the ability of the macroscopic finite element model by considering the mesoscopic deformation of the textile material, particularly the bending stiffness of the tows [195]. Barbagallo et al. [196] Introduce second-order terms to describe the in-plane and out-of-plane bending stiffness shown to reduce wrinkling onset during the deep drawing simulation. Further, a second-gradient continuum model discussed in Barbagallo et al. [197] has captured S-shaped macroscopic deformations during a bias extension test of unbalanced woven fabric. This suggests that a second-gradient continuum approach is a useful tool for modelling the behaviour of fabric reinforcements.

Discrete Approach

In this model, each element of the fabric including fibre bundles (tows) and stitches, is modelled as a discrete entity using finite elements. Since this modelling approach is concerned with the draping of overall reinforcement and interactions between individual tows, simple elements are used to provide computational flexibility. Boubaker et al. [198] modelled the mesostructure of a woven fabric as a lattice in which the beam elements (representing the warp and weft of the fabric) are interconnected by frictionless hinges (representing interlacing points). Therefore, these types of models consider the interaction between warp and weft directions via contact behaviour and relative motions between yarns. Figure 2.35 a&b refers to a unit cell of an FE model used for discrete simulations of forming processes (a simple unit cell with 216 degrees of freedom (DOF)) and to analyse the in-plane shear deformation of plain-woven fabric (a unit cell with 47214 DOF), respectively [182]. In the simple unit cell (Figure 2.35a), the friction and relative displacement between yarns are described by modelling the yarns as shell elements. However, it is challenging to use the FE model shown in Figure 2.35b in practice to simulate the fabric-forming process due to the significantly high computational cost and time.

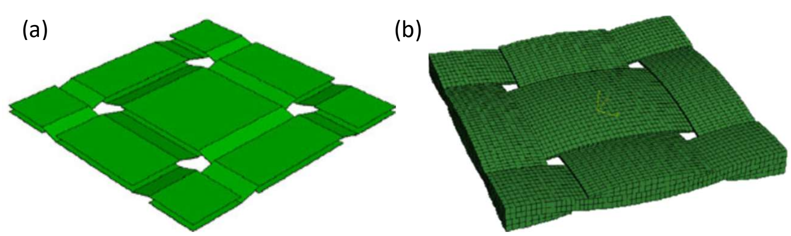

Figure 2.35: Discrete modelling of a plain-woven fabric unit cell with shell elements to simulate (a) the fabric forming process (216 DOF) (b) the behaviour (47214 DOF) [182]

Semi-Discrete Approach

This approach is a combination of both continuous and discrete models. The finite element is designed based on the behaviour of the mesoscopic representative unit cell. As in the discrete approach, the material behaviour is separated based on deformation (such as in-plane bending, tensile, and out-of-plane bending), and all deformations are considered within the unit cell defined as the continuous approach [195]. The objective of the semi-discrete approach is to model the fabric at the mesoscopic level while keeping a limited number of degrees of freedom. This integration of both approaches allows for a more comprehensive understanding of the material behaviour, capturing both macroscopic and mesoscopic effects, and this approach can be used to determine the coupling between deformations considered as a limit of discrete models.

Harrison et al. [67] improved the hybrid element model by replacing the truss elements with the beam elements. The latter represents not only tensile stiffness but also in-plane and out-plane bending stiffness and torsional stiffness (Figure 2.36). The nodes at the ends of the membrane element connect to one end of the beam element via the zero-torque hinge connection element. The hinge elements limit the relative position of the nodes while permitting the connected beam elements to rotate freely. This model is computationally expensive. This is an accurate method of modelling the forming behaviour of woven engineering textiles in that it relates the macroscale mechanical properties of the fabric to the properties of the structural elements inside the mesh.

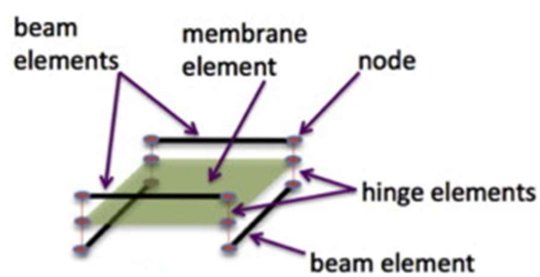

Figure 2.36: Unit cell of Mutually Constrained Pantographic Beam & Membrane Mesh Model [67]

2.8.2. Non-Crimp Fabrics Forming Simulations

2.8.2.1. Biaxial Non-crimp Fabrics

In contrast to woven fabric, stitches in NCFs avoid tow-undulation and increase the handling capabilities of the fabrics, making them ideal for automated manufacturing. On the other hand, the more regular structure and inherent stiffness of woven fabrics make them easier to model compared to the complex and variable structure of NCFs (i.e., tows can be oriented in different directions with different types of stitch patterns. In addition, the types of stitching materials also affect the complex structures of NCFs) [199]. However, with the advancement of modelling techniques and the availability of more detailed material data, the gap between woven and non-crimp fabric modelling is gradually narrowing.

Finite element simulations are more developed for analysing the forming behaviour of woven fabrics due to simple structural patterns and well-defined deformation modes. In contrast, fewer studies, have been presented on the constitutive modelling and numerical forming of NCFs which present unique challenges due to their more complex structure and deformation characteristics. Mesoscale constitutive models offer a powerful tool for simulating different fabric-forming processes, and they are particularly effective for analysing specific challenges related to NCFs forming. Creech & Pickett [200] developed a mesoscopic forming model for a biaxial NCF to determine several deformation mechanisms. The model has two separate ply layers where one layer consists of solid and bar elements used to model the individual tows and stitches, respectively. This model produced greater fabric deformation information than either the mapping technique or the FE continuum approach. Although there is no significant effect on draping, Sirtautas et al. [201] added a special feature of 'gap elements' to a similar model to pair the infusion model to represent resin flow. Pham et al. [202] developed another mesoscopic forming model for a biaxial NCF and modelled a single tow by a single beam element to improve computational efficiency. Bel et al. [203] experimentally quantified a significantly higher tow-sliding in a biaxial NCF than in woven fabrics and developed an efficient semi-discrete model [204] to determine this tow-sliding with a good agreement between the experiment and the simulation. Information obtained from the mesoscale constitutive model has shown promising results with a detailed description of the internal structure of the reinforcement (i.e., capturing the individual behaviour of tows) and a better representation of the anisotropic behaviour of fabric during forming. However, modelling fabric forming at the level of individual tows can significantly increase computational complexity (i.e., computational time and cost) compared to continuous approaches.

Variations in the mesoscale architecture of the NCFs can significantly affect the forming behaviour. Therefore, the choice of modelling route may vary from one fabric to another. For example, the shear behaviour of chain-stitched biaxial NCF (with high stitch stiffness) can be very similar to that of a woven fabric and a macroscale continuum approach may be appropriate. Yu et al. [187] modified a non-orthogonal model originally developed for macroscale woven materials and successfully captured the asymmetric shear behaviour of biaxial NCF. However, this model lacks a mechanism for defect prediction. Chen et al. [205] focused on a defect-oriented non-orthogonal constitutive model for biaxial NCFs with a pillar-stitch pattern. Unlike Yu et al. [187], this model addresses macroscale wrinkling and other distortions (i.e., fibre compression and mesoscale wrinkling) that occur during forming. In addition, the constitutive model presented by Khiêm et al. [144] is more versatile (applicable to a wider range of NCFs) and captures the global elastic behaviour of biaxial NCFs under various loading conditions. This model provides computational efficiency due to its averaging-based approach.

2.8.2.2. Uniaxial Non-crimp Fabrics

The forming simulations discussed in Section 2.8.2.1 are related to biaxial NCFs, and fewer studies have been focused on unidirectional non-crimp fabrics. They are less commonly used because their anisotropic nature complicates modelling and forming processes [206]. Note that the forming simulations of all the UDNCFs discussed in this section are quasi-UDNCF (stitches are perpendicular to the main tows and contain a small weight fraction of additional glass fibre tows, orientated transverse to the main fibre direction to stabilise the fabric).

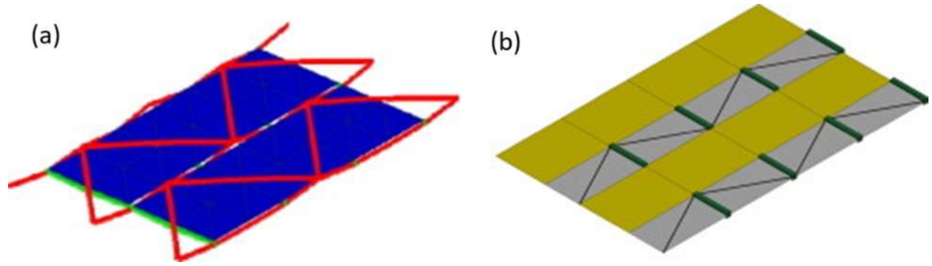

Figure 2.37: Modelling of UDNCF using different approaches (a) Meso-model [207] (b) Macro-model [208]

Among the UDNCF forming simulation studies, only a few studies have focused on meso-models of UDNCF fibre structures [207] [209]. In the mesoscopic fabric models, the main tows, additional glass stabilising tows and stitches are each modelled separately, and the three components are connected edge to edge i.e., the main tows are modelled by shell elements whereas the stitches and the additional glass tows at the back of the fabric are modelled by bar elements with different material laws (see Figure 2.37a). Kärger et al. [209] discussed the draping simulation of meso-model UDNCF using a patch approach i.e., combining the advantages of both kinematic mapping and FEM. The draping simulation using the kinematic approach shows low calculation time, however, it produced inaccurate results for complex geometries. The finite element method allows for defining different properties along the material directions and includes fibre slip during shear loading, however, it gives high computational time. The combined approach proposed by Kärger et al. [209] uses kinematic mapping for areas with low deformation and FEM for areas with high deformation. This allows for a more accurate simulation of the draping process. To improve the computational efficiency of forming simulations for UDNCFs, researchers are increasingly focusing on macroscale material models (see Figure 2.37b) [60] [208] with FEM. This approach allows for efficient simulation of large-scale forming processes while capturing the essential fabric deformation mechanisms, i.e., macroscale models consider the fabric as a continuum material with averaged properties, reducing the computational cost compared to meso-models that explicitly represent individual fibres.

The macroscopic forming model of UDNCF introduced by Schirmaier et al. [53] allowed for the prediction of fibre orientation and shear angle during hemispherical forming in good agreement with experimental results. However, this model involves the calibration of several input parameters as the approach couples several deformation modes. The study by Schäfer et al. [210] builds upon the work of Schirmaier et al. [53] by introducing a simplified hyperelastic forming model for UDNCF. This model reduces complexity by eliminating the coupling and focuses only on the nonlinear elastic stiffness. The results of the model agree well with the experimental data; however, some limitations were identified due to the low complexity of the model. The study by Ghazimoradi and Montesano [211] introduced notable improvements over the model proposed by Schäfer et al. [210] by implementing an anisotropic hyperelastic material model. This model can more accurately capture the nonlinear shear deformation response and in-plane shear-extension coupling, critical aspects of UDNCF behaviour often neglected by other macroscopic models. Schäfer et al. [212] recently proposed a new hyperelastic macroscopic forming model based on Schäfer et al. [210] (the prior work) that incorporates a strain energy density rather than non-linear stiffnesses. Furthermore, the new model reconsiders the coupling of transverse tension and in-plane compression in the deformation and offers a more comprehensive and accurate approach to modelling the behaviour of UDNCF.

Recent advances in the macroscopic forming simulation of UDNCF are reflected in the predictive capabilities and growing accuracy of these models. However, challenges remain for further improvements of high accuracy and computationally efficient models with complex loading scenarios. Furthermore, all the studies discussed in this section are related to quasi-UDNCF and no study related to the simulation of pure-UDNCF (i.e., with compliant stitches perpendicular to the main tows and containing no additional stabilising fibres) has been proposed so far. Therefore, investigating the forming simulation of pure-UDNCF, a less explored variant of non-crimp fabrics, holds the potential to significantly advance the field of materials modelling and simulation.

2.9. Conclusion of Literature Review

This chapter explores current engineering textile materials and their forming mechanics. The methods used for fabric characterisation, forming and simulation are discussed in detail, along with the advantages and disadvantages of each method. This literature review will be used as a framework for material characterisation and isolation of mechanical properties in this research.

Research on the forming behaviour of unidirectional non-crimp fabrics (UDNCFs) lags behind biaxial fabrics including woven and non-crimp fabrics. Among the studies on UDNCFs, most existing studies focus on quasi-UDNCFs (i.e., UDNCFs that include a small amount of stabilising glass fibre transverse to the main fibre direction). This research focuses on pure-UDNCF which does not include stabilising fibres. Therefore, the gaps identified for pure-UDNCF in the literature review are outlined below.

- Limited Experimental Analysis

Shear: No in-depth analyses of how pure-UDNCFs respond to shear forces are reported. This knowledge is essential for optimising forming processes and preventing defects.

Stitch strain: Experiments conducted to determine the tensile strain in the stitch direction are minimal. Although quasi-UDNCF exhibits this behaviour to some extent, less attention has been given to stitch strain experiments. Tensile strain in the stitch direction is a significant component of pure-UDNCFs, and a solid understanding of this is essential for complicated shape formation.

- Forming Analysis

Formability: Limitations of pure-UDNCFs in terms of processability are not evident in the literature. This includes identifying the optimum shapes that can achieve the best mechanical properties without defects.

Fixation methods: Fixation methods applied to single-layer fabrics have not been fully explored in the literature. Therefore, studies should be conducted on how to produce high-quality specimens and how to remove specimens from moulds without damaging the specimens.

Full-Field Measurements: As stated in the literature, full-field measurement methods taken for the analysis of formed fabric samples mostly study the shear angle. Full-field measurement techniques should be identified to analyse the stitch strain of pure-UDNCFs during forming. This can provide valuable insight into fabric behaviour.

- Numerical Modelling Deficiencies

Accuracy of Models: Existing numerical models of various engineering fabrics cannot be used to accurately capture the behaviour of pure-UDNCF (even quasi-UDNCFs). Therefore, further development of these models is required to obtain the unique characteristics of pure-UDNCFs.

Validation of Models: If numerical models for UDNCF are present, there may be a potential gap regarding the validation of existing numerical models. More experimental data on pure-UDNCF are therefore needed to confirm the accuracy of these models

Chapter 3 Shear & Tensile Experiments Using Standard Tests

3.1. Introduction

In most engineering fabrics, shearing is a key deformation mechanism during draping. Shear deformation of woven fabrics involves the in-plane rotation of the tows at the crossover points and the relative sliding of these tows against each other [7]. The shear deformation of non-crimp fabrics involves the relative sliding of unidirectional tows, which differs from woven fabrics due to the presence of stitches. In the case of pure-unidirectional non-crimp fabric (in pure-UDNCF, stitches are perpendicular to the glass tows and contain no additional stabilising fibres), the low-stiffness stitches are the main load-bearing element in the direction orthogonal to the fibre direction, therefore, large transverse strains can be reached during draping. Thus, compared to biaxial fabrics, the in-plane deformation modes of pure-UDNCF are complex and dominated by transverse extension and shear.

This chapter begins with a detailed description of three engineering fabrics: pure-UDNCF and two woven glass fabrics (plain and twill). The woven fabrics are more typical engineering fabrics, for which test procedures are well-established and are used for comparison with the behaviour of the pure-UDNCF. This helps to understand how meso-structural differences in fabric architecture influence mechanical performance. Woven fabrics have interlaced warp and weft tows, providing a stable, interlocked structure. This structure allows them to exhibit certain mechanical properties and deformation behaviours, such as better in-plane shear resistance and well-defined load distribution paths. Compared to woven engineering fabrics, the characterisation process of non-crimp fabrics is less established, especially those NCFs with compliant stitching. Non-crimp fabrics have fibres laid straight and held together by stitching. The stitching parameters (i.e., stitch stiffness, gauge, length, and pattern) can affect how the fabric drapes, stretches and reacts to forces and add another layer of complexity to the characterisation process.

The uniaxial bias extension (UBE) and the picture frame (PF) tests are commonly used to characterise the shear behaviour of engineering fabrics. In this chapter, a preliminary investigation of the in-plane forming mechanics of the pure-UDNCF is conducted. As will be seen, this preliminary investigation reveals a significant difference between the results of the two shear tests, with the measured shear stiffness in the PF test being significantly **higher** than that of the UBE test. This unusual observation, which is not seen for the two woven fabrics, prompts further investigations to understand the reason for the difference. The aim is to understand if the different behaviour in the two tests is real, or simply a problem related to the use of the tests for this particular fabric. To this end, various techniques to explore the possible influence of the boundary conditions and the internal friction of the PF rig are considered.

The structure of this chapter is as follows: Section 3.2 describes the details of the fabrics used in this study. Sections 3.3 and 3.4 explain the experimental setups and analysis for the standard UBE and PF tests respectively. The results of the two standard shear tests of pure-UDNCF are compared in Section 3.5. Sections 3.6 to 3.9 explore the possible influence of the boundary conditions of the PF test and aim to minimise the experimental error. A standard tensile test of pure-UDNCF along the stitch direction is covered in Section 3.10 and the chapter summary is provided in Section 3.11.

3.2. Materials

The thesis focuses mainly on the characterisation of the forming mechanics of pure-unidirectional non-crimp glass fabric supplied by Johns Manville. Two more woven glass fabrics (i.e., plain (GF-PL-290-100) and twill from EasyComposites and Johns Manville, respectively) were also characterised to compare the shear properties with pure-UDNCF i.e., ensure the reliability of the testing procedures.

Close-up images of the three fabrics are shown in Figures 3.1a, 3.2a and 3.3. Table 3.1 summarises the details of each fabric. The weights of five samples (100 × 100mm^2) were measured using a weighing scale (KERN PCB 6000-1) with 0.1g accuracy to calculate the average areal density. The widths of the tows and the gap in the plain-woven fabric were measured using ImageJ software [146] and, out of ten measurements, the average values were calculated. A digital vernier calliper was used to measure the thicknesses of fabrics. The average thickness of each fabric was calculated from measurements taken at ten random places. Compared to plain-woven fabrics (0.3kgm^{-2}), twill-woven (1.17kgm^{-2}) and pure-UDNCF fabrics (1.37kgm^{-2}) show approximately four times higher areal densities (see Table 3.1). This difference can be attributed to several key factors related to fibre architecture and packing density. The plain-woven fabric has fewer fibres or filaments per tow than the twill-woven and pure-UDNCF (see Figure 3.1, note that no information on the fibre bundles of each fabric is provided). In addition, the plain weave has the lowest fibre volume fraction due to larger gaps, which can further contribute to reducing the areal density. The measurements obtained using the ImageJ [146] software were then incorporated into the textile generation software, TexGen [213] to create models of the plain-woven (see Figure 3.1b) and twill-woven glass fabrics (see Figure 3.2b). TexGen software is simple to use when creating models for 2D woven fabrics. However, scripting is essential for creating non-crimp fabric models, particularly those with more complex or customised structures. Therefore, the TexGen models were generated only for woven fabrics in this study.

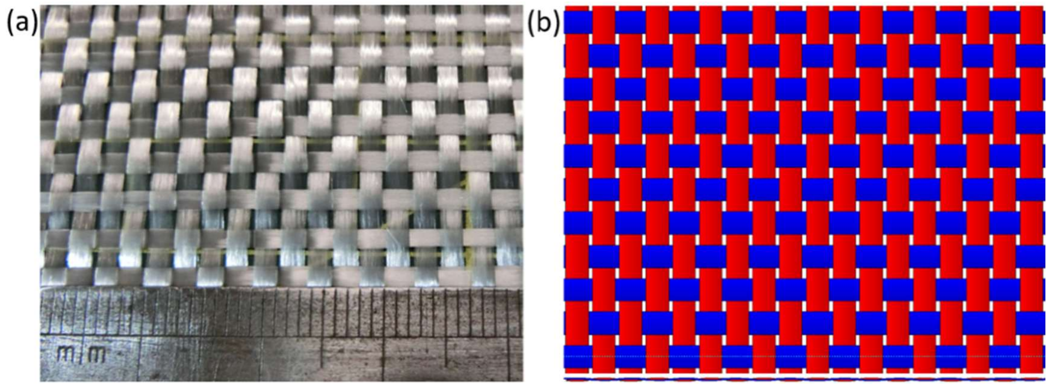

Figure 3.1: Plain-woven glass fabric (a) close-up image (b) TexGen model

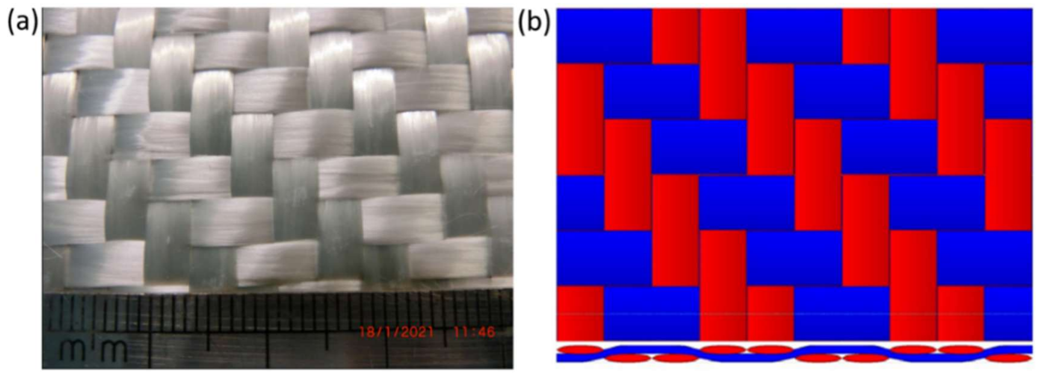

Figure 3.2: Twill-woven glass fabric (a) close-up image (b) TexGen model

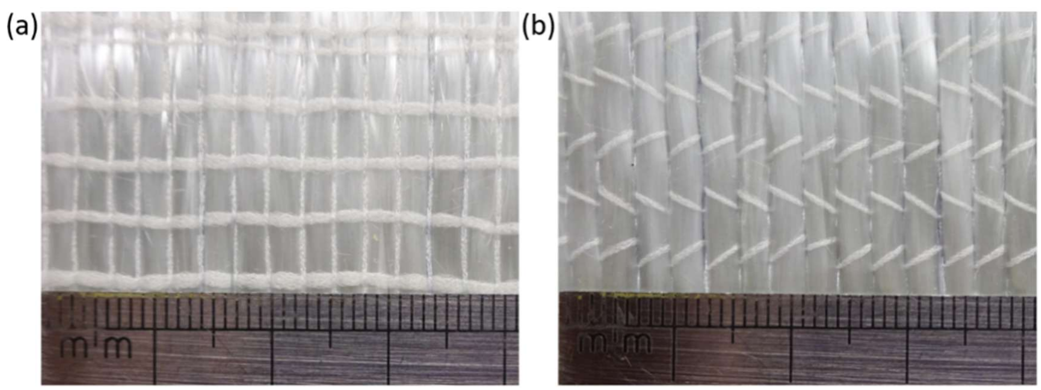

Figure 3.3: Close-up images of pure-unidirectional tricot-chain stitched glass fabric (a) front (b) back

Table 3.1: Details of the three different glass fabrics: Plain woven, Twill woven and pure-UDNCF

		Plain-woven (GF-PL-290-100)	Twill-woven (E-glass, JM StarRov® 886)	Pure-UDNCF (JM StarRov® 886 - 2400 tex)
Type		1x1	2x2	Unidirectional tricot-chain stitched
Width of the roll/ m		1	1.65	1.45
Warp width/ mm		1.7 ± 0.1	3.6 ± 0.2	2.6 ± 0.5
Weft width/ mm		1.7 ± 0.2	3.6 ± 0.2	-
Thickness/ mm		0.26 ±0.03	1.10 ± 0.03	1.10 ± 0.03
Unit cell size (mm^2)		3.4 x 3.4	14.4 x 14.4	-
Stitched yarn width/ mm	chain	-	-	0.6 ± 0.1
	tricot			0.6 ± 0.1
Average gap/ mm	warp	0.5 ± 0.1	0	0
	weft	1.2 ± 0.1		
Average areal density/ kgm^{-2}		0.300± 0.011	1.170± 0.016	1.370± 0.014

3.3. Uniaxial Bias Extension Test

The uniaxial bias extension (UBE) test is used to determine the shear behaviour of the engineering fabrics. The primary focus of this chapter is on the characterisation of pure-UDNCF fabrics. Before performing the UBE test on pure-UDNCF, the test was performed on plain woven fabric following previous studies [6] [67] [113] and then on twill woven fabric to understand the best practice and to ensure the reliability of the standard testing method, i.e., to determine whether the standard method used for engineering fabrics would also be adequate for the pure-UDNCF. The UBE tests of woven fabrics were further performed with anti-wrinkle plates to obtain accurate measurements at higher shear angles as mentioned in Harrison et al. [101]. To improve the impact of this work, a protocol describing the process of preparing test specimens, conducting tests, and analysing results for the UBE test on woven engineering fabrics, has been published online on Protocols.io [214].

3.3.1. Experimental Set-up

3.3.1.1. Sample Preparation

First, the fabric was placed on a flat surface (cutting board) and manually adjusted to maintain the initial inter-fibre angle (angle between the warp and weft tows) of 90° (i.e., to avoid pre-shear). A parallel line to the weft tows was drawn on the fabric, and a template was positioned at an angle of 45° to the drawn line (see Figure 3.4a). A specimen size of 400×200mm^2 was selected for this study, making the specimen width to unit cell size ratio about 59 for the plain weave, but only around 14 for the twill weave. This ratio can influence the cohesion of the sample during the UBE test. The template was adjusted to the required angle using a protractor. The outlines, gridlines, and diagonal lines in Region A (see Figure 2.11) were then marked using a black Sharpie pen (Figure

3.4b). It is necessary to always mark the lines on a single tow as a continuous line for post-specimen analysis. The specimens were then cut through the marked outline using a rotary cutter (Figure 3.4c). Replacing scissors with a rotary cutter helps to minimise the addition of pre-shear during the cutting of the samples and produces a better finish on the edges of the samples (see Figure 3.4d). A horizontal line was marked at the back of the specimen (across the midsection) for the examination of the wrinkling onset.

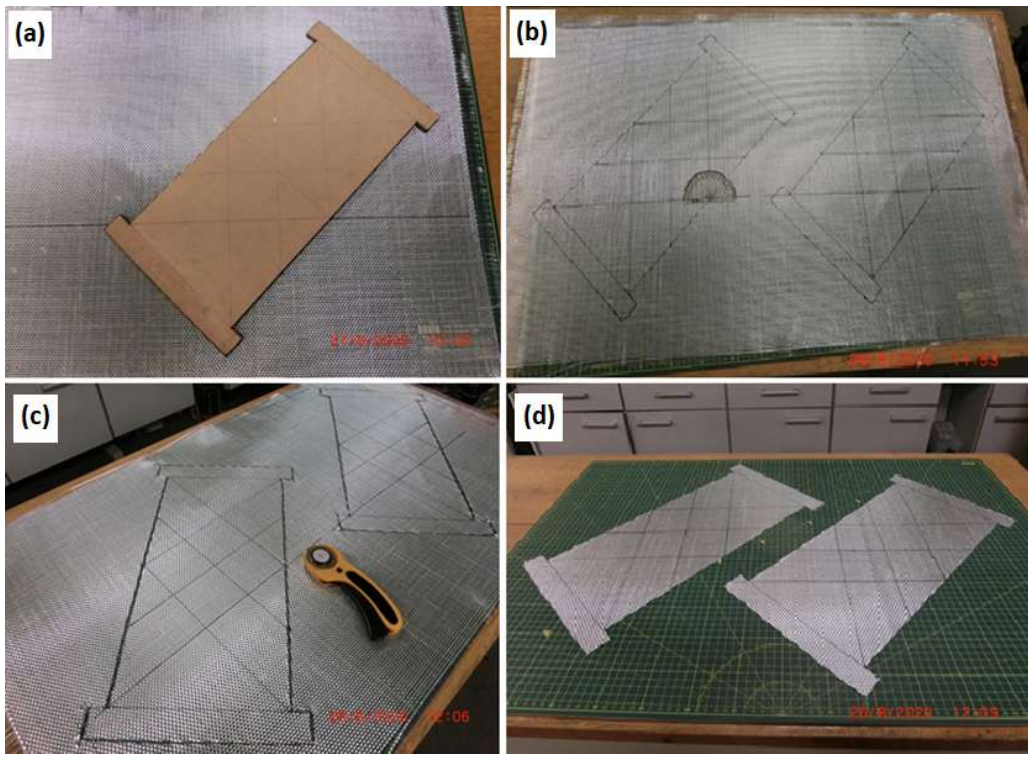

Figure 3.4: UBE Specimen preparation (a) placing the template (b) marking outlines, gridlines, and diagonal lines (c) cutting the specimens using a rotary cutter (d) specimens with better-finished edges

The modified version of the UBE test [67] involves bonding aluminium (Al) foil to both the clamping region and 'Region C' (see Figure 2.11) using cured epoxy resin to allow easier drilling of holes and to mitigate intra-ply slip [67]. Therefore, another template was prepared based on the measurements of the clamping area (30×240mm^2) and Region C. The Al foil was folded in half and the template was positioned with the clamping area along the folded edge (see Figure 3.5a). Then cut along the lines marked by the template. Using this method, both sides of the sections can be cut at the same time (Figure 3.5b).

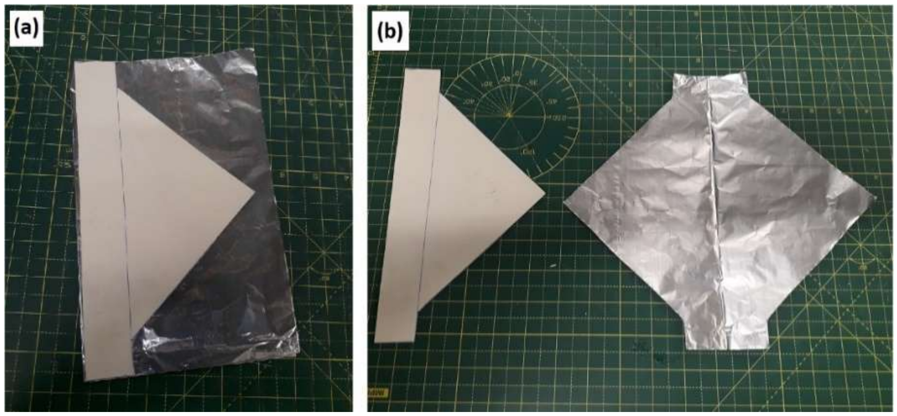

Figure 3.5: Cutting Al sections (a) Positioning the template close to the folded end of the Al sheet (b) Separated Al section

The work surface should be prepared before applying epoxy resin (half of the cut Al section was inserted into the sample - see Figure 3.6a) to protect other areas of the sample and the work surface from the adhesive. Using a nozzle glue gun, an appropriate amount of epoxy resin (Permabond ET500) was applied to half of the Al section (see Figure 3.6b), and the resin was then evenly dispersed by a stick (see Figure 3.6c). In practice, externally mixing the resin with disposable cups (see Figure 3.6d) is faster than using a glue gun with a nozzle because slow resin delivery from nozzles takes longer. However, care must be taken to thoroughly mix the resin and hardener before applying to the specimen.

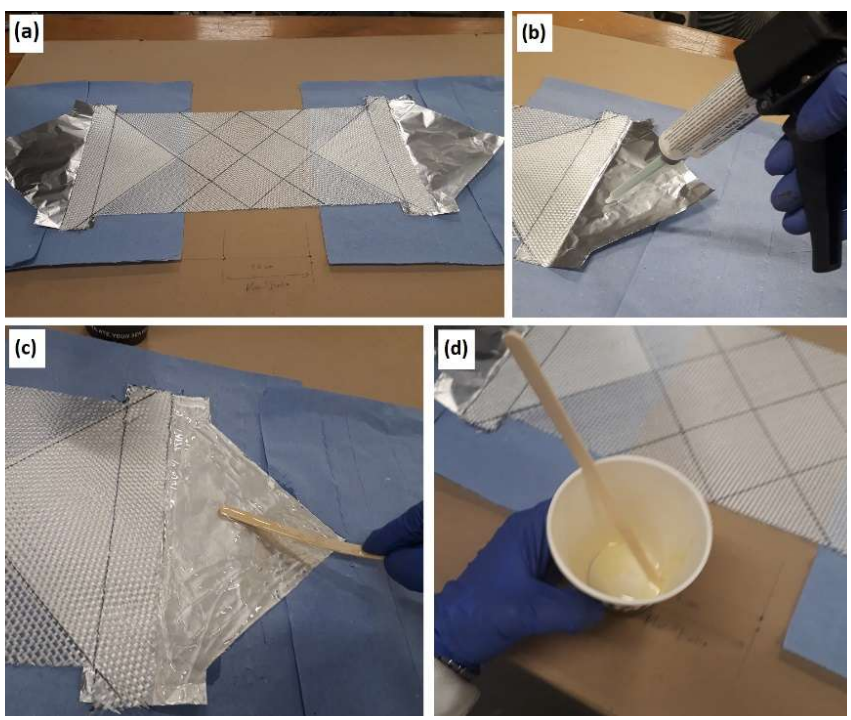

Figure 3.6: (a) Preparing the work surface before applying the resin (b) applying the resin with a nozzle glue gun (c) spreading the resin evenly with a stick (d) the external mixing cup

The adhesive was applied to both exposed sections of the foil at the same time and then attached to the sample. This technique involves applying the resin to the specimen in a semi-cured condition before bonding. The sample was then flipped, and the procedure was repeated. The adhesive was applied to cover only the C region and both sides of the clamp area, ensuring that the other regions were not contaminated. The samples were then left for 48 hours to fully cure the epoxy resin before drilling the holes (to allow the sample to be mounted to the clamps). Figure 3.7 shows the prepared UBE specimens before drilling and how the specimens should be stored for curing.

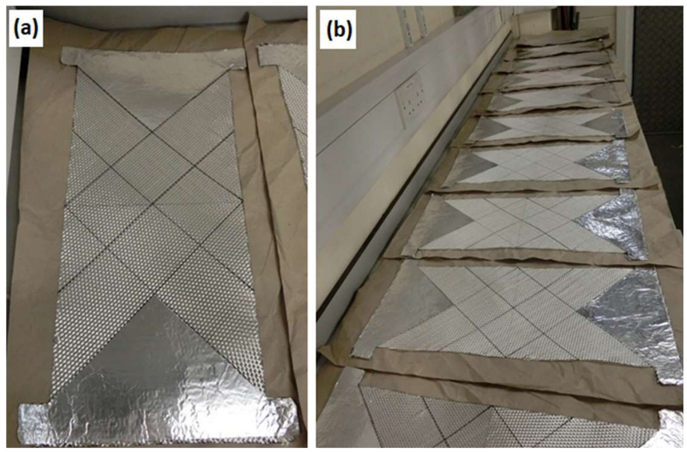

Figure 3.7: Prepared UBE specimens (a) one (b) all ten

After 48 hours, the holes were drilled carefully, without deforming the specimens. The completed specimen of each fabric for the UBE test is shown in Figure 3.8. For biaxial fabrics, the UBE specimen can be divided into three Regions A, B and C (see Figures 3.8a & b) similar to Figure 2.11. The B regions of the pure-UDNCF sample can be further divided into two, namely, B1 and B2 (see Figure 3.8c). In the B1 Regions, one end of the tows is constrained, and both ends of the stitches are unconstrained whereas in the B2 Regions, one end of the stitches is constrained, and both ends of the tows are unconstrained (see Figure 3.8d).

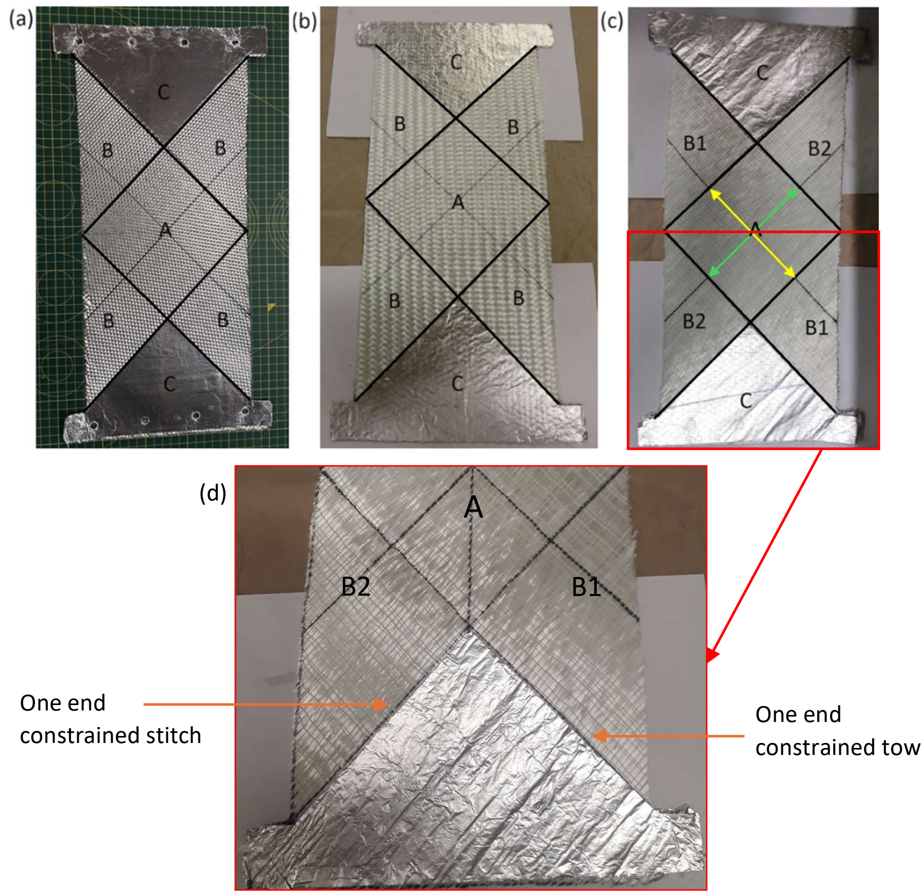

Figure 3.8: UBE specimens (a) plain-woven (b) twill-woven (c) pure-UDNCF, the yellow and green arrows indicate the initial chain-stitch direction and the tow direction, respectively. (d) a magnified image of (c)

3.3.1.2. Loading and Clamping the Specimen

The UBE experiments were performed on a Zwick Z2 tensile testing machine mounted with a 2kN load cell (this test can be performed with any universal testing machine having a load cell with sufficient resolution to measure the force accurately). The strain rate was fixed at 200 mm/min with a maximum upper force limit of 1kN. Engineering fabrics exhibit rate-independent behaviour during shear deformation because the deformation mechanisms primarily involve tow rotation and frictional sliding, leading to a response largely unaffected by strain rate [114]. However, it is important to select an optimal strain rate that will ensure that the test accurately captures the material behaviour while maintaining practical test duration. Standard force and travel (displacement) were set as the parameters of the report which would be used for post-test analysis.

The UBE test was conducted in two setups: with and without anti-wrinkle plates (AWPs) [113]. Both experiments were performed with five repeats. Figure 3.9 shows the installation of the UBE test specimen on the machine without AWP. After installing the specimen, the initial inter-fibre angle needs to be verified before the test to ensure that the pre-shear angle before the test is less than 0.5° to obtain accurate results [113].

Figure 3.9: UBE test setup without anti-wrinkle plates

With Anti-wrinkle Plates (AWPs) Setup

UBE test was further extended with AWPs to obtain accurate measurements at higher shear angles following [101]. Two parallel Perspex plates with a 2mm gap were used as the AWPs (see Figure 3.10a). The gap between Perspex sheets depends on the thickness of the fabric. In this study, the thicknesses of the specimens were kept below 2mm even after bonding the Al foil. This is important to avoid the contribution of additional frictional force to the total axial force. Prior to the testing, the plates were cleaned using acetone. The AWPs were then placed in the middle of the two tensile testing clamps using three-finger double adjustment clamps fixed to two parallel stands mounted on the test bed (see Figure 3.10b). The plates were hinged on one side and the specimens were loaded by opening one plate of the setup. After installing the specimen, the other side of the AWP was tightened by the G-clamps (a low tightening pressure of 1Nm was used to maintain the 2mm gap between the two plates – see Figure 3.10c). Finally, the initial inter-fibre angle was verified before the test (Figure 3.10d).

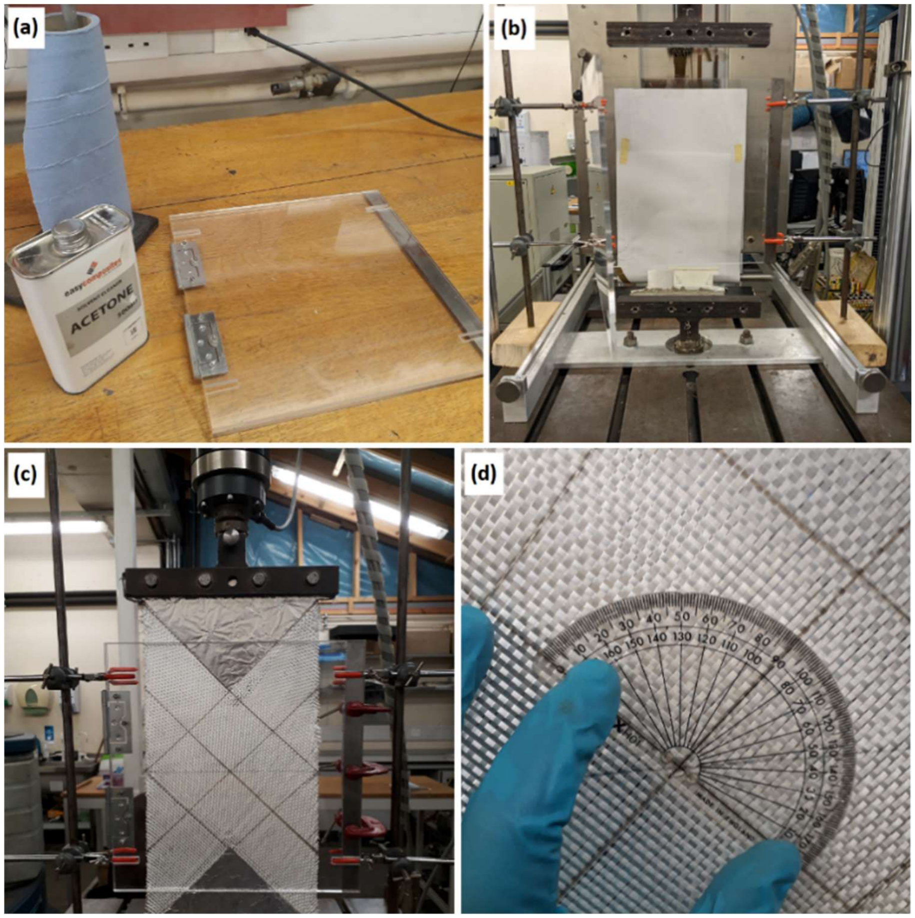

Figure 3.10: (a) Cleaned AWPs (b) clamping the AWPs (c) completed UBE test setup with AWPs (d) verifying the pre-shear angle before performing the test

3.3.1.3. Video Setup

The manual image processing technique (i.e., ImageJ [146]) was used for post-UBE test analysis; thus the front of the experiments was recorded using a digital camera positioned orthogonal to the surface of the specimen (Casio EX-ZR700). In addition, the back of the test specimen was filmed by a smartphone camera at an oblique angle (see Figure 3.11) to investigate the wrinkling behaviour of the specimens. The force of the machine was set to zero before performing the test. The start button was then pressed while the countdown began. The countdown was announced aloud so that the cameras could record it to allow for the exact start point to be found during post-test analysis of the resulting video.

Figure 3.11: Positioning a smartphone at an oblique angle

3.3.2. Measurements of Fibre Angle and Strain in the Stitch Direction

3.3.2.1. Manual Image Analysis

The captured videos of each test were accurately cropped using video editing software [215] at the exact start of the test. Finding the precise start point of the test is important as this is where the shear angles at known displacements are determined relative to the initial measurements of the specimen. The cropped videos (both front and back) were then converted to still frames using the software VirtualDub [216] and the frame rate was set to two frames per second (the frame rate of the videos is equal to 30 frames per second. Therefore, every 15th frame of the video is saved). Among other video processing software, VirtualDub is recommended for this analysis because it facilitates saving the exact still frame required based on the frame rate of the video. Since the strain rate is 200mm/min, the displacement between the two frames can be calculated as 1.7mm (200/(60x2)).

Shear Angle Measurements

The most significant step in the post-experimental analysis of these tests is manual image analysis. ImageJ software [146] was used to measure the shear angle of each frame. The shear angles of the standard UBE test were measured using the following steps, and the measurement method for other tests is similar to this method.

When measuring inter-fibre angles, it is critical to minimise the associated human errors. Figure 3.12 shows the method used to determine the inter-fibre angle of the specimen. After loading the picture (still frame) to ImageJ, the picture was zoomed to the level of 400% where the image appears as a set of individual pixels (see Figure 3.12a). The colour of the pixels in the middle of the drawn lines is darker than the pixels at the edges of the line. Thus, the angle tool traced three points of the inter-fibre angle across the middle pixels (dark colour). When the cursor moves close to the certain traced point, the arrowhead of the cursor switches to the hand icon as shown in Figure 3.12b. The exact coincidental line can be drawn by moving the traced point along the marked line in the specimen. This technique therefore minimises the standard deviation of the measurements and enhances the reliability of the analysis. Figure 3.12c illustrates a perfectly drawn inter-fibre angle after zooming out the image. To improve the accuracy of the data, the vertically opposite angles were measured (see Figure 3.12d) and the average was calculated. The inter-fibre angle was measured in each image based on this method until the crosslines in the middle of Region A became distorted or difficult to measure due to wrinkle formation.

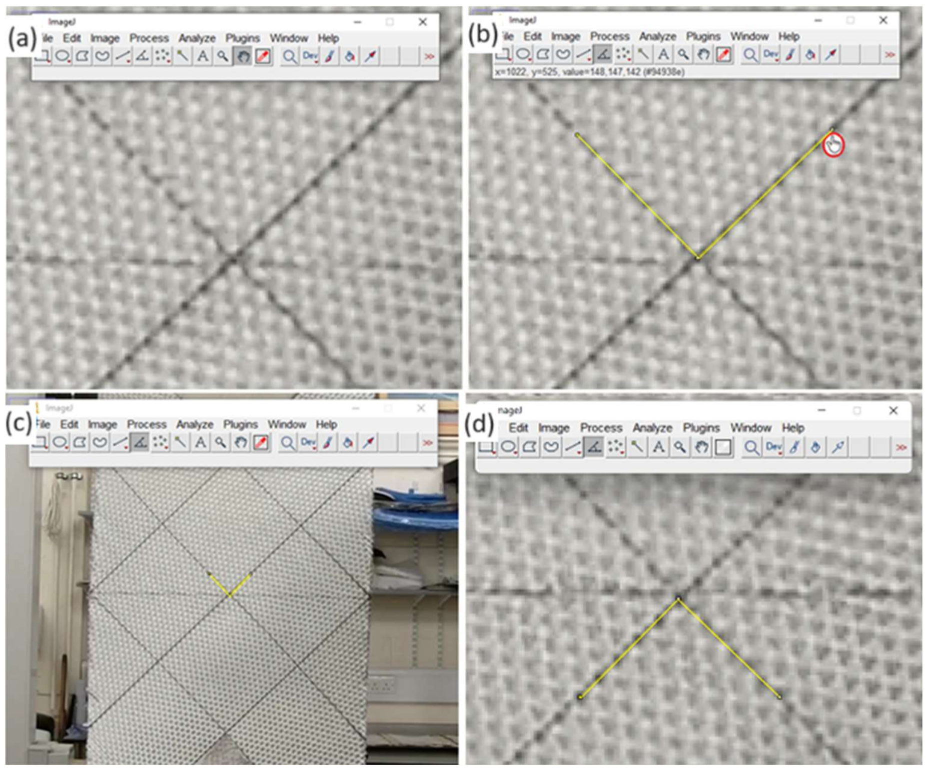

Figure 3.12: Inter-fibre angle measuring technique using ImageJ (a) 400% zoomed image (b) tracing the inter-fibre angle using angle tool (c) zoomed out image (d) measuring the vertically opposite angle

Stitch Strain Measurements

The stitch strains of the standard UBE test of pure-UDNCF at given displacements were measured using ImageJ software following the steps below. The stitch strain measurement method for other tests, i.e., octagonal-shaped and simple shear tests discussed later in Chapter 4, is similar to this method. The length of the clamp (240mm) was set at the beginning as the global scale (see Figure 3.13a), and the side length of Region A (L_A – see Figure 3.13b) was measured. The stitch lengths at given displacements (the saved still frames) were measured for all these specimens using the line tool in the ImageJ software (similar to the method used to measure the initial side length of Region

A). The experimental stitch strain of each test was calculated as the ratio of the change in length experienced by the specimen to its original length.

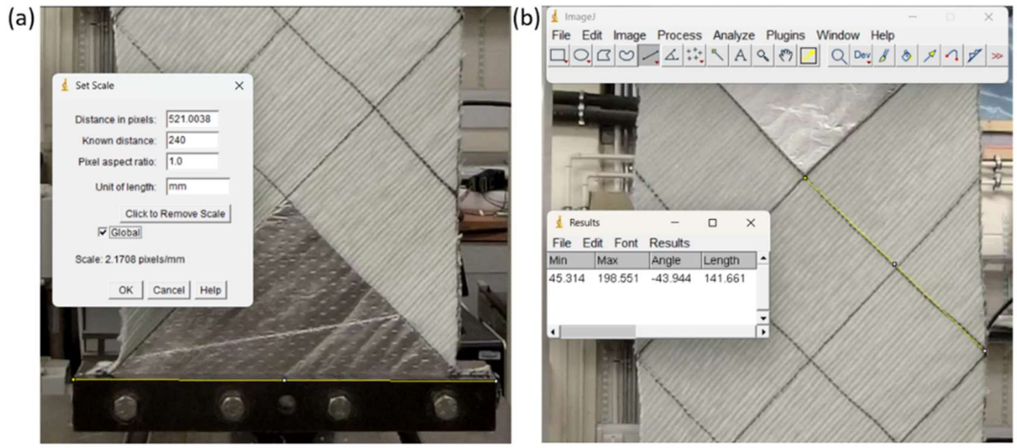

Figure 3.13: (a) Scaling in ImageJ software (b) measuring the side length of Region A

3.3.2.2. Wrinkle Analysis

The back-camera videos were split into still frames to investigate the onset of wrinkling. In these experiments, the wrinkling onset was determined by observing the horizontal line drawn at the back of the specimen (see Figure 3.14a). When the tensile force is applied to the specimen, the horizontal line tends to deform at one point (see Figure 3.14b&c, the straight horizontal line begins to turn into a curved line). The shear angle measured at this point is the wrinkle onset angle. The back camera was mounted at an oblique angle to allow for better observation of wrinkle formation. Most importantly, to obtain an accurate wrinkle onset angle, both front and back videos should be aligned with the start time (time-synchronized).

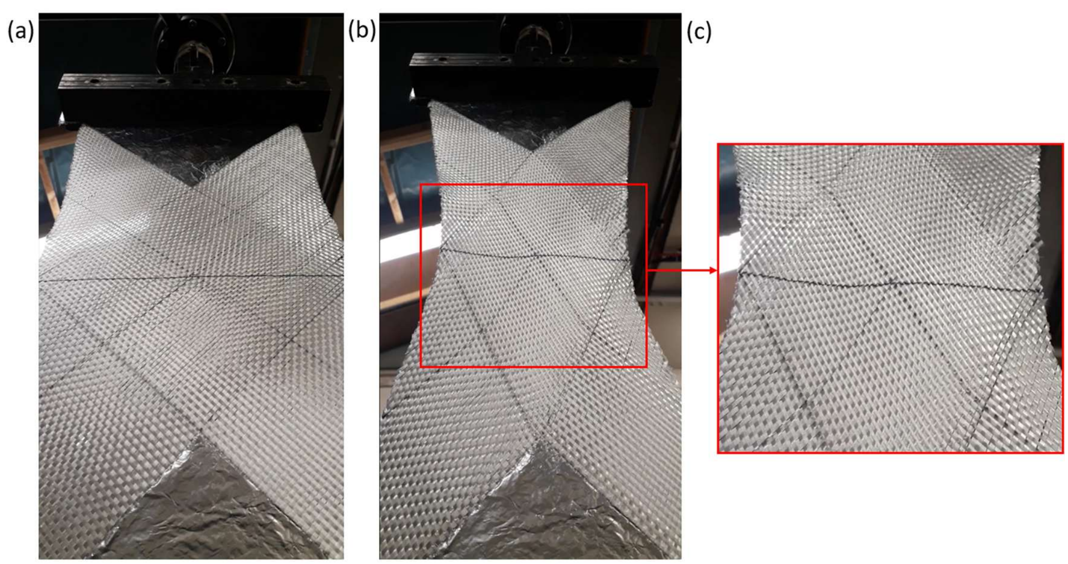

Figure 3.14: Wrinkle onset analysis of UBE test (a) The horizontal line drawn in the middle of the undeformed specimen (b) onset of the horizontal line deformation (c) a magnified image of (b)

Determining the wrinkle onset angle is a challenge because the formation of wrinkles can occur in various ways (see Figure 3.15). Since the specimen is sensitive to small disturbances induced during the sample preparation, the specimens can form different shapes of wrinkles under the same displacement. In some samples, the middle line shows a better sinusoidal wave (see Figure 3.15a) however in other cases the line distorted the perfect sinusoidal curve and bent more backwards (see Figure 3.15b) or towards (see Figure 3.15c) the back camera. Therefore, defining a method for determining the wrinkle onset angle is important. In this analysis, the still frames were moved backwards from the end frame when determining the wrinkle onset. At one point, the centre line begins to appear as a continuous line. This point can also be observed in most cases as Region A changes from matte to gloss due to the disappearance of the wrinkle formed. The wrinkle onset angle was then determined using the corresponding front still frame (obtained from the time-synchronized front camera). To improve the accuracy of measurements, the inter-fibre angle was measured three times, and the average value was used to estimate the wrinkle onset angle.

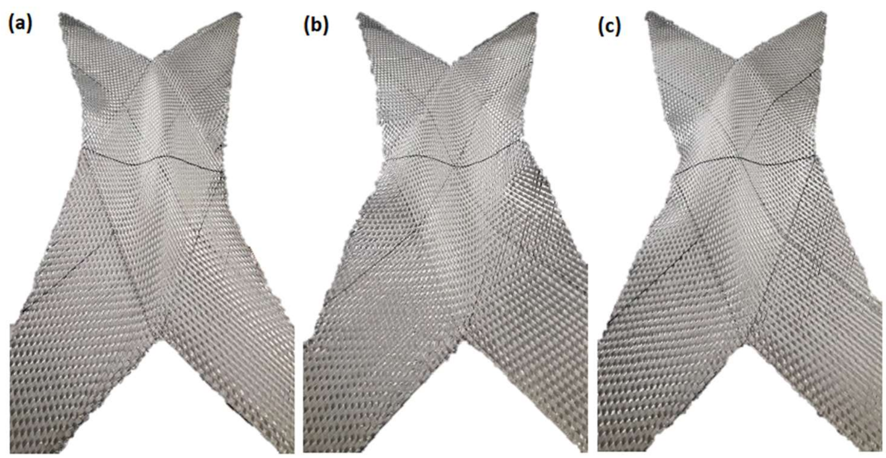

Figure 3.15: Different shapes of wrinkles formed in three different specimens under the same displacement

3.3.3. Results and Analysis

3.3.3.1. Plain Woven Fabric

Measured Versus Theoretical Shear Angle

UBE test results on woven fabrics are discussed first to understand the simpler, more predictable deformation behaviour that can provide a comparative basis for interpreting the more complex behaviour of pure-UDNCF. As shown in Figure 3.16, in-plane shear kinematics were measured for plain woven glass fabric with and without AWPs. The inter-fibre angles at given displacements were measured using the image analysis as stated in Section 3.3.2.1 and the measured shear angles were then determined by the difference between the initial inter-fibre angle and inter-fibre angle at a given displacement. The related theoretical shear angles at various crosshead displacements were determined by Eq.2.6 represents pin-joined net kinematics, in which the fibres are assumed to be inextensible and there is no intra-ply slip [66].

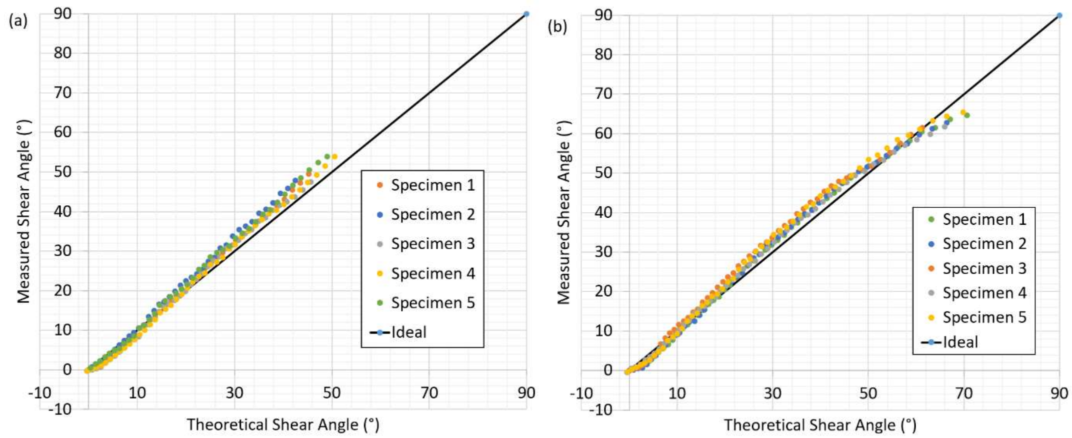

Figure 3.16: Measured versus theoretical shear angle curves (a) without AWP (b) with AWP

The samples performed without the AWP show a slight variation of data at higher shear angles and the divergence of the measured shear angle continues until the angle becomes unreliable (see Figure 3.16a). There may be considerable in-plane bending stiffness since the measured kinematics are higher than the theoretical prediction [6]. The maximum measured shear angle in the AWP-free UBE test is approximately 50°. However, the measured shear angles move towards the ideal line in UBE specimens with AWP at higher shear angles (above 50°) and eventually, shift below the theoretical shear angle (see Figure 3.16b) due to the predominance of other modes of deformation (such as intra-ply slippage) [6]. Compared to the UBE test without AWP, the addition of AWP increases the maximum shear angle reading above 60° and lowers data variance. Therefore, adding AWP can minimise out-of-plane wrinkling and allow for more precise measurements of shear angles.

Normalised Force vs Measured Shear Angle

To improve the reliability of the calculation, the axial force was corrected by subtracting the force at the beginning of the test (i.e., even if the force of the machine is neutralised before the test begins, very little force may be recorded at the start). The corrected force is then normalised by dividing the initial side length of the Region A (L_A, see Figure 2.12) to minimise the error caused by the variability in the dimension of the specimen.

According to Figure 3.17, the force required to deform the fabric is low at the beginning and gradually increases with the increasing measured shear angle, both with and without AWP. At a moderate shear angle, the normalised force rapidly increases due to the slippage between fibres, and transition from inter-ply to intra-ply shear deformation occurs. Beyond that point, the normalised force increases steadily with changes in the deformation modes of the fabrics (e.g. intra-ply slip). Due to the formation of wrinkles, the UBE test without AWP can only measure a shear angle of approximately 50° (see Figure 3.17a). At high shear angles (above 50°) the increase of the normalised force can clearly be seen in the results of UBE with AWP (see Figure 3.17b).

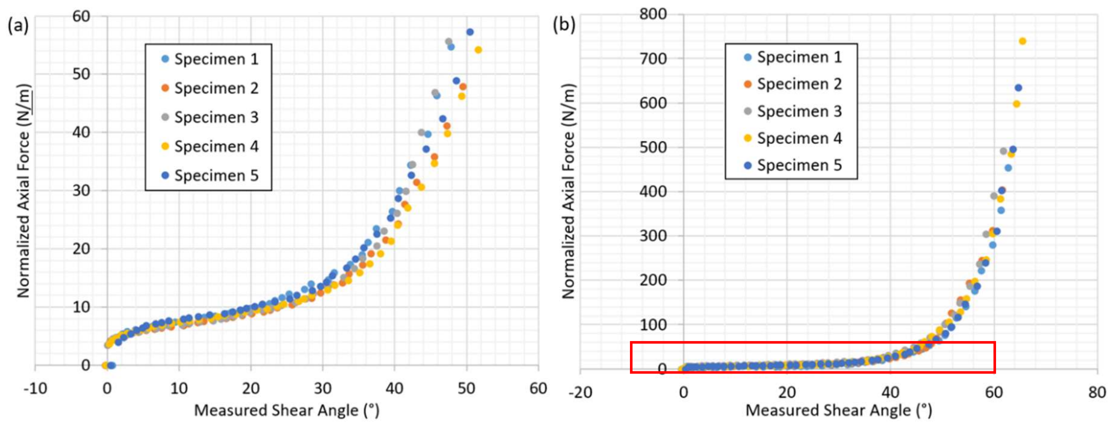

Figure 3.17: Normalised axial force vs measured shear angle curves (a) without AWP (b) with AWP

To better compare the normalised force vs shear angle curves with and without AWP, the Y axis of the graph with AWP was rearranged with the normalised force up to 60Nm^{-1} (see Figure 3.18, this is a magnified image of the red square region in Figure 3.17b). The normalised force of the specimens with AWP shows a small increment at low shear angles relative to the specimen without AWP (see Figure 3.17a). For instance, the normalised force at the first displacement (1.7 mm) of all samples without AWP was estimated between 3-4Nm^{-1} (see Figure 3.17a). However, the values are shown to be increased to 4-5Nm^{-1} in the specimens with AWP except for specimen 2 (see Figure 3.18). This slight difference may be due to the action of the frictional forces between the specimen and the AWP due to misalignment.

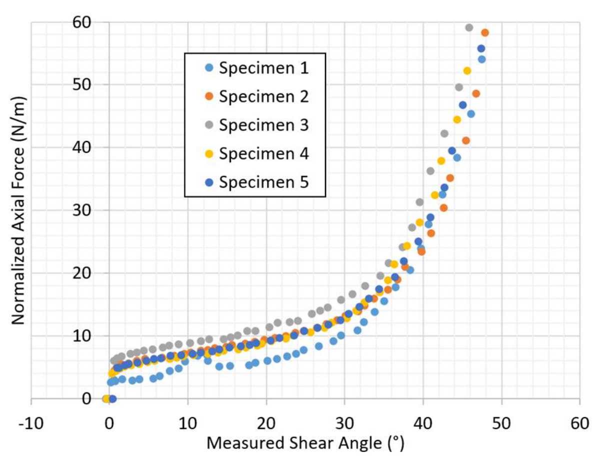

Figure 3.18: Normalised force vs shear angle curves with AWP (normalised force up to 60 N/m)

Comparison of Test Results with and without Anti-wrinkle Plates

Average curves of two experiments (with and without AWP) are plotted for a better comparison. As shown in Figure 3.19a, the two average curves overlap until the measured shear angle is 50° and a small deviation of the data can be observed beyond 50° of the measured shear angles of the average curve without AWP. The main reason for this slight deviation is that the developed wrinkles interfere with the measurement of the image analysis process. The average curve with AWP allows for more data points of the measured shear angle (beyond 60°) and improves the reliability of the experiment. The measured kinematics are higher than the theoretical prediction, suggesting significant in-plane bending stiffness. This observation has been used to estimate the in-plane bending stiffness through inverse modelling [6].

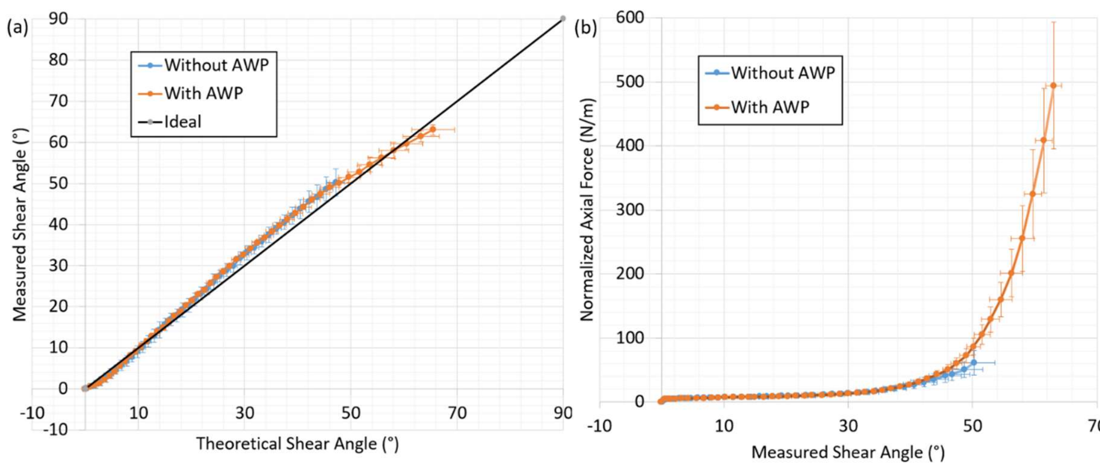

Figure 3.19: Average curves of UBE tests with and without AWP (a) measured versus theoretical shear angle (b) normalised force vs shear angle, the error bars indicate +/- 1 standard deviation of five specimens

Figure 3.19b depicts the average normalised force versus measured shear angle curves of UBE tests with and without AWP. The gradient of the average curve with AWP is greater than that of the average curve without AWP. The graph with two average curves was scaled down to 100 Nm^{-1} for better observation (see Figure 3.20). This inclination is that the angles measured are higher than the actual angles due to wrinkle formation during the AWP-free UBE experiment.

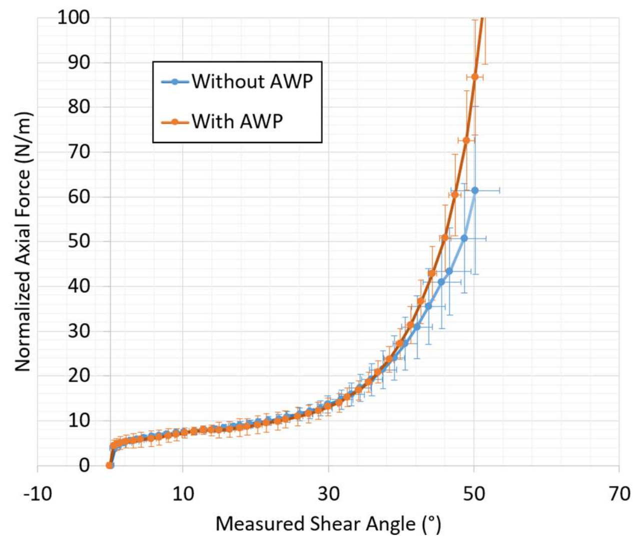

Figure 3.20: Normalised force vs shear angle average curves with and without AWP (normalised force up to 100 N/m), the error bars indicate +/- 1 standard deviation of five specimens

To overcome the frictional forces between the specimen and the AWP caused by misalignment and to improve the reliability of the UBE test with more precise data, Harrison et al. [101] proposed combining shear angle data without AWP prior to wrinkle onset (below 30°, i.e., selecting the initial part of the plot by the tests without the AWP would omit the influence of the screen friction from the final dataset) and shear angle data with AWP after wrinkle onset (above 30°, i.e., at high shear angles, the thickness of the fabric decreases due to deformation, reducing the effect of screen friction). Blue dots in Figure 3.21 represent the plotted data points after combining with and without AWP in this analysis. The red line is the data-fitted sixth-order polynomial trend line (R-square value = 0.9907).

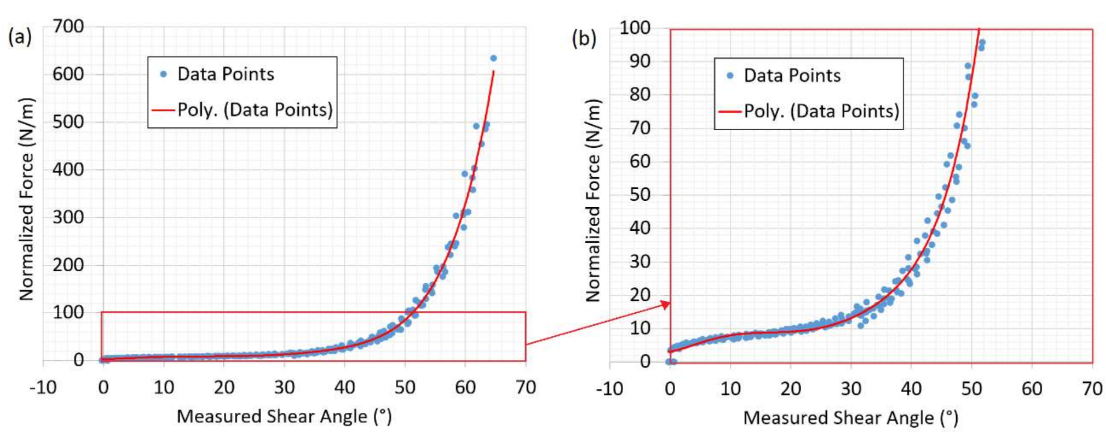

Figure 3.21: Combined normalised axial force vs shear angle data (a) normalised force up to 700 N/m (b) normalised force up to 100 N/m for better observation

Pre-shear Analysis

As stated in Section 2.5.2.1, past experimental research shows that accurate results can be observed by maintaining the initial inter-fibre angle close to 90˚ i.e., a pre-shear angle below ~0.5° and a standard deviation of the measurements less than ~2° [113]. Before performing the test, the initial inter-fibre angle of each specimen was always verified after the specimens were installed in the test machine. The first still frame was used during the image analysis to measure the exact initial inter-fibre angle, and the pre-shear values are summarised in Table 3.2 for all the specimens evaluated. From each sample, three measurements were taken to determine the average. According to the table, all initial inter-fibre angles are within a tolerance of 2°, and average pre-shear measurements are within a tolerance of 0.5° (except specimen 2 without AWP), as recommended by Alsayednoor et al. [113].

Table 3.2: Pre-shear measurements of tested specimens with and without AWP

	Initial Inter-fibre Angle (°)						Measured Shear Angle (°)	Average Measured Shear Angle (°)	SD (°)
	Specimen No.	Measurement _1 (°)	Measurement _2 (°)	Measurement _3 (°)	Average (°)	SD (°)			
Without AWP	1	90.1	90.7	90.0	90.3	0.4	-0.3	0.1	0.5
	2	89.4	89.2	89.4	89.3	0.1	0.7		
	3	90.3	90.5	90.0	90.3	0.3	-0.3		
	4	90.1	90.5	90.0	90.2	0.3	-0.2		
	5	89.7	89.7	89.3	89.6	0.2	0.4		
With AWP	1	90.0	89.3	89.6	89.6	0.4	0.4	-0.1	0.4
	2	90.1	90.2	90.0	90.1	0.1	-0.1		
	3	89.9	90.0	89.5	89.8	0.3	0.2		
	4	90.4	90.7	90.4	90.5	0.2	-0.5		
	5	90.4	90.0	90.6	90.3	0.3	-0.3		

Wrinkle Analysis

The results of the wrinkle onset angle of the specimens with and without AWP are shown in Table 3.3. According to the results, the wrinkle onset angle in the specimens with AWP moves to elevated shear angles. Therefore, applying the Perspex screen can delay wrinkle formation and increase the number of reliable data points that can be obtained. When comparing the wrinkle onset angle obtained in previous studies on the same fabric [101] (46.4°), the average wrinkle onset angle with AWP was found to be approximately the same (46.8°); however, the standard deviation of the current result showed a significant reduction when compared to the previous study (i.e., from 2.7˚ to 1.7°). This difference may be the new inter-fibre angle measurement technique explained in Section 3.3.2.1.

Table 3.3: Comparison of wrinkle onset angle with and without AWP for plain-woven fabric

	Inter-fibre Angle (°)						Wrinkle onset angle (°)	Average Wrinkle onset angle (°)	SD (°)
	Specimen No.	Measure ment _1 (°)	Measure ment _2 (°)	Measure ment _3 (°)	Average (°)	SD (°)			
Without AWP	1	53.4	53.6	53.1	53.4	0.3	36.6	35.5	2.6
	2	54.7	54.9	54.2	54.6	0.4	35.4		
	3	57.2	57.3	57.1	57.2	0.1	32.8		
	4	56.1	56.8	56.5	56.5	0.4	33.5		
	5	50.8	50.7	50.5	50.7	0.2	39.3		
With AWP	1	45.2	44.9	44.8	45.0	0.2	45.0	46.8	1.7
	2	42.6	42.6	42.4	42.5	0.1	47.5		
	3	43.4	43.5	43.0	43.3	0.3	46.7		
	4	40.7	40.5	40.5	40.6	0.1	49.4		
	5	44.3	44.5	44.4	44.4	0.1	45.6		

Figures 3.22 and 3.23 show the specimens with and without AWP at 65mm displacement, respectively. Due to the formation of wrinkles, the middle horizontal line in all specimens without AWP is deformed (see Figure 3.22), however, the specimens with AWP at the same displacement are almost straight (see Figure 3.23). This comparison demonstrates how adding a Perspex screen delays the formation of wrinkles i.e. the results imply that following best practices can effectively characterise the shear behaviour of the plain weave fabric.

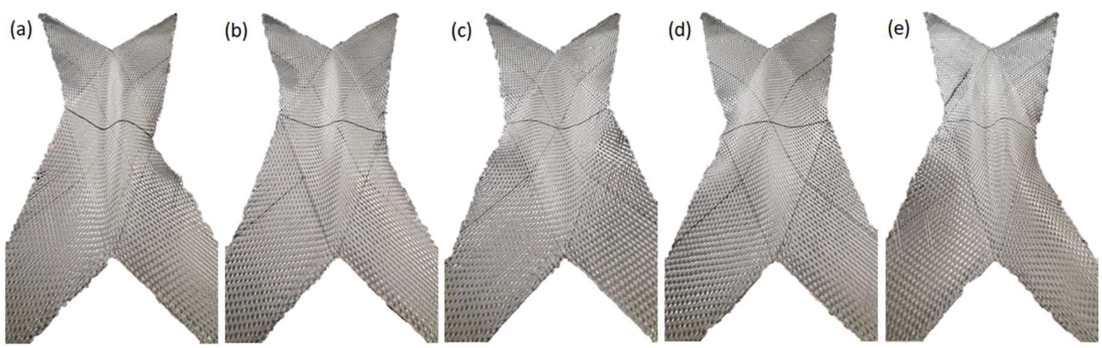

Figure 3.22: UBE glass fabric specimens without AWP at a displacement of 65mm during the tests (a) specimen 1 (b) specimen 2 (c) specimen 3 (d) specimen 4 (d) specimen 5

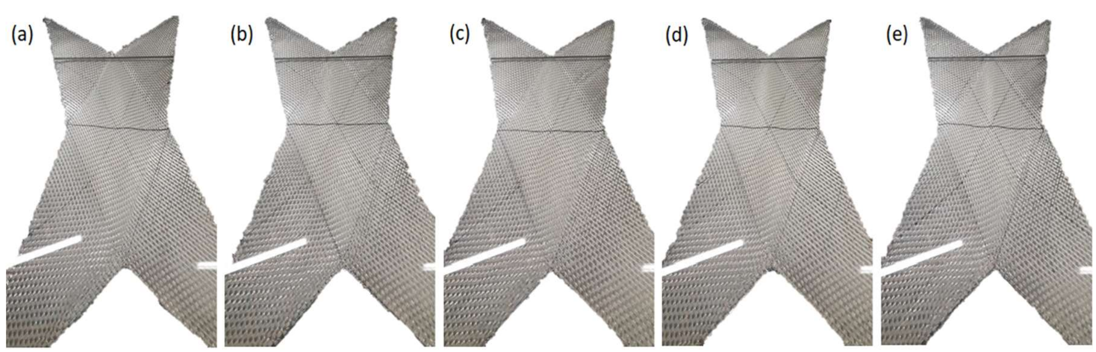

Figure 3.23: UBE glass fabric specimens with AWP at a displacement of 65mm during the tests (a) specimen 1 (b) specimen 2 (c) specimen 3 (d) specimen 4 (d) specimen 5

3.3.3.2. Twill Woven Fabric

Measured Versus Theoretical Shear Angle

Figure 3.24 compares the measured versus the theoretical shear angle average curves of twill-woven glass fabric with and without AWP. Both curves are significantly closer together and follow a similar pattern. The measured shear angles are close to the ideal line up to 30° shear angles, and the measured kinematics are not higher than the theoretical prediction. This suggests that either the in-plane bending stiffness of the twill woven fabric used in this study is insignificant or perhaps the size of the UBE specimen used (200x400 mm^2) is too large to show the effect of in-plane bending stiffness; it is known from that the shear angle shows increased sensitivity to the effects of in-plane bending stiffness with decreasing sample size [6]. However, another possibility is that deformation mechanisms other than shear occur in the twill weave fabric, such as uncrimping or intra-ply slip, and these obscure the effects of the in-plane bending stiffness. Beyond 30° of shear, a significant deviation from ideal kinematics can be seen at higher shear angles. The difference below the ideal line indicates that the estimated shear angle is less than the ideal predictions and is a strong indicator that the loose meso-structure of this twill weave fabric permits not just shear but also intra-ply slip. This suggests the specimen-to-unit cell size ratio is too low (around 14) and the cohesion of the fabric is compromised, leading to significant intra-ply slip.

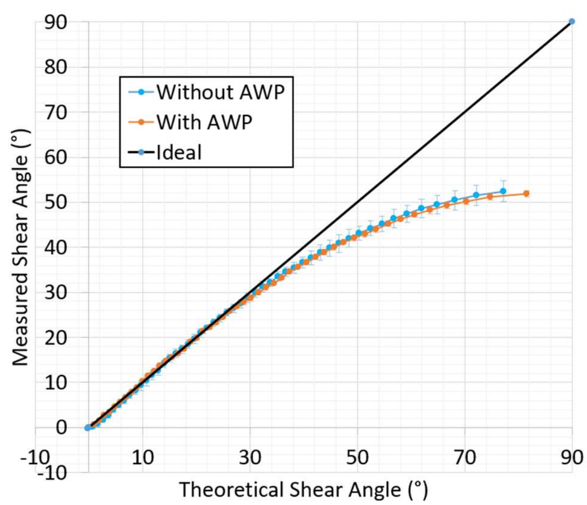

Figure 3.24: Measured versus theoretical shear angle average curves of twill-woven fabric with and without AWP, the error bars indicate +/- 1 standard deviation of four specimens

During the experiment, no wrinkling was observed for the twill-woven fabric (see Figure 3.25). However, the UBE test of twill-woven fabric was still tested with AWP (see Figure 3.26), and no significant difference was observed. The magnitude of the wrinkle is determined not only by the forming properties of the fabric but also by the size of the UBE specimen, i.e., large samples produce severe wrinkles at low shear angles [6]. Again, the results imply that the specimen size for this twill-woven fabric is insufficient to form wrinkles due to the small specimen vs unit cell size ratio (around 14). Because the onset of wrinkles is not visible, it would not be possible to estimate the torsional stiffness of the sheared twill woven fabric from the UBE test (via inverse modelling), as recommended by Harrison et al. [6]. Replacing the existing size with larger specimens may possibly lead to the formation of wrinkles at low shear angles, although handling such large samples would be challenging. The main conclusion from testing this twill weave fabric is that even testing simple woven engineering fabrics using the UBE test can be problematic, and care has to be taken when choosing a high enough specimen/unit cell size ratio to avoid the occurrence of other deformation mechanisms during the test, such as intra-ply slip.

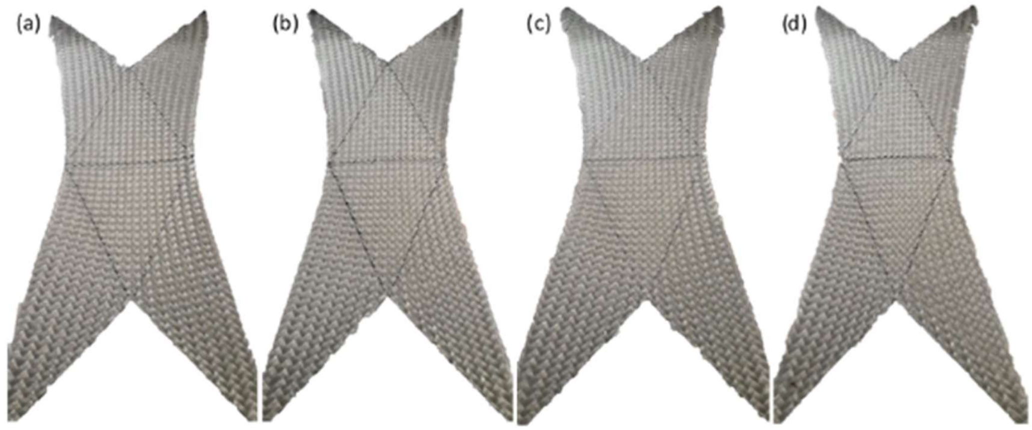

Figure 3.25: UBE twill-wove glass fabric specimens without AWP at a displacement of 65mm during the tests (a) specimen 1 (b) specimen 2 (c) specimen 3 (d) specimen 4

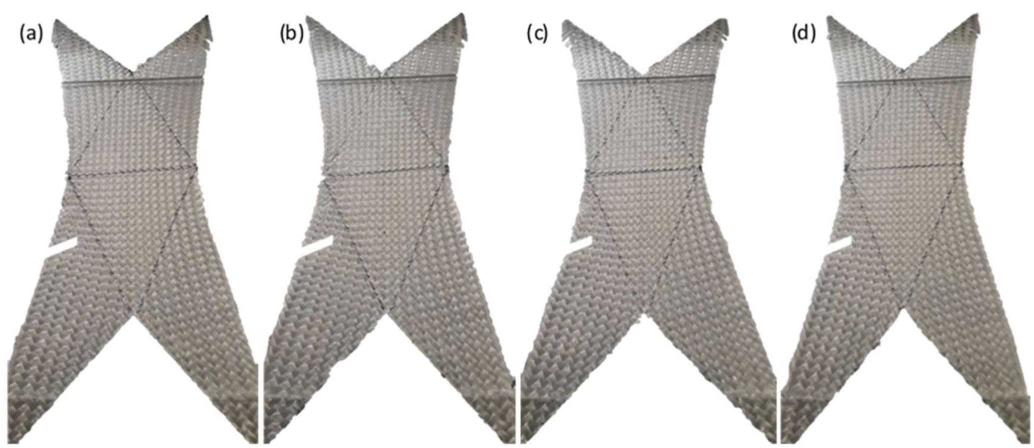

Figure 3.26: UBE twill-wove glass fabric specimens with AWP at a displacement of 65mm during the tests (a) specimen 1 (b) specimen 2 (c) specimen 3 (d) specimen 4

Normalised Force vs Measured Shear Angle

Figure 3.27 shows the normalised force (force divided by the specified length of Region A) versus the measured shear angle average curves of twill-woven glass fabric with and without AWP. As expected, both curves show a similar trend as there was no observation of wrinkles. Comparing Figures 3.21 & 3.27, it is apparent that the heavier twill weave fabric (about 4x heavier) has a much greater shear resistance than the lighter plain weave fabric (by a factor of about 7-9x), even though intra-ply slip is thought to occur in the twill weave specimen, and the weave structure of the twill weave is traditionally thought to be more formable than a plain weave structure.

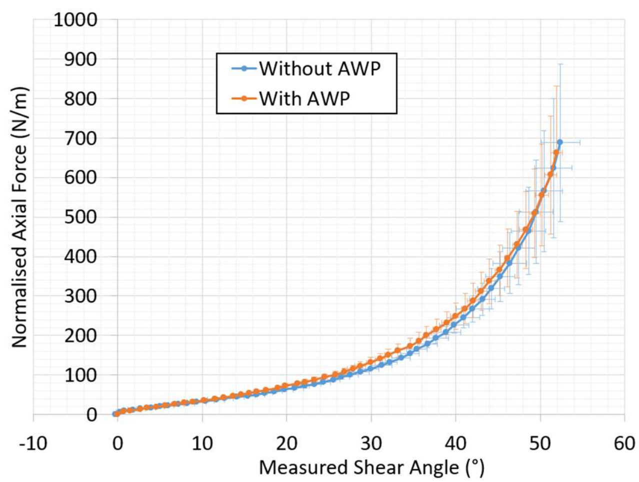

Figure 3.27: Normalised axial force vs measured shear angle average curves of twill-woven fabric with and without AWP, the error bars indicate +/- 1 standard deviation of four samples

3.3.3.3. Pure Unidirectional Non-Crimp Fabric

This section focuses on the UBE test of pure-UDNCF, a complex fabric along with the knowledge and practice of woven fabrics discussed in the previous Sections 3.3.3.1 and 3.3.3.2. The deformation behaviour of these three fabrics, i.e., plain-woven, twill-woven and pure-UDNCF, is compared in Section 3.3.3.4 to understand how the structural changes affect the mechanical performance.

Measured Versus Theoretical Shear Angle

Figure 3.28 shows the measured versus the theoretical shear angle average curve of pure-UDNCF. Compared to the ideal curve, the average is much lower, and the deviation increases as the shear angles increase. This implies that the UBE test of pure-UDNCF deviates significantly from pin-jointed net kinematics, which is discussed in detail in the following section.

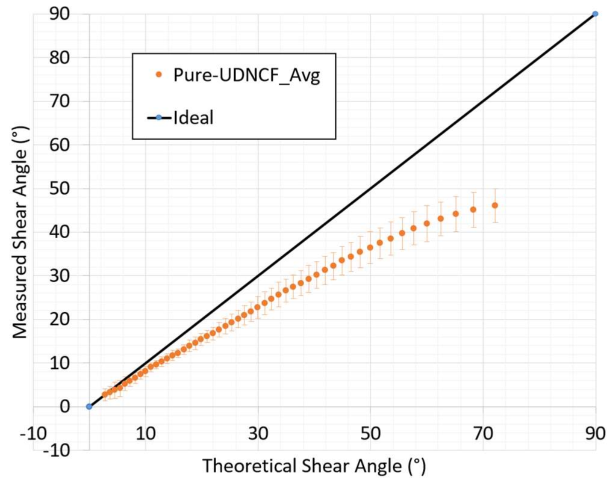

Figure 3.28: Measured versus theoretical shear angle average curve of pure-UDNCF, the error bars indicate +/- 1 standard deviation

Normalised Force vs Measured Shear Angle

According to Figure 3.29, the force required to deform the fabric is initially low and gradually increases as the measured shear angle increases. The pre-shear angle of all the specimens varied between 1˚ and 4˚. Maintaining the pre-shear angle of less than 0.5˚ is difficult because of the tension in the stitches. In the UBE test, the tows and the stitches of the fabric are in ±45˚ direction to the axial force. Because the fabric has no other stabilising fibres, the chain stitches are tensioned, allowing the fabric to have an inherent pre-shear configuration. At shear angles 5˚- 20˚, the standard deviation of the average curve is low (i.e., all curves present close to each other), and beyond 20˚, divergence begins and increases at high shear angles. The deformation mechanisms may become more complex beyond 20˚, involving fibre reorientation, & variable stitch interactions, which introduce greater variability in the response, reflected as an increased standard deviation

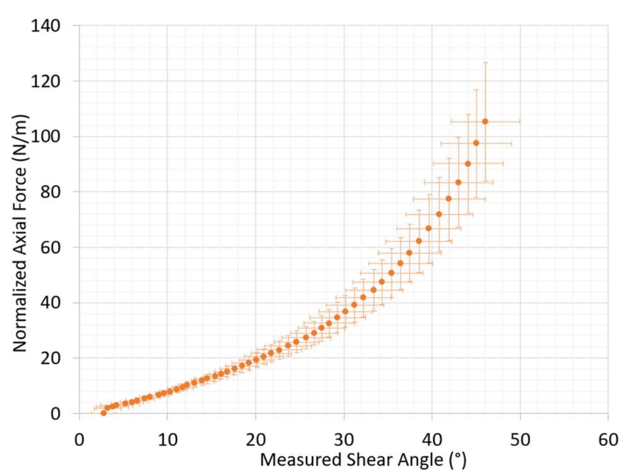

Figure 3.29: Normalised axial force vs measured shear angle curves of pure-UDNCF, the error bars indicate +/- 1 standard deviation of four specimens

The pure-UDNCF is made up of warp-directional tows that are stitched together in a tricot-chain pattern. Therefore, both tows and stitches contribute to the shear properties of the fabric. The shear resistance produced by the stitches is determined by the type of stitching yarns used and the stitching parameters, i.e. tricot stitching pattern provides greater stability or shear resistance than the chain stitching pattern [46] [217]. The stitching yarns are smaller in size and have significantly lower tensile stiffness than the tows in the pure-UDNCF. Even though the stitches have lower tensile stiffness, they hold the fibres in place effectively. The stitches help maintain the structural integrity of the fabric, reducing stress concentration, which can cause the onset of wrinkles. Figure 3.30 shows all four pure-UDNCF specimens at a displacement of 65mm. The formation of wrinkles is not visible. However, the horizontal line marked in the centre of the specimen is slightly bent. The pure-UDNCF specimens experience an additional type of deformation during the UBE test i.e., stretching in the stitch direction. This can be observed by monitoring the side lengths of Region A, L_A and L'_A in the specimen (see Figure 3.31a&b). The side lengths are approximately equal on either side of Region A at the beginning of the UBE test but increase along the stitch direction of pure-UDNCF. In addition, Figure 3.31b shows that the in-plane bending contribution is minimised in the UBE test for this fabric, as the tow direction remains almost straight at the transition between Regions A and B. Also, the Pure-UDNCF UBE test specimen confirms that it follows unusual kinematics as Region B2 (bottom) is observed to buckle out of the plane. This is difficult to see in Figure 3.31b due to the perspective of the photo but is very clear when conducting the test. For woven fabrics, the side lengths of Region A remain constant during the test (Figures 3.31c&d). Because no stabilising tows are present in the UDNCF (the fabric is a pure-UDNCF, not a quasi-UDNCF), there is no tendency towards pure shear kinematics with increasing specimen size, and so without stabilising tows, the asymmetric UBE test kinematics shown in Figure 3.31a&b is inevitable, no matter the sample size or shape [45].

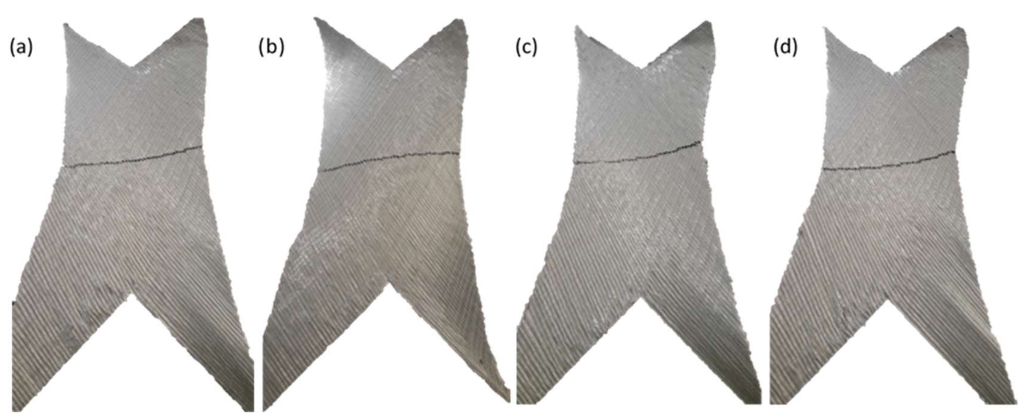

Figure 3.30: UBE UD stitched glass fabric specimens at a displacement of 65mm during the tests (a) specimen 1 (b) specimen 2 (c) specimen 3 (d) specimen 4

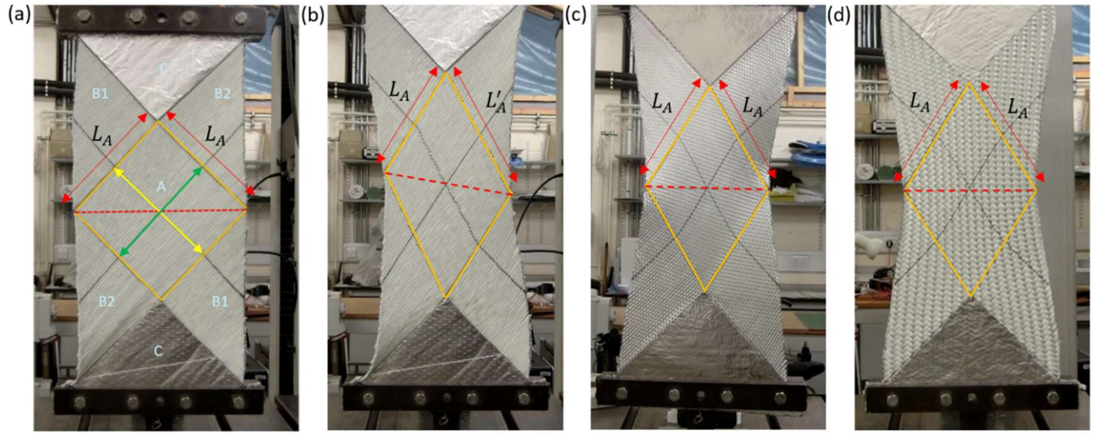

Figure 3.31: Uniaxial bias extension specimens (a) undeformed pure-UDNCF, the yellow and green arrows indicate the initial chain-stitch direction and the tow direction, respectively (b) deformed pure-UDNCF (c) deformed plain-woven (d) deformed twill- woven, all deformed specimens are at 30˚ shear angle. The red dashed line marked in the figures indicates that the deformation within the A region of the pure-UDNCF is not pure shear.

3.3.3.4. Comparison of the UBE Results of Different Fabrics

Measured Versus Theoretical Shear Angle

When all three fabrics are compared, only the plain-woven fabric kinematics lie above the ideal line at moderate shear angles, due to the effect of in-plane bending stiffness (see Figure 3.32) as discussed in Section 3.3.3.1. This effect does not occur in twill-woven fabrics, where the curve is close to the ideal line up to shear angles of 30° and then deviates below the ideal curve (the estimated shear angle is less than the ideal predictions) probably due to some degree intra-ply slip, caused by the low specimen/unit cell size ratio in this test. The pure-UDNCF exhibits a much lower shear angle compared to the ideal kinematic line, even at low shear angles. This demonstrates that stretching in the stitch direction is significant even at very low shear angles. Similar kinematics were also observed in previous studies [45] [118] [55] for non-crimp fabrics.

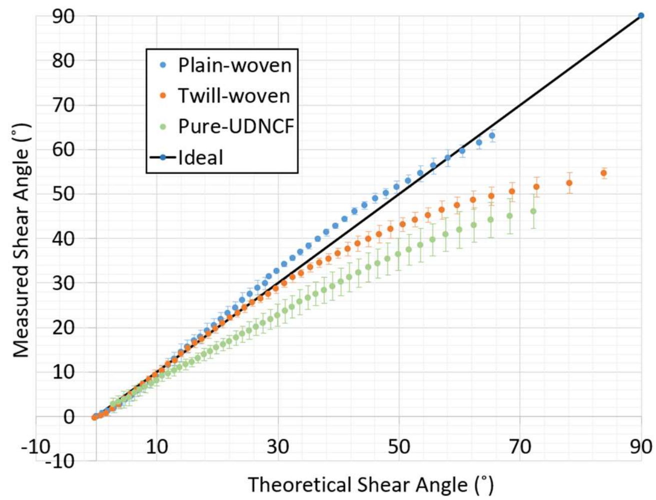

Figure 3.32: Comparison of measured versus theoretical shear angle curves of plain-woven, twill-woven and pure-UDNCF, the error bars indicate +/- 1 standard deviation

Normalised Force vs Measured Shear Angle

It is interesting to directly compare the shear stiffness of the three fabrics, as measured using the UBE test. Figure 3.33 shows that the twill-woven fabric has the highest shear stiffness of the three fabrics. Both pure-UDNCF and plain-woven fabrics exhibit low shear stiffnesses at low shear angles; however, beyond 10˚of shear, the force required to shear the pure-UDNCF is higher than that of plain-woven fabrics (Figure 3.33b) due to the deformation of the stitches and tow compaction. Pure-UDNCF does not achieve large shear angles as woven fabrics at similar displacements due to stitch stretching that lowers the shearing of the fabric. According to Figure 3.33b, the log scale of normalised force vs measured shear angle curves of twill-woven and pure-UDNCF show similar shapes, however, the pure-UDNCF shows lower normalised force than that of twill-woven fabric. This may be due to the stretching of stitches reducing the effective load transferred to the tows.

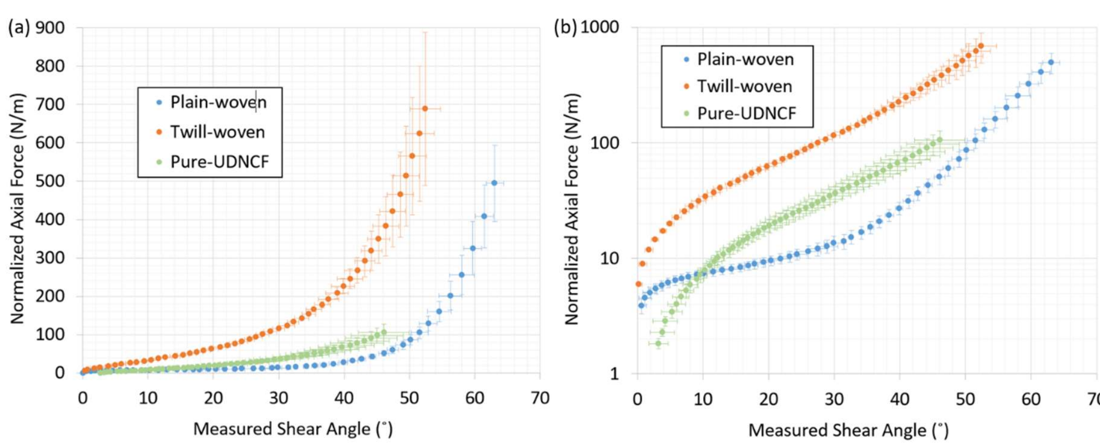

Figure 3.33: (a) A comparison of normalised axial force vs measured shear angle average curves of plain-woven, twill-woven and pure-UDNCF (b) a log graph of (a), the error bars indicate +/- 1 standard deviation

3.4. Tightly-clamped Picture Frame Test

The tightly-clamped PF test discussed in this section is performed on pure-UDNCF, as the pure-UDNCF specimens experienced unusual deformation during the UBE test i.e., stretching in the stitch direction, virtually no change in tow direction between the boundary of Regions A and B of the test specimen and out-of-plane buckling in Region B, all of which are absent in woven fabrics. In the PF test, all four sides of the specimen are clamped, limiting the strain in the stitch direction. The PF test was performed to obtain almost pure shear behaviour with a uniform deformation across the specimen (though the clamped boundary does lead to significant in-plane bending of the tows, as discussed in Section 3.4.2.3). This PF test method is referred to as the 'Tightly-clamped Picture Frame Test', and follows the recommended procedure of the benchmark study on engineering textiles [120].

3.4.1. Experimental Set-up

3.4.1.1. Sample Preparation

Four samples of pure-UDNCF were prepared based on the dimensions shown in Figure 2.16b. A template was placed on the fabric and sketches were drawn (see Figure 3.34a). The specimens were then cut along the drawn lines with a rotary cutter and a scissor (see Figure 3.34b). For the post-examination of the wrinkling onset, a horizontal line was drawn across the back of the specimen (across the midsection when the sample was rotated to 45°). To improve handling during the sample drilling, four Al foils were adhered to each side of the clamping area (see Figure 3.34c). Before drilling, the samples were kept for 48 hours to cure the epoxy resin. A completed specimen for the PF test is shown in Figure 3.34d.

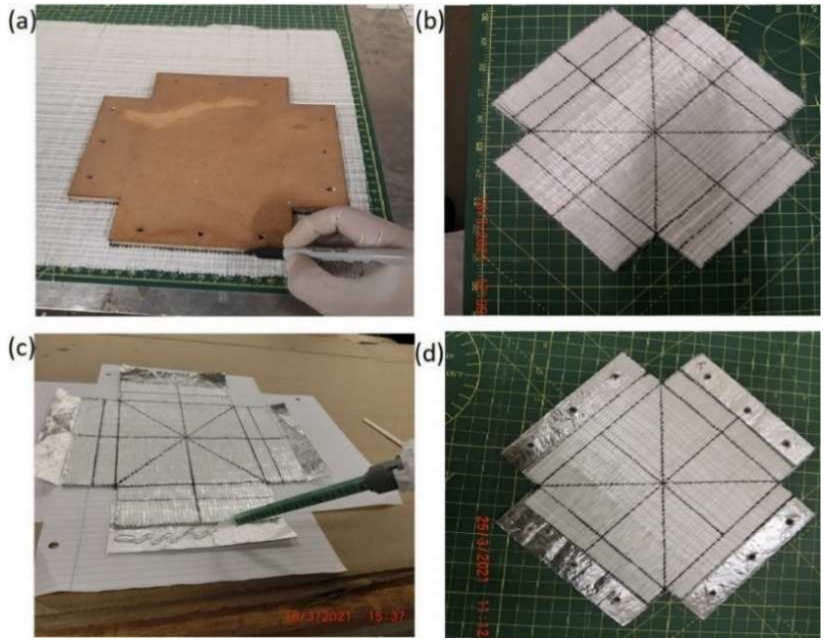

Figure 3.34: PF specimen preparation (a) placing a template and marking outlines (b) properly cut specimen (c) adhering Al foil to the clamping areas (d) prepared PF specimen

3.4.1.2. Loading and Clamping the Specimens

The prepared samples were clamped into the PF rig with a 170mm side length. The tests were performed on the Zwick Z2 tensile testing machine. The strain rate was set to 1 mm/s with a maximum upper force limit of 1kN, and the standard force and travel (displacement) were set as the test report parameters. The tests were filmed using two cameras, one on the front and one on the back. The post-test analysis to determine the shear angle is similar to the UBE test. The theoretical shear angle of the PF test was calculated using Eq.1.10, and the force was normalised by dividing the axial force by the side length of the rig (170mm). The complete PF test setup is shown in Figure 3.35.

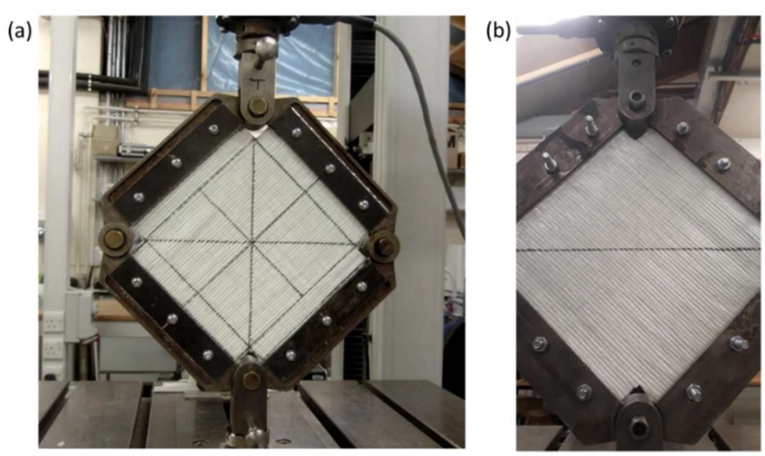

Figure 3.35: Picture frame test setup (a) front (b) back

3.4.2. Results and Analysis

3.4.2.1. Measured Versus Theoretical Shear Angle

Figure 3.36a shows the measured versus theoretical shear angle average curve of pure-UDNCF specimens in the PF test. The measured shear angles of all PF samples overlap and are close to the ideal curve. The average curve indicated a minor deviation from the ideal curve at high shear angles. In contrast to the standard UBE test, the PF test clamps all four sides of the specimen, resulting in uniform deformation across the specimen. While the clamping restricts in-plane fibre movement, it cannot completely prevent out-of-plane deformations. As a result, at high shear angles, fibres tend to wrinkle. Note that the wrinkles tend to occur along the stitch direction rather than the tow direction, facilitated by the very low out-of-plane bending stiffness of the sheet in this direction (as opposed to in the tow direction, which has a much higher out-of-plane bending stiffness, resisting the low-wavelength buckles evident in Figure 3.36b). The presence of wrinkles reduces the reliability of the measurements. Thus, at high shear angles, there is a minor deviation of the average curve below the ideal line (see Figure 3.36a).

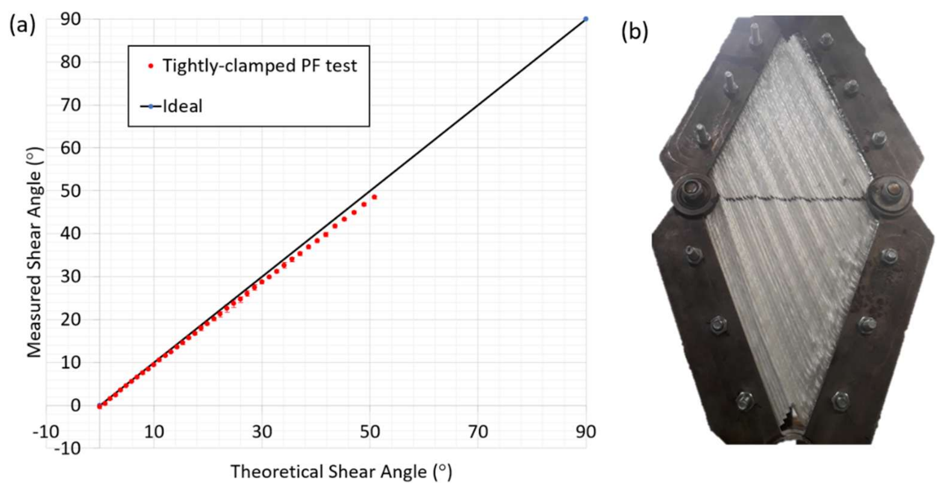

Figure 3.36: (a) Measured vs theoretical shear angle average curve of pure-UDNCF in the PF test, the error bars indicate +/- 1 standard deviation of four samples (b) wrinkle behaviour of the tightly-clamped PF test

3.4.2.2. Normalised Force vs Measured Shear Angle

Figure 3.37 shows the normalised axial force vs measured shear angle average curve of pure-UDNCF specimens in the PF test. The resultant curve shows a gradual increase in normalised force, however, the variability between the test repeats is high, resulting in a large standard deviation. Schirmaier et al. [44] and Ghazimoradi et al. [46] have observed similar behaviour in the PF test for two different quasi-UDNCFs. In addition, a notable initial jump in axial force can be observed in the PF test results (see Figure 3.37). In the literature, many groups have obtained a similar jump at the beginning of the PF test [120] [218] [219] [154], however, there is no evidence to support further analysis of such an observation. Section 3.8 will analyse and discuss this issue in more detail.

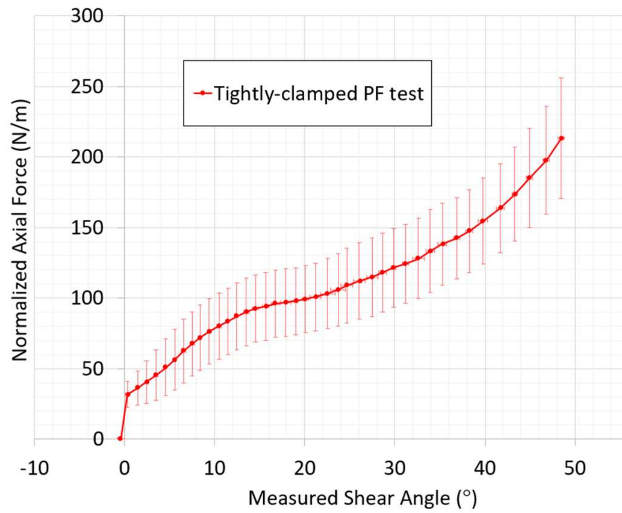

Figure 3.37: Normalised axial force vs measured shear angle average curve of pure-UDNCF in the PF test, the error bars indicate +/- 1 standard deviation of four specimens

3.4.2.3. In-plane Bending of Tows During the PF Test

The tightly-clamped PF test is designed to evaluate in-plane pure shear properties of engineering fabrics. As expected, all PF tests of pure-UDNCF show significant in-plane bending at the ends of the tows (close to the clamps, see Figures 3.38 and 3.36b). This increases with increasing shear angle. Therefore, the axial force measured during the PF test is a combination of shear and in-plane bending forces. Other researchers have discussed similar kinematics during the PF test. According to Willems et al. [110], there is a local bending phenomenon that occurs especially along the edges of the frame, and this bending is particularly noticeable in the parts of the arm that are considered 'stiff' (see Fig.5c in Willems et al. [110]). This phenomenon was further investigated by Krogh et al. [111] on satin-woven carbon-fibre prepreg samples with three different PF arm geometries, i.e., full arms, arms with cutting slits and removing the transverse tows. S-shaped deformation is clearly observed in samples without transverse tows (see Fig.8 in Krogh et al. [111]) and as the shear angle increases, the in-plane bending effect increases.

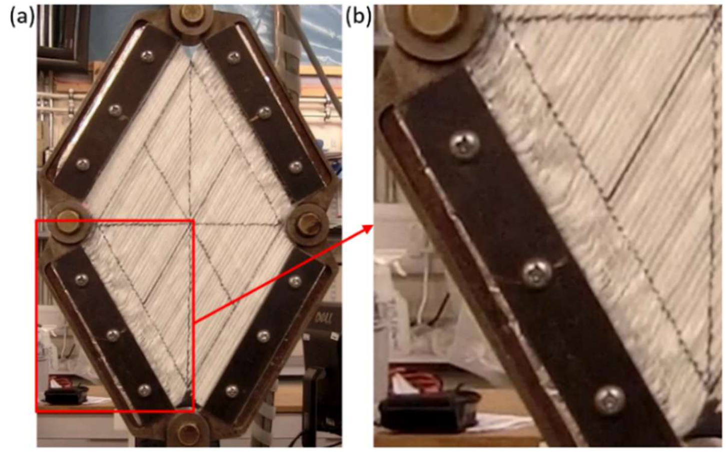

Figure 3.38: In-plane bending is visible at the end of the tows of the PF test (a) the specimen at 30˚of the shear angle (b) a magnified image of (a)

3.4.2.4. Wrinkle Analysis

The wrinkle onset angle of pure-UDNCF in the PF test was determined using a similar procedure described in Section 3.3.2.2 for the standard UBE test. Table 3.4 shows the results of the wrinkle onset angle of the pure-UDNCF specimens. The average wrinkle onset angle is 30.7˚, however, the wrinkle onset angle of each specimen varies from 21.7˚ to 37.8˚. According to Figure 3.37 beyond the average wrinkle onset angle (30.7˚), the normalised axial force gradually increases. Therefore, it can be assumed that when the specimen is subjected to high in-plane shear deformation, the fabric may be more susceptible to initiate out-of-plane wrinkles, although it is noted that wrinkles appeared in pure-UDNCF during the PF test, but not in the UBE test. The onset of wrinkling in the PF test is influenced by misaligned fibre tension, i.e. more tension suppresses wrinkling, and more compression encourages wrinkling (see Section 2.5.2.2). Therefore, among these four samples, specimens no.1 and no.3 are the most compressed and tensioned specimens, respectively. A comparison of the two standard shear test results helps determine whether pure-UDNCF behaves differently in the two tests and, if so, what accounts for the difference in wrinkling.

Table 3.4: wrinkle onset angle of the PF test for pure-UDNCF

Specimen No.	Inter-fibre Angle (°)					Wrinkle onset angle (°)	Average Wrinkle onset angle (°)	SD (°)
	Measurement _1	Measurement _2	Measurement _3	Average	SD			
1	68.2	68.4	68.3	68.3	0.1	21.7	30.7	7.1
2	61.4	61.5	61.1	61.3	0.2	28.7		
3	52.4	52.1	52.2	52.2	0.2	37.8		
4	55.5	55.1	55.2	55.3	0.2	34.7		

3.5. Comparison of UBE and PF Test Results of Pure-UDNCF

3.5.1. Measured Versus Theoretical Shear Angle

When comparing the measured vs theoretical shear angle curves of the standard UBE and tightly-clamped PF tests, the PF test exhibits more ideal kinematics than the UBE test (see Figure 3.39) i.e., unlike the PF test, significant stretching in the stitch direction means the UBE results are lower than the ideal kinematic prediction. The amount of stretching depends on the properties of the stitches. Variations in the stitch density (see Figure 3.40), tension, and placement can introduce inconsistencies in how different samples behave under stress. Therefore, the standard deviation of the UBE average curve can be high.

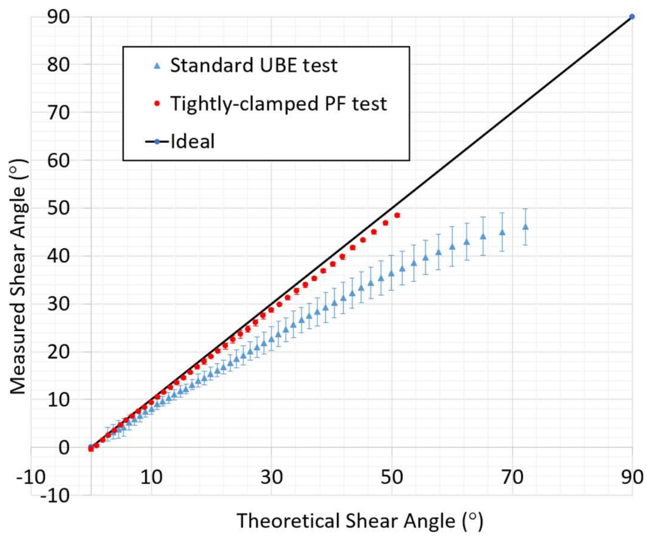

Figure 3.39: Comparison of measured versus theoretical shear angle curves in standard UBE and tightly-clamped PF shear tests for pure-UDNCF, the error bars indicate +/- 1 standard deviation of four samples

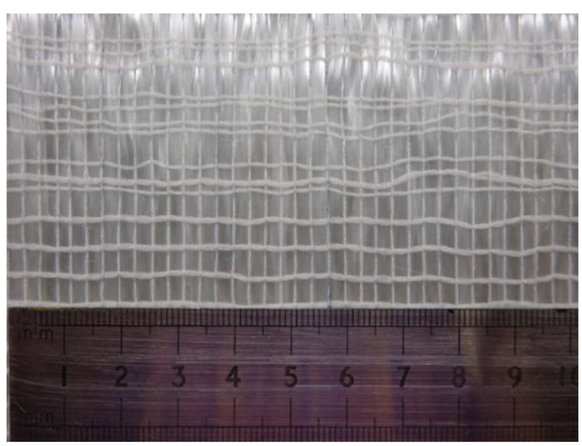

Figure 3.40: Variation of stitch density on the front surface of pure-UDNCF

3.5.2. Normalised Force vs Measured Shear Angle

Figure 3.41 compares the normalised force vs measured shear angle curves of the UBE and PF tests on the pure-UDNCF. The results are very different, with the PF result being many times higher than the UBE result, especially at low shear angles. For example, at 5˚ the PF test result is 16 times higher, at 10˚ it is 10 times higher and at 30˚ it is about 3 times higher than the UBE test - see Figure 3.41. This difference in the results generated by the two test methods is notably greater than that reported by Schirmaier et al. [44] or Ghazimoradi et al. [46], who tested quasi-UD NCFs, and merits further investigation. Much of the work presented in subsequent sections, and also Chapter 4, is motivated by this observed discrepancy.

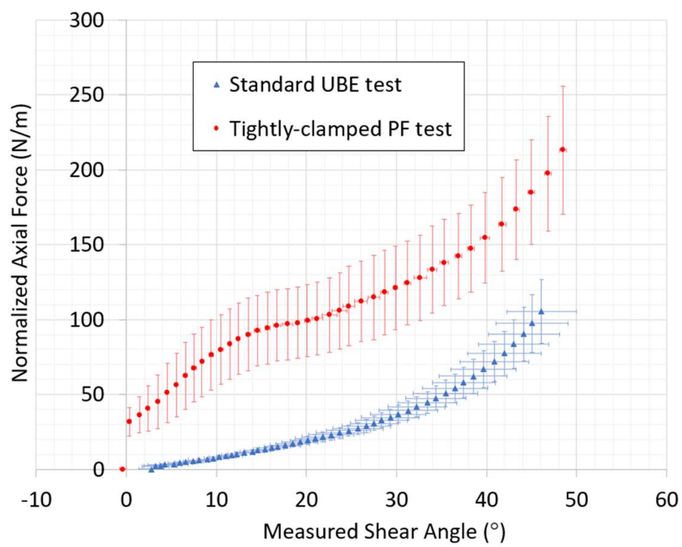

Figure 3.41: Comparison of normalised axial force versus measured shear angle curves in UBE and PF shear tests for pure-UDNCF, the error bars indicate +/- 1 standard deviation of four samples

Figure 3.42 compares the two test specimens at a shear angle of 25°. The kinematic behaviour of the UBE test (see Figure 3.42a) is asymmetric, in contrast to the symmetric deformation of the PF test (see Figure 3.42b). Stitch extension is visible when comparing the side lengths of Region A in the deformed UBE specimens, the value of L_A along the stitch direction increases to L'_A due to the stitch strain (see Figure 3.42a). Ghazimoradi et al. [46] described similar kinematics during their UBE tests on a quasi-UDNCF specimen (see Fig.2 in Ghazimoradi et al. [46]). Schirmaier et al. [44] also reported unusual kinematics in their UBE tests, with their test specimen vaguely resembling the shape of Region A in Figure 3.42a (see Fig.8 in Schirmaier et al. [44]), but with less homogeneity in the strain field. Figure 3.42 can also be used to compare the wrinkling behaviour of pure-UDNCF during the two shear tests. In the UBE test, the stitches stretch to accommodate the deformation, effectively reducing the stress concentration that causes buckling or wrinkling. In the PF test, all four sides are clamped, hence, the fibres cannot reorient or redistribute the stresses as in the UBE test.

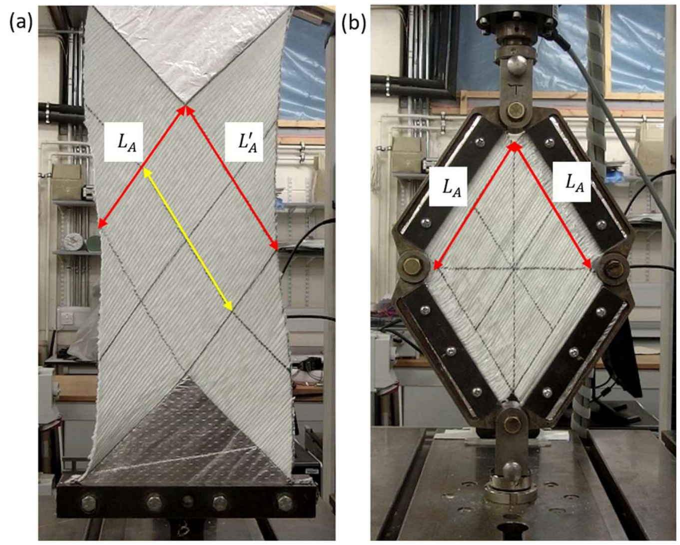

Figure 3.42: pure-UDNCF specimens at the shear angle of 25° (a) Standard UBE test (yellow arrow indicates the direction of stitch strain) (b) tightly-clamped PF test

Returning to the force measurements in Figure 3.41, the very large discrepancy between the PF and UBE test results for the pure-UDNCF, especially at low shear angles, presents a puzzle with two possible explanations, namely (a) experimental error or (b) a true change in the forming behaviour of the fabric between the two shear tests. In exploring option (a) two modifications of the tightly-clamped PF test are considered in Section 3.6, and friction of the PF rig is measured in Section 3.8.

3.6. Modifications of the Picture Frame Test

3.6.1. Pre-Displaced Tightly Clamped Picture Frame Test

3.6.1.1. Theory

Because the shear stiffness of pure-UDNCF measured using the PF test was significantly higher than that measured by the UBE test, this motivated exploration of whether the cause is due to possible experimental error in the PF test. As discussed in Section 2.5.2.2, fibre misalignment in the PF test (see Figure 2.18), can lead to significant force overestimation due to tensile strain of the fibres. Therefore, a first modification of the tightly-clamped PF test procedure is proposed to reduce sensitivity to sample misalignment by pre-displacing the PF rig prior to loading the undeformed sample. There are two methods of pre-displacing, namely, positive, and negative. Figure 3.43b shows the positive pre-displacement of the rig by moving the rig upward. Figure 3.43c shows the negative pre-displacement by moving the rig downward. For the University of Glasgow PF frame rig, which has a side length of 170mm, an initial displacement of 4mm was selected. The test was later repeated with a 6mm initial displacement. The initial displacement can be expressed as a fraction of the PF side length to obtain the 'normalised pre-displacement'. Therefore, the normalised initial displacement is 0.0235 (4/170), relating to an initial rig shear angle of approximately 2°. Rig shear angle is defined as the difference between the initial frame angle of the standard PF test (90˚ - see Figure 3.43a) and the initial frame angle of the pre-displaced test.

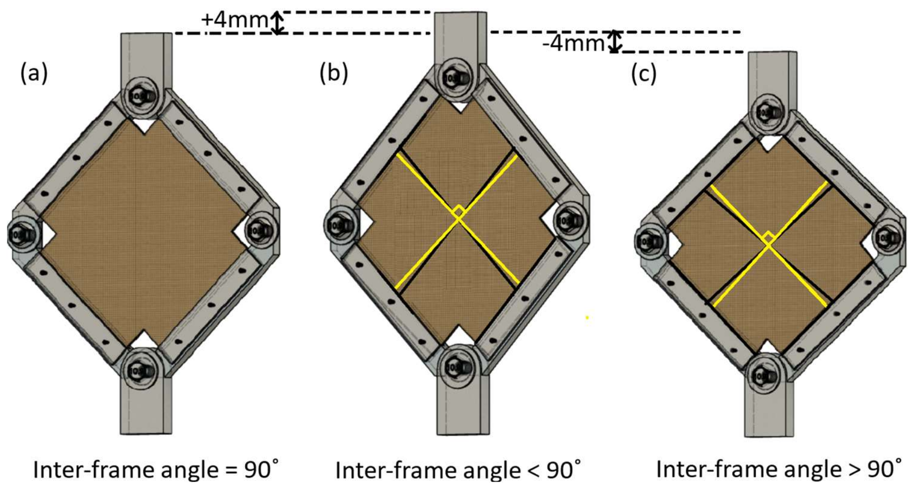

Figure 3.43: (a) Standard PF rig (b) positive pre-displaced rig (c) negative pre-displaced rig. The angles between the two black and yellow lines represent the initial frame angle and tow-stitch angle, respectively

The analysis assumes that the specimen can be loaded into the pre-displaced rig while maintaining the initial tow-stitch angle, unsheared, at 90˚. The idea behind the pre-displaced PF rig method is to minimise misalignment error by intentionally inducing compressive stress in the fibre directions during the test. Care must be taken with pre-displacement values because high values can introduce unwanted buckling in the fibres during the test. The maximum initial displacement that could be used in this investigation without affecting the original dimensions of the region of interest (i.e. shear region) was found to be 6mm (though to fix the specimen to the PF rig without deforming it, the edges of the clamping area had to be trimmed slightly). Compared to the side length of the rig, the normalised pre-displacement (0.0353) is low. Based on this method, the theoretical axial engineering strain of the fibres versus tow shear angle was determined (assuming the tows are perfectly clamped in the PF rig). The theoretical tow shear angle vs axial engineering strain predictions, corresponding to positive and negative pre-displaced PF rigs, are shown in Figure 3.44. Here ε_p and δ_p represent the engineering strain and the theoretical tow shear angle of the positive pre-displaced PF rig, respectively and are given in Eqs.3.1 and 3.2, see Appendix A and Appendix B for derivation. ε_n and δ_n represent the engineering strain and theoretical tow shear angle of the negative pre-displaced PF rig, respectively and given in Eqs.3.3 and 3.4, see Appendix C and Appendix D for the derivation.

$$\varepsilon_p = \frac{\left\{\dfrac{d_1 \sin\ {}_2 + \left[\frac{L_{pf}}{2}\right] \sin\theta_2}{sin\left(\tan^{-1}\left[\dfrac{(\tan\theta_2)\left(2d_1 + L_{pf}\right)}{L_{pf} - 2d_1}\right]\right)}\right\} - \left\{\sqrt{2}\left(\left[\frac{L_{pf}}{2}\right]\cos\theta_1 - \dfrac{\left[\frac{L_{pf}}{2}\right]\cos\theta_1\,(\cos\theta_1 - \sin\theta_1)}{\cos\theta_1 + \sin\theta_1}\right)\right\}}{\left\{\sqrt{2}\left(\left[\frac{L_{pf}}{2}\right]\cos\theta_1 - \dfrac{\left[\frac{L_{pf}}{2}\right]\cos\theta_1\,(\cos\theta_1 - \sin\theta_1)}{\cos\theta_1 + \sin\theta_1}\right)\right\}} \tag{3.1}$$

$$\delta_p = \frac{\pi}{2} - 2\tan^{-1}\left\{\frac{tan\left(acos\left[\frac{1}{\sqrt{2}} + \frac{D}{2L_{pf}}\right]\right)(2d_1 + L_{pf})}{L_{pf} - 2d_1}\right\} \tag{3.2}$$

where, θ_1 and θ_2 represent the initial frame angle and the frame angle at a given displacement (see Eq.A2 & Eq.A7, Appendix A) in the positive pre-displaced PF rig test. L_{pf} is the side length of the PF rig, and d_1 is a constant that depends on the amount of pre-displacement (see Eq. A11, Appendix A). D is the displacement of the machine crosshead at a given time.

$$\varepsilon_n = \frac{\left\{\dfrac{\left(\left[\frac{L_{pf}}{2}\right]\sin\theta_2' - d_1'\sin\theta_2'\right)}{sin\left(\tan^{-1}\left[\dfrac{(\tan\theta_2')\left(L_{pf} - 2d_1'\right)}{L_{pf} + 2d_1'}\right]\right)}\right\} - \left\{\sqrt{2}\left(\left[\frac{L_{pf}}{2}\right]\cos\theta_1' + \dfrac{\left[\frac{L_{pf}}{2}\right]\cos\theta_1'\left(\sin\theta_1' - \cos\theta_1'\right)}{\sin\theta_1' + \cos\theta_1'}\right)\right\}}{\left(\sqrt{2}\left(\left[\frac{L_{pf}}{2}\right]\cos\theta_1 - \dfrac{\left[\frac{L_{pf}}{2}\right]\cos\theta_1\,(\cos\theta_1 - \sin\theta_1)}{\cos\theta_1 + \sin\theta_1}\right)\right)} \tag{3.3}$$

$$\delta_n = \frac{\pi}{2} - 2\tan^{-1}\left\{\frac{tan\left(acos\left[\frac{1}{\sqrt{2}} + \frac{D'}{2L_{pf}}\right]\right)(L_{pf} - 2d_1')}{L_{pf} + 2d_1'}\right\} \tag{3.4}$$

where, θ_1' and θ_2' represent the initial frame angle and the frame angle at a given displacement (see Eq.C2 & Eq.C7 in Appendix C) in the negative pre-displaced PF rig test. d_1' is a constant that depends on the amount of pre-displacement (see Eq.C11, Appendix C). D' is the displacement of the machine crosshead.

The negative pre-displaced method shows positive engineering strain (stretching) in the tow direction (see Figure 3.44), which increases the force required to extend the PF rig due to increased tow tension. In contrast, the positive pre-displaced method produces negative axial engineering strain (compression) with increasing shear angle. Therefore, the fibres are compressed (or more likely, buckle) in the positive pre-displacement method. As a result, the axial tensile strain of the tows/fibres becomes compressive when the rig is pre-displaced in the positive direction, mitigating any unintended fibre tension due to accidental sample misalignment. Therefore, the positive pre-displaced method was selected to reduce the tow tension in the PF test.

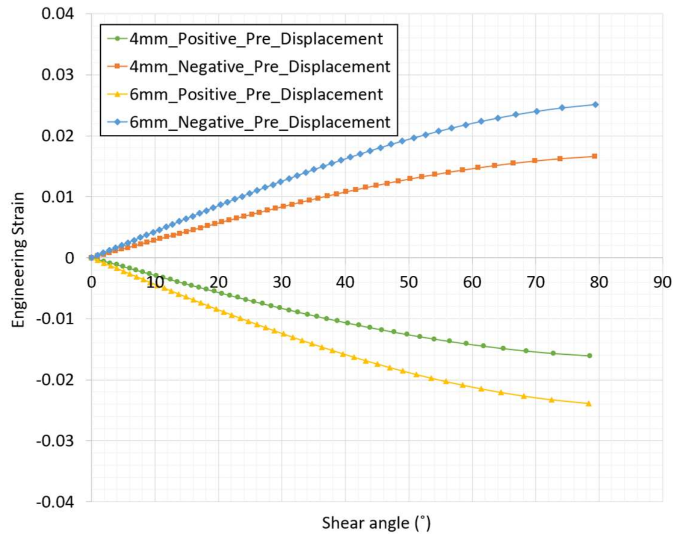

Figure 3.44: Engineering strain vs shear angle of positive and negative pre-displaced PF rig for a relative initial displacement of +/- 4mm and +/- 6mm, corresponding to an initial rig shear angle of approximately 2˚and 3˚, respectively

3.6.1.2. Loading and Clamping the Specimens

Eight specimens (four specimens each for 4mm and 6mm positive pre-displacement method) were made from pure-UDNCF with standard specimen dimensions following the specimen preparation method in the tightly-clamped PF test (see Section 3.4.1.1). The specimens were then loaded into the positively pre-displaced rig (where the direction of tows is positioned +45° to the direction of applied tensile force) while maintaining the initial inter-fibre angle of the specimens at 90˚. During the test, a spacing bar (see Figure 3.45) is used to keep the initial position at the exact pre-displaced angle of the rig and to mark the drill holes for clamping bolts.

Figure 3.45: The spacing bar used to maintain the initial position at the exact pre-displaced angle of the rig

All the tests were performed on the Zwick Z2 tensile testing machine with the same parameters as the tightly-clamped PF test. Based on the test geometry change, the theoretical shear angle of the positive pre-displaced PF test (δ_p) can be calculated as Eq. 3.2 (see Appendix B for derivation).

3.6.1.3. Results and Analysis

The first modification to the tightly-clamped PF test procedure is to propose a method to reduce fibre misalignment, a commonly reported inevitable experimental error, by pre-displacing the PF rig. Figure 3.46a depicts the average curves of the measured shear angle versus the theoretical shear angle in reference to the ideal curve (i.e., assuming that the fibres are inextensible [66]). The image analysis method was used to determine the shear angles at various crosshead displacements, and the theoretical shear angle was calculated using Eq.3.2 for the 4mm and 6mm pre-displaced PF tests. All the averaged curves overlap and are close to the ideal curve. However, at high shear angles, the results show a minor deviation below the ideal line, probably due to the formation of wrinkles, which reduces the reliability of the shear angle measurements.

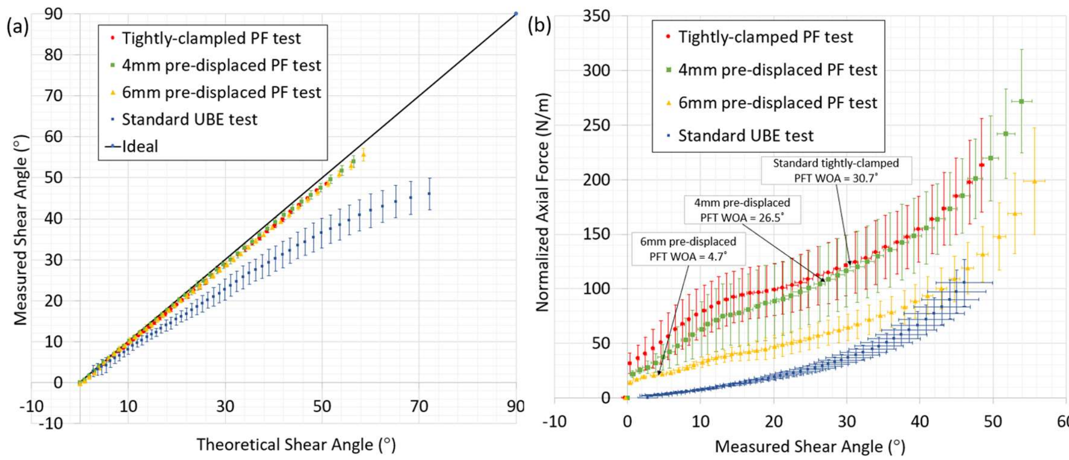

Figure 3.46: Comparison of standard UBE, tightly-clamped PF and pre-displaced PF rig tests average curves (a) measured vs theoretical shear angle curves (b) normalised axial force vs measured shear angle average curves, the error bars indicate +/- 1 standard deviation of four samples

The normalised force (axial force divided by the side length of the rig, 170mm), versus the measured shear angle response for each pre-displaced PF test were compared with the tightly-clamped PF test, as shown in Figure 3.46b. Both pre-displaced PF tests show lower normalised shear force data than the tightly-clamped PF test result. The 4mm pre-displaced tightly-clamped method shows a modest reduction compared to the tightly-clamped method at low shear angles (less than 25˚), this reduction is noticeable only at low shear angles but becomes insignificant at higher shear angles (above 25º). In contrast, the 6mm pre-displaced tightly-clamped method shows a much larger reduction, even to high shear angles. The pre-displaced results show that the initial displacement of the rig has a significant influence on the measured shear stiffness of the specimen. Presumably, this is because the compression induced along the tow direction with increasing shear angle reduces any tow tension caused by random sample misalignments and in-plane fibre bending [220]. Corroborating this idea, the average wrinkle onset angle (WOA) of the 6mm pre-displaced results (an effective proxy measure of compressive stresses in the sheet) moves to lower shear angles (4.7˚)

compared to the 4mm pre-displaced method (26.5˚) and the tightly-clamped PF test (30.7˚). However, the standard UBE test still shows the lowest axial force of all the tests (see Figure 3.46b).

3.6.2. Low- & High-Pressure Clamped Picture Frame Test Using G-Clamps

To mitigate the impact of experimental errors during the PF test, a second modification was to replace the rigid bolting of the specimen with G-clamps with two different tightening pressures (low and high, corresponding to torques of 1Nm and 5Nm, respectively) to determine how the clamping condition affects the measured force (see Figure 3.47a). Note that here 'high' pressure clamping imposed by the G-clamps is still expected to produce a significantly lower clamping pressure than the 'tight' clamping condition imposed when using bolts. This method is also used by McGuiness et al. [220], Schirmaier et al. [44], Ghazimoradi et al. [46] and Senner et al. [60] though the clamping pressure used in those investigations is not specified.

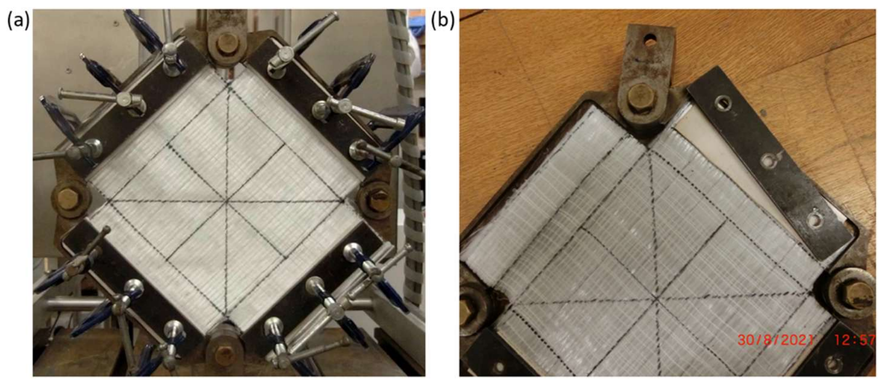

Figure 3.47: PF test setup with G-clamps (a) front view (b) showing the positioning of rubber strips under the clamps to distribute pressure more evenly

3.6.2.1. Experimental Set-up

The new clamping technique does not require sticking aluminium foil or drilling the samples (for bolt holes). To distribute pressure evenly, eight silicon rubber strips were placed on either side of the sample underneath the clamps (see Figure 3.47b). The tests were performed in the Zwick Z2 tensile testing machine using the same testing parameters used in the tightly-clamped and positive pre-displaced PF tests.

3.6.2.2. Results and Analysis

Figure 3.48a depicts the average curves of the measured shear angle versus the theoretical shear angle in reference to the ideal prediction. The theoretical shear angle was calculated using Eq1.10 for the tightly-clamped and G-clamped PF tests. The averaged curves overlap with slight deviations below the ideal line at high shear angles because wrinkles form, reducing the reliability of shear angle measurements.

The normalised force, versus the measured shear angle response for each low and high-pressured clamped PF test using G-clamps were compared with the tightly-clamped PF test, as shown in Figure 3.48b. Compared to the tightly-clamped PF test, both G-clamped test methods (high and low-pressure) show a large reduction in normalised shear force; even the high-pressure G-clamped PF test result is significantly lower than that of the tightly-clamped PF test. The tightly-clamped method prevents slip in the clamping area because the specimen is tightly bolted in the rig (see Figure 3.35). In contrast, in the G-clamped method, the ends of the tows can slip from within the clamps due to the lower clamping pressure and the presence of rubber strips placed on either side of the sample (see Figure 3.47b). Therefore, any induced tow tension in the G-clamped test specimens will be more easily dissipated.

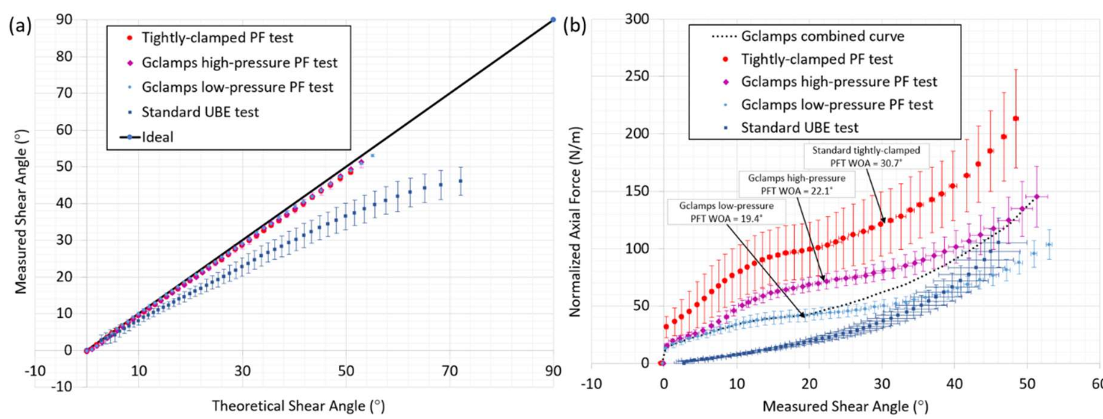

Figure 3.48: Comparison of standard UBE, tightly-clamped PF and Low- & high-pressure clamped PF tests average curves (a) measured vs theoretical shear angle curves (b) normalised axial force vs measured shear angle average curves, the error bars indicate +/- 1 standard deviation of four samples

Figure 3.49 compares the wrinkling behaviour of high and low-pressure G-clamps PF test specimens at the same shear angle. The low-pressure G-clamped specimen shows a significant volume of wrinkles with larger amplitudes, indicating that it promotes wrinkling at lower shear angles than the high-pressure G-clamp specimen. In addition to serving as an indicator of low misalignment tensile stresses, wrinkling can provide a lower-energy (and therefore lower force) mode of deformation for the specimen during the test as it results in less in-plane compression and shear. It may therefore result in the measured force being lower than the true signal and represents an opposite (but probably less severe) error than that resulting from fibre tension due to sample misalignment.

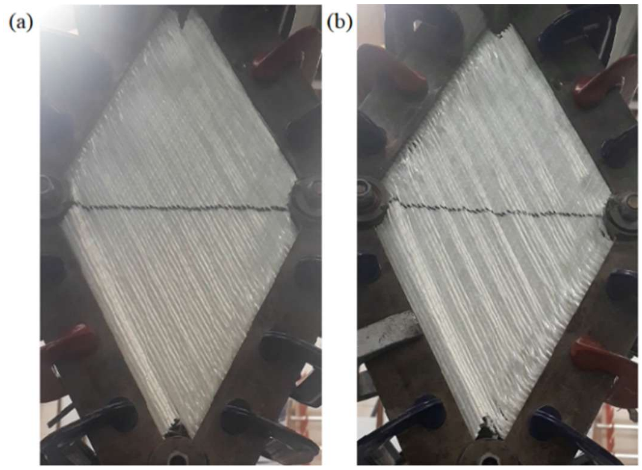

Figure 3.49: Wrinkling behaviour of G-clamps PF test specimens at 35˚ shear angle (a) high-pressure G-clamp (b) low-pressure G-clamp

Low-pressure G-clamped results have very little additional contribution due to fibre tension i.e., high noise-to-signal ratio. However, wrinkle formation at the early stages of the test may lead to underestimates of the true signal. Therefore, once the specimen begins to wrinkle, the measured force from the low-pressure G-clamped may be less reliable (beyond about 19.4˚). In contrast, the high-pressure G-clamped results may contain some additional contribution from fibre tension at low shear angles due to the higher clamping pressure (i.e. the signal-to-noise ratio is low at small angles), however, this tension will be dissipated at higher shear angles due to the greater forces involved in shearing the specimen and the non-rigid boundary condition at the clamps. The measured data in the high-pressure G-clamped is therefore likely to be more reliable at high shear angles as the noise-to-signal ratio grows relatively large (at least compared to the tightly-clamped PF test). Therefore, one tentative approach might be to combine both high and low-pressure G-clamped data. For example, beyond the wrinkle onset angle of the low-pressure G-clamped PF test, the weighted average of both the low and high-pressure G-clamped PF test results, W, can be calculated using Eq.3.5 where, w_L and w_H represent linear weighting function applied to values (i.e., at 19.4˚ of shear, w_L and w_H are 100 and 0, respectively, and decrease/ increase linearly as they approach the final shear angle of the test measurement), and X_L and X_H are the data values from the low and high G-clamp pressure PF tests, respectively. The resulting combined G-clamped test curve (indicated by the black dotted lines in Figure 3.48b)

$$W = \frac{w_L X_L + w_H X_H}{w_L + w_H} \tag{3.5}$$

3.7. Comparison of All the Shear Test Results

Figure 3.50 compares the normalised force vs measured shear angle average curves of all PF tests and the standard UBE test. The resulting combined G-clamped test curve (black dotted lines) is almost identical to the 6mm pre-displaced tightly-clamped PF test result (see Figure 3.50). This could simply be a coincidence, or it could be postulated that using two distinct approaches to obtain similar results allows for mutual verification of both methods. To explore this assumption, Figure 3.51 compares the wrinkling behaviour of high and low-pressure G-clamped PF test specimens, and the 6mm pre-displaced PF test specimens, all at a 30˚ shear angle (according to Figure 3.50, the 6mm pre-displaced PF test shows an intermediate force between the high and low-pressure G-clamped test curves at 30˚ shear angle). The wrinkle behaviour (i.e., the amplitude and number of wrinkles) of the 6mm pre-displaced PF test method lies between the high and low-pressure G-clamped specimens. Therefore, it does seem reasonable to expect that the specimens will behave similarly and produce comparable results during the two different PF test modifications (G-clamped and 6mm pre-displaced). In practice, the combined (low & high) G-clamped PF test is preferred over the 6mm pre-displaced test method because, even though twice the number of tests need to be performed, the method saves time by simplifying test sample preparation. However, the standard UBE test results remain lower in axial forces than the PF test curve (see Figure 3.50).

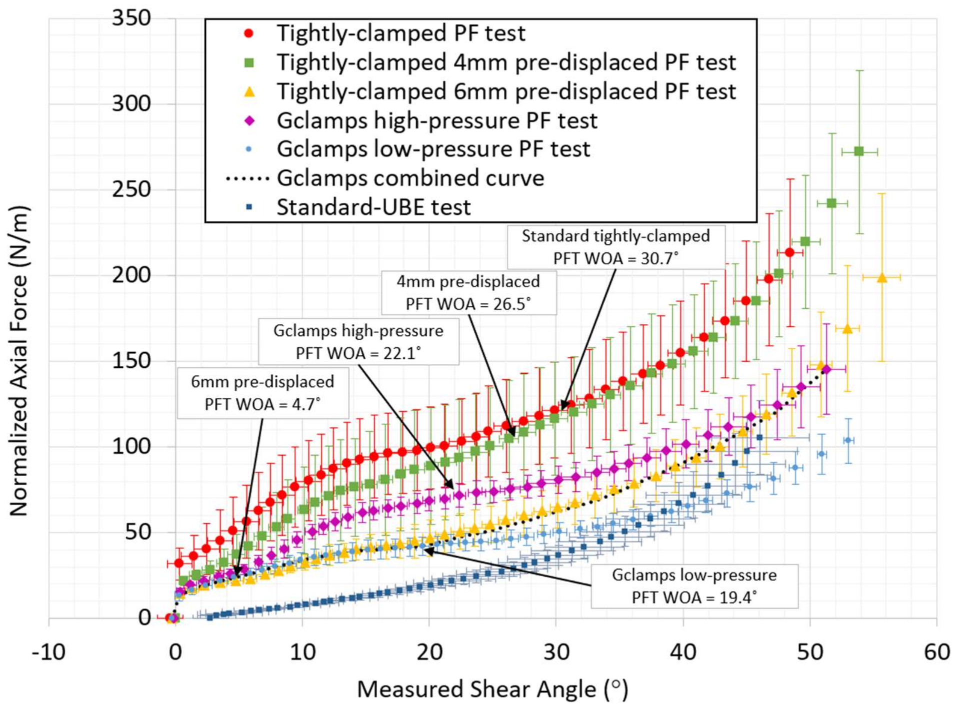

Figure 3.50: Comparison of normalised axial force vs measured shear angle average curves of all PF tests and the standard UBE test; the error bars indicate +/- 1 standard deviation of four samples

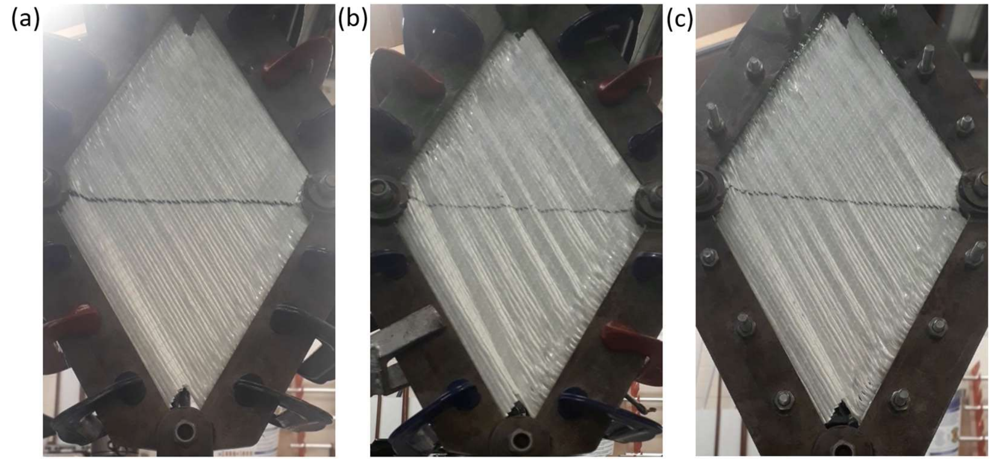

Figure 3.51: Wrinkling behaviour of PF test specimens at 30˚ of shear angles for the: (a) high-pressure G-clamped PF test (b) low-pressure G-clamped PF test and (c) tightly-clamped 6mm pre-displaced PF test

Note that PF tests were also performed in the negative bias directions to determine whether axial force depends on the shear direction (relative to the stitching). Due to the symmetric architecture of this pure-UDNCF, no significant difference was observed (i.e., average results were present within the +/-1SD - see Figure 3.52).

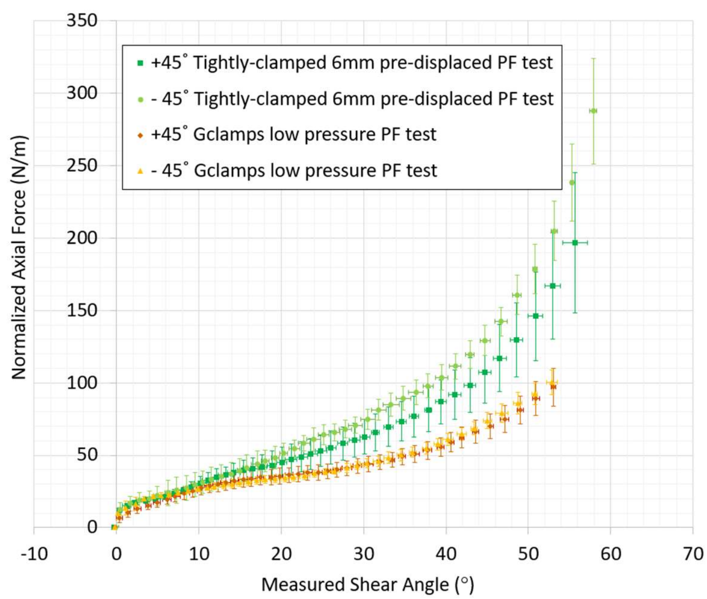

Figure 3.52: Comparison of normalised axial force vs measured shear angle curves of selected PF tests in positive and negative bias directions. The error bars indicate +/- 1SD of four specimens.

3.8. Measuring Friction in the Picture Frame Rig

3.8.1. Theory

After modifying the tightly-clamped PF test by varying the boundary conditions (Section 3.6), the results revealed significant reductions in axial force. However, the standard UBE test results still indicate lower axial force compared to the resultant PF test curve (see Figure 3.50). Therefore, it was interesting to determine if possible friction in the PF may have increased the axial force measured in the PF test. As discussed in Section 2.5.2.2, the PF rig consists of four identical bars that hinge each other by bearings. A source of friction in the PF test can come from the bearings or hinges, resulting in resistance to frame rotation. Therefore, friction can lead to overestimation of the mechanical stiffness of the fabric. Adding extra weights, for example, G-clamps (see modifications of the PF test discussed in Section 3.6.2) can increase the frictional force measured in the test. Therefore, the idea behind this test is to quantify friction and then isolate the actual fabric shear response based on those results. Note that prior to conducting the tests reported in previous sections, a test to measure friction in the unloaded PF rig was performed and suggested very little friction. This more in-depth investigation was prompted due to the difference between the PF and UBE test results on the pure-UDNCF.

3.8.2. Experimental Set-up

Lubricating oil was applied to the bearings of the PF rig prior to testing to reduce friction. First, the rig was tested without any additional weights. Weights were then added to the rig (see Table 3.5), ensuring they were evenly distributed in each arm of the PF rig (see Figure 3.53). The PF test was first performed on the empty rig using the Zwick Z2 tensile testing machine with a 2kN load cell. The standard force and displacement were set as the test report parameters, and the test was filmed using a camera. The frame angles at the selected displacements were measured using ImageJ [146] software to determine the shear angle of the rig at each displacement.

Table 3.5: Additional weights used to evaluate the friction of the PF rig

	Total Weight (g)	Additional Weight (g) (Total weight – Empty rig weight)
Empty Rig (i.e., rig without Clamps) (Figure 3.53a)	1683.9	0
Rig + 12 nuts & bolts + 4Plates (Figure 3.53b) Weight of 4 plates = 408.2g	2181.2	497.3
Rig + 1 set of 4Clamps + 4Plates (Figure 3.53c) Weight of a clamp = 140-143g	2662.1	978.2
Rig + 2 sets of 4Clamps (Figure 3.53d) Weight of a clamp = 135-136g	3206.9	1523
Rig + 3 sets of 4Clamps (Figure 3.53e) Weight of a clamp = 120-123g	3692.1	2008.2
Rig + 4 sets of 4Clamps (Figure 3.53f) Weight of a clamp = 135-136g	4237.1	2553.2
Rig + 5 sets of 4Clamps (Figure 3.53g) Weight of a clamp = 212-215g	5092.6	3408.7

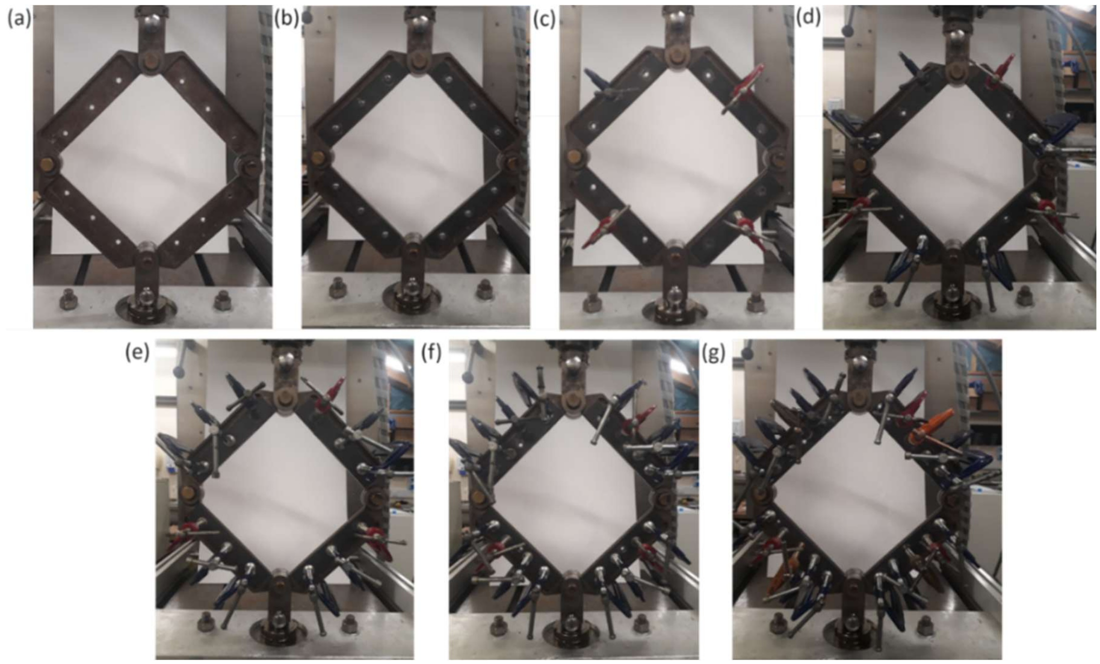

Figure 3.53: Friction tests of the PF rig (a) Empty rig (b) Rig with 12 nuts & bolts and 4Plates (c) Rig with 4Plates and 4G-clamps (d) Rig with 4Plates and 8G-clamps (e) Rig with 4Plates and 12G-clamps (f) Rig with 4Plates and 16G-clamps (g) Rig with 4Plates and 20G-clamps

3.8.3. Results and Analysis

Figure 3.54 shows the normalised force vs measured shear angle average curves of the PF test empty rig with different addition weights. The friction of the rig increases with the increase of the shear angle (even without any additional weights – see Figure 3.54). More significantly, the initial jump increases with the addition of weights. Table 3.6 summarises the change in the initial jump with the additional weight.

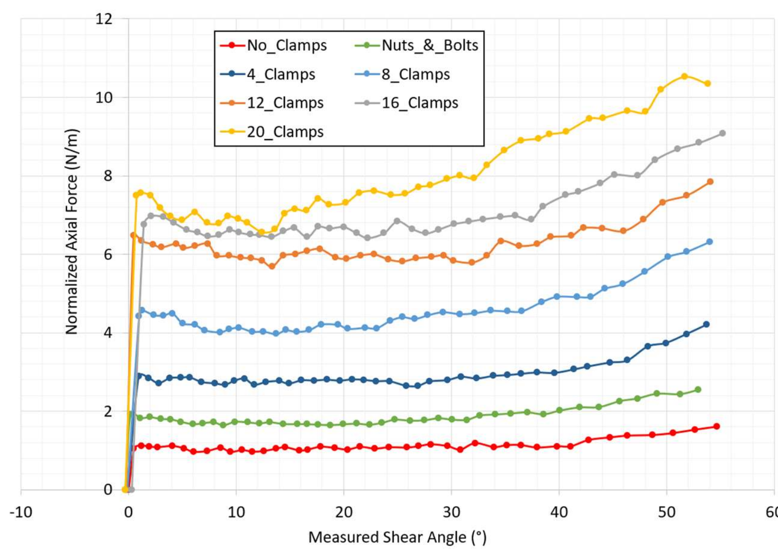

Figure 3.54: A comparison of the normalised axial force vs measured shear angle curves of the PF rig with different additional weights

Table 3.6: Initial 'jump' related to additional weights during the PF test

	Total Weight (g)	Additional Weight (g) (Total weight – Rig weight)	Initial Jump (N/m)
Empty Rig (i.e., rig without Clamps) (Figure 3.53a)	1683.9	0	1.0
12 nuts & bolts + 4Plates (Figure 3.53b)	2181.2	497.3	1.9
4 Clamps (Figure 3.53c)	2662.1	978.2	2.9
8 Clamps (Figure 3.53d)	3206.9	1523	4.4
12 Clamps (Figure 3.53e)	3692.1	2008.2	6.5
16 Clamps (Figure 3.53f)	4237.1	2553.2	6.8
20 Clamps (Figure 3.53g)	5092.6	3408.7	7.5

The results imply that the friction of the bearings significantly contributes to the axial force. Static analysis of the PF rig provides a more comprehensive understanding of the forces acting on the rig during the test (see Appendix E). This allows an understanding of the effect of frictional forces on the axial force measured by the load cell. This adjustment is critical to the accuracy of shear test results. Without additional weights, the PF test shows relatively negligible friction (when manually pulling the rig, there appears to be no friction). The initial jump in axial force increases with the addition of weight (see Figure 3.54). It is worth noting that in the literature, although some PF studies [120] [218] [219] [154] also show an initial increase in force, they assume no friction in the rig.

For overall results, the contribution of friction may vary. The complication, however, is that when a fabric is sheared it naturally creates a load on the PF rig. The friction contribution of the rig therefore depends on the stiffness of the material, i.e., the stiffer the material, the higher the friction contribution. This is an iterative loop. This can be understood by performing the PF test on samples of the same material of varying thicknesses (see Figure 3.55a&b). Figure 3.55c compares the normalised axial force vs measured shear angle curves of Silicone rubber sheets with two thicknesses i.e., thin (0.5mm) and thick (2mm). The weight difference between these two specimens is only a few grams (i.e., the weight difference cannot be interpreted as adding significant extra weight). However, there is a clear difference between the initial measurements of the two curves (see Figure 3.55c). This shows that the resistance of the materials also induces a frictional contribution from the PF rig. Therefore, two types of friction acting on the rig can be identified, one caused by additional weights and the other by the resistance created by the material at the joints.

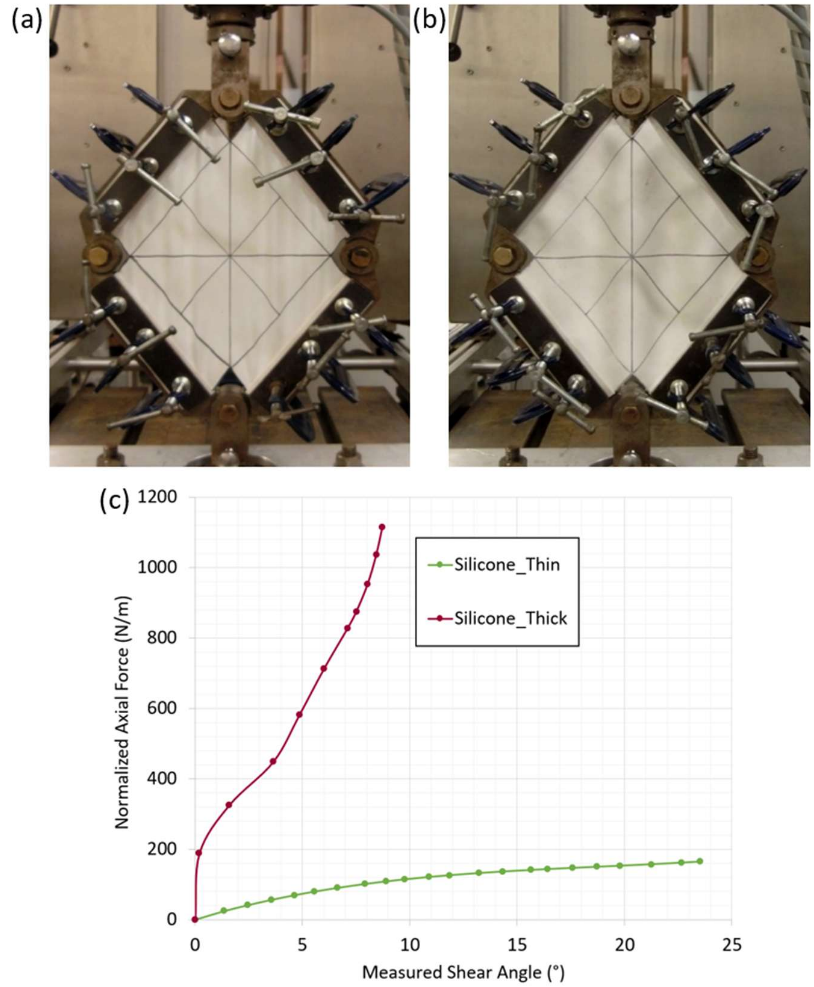

Figure 3.55: PF test with Silicone sheets (a) thin (b) thick (c) normalised axial force vs measured shear angle curves

Furthermore, the PF test with G-clamps was performed on plain and twill woven fabrics (see Figure 3.56a&b, respectively) to see how the friction of the PF rig affects the woven glass fabrics. The resultant normalised axial force vs measured shear angle curves were compared with the pure-UDNCF (Figure 3.56c&d). Compared to plain-woven fabric, the twill-woven and pure-UDNCF show an initial jump in force of more than twice that of the plain weave (see Figure 3.56d). Table 3.1 shows considerable variations in fabric properties between twill-woven and pure-UDNCF compared to plain-woven (ex: thickness and areal density). It can be concluded that the friction varies due to the material properties although the amount of extra load acting on the fabric is the same. Therefore, it is difficult to estimate the exact amount of friction.

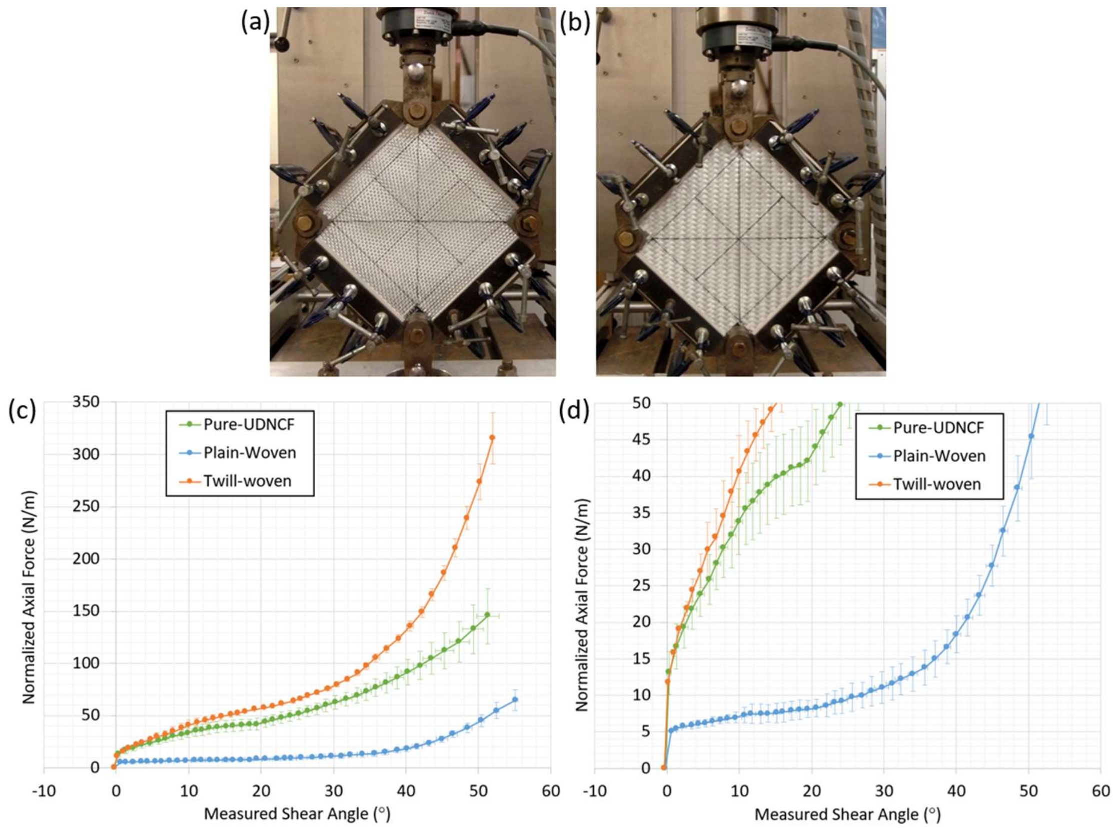

Figure 3.56: PF test with woven fabrics (a) Plain-woven (b) Twill-woven (c) comparison of normalised axial force vs measured shear angle curves of all three glass fabrics (d) normalised axial force of graph (c) up to 50 N/m for better observation

Before proceeding with further testing, it was decided to replace the bearings of the rig. However, due to time constraints, all these experiments cannot be repeated using the repaired PF rig. Material and Manufacturing Research Group (MMRG) of the University of Glasgow continued the investigation on the PF rig and discovered that the results did not improve after the bearings were replaced. Furthermore, they observed that the contacting faces of the bars (see Figure 3.57a) were scratched i.e., not smooth (see Figure 3.57b). This could explain why axial force increases with increasing shear angle even without additional weights (see Figure 3.54), as friction in the contacting faces of the bars can cause a nonlinear increase in axial force, especially at higher shear angles where contact pressure and relative movement are more significant. It was decided that the surfaces be polished, and thinner PTFE (Teflon™) washers be placed between the contracting faces to minimise this friction contribution. To account for the frictional contribution measured in the present study, it was considered reasonable to remove the measured initial jump from the current PF test results (i.e. to eliminate the friction due to the additional weights).

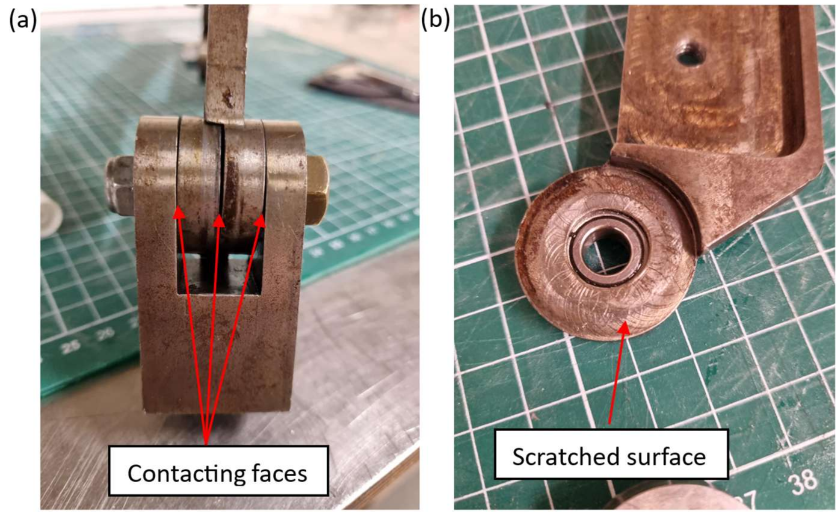

Figure 3.57: (a) Contact faces of the bars of the picture frame rig (b) starched surface

3.9. Comparison of Friction-Modified G-clamped PF Test Curves

Figure 3.58 compares the normalised force vs measured shear angle average curves of the friction-modified PF and the standard UBE tests. To adjust the curves, the initial jumps due to the additional weights of 1.9 Nm^{-1} and 6.5 Nm^{-1} (see Table 3.6) were deducted from the tightly-clamped PF test and G-clamps combined curves, respectively. This adjustment could make a difference in the results from multiple published PF investigations (different initial jumps, see Fig.12 in Kahavita et al. [221]) and further narrow the gap between the results reported in Fig.16 in Kahavita et al. [221] (for the convenience of the reader, a copy of Fig.16 in Kahavita et al. [221] is included in this report, see Figure 3.59). Even after eliminating the misalignment error and the friction of the rig, the normalised force measured in the standard UBE test is still lower than that measured in the modified PF tests, however, the difference is smaller than initially measured (see Figure 3.58). The modified PF test result is higher by a factor of 5X at 5˚, 2X at 10˚ and 1.5X at 30˚, whereas the tightly-clamped PF test result is higher by a factor of 16X at 5˚, 10X at 10˚ and 3X at 30˚. This difference is nevertheless considerable.

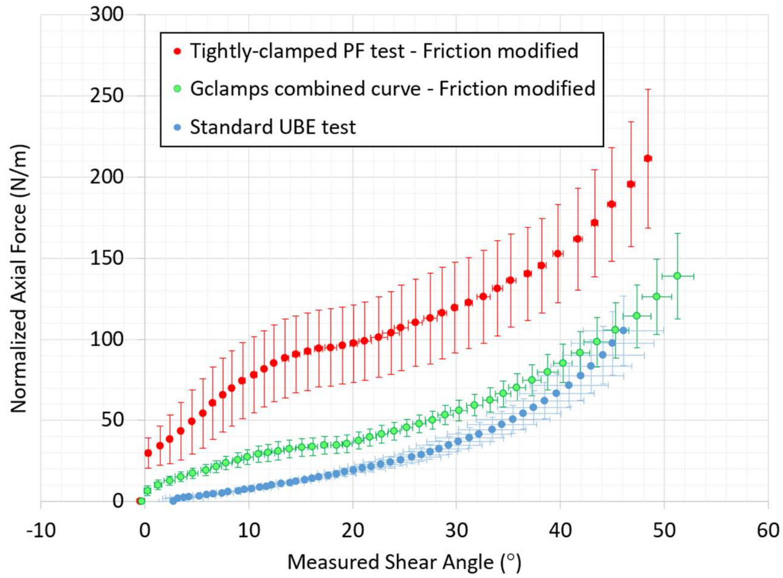

Figure 3.58: Comparison of normalised axial force vs measured shear angle curves of standard UBE test, friction modified tightly-clamped PF test, and resultant G-clamped PF test combined curve

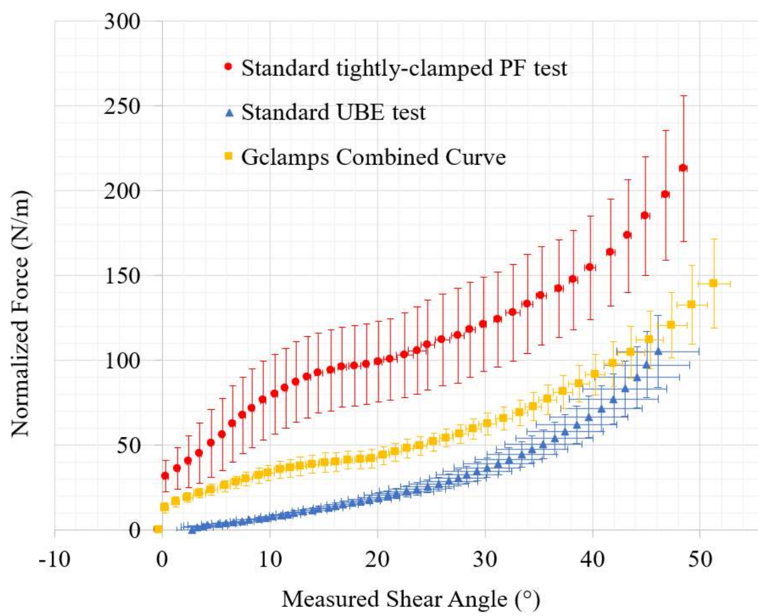

Figure 3.59: Comparison of normalised axial force vs measured shear angle curves of standard UBE test, tightly-clamped PF test (with rig friction), and resultant G-clamped PF test combined curve (with rig friction) [221]

Figure 3.60 compares the results for woven fabrics for both UBE and PF tests. Both curves overlap at low shear angles (until 20˚ and 12˚ for plain and twill woven fabrics, respectively) and then at higher shear angles, the UBE shows higher normalised axial forces than the PF test. As expected, for woven fabrics, UBE results are higher than the PF results at high shear angles due to the extra contribution of Region B of the test specimens (see Figure 3.8). This effect has been analysed in detail in some studies [114], [45] and can account for the difference.

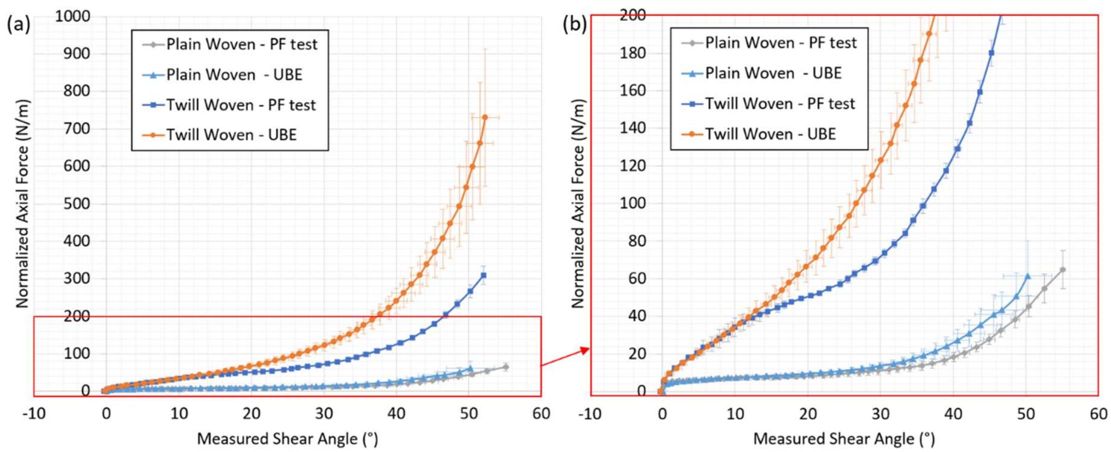

Figure 3.60: Comparison of normalised axial forces vs measured shear angle curves of UBE and PF test results for plain and twill woven fabrics.

In contrast to woven fabrics, the results obtained for pure-UDNCF are measured to be higher in the PF test than in the UBE test (see Figure 3.58, green and blue curves). Given that the in-plane bending stiffness of pure-UDNCF is likely to be higher than for woven fabrics due to the lack of weaving, the difference between the PF and UBE results could potentially be due to a sizable contribution to the force measured in the PF test, due to in-plane bending, a contribution which is largely absent in the UBE test; recall the lack of bending of the tows at the transition between Regions A and B in the UBE test specimen, see Figure 3.31. Alternatively, the difference between the PF and UBE results could also be due to a decrease in the shear resistance of the pure-UDNCF in the UBE test, due to the observed stretching in the stitch direction. This stretching is likely to reduce the shear stiffness of the fabric. Because the various stiffnesses of a fabric can significantly influence its behaviour in forming simulations, it is important to understand whether the shear stiffness of the pure-UDNCF really does decrease with increasing stretch in the stitch direction. Consequently, this possibility will be explored further in Chapter 4 with the introduction of several new test methods.

3.10. Tensile Test

3.10.1. Methodology

Tensile testing helps to understand how the material behaves when a load is applied along the stitch direction. Since the stitches are perpendicular to the glass tows, they play a significant role in the distribution of the tensile load and the overall mechanical performance of the fabric. A tensile test was performed on the stitch direction of pure-UDNCF following the ISO 13934-1. Four samples with an initial length along the stitch direction, L_T of 50mm and an initial width of the specimen, W_T of 200mm, were prepared to test the tensile properties of the pure-UDNCF in the stitch direction at a strain rate of 20mm/min (see Figure 3.61). The clamping regions of the specimens were bonded with Al foil using epoxy resin to allow easier drilling of holes and gripping. The engineering strain in the stitch direction during the tensile test, ε_T is calculated as a function of the displacement, D_T (see Eq.3.6).

$$\varepsilon_T = \frac{D_T}{L_T} \tag{3.6}$$

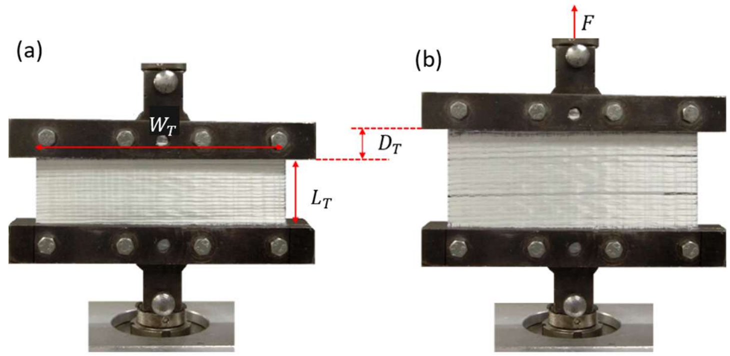

Figure 3.61: Tensile test specimen of the pure-UDNCF in the stitch direction (a) Undeformed (b) Deformed

3.10.2. Results and Analysis

The tensile test specimen is subjected to just one low-energy deformation mechanism (stitch tensile strain). It has no contribution from shear or in-plane bending. Figure 3.62 shows the results of tensile tests on pure-UDNCF in the stitch direction. To normalise the force, the axial force was divided by the initial width of the specimen (W_T, see Figure 3.61). The stitch strain of tensile specimens was calculated by dividing the standard travel by the initial length of the tensile specimen along the stitch direction, L_T (see Eq.3.6). According to Figure 3.62, the force initially increases with increasing stitch strain because the stitches progressively engage and bear the load. However, after reaching a certain point, the force starts to decrease. Once the stitches reach their tensile strength limit, they start to break, leading to a drop in force.

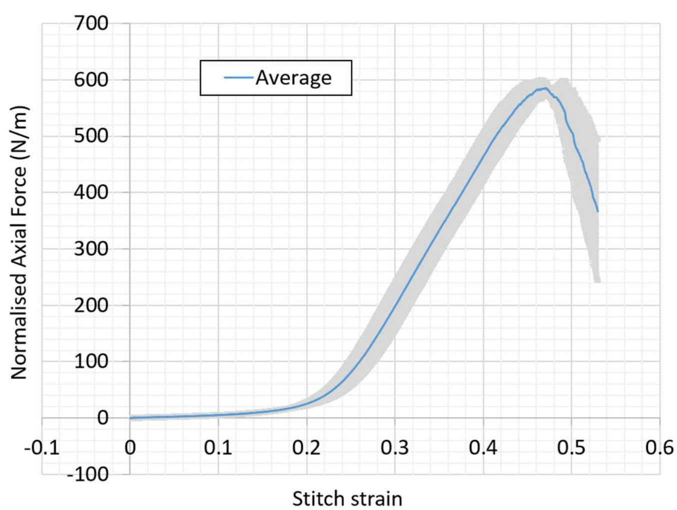

Figure 3.62: Normalised tensile force vs stitch strain of pure-UDNCF in the stitch direction. The shaded region indicates +/- 1SD, calculated from four repeat test results.

3.11. Chapter Summary

This chapter focused on the shear and tensile characterisation of pure-unidirectional non-crimp fabric (stitches are perpendicular to the glass tows and contain no additional stabilising fibres) using standard test methods. First, the uniaxial bias extension test was performed on two woven glass fabrics (plain and twill) to obtain a best practice before performing on pure-UDNCF. Later, the deformation of woven fabrics was compared with the pure-UDNCF, and the finding implies that the presence of stitches in pure-UDNCF has an unusual effect on mechanical performance compared to that seen for woven fabrics. The in-plane shear behaviour of a pure-UDNCF was then measured using another common test, the tightly-clamped picture frame test. The normalised force curves of the two shear tests initially suggested a significant difference, with the tightly-clamped PF test result being dramatically higher than the standard UBE test result. This was unexpected. Typically, for most biaxial woven fabrics, the shear results of these two tests are expected to be reasonably close (assuming no misalignment errors in the PF test, which in practice can be considerable and difficult to avoid). The UBE test may typically produce a slightly higher axial force than the PF test due to the 'extra' force contribution in areas other than the region of interest of the specimen. The difference in behaviour in the tightly-clamped PF test and the standard UBE test (the tightly-clamped PF test result being much higher) could have been due to: (a) experimental error in the PF test (i.e., tow misalignments, clamping conditions and friction of the PF rig) or (b) a real change in shear resistance of the fabric in the two tests. Stretching in the stitch direction of pure-UDNCF during the UBE test may fail to offer an accurate estimate of the true in-plane pure shear behaviour of the material. Also, stitch stretching reduces the contribution of in-plane bending in the UBE test, while the PF test may measure a significant contribution from in-plane bending.

This chapter first focused on exploring option (a) which involved modifications to the tightly-clamped PF test and considered potential friction in the PF rig. To explore option (a) two variations on the tightly-clamped PF test have been considered.

- **Misalignment error:** Positive pre-displaced tightly-clamped PF testing was performed to minimise fabric tension caused by misalignment. The 6mm pre-displaced method shows a significant reduction in the normalised axial force compared to the tightly-clamped PF test. The reason for this reduction in normalised force is that the tows undergo compressive stresses rather than tension. This is evidenced by the onset of wrinkling at low shear angles.
- **Clamping condition:** In this method, the tight clamping of the PF test (nuts and bolts) was replaced by G-clamps. The G-clamp method was performed with two different tightening pressures (low and high) to determine how the clamping condition affected the measured shear force. Based on wrinkling observations, a progressively weighted combination of the two G-

clamp PF test results was suggested as an optimum compromise, with the low clamping pressure taking precedence at low shear angles (low forces) and the high clamping pressure taking precedence at high shear angles (high forces).

The resulting combined G-clamped PF test curve presents close to the 6mm pre-displaced PF test curve, suggesting that these two distinct approaches may achieve similar results. In practice, the combined (low and high pressure) G-clamped PF test is preferred over the tightly-clamped 6mm pre-displaced test method because, even though twice the number of tests need to be performed, the method saves time by simplifying test sample preparation.

By reducing misalignment and clamping errors, the axial force was significantly reduced, and the accuracy of the PF test improved, however, the standard UBE test results still showed less axial force than the PF test curve. Experiments were then performed to investigate whether the friction in the PF was the cause of at least part of the high forces observed in the PF test.

- **Frictional contribution of the PF test:** Adding extra weight (i.e. increasing the number of G-clamps used in the test) causes increased friction in the bearings. Moreover, the friction experienced by the rig varies according to the stiffness of the material. Therefore, separating the frictional force from the total axial force of the PF test is difficult. To improve the accuracy of the results, the initial jump noted throughout the test results was subtracted from the test data.

Nevertheless, even after eliminating the misalignment and the friction error in the PF test, the normalised force measured in the UBE test is still significantly lower than that measured in the modified PF tests, and while the difference is much smaller than initially measured, it is still significant. Therefore, it seems likely that there is a true change in the shear resistance of the fabric between the two shear tests i.e., possibly a coupling between shear stiffness / tensile strain in the stitch direction, and between tensile stiffness in the stitch direction / shear strain. In addition, a contribution from the in-plane bending could be playing a role in the PF test. As a result, the axial force measured in the PF test of the pure-UDNCFs may be a combination of shear and in-plane bending. In the UBE test, stretching in the stitch direction may help to minimise the contribution from in-plane bending of the tows. While these postulates may explain the difference in the measured behaviour in the two shear tests; this remains to be proven. Chapter 4 focuses on providing such proof.

Chapter 4 Shear Experiments Using New Characterisation Tests

4.1. Introduction

Chapter 3 concluded that the normalised force measured in the modified picture frame (PF) tests is much higher than that of the uniaxial bias extension (UBE) test, even after correcting for friction in the rig and misalignment error. Comparing the UBE and PF test results of woven fabrics (plain and twill), at higher shear angles the axial force of the UBE test is higher than the PF test due to the extra contribution of B regions in the UBE specimens. Therefore, the UBE and PF results obtained for pure-unidirectional non-crimp fabric (pure-UDNCF) are unexpected and are not usual in woven fabrics. The difference in the results of pure-UDNCF in the two shear tests could therefore be due to **a real and significant change in the forming behaviour of the fabric when subjected to the two different test conditions i.e., the inherent behaviour of pure-UDNCF in the two shear tests.** Stretching in the stitch direction was observed during the UBE test, but not in the PF test due to the constrained boundary conditions. Therefore, there is possibly a coupling between shear stiffness - tensile strain in the stitch direction, and between tensile stiffness in the stitch direction - shear strain. In addition, the reduced UBE force could be due to a relatively low contribution from in-plane bending to some extent. The objective of this chapter is to create new experiments to explore this hypothesis by creating well-defined kinematics, but with different amounts of shear vs stitch strain, i.e., different combinations of shear and tensile strain in the stitch direction. In addition, the results of Chapter 3 suggest that there is a considerable in-plane bending contribution in all PF tests. Therefore, this chapter further aims to investigate new areas of deformation space using the PF test (in addition to the modifications outlined in Chapter 3). To well-model the forming behaviour of the pure-UDNCF, it is necessary to separate the contributions to the measured axial force from shear, in-plane bending, and stitch tension. The ultimate objective of this chapter is to decouple the forces acting on the pure-UDNCF using selected experiments.

The structure of this chapter is as follows: Sections 4.2 to 4.4 discuss several entirely new test methods to explore the inherent behaviour of pure-UDNCF. Also, a new ‘pre-stretched specimen’ PF test method is introduced in Section 4.5. The force results of each test are summarised in Section 4.6, and a method for decoupling the force contribution is detailed in Section 4.7. The chapter summary is provided in Section 4.8.

4.2. Cruciform Bias Extension (CBE) test

The shape of the standard UBE specimen was modified to an octagonal shape. Regions C (see Figure 4.1) are bonded with aluminium foil, consequently, the actively deforming region of the specimen is of a cruciform shape (including Regions A and B) (see Figure 4.1). Alternative bias-extension test geometries have been used previously by various researchers, including Potluri et al. [65] Harrison et al. [66] and Krogh et al. [55].

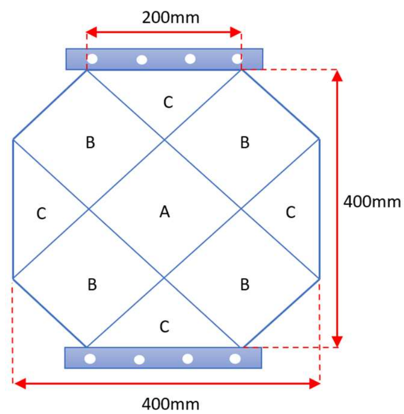

Figure 4.1: A diagram of the octagonal-shaped test specimen

4.2.1. Sample Preparation and Testing

Samples of pure-UDNCF were created using the dimensions given in Figure 4.1. To ensure the C Regions remain undeformed, Al foil was bonded to all four C Regions of the octagonal-shaped specimen using epoxy resin. As a result, the shape of the active region of the specimen is cruciform shape (see Figure 4.2, referred to here as Cruciform Bias Extension, 'CBE' test). As with UBE kinematics for pure-UDNCFs (see Figure 3.8c), the CBE specimen can be further divided into four regions, namely, A, B1, B2 and C (i.e., in Region B1, both ends of the tows are constrained whereas the ends of the stitches are unconstrained. Conversely, in Region B2 both ends of the stitches are constrained while the ends of the tows remain unconstrained). Tests were performed in a Zwick Z2 tensile testing machine using the same testing parameters used for the standard UBE test. The shear angle and the engineering strains of Region A and all four B Regions of the CBE specimens were measured as a function of displacement using ImageJ software [146].

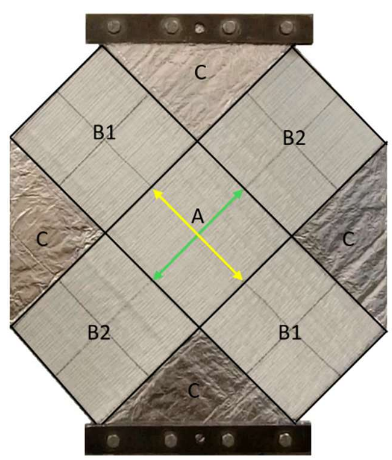

Figure 4.2: A CBE specimen (a) undeformed, the yellow and green arrows indicate the initial chain-stitch and tow directions, respectively

4.2.2. Results and Analysis

According to Figure 4.3a, the shear angle of the CBE specimen is lower than the theoretical pin-jointed net prediction at low shear angles and the deviation increases as the shear angle increases. This implies that stretching of the stitch becomes significant even at low-shear angles. Similar to the average curve of the standard UBE test, the CBE curve also shows the same kind of deviation from the ideal pin-jointed net curve; the difference is that the average CBE curve begins at the (0,0) point, whereas the standard UBE curve begins at an initial pre-displaced angle. The supportive lateral C regions in the CBE specimens maintain the initial inter-fibre angle at around 90° (the pre-shear angle is less than 0.5˚). The pre-shear angle of all specimens in the standard UBE test varied from 1° to 4°. Because of the tension in the stitches, it is difficult to keep the pre-shear angle in the UBE test less than 0.5° i.e., the fabric has no other stabilising fibres, and the chain stitches are tensioned, allowing the fabric to have an inherent pre-shear configuration (see Figure 4.4a). Previous experimental studies suggest keeping the pre-shear angle below ~0.5° and the standard deviation of the initial inter-fibre angle measurements within ~2° yields more accurate results [113]. Therefore, the CBE test yields more precise readings than the standard UBE test. In addition, Figure 4.4c shows the standard UBE kinematics are poorly constrained and the specimen 'does its best' to minimise in-plane bending. Compared to the standard UBE test, the in-plane bending is much better defined in the CBE test (see Figure 4.4b&d).

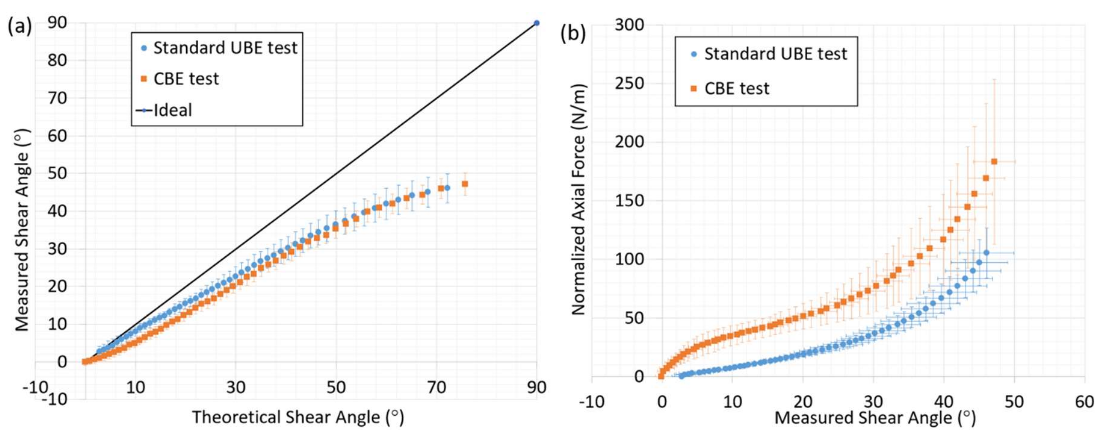

Figure 4.3: Comparison of the standard UBE and CBE tests (a) measured vs theoretical shear angle curves (b) normalised axial force vs measured shear angle curves. The error bars indicate +/- 1SD of four specimens.

The axial force is normalised by dividing the specified length of Region A in each specimen (see Figure 4.4a&b) to make the results independent of the size of the tested specimen. According to Figure 4.3b, the force required to deform the fabric is initially low and gradually increases as the measured shear angle improves. Compared to the standard UBE test, CBE specimens show higher axial forces due both to the large contribution of the B Regions and also due to the in-plane bending contribution which is largely absent in the UBE test (see Figure 4.4b&d).

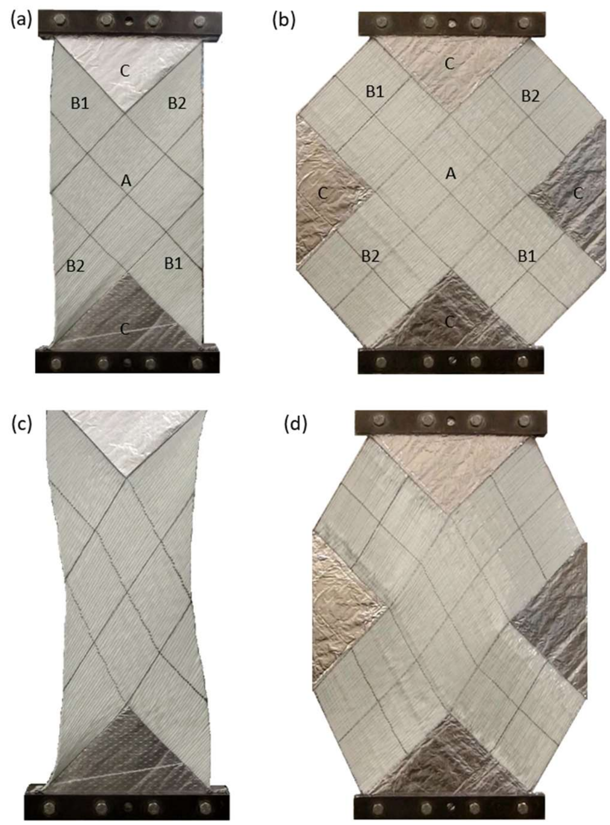

Figure 4.4: Comparison of standard UBE and CBE specimens (a) undeformed UBE (b) undeformed CBE (c) deformed UBE at 30˚ of shear angle (b) deformed CBE at 30˚ of shear angle

4.2.2.1. Stitch Strain Analysis

Figure 4.5 shows the kinematics of each region of the CBE specimen. Region A has the highest shear angle (52˚), while the two B Regions have maximum shear angles of 30˚, more than half that of Region A (see Figure 4.5b). The stitch strain in B2 Regions increases due to the bonding of both ends of the stitches to the Al sheets, which causes the stitch stretching to be greater than in Region A (see Figure 4.5c). In contrast, the stitch strain in the B1 Regions is almost zero due to the bonding of the two ends of the tows to the Al sheets. Therefore, while each of the three deformable regions within this specimen is subject to different combinations of shear and stretching along the stitch direction, the uniformity of the strain field in each region means analysis of the different contributions to the total measured force in this test may be feasible.

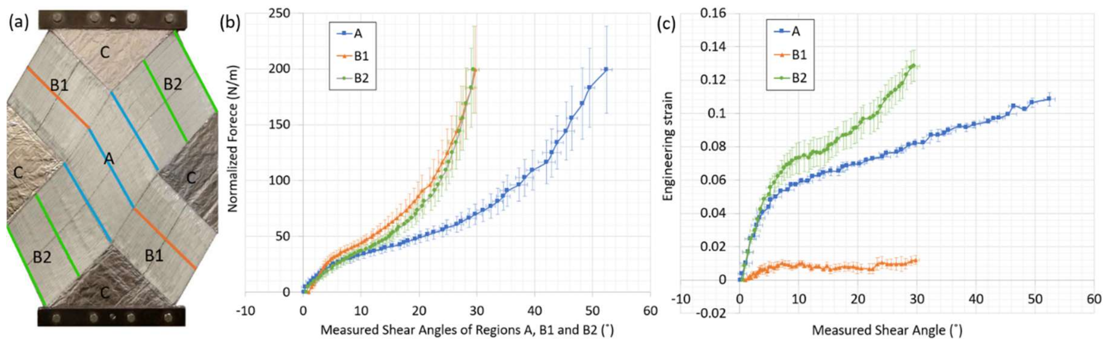

Figure 4.5: (a) Deformed CBE specimen, the coloured lines indicate the stretching measurements from each Region (blue, yellow, and red lines for the B1, B2, and A Regions, respectively) (b) normalised axial force vs measured shear angle of Region A, B1 and B2 (c) engineering strain vs measured shear angle of each region

When the stitch strain in region A of the standard UBE and CBE specimens is compared (see Figure 4.6), the stitch strain in standard UBE specimens is low at low shear angles. This could be due to the tension in the stitches at the beginning of the tests (see Figure 4.4a). However, as the measured shear angle increases, the stitch strain of the CBE specimens decreases compared to the standard UBE stitch strain. Figure 4.4c&d shows two specimens with nearly equal shear angles (around 30˚). The CBE specimen shows high in-plane bending compared to the standard UBE test, and Figure 4.7 highlights the in-plane bending areas in the specimen. Aside from the areas highlighted, there is a contribution of the in-plane bending in the stitch direction too. However, its contribution is negligible. Therefore, the CBE specimen experiences three low-energy deformation modes (compared to the stretching of the tows): shear, tensile strain in the stitch direction, and in-plane bending. Extracting the shear/tensile behaviour from the CBE test analytically is extremely difficult due to the complexity of the kinematics in the different B Regions, however, the test will be useful for evaluating numerical predictions later, after an appropriate constitutive model is implemented in a FEA code.

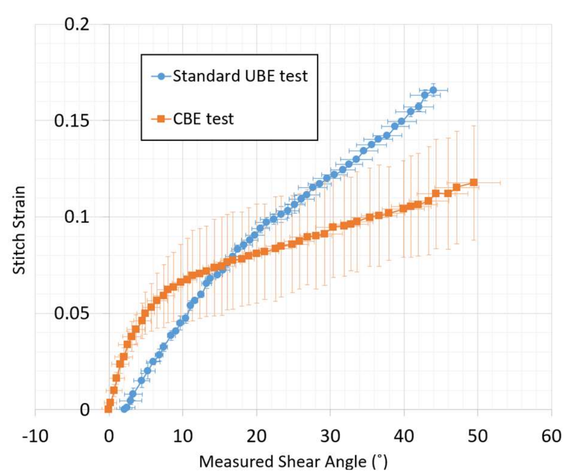

Figure 4.6: Stitch strain vs measured shear angle curves of region A for standard UBE and CBE specimens. The error bars indicate +/- 1SD of four specimens.

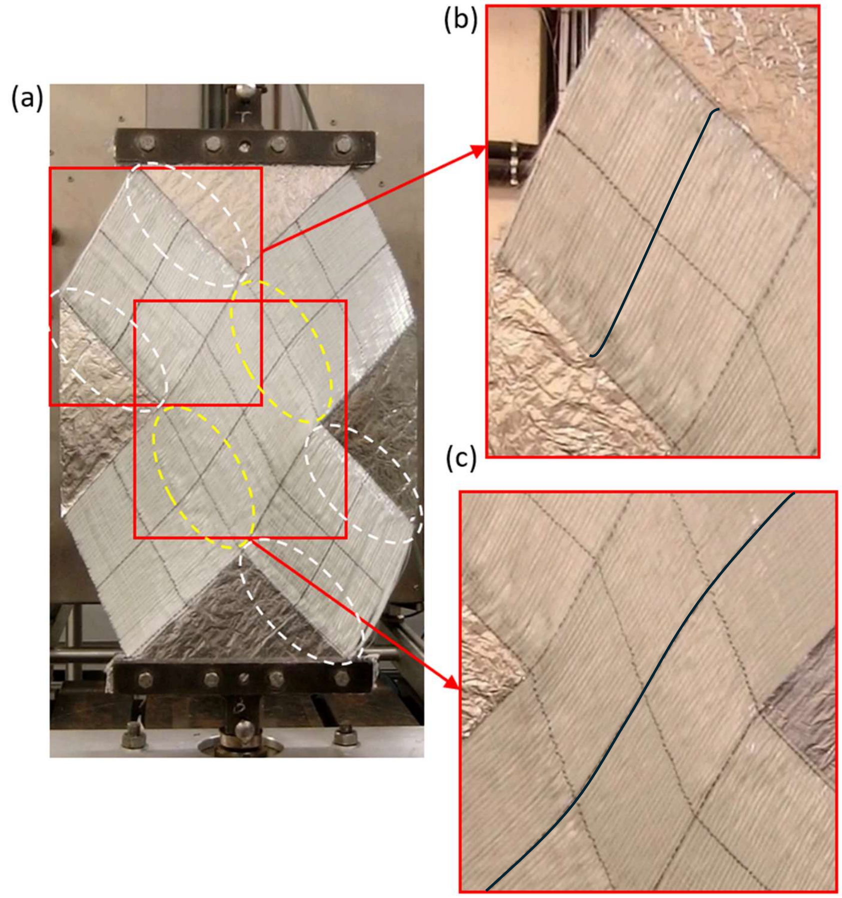

Figure 4.7: (a) A CBE specimen at 30˚ of shear angle, marked areas show in-plane bending of tows (yellow – high, white – low) (b) & (c) magnified images of (a)

4.3. Parallelogram Shear-Stretch (PSS) Test

4.3.1. Theory

A second new test has been devised to access alternative kinematics in terms of the (shear angle) – (tensile stretching) parameter space. A schematic diagram of the so-called Parallelogram Shear-Stretch (PSS) test specimen employing 2 sheets of bonded aluminium, is shown in Figure 4.8. This test creates well-defined homogenous deformation across the entire specimen, making it easier to analyse than the CBE test (an initial prototype of this test is shown in Appendix F).

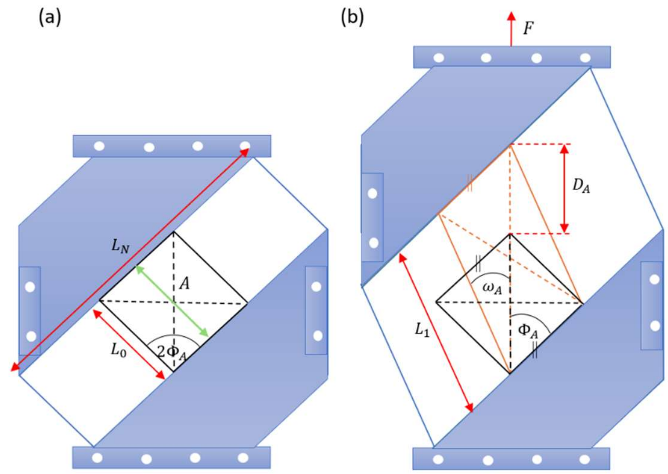

Figure 4.8: PSS specimen (a) Undeformed, the green arrow indicates the initial chain-stitch direction (b) Deformed, the shape of Region A shifts from square (black) to parallelogram (orange)

The region of interest in the PSS specimen is initially rectangular, with the tows oriented exactly at 45° (bias) direction to the applied force. During the deformation, the original shape of Region A transforms into a parallelogram (see Figure 4.8b). Based on the geometry change, the theoretical shear angle, θ_A, is determined by the difference between the initial tow-stitch angle ($2\Phi_A = \pi/2$), and the tow-stitch angle at a given displacement, $(\Phi_A + \omega_A)$, as shown in Eq. 4.1.

$$\theta_A = \frac{\pi}{2} - \left[\frac{\pi}{4} + atan\left(\frac{L_0}{L_0+\sqrt{2}D_A}\right)\right] \tag{4.1}$$

where, L_0 and D_A are the initial length of Region A (see Figure 4.8) and the displacement of the machine crosshead, respectively (see Appendix G for derivation). The **theoretical** engineering strain in the stitch direction during the PSS test, α_A, is calculated as a function of the displacement, see Eq.4.2; where, ω_A is the changing angle between the tow and the stitch directions with increasing machine crosshead displacement (see Appendix G for derivation).

$$\alpha_A = \left[\frac{1}{\sqrt{2}\,cos\,\omega_A} + \frac{D_A}{L_0 cos\,\omega_A}\right] - 1 \tag{4.2}$$

where,
$$\omega_A = \left(\frac{\pi}{4} - \theta_A\right) \tag{4.3}$$

The **experimental** engineering strain in the stitch direction during the PSS test, β_A, is calculated using Eq 4.4. L_1 is the stitch length measured using ImageJ [146] at a desired displacement. Subsequent comparison between Eq. 4.2 and 4.4 (see Section 4.4.3.1), reveals how closely the PSS specimen follows this ideal kinematic prediction.

$$\beta_A = \frac{L_1 - L_0}{L_0} \tag{4.4}$$

4.3.2. Sample Preparation and Testing

Four PSS specimens were prepared. All the tests were performed in the Zwick Z2 tensile testing machine using the same testing parameters as in the standard UBE and CBE tests. To induce well-defined kinematics, the lateral edges of the PSS specimen are clamped and fixed to linear bearings that allow travel only in the vertical direction (see Figure 4.9). The manual image processing technique (with ImageJ software [146]) was used to measure the shear angle and stitch strain as a function of the displacement during the test.

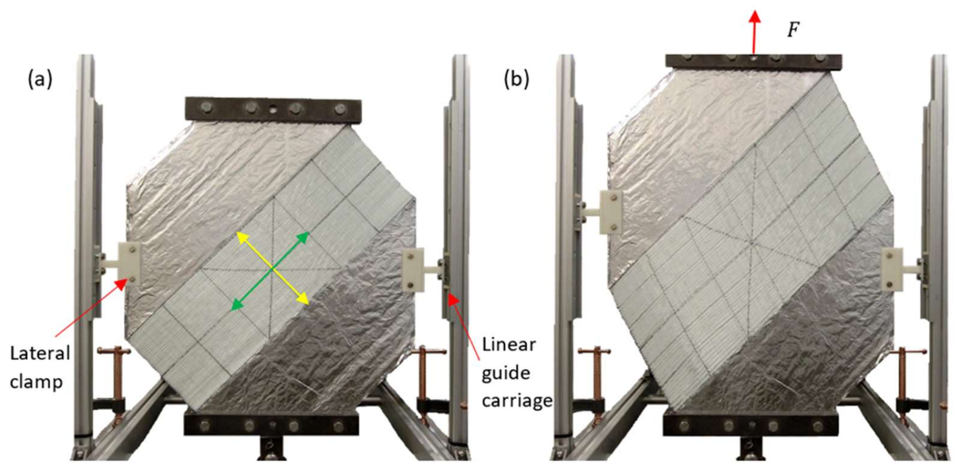

Figure 4.9: PSS specimen (a) undeformed (b) deformed, the yellow and green arrows indicate the initial chain-stitch direction and the tow direction, respectively

4.3.3. Results and Analysis

Figure 4.9b shows that the PSS sample has well-defined homogenous kinetics and looks suitable for analysis. As stated in Section 4.2.3, the CBE specimen generates in-plane bending of the tows. In contrast, the PSS specimen eliminates the contribution of in-plane bending (there is a contribution of in-plane bending in the stitch direction, but it is minimal compared to the other deformations). Therefore, the PSS specimen experiences only two low-energy deformation modes, i.e., shear and tensile strain in the stitch direction.

According to Figure 4.10a, the average shear angle curve of the PSS test closely follows the theoretically imposed kinematics. The theoretical shear angle of the PSS specimen was determined using Eq. 4.1. The PSS specimens show uniform deformation with a maximum shear angle of 15˚, due to the low initial angle between the stitches and axial force (45˚).

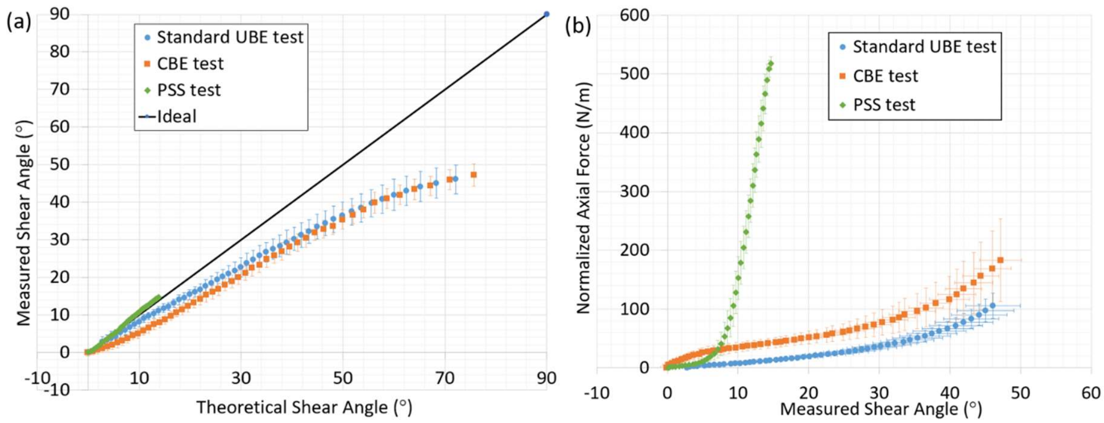

Figure 4.10: Comparison of standard UBE, CBE and PSS tests (a) measured vs theoretical shear angle curves (b) normalised axial force vs measured shear angle curves. The error bars indicate +/- 1SD of four specimens

A comparison of normalised force vs measured shear angle curves for the UBE, CBE and PSS tests is shown in Figure 4.10b. To normalise the force, the axial force of the PSS was divided by the effective length of the specimen in the tow direction (i.e. L_N (see Figure 4.8a). At low shear angles (less than 5˚), the normalised force of the PSS test follows the standard UBE test (see Figure 4.10b). Beyond the shear angle of 5˚, the curve shows a significant increase in the force. Initially, it was assumed that the increase in the force was due in part to possible friction in the linear bearings, consequently, one PSS test was performed without bearings. The results indicate that linear bearings have no effect of friction and without them, the reliability of the test is reduced (see Appendix H). The significant increase in normalised force can be attributed to the inherent behaviour of pure-UDNCF during the test.

4.4. Simple Shear (SS) Test

4.4.1. Theory

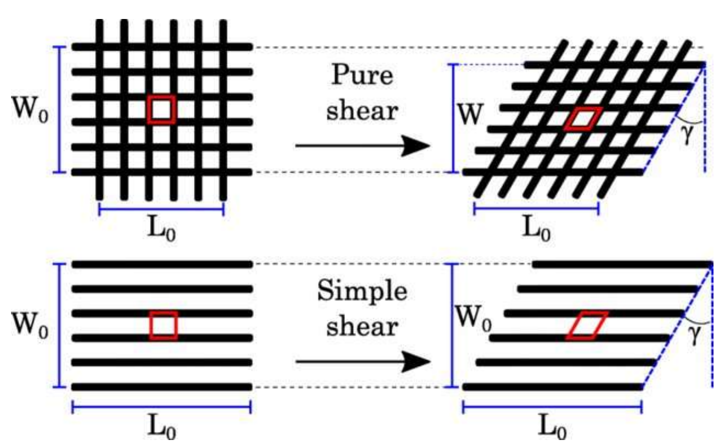

Figure 4.11: Comparison of pure and simple shear deformation of fabric reinforcements [55]

Fabric shear kinematics are classified into two types: pure and simple shear. Usually, pure shear is dominant in biaxial fabrics due to the presence of fibres in two perpendicular rigid directions allowing fibre rotation. Simple shear is dominant in unidirectional fabrics because the presence of fibres in one direction allows them to slip along the fibre axis (see Figure 4.11) [55] [118] [53]. The kinematics of pure-UDNCF used in this investigation are of two types, pure shear and tensile strain in the stitch direction. Simple shear is a mixed-mode deformation containing a combination of both. A new test method was developed to measure the simple shear of pure-UDNCF (referred to here as the 'SS' test) i.e., well-defined kinematics with different amounts of stitch strain. The SS test samples yet another region of the (shear angle) – (tensile stretching) parameter space and was designed by increasing the initial angle between the stitch and axial displacement direction to 90˚ (see Figure 4.12a). Specimens were laterally clamped with linear bearings, allowing only vertical movement. Care was taken as this test applies an undesirable but small torque on the load cell (in this case about 13.5Nm).

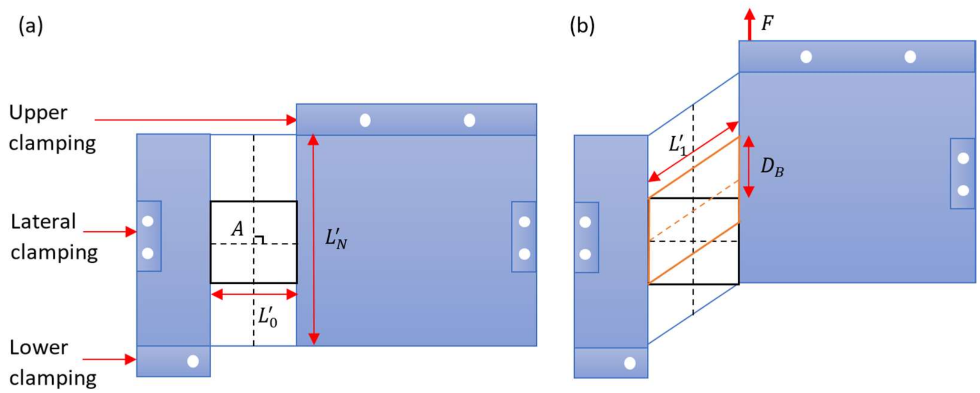

Figure 4.12: SS test specimen (a) Undeformed (b) Deformed, shape of central region A shifts from square (black) to parallelogram (orange)

Figure 4.12b depicts the dimensional changes caused by deformation during the SS specimen. The **theoretical** shear angle, θ_s, of the SS test can be derived as a function of the machine displacement, D_B, and the initial specimen length, L'_0, as shown in Eq. 4.5 (see Appendix I for derivation).

$$\theta_s = tan^{-1}\left(\frac{D_B}{L'_0}\right) \tag{4.5}$$

The **theoretica**l engineering strain in the stitch direction during the SS test, α_s, is calculated as a function of the displacement (see Appendix I for derivation).

$$\alpha_s = \frac{\left[\sqrt{(L'_0)^2 + D_B^2}\right] - L'_0}{L'_0} \tag{4.6}$$

The **experimental** engineering strain in the stitch direction during the SS test, β_s, is calculated using Eq. 4.7 where, L'_1 is the stitch length at a given displacement (see Figure 4.12b) measured using ImageJ [146].

$$\beta_s = \frac{L'_1 - L'_0}{L'_0} \tag{4.7}$$

As with the PSS test, a comparison between Eqs 4.6 and 4.7 in the SS test (see Section 4.4.3.1), reveals how closely the tests follow the ideal kinematic prediction (see Figure 4.14a).

4.4.2. Sample Preparation and Testing

Four SS test specimens were prepared based on the dimensions given in Figure 4.13a. All tests were performed on a Zwick Z2 tensile testing machine mounted with a 2kN load cell, using the same testing parameters as the standard UBE, CBE and PSS tests. The front of the experiments was captured using a digital camera for post-test analysis (similar to other shear tests, ImageJ [146] was used to measure the shear angle at a given displacement and stitch stretching). Figure 4.13b shows the deformed SS specimen.

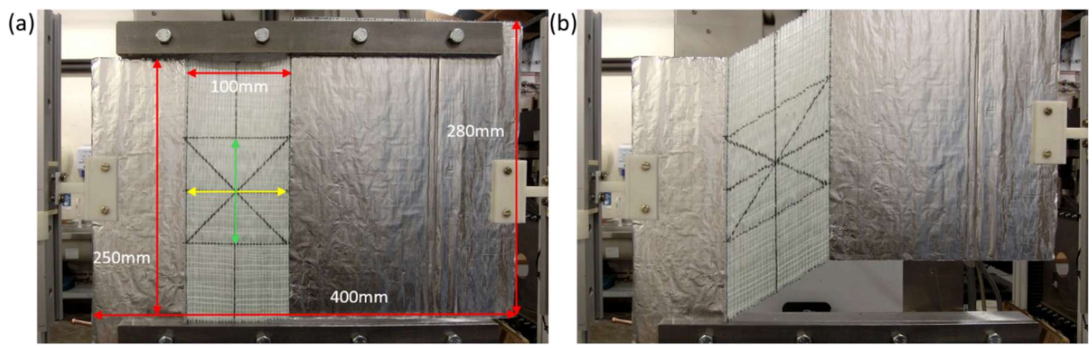

Figure 4.13: SS specimen (a) Undeformed, the yellow and green arrows indicate the initial chain-stitch direction and the tow direction, respectively (b) Deformed

4.4.3. Results and Analysis

The SS test was designed by increasing the initial angle between the stitch and axial displacement direction to 90˚. Both PSS and SS curves lie close to the ideal kinematic prediction (see Figure 4.14a) and the SS test achieves higher shear angles (≈45˚) than the PSS test (≈15˚) due to increasing the initial angle between the stitches and axial force to 90˚ (see Figure 4.15). Although the shapes of the specimens in both tests (PSS and SS) differ, the fabric orientation in the area of interest is similar, i.e. both ends of the chain stitches are constrained (bonded to Al) and both ends of the tows are unconstrained. The key difference between these two tests is the difference in the angles between tows and stitches relative to the direction of displacement. In the PSS test, both stitches and tows are oriented in the bias direction with respect to the direction of displacement (see Figure

4.15a). In contrast, chain stitches are oriented normal to the direction of displacement in the SS test, while the tows are oriented along the direction of displacement (see Figure 4.15b). Therefore, the SS test increases the amount of stitch strain while maintaining uniform deformation.

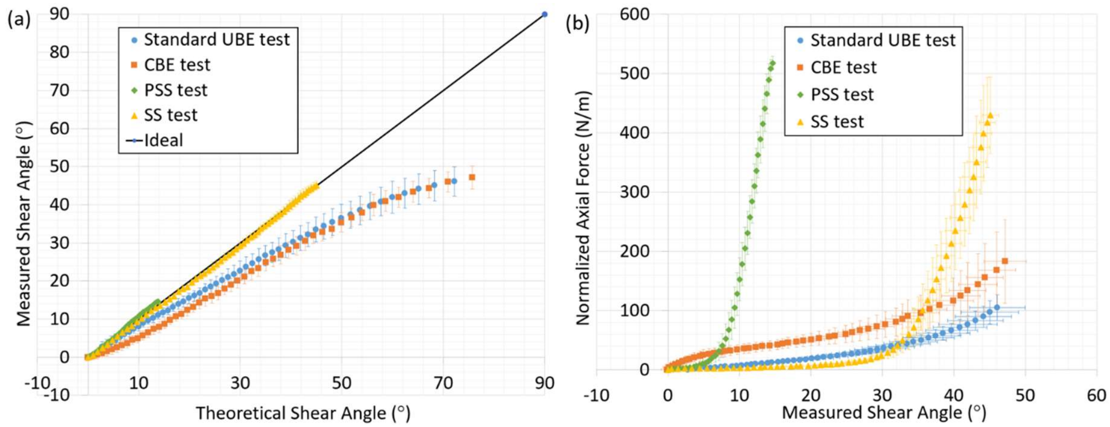

Figure 4.14: Comparison of UBE, CBE, PSS and SS tests (a) measured vs theoretical shear angle curves (b) normalised axial force vs measured shear angle curves. The error bars indicate +/- 1SD of four specimens.

In the SS test, the axial force is divided by the effective length of the specimen in the tow direction (i.e. L'_N, see Figure 4.12a). The average normalised axial force of the SS test is low up to a shear angle of 30˚, even lower than the UBE test (see Figure 4.14b). Although the standard UBE test has the least constraints, the normalised force is slightly higher than the SS test because it includes an extra contribution from Regions B1 and B2. Beyond a shear angle of 30˚, the SS test also shows a significant increase in the axial force, similar to the PSS test, indicating the inherent behaviour of the pure-UDNCF. In addition, the stitches have an in-plane bending contribution, similar to PSS specimens, but it is negligible. Consequently, the SS specimens also experience only two low-energy deformation modes i.e., shear and tensile strain in the stitch direction.

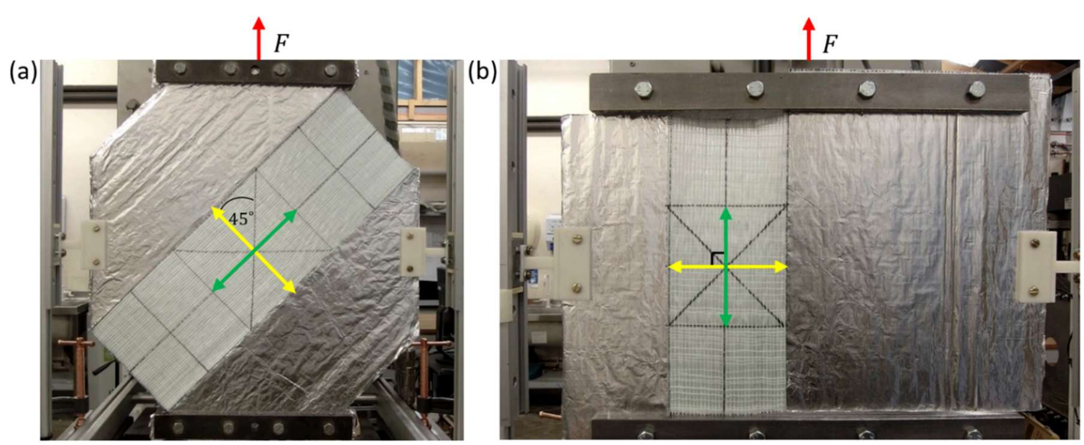

Figure 4.15: The directions of axial force (red arrow), the initial chain-stitch direction (yellow) and the tow (green) (a) PSS test (b) SS test

4.4.3.1. Stitch Strain Analysis

As shown in Figure 4.16a, values obtained from theoretical equations (for PSS Eqs.4.1 & 4.2 and SS Eqs.4.5 & 4.6) match closely with the measured strain in the stitch direction, demonstrating that the fabric kinematics of the PSS and SS tests are well-defined. Compared to the theoretical prediction, the experimental results are slightly lower for both tests at high shear angles, possibly due to stitch failure. Figure 4.16b shows the experimental stitch strain in Region A of each specimen vs measured shear angles. Both PSS and SS tests show much greater stretch in the stitch direction than the standard UBE and CBE tests.

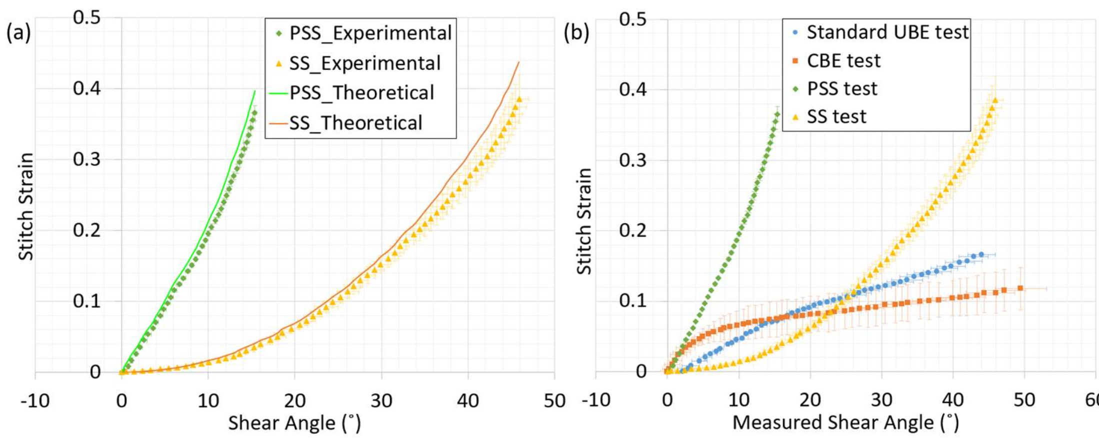

Figure 4.16: (a) Comparison of the average theoretical and experimental stitch strains in Region A of the PSS and SS specimens (b) experimental stitch strain in Region A vs measured shear angle curves in different shear tests. The error bars indicate +/- 1SD of four specimens.

4.5. Picture Frame Test with Pre-Stretching in Stitch Direction

Stretching in the stitch direction of pure-UDNCF is visible during the standard UBE test as two of the four sides of the specimen are clamped orthogonal to the bias direction. The clamping of the tows is only at one end, leaving the other end free. Because the stitches have only a small tensile stiffness, stretching in the stitch direction is possible. In contrast, in the PF test, all four sides are clamped orthogonal to the fibre direction, this prohibits stretching in the stitch direction and the fabric deforms by shearing (in addition to shear, the tightly-clamped PF test and other modified PF tests presented in Chapter 3 of the pure-UDNCF show notable in-plane bending of tows).

The idea behind the new characterisation tests discussed in this chapter (CBE, PSS and SS tests) is to explore a wider deformation space i.e., different combinations of shear and tensile strain in the stitch direction (with better control of in-plane bending). The PF test using pre-stretched pure-UDNCF specimens also aims to provide insights into unexplored areas of the deformation space. As concluded in Chapter 3, the combined (low- and high-pressure) G-clamped PF test method was used to perform the PF test with pre-stretching along the stitch direction (i.e., this clamping method reduces misalignment error in the PF test). The new modification involves stretching the fabric in the stitch direction to a given percentage strain, before inserting the specimen into the PF rig. Pre-stretching in the stitch direction applies tension to the stitches.

4.5.1. Samples Preparation

PF test was performed at three different stitch strain percentages i.e., 5%, 10%, and 20%. This section describes the method used to perform the PF test on a 10% pre-stretched fabric. First, a 30cm length of pure-UDNCF was cut along the stitching direction. The fibre was then stretched by 10% (the stitches were carefully stretched along a straight line, perpendicular to the tow directions until it reached 33 cm), and weights were placed around the extended fabric to maintain the stretch (see Figure 4.17).

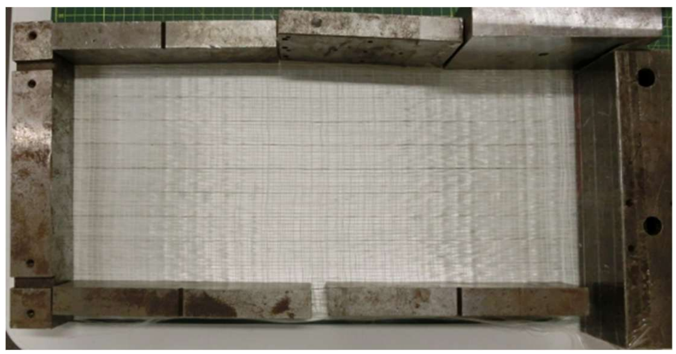

Figure 4.17: Placing weights to keep the stretched fabric within a specific stretch limit

The outer lines of the specimen were marked with the standard specimen template (the dimensions are given in Figure 2.16b). Figure 4.18 shows the fabric after marking the inner and outer lines of the specimen. The specimens were then cut along the outer lines using a rotary cutter.

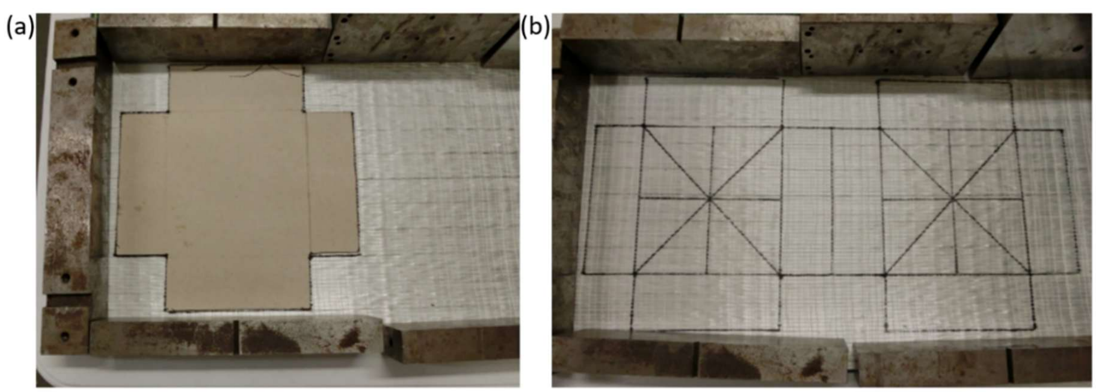

Figure 4.18: Marking outer lines (a) Marked specimen prior to cutting

Figure 4.19 shows how the specimen shrank or returned to its original position after releasing the pre-stretching of the fabric compared to the template.

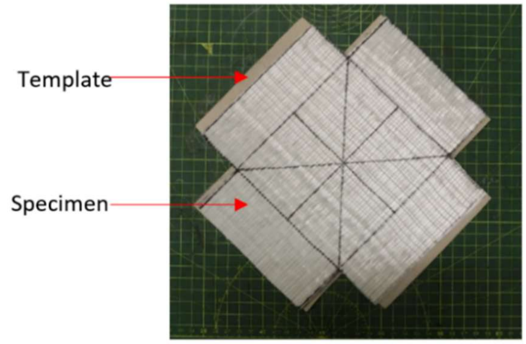

Figure 4.19: Comparison of dimensions of 10% pre-stretched PF specimen and the template

ImageJ [146] was used further to verify the stretching percentage of the specimen. First, a known length (200mm) was set as the global scale (see Figure 4.20a), and the length along the tow direction (134.8cm, see Figure 4.20b) and stitch direction (121.3mm, see Figure 4.20c) of the central region were measured. The difference between the two directions indicates a 10% shrinkage along the stitch direction.

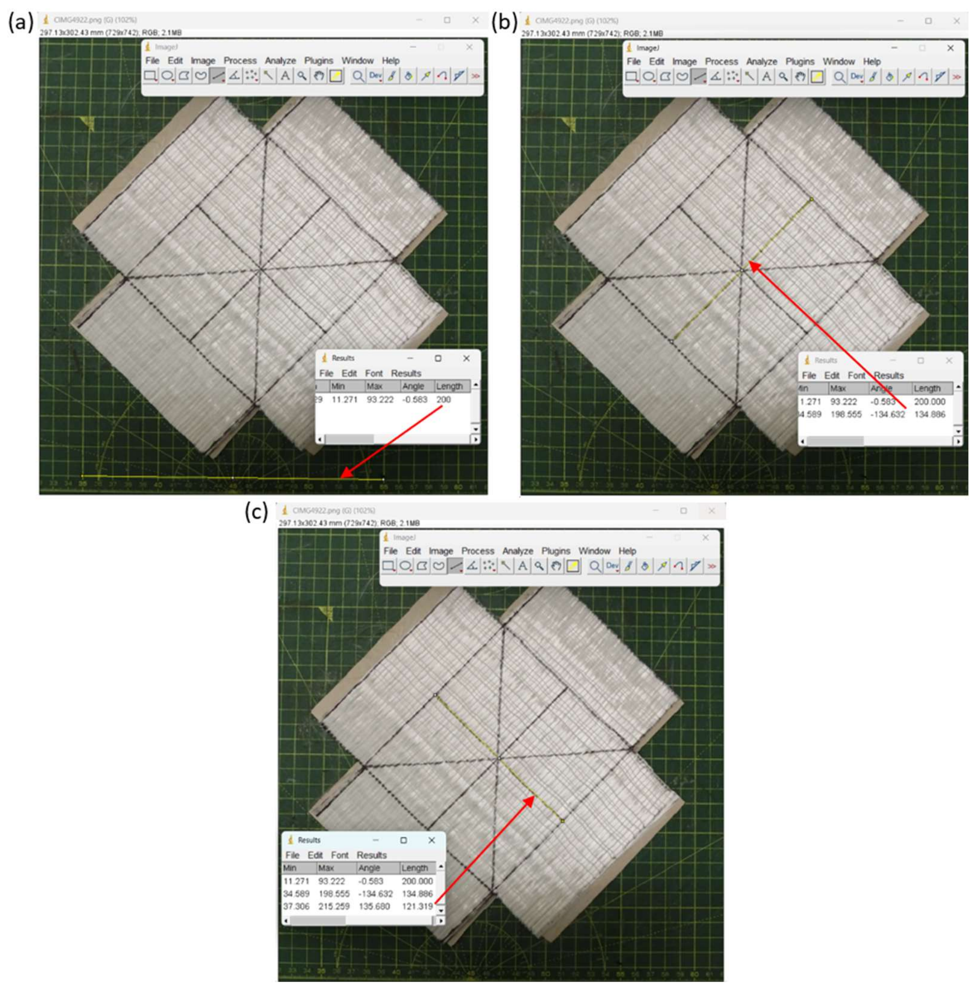

Figure 4.20: (a) Setting the scale (b) measuring the length of the region of interest along the tow direction (c) measuring the length of the region of interest along the stitch direction

4.5.2. Loading and Clamping the Specimens

Figure 4.21 shows a new template of the region of interest of the standard PF specimen (the central region). The new template ensures the specimen was stretched precisely when fixed to the PF rig (see Figure 4.22).

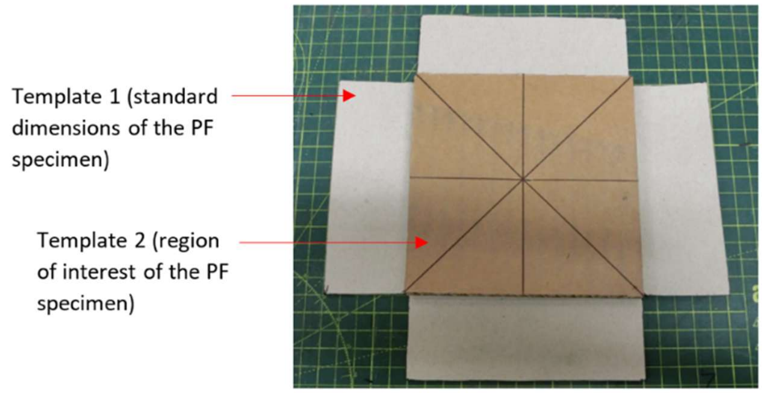

Figure 4.21: Template of the region of interest

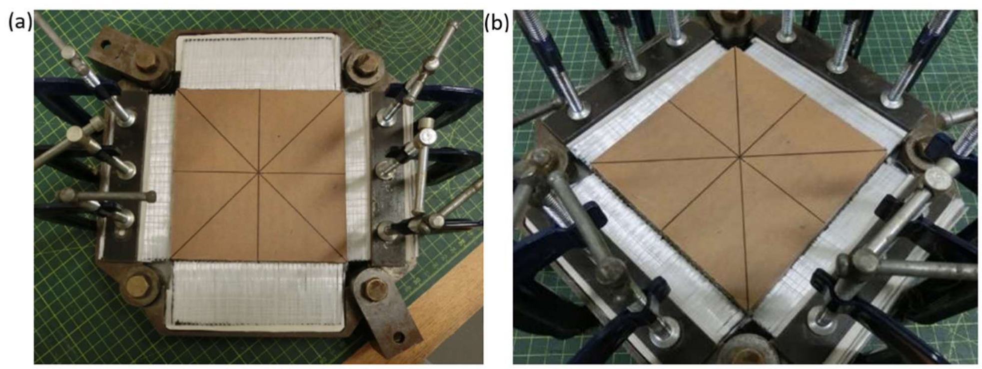

Figure 4.22: Ensuring that the specimen stretched precisely when mounting to the PF rig

Figure 4.23 shows the PF setup after being mounted to the tensile testing machine. ImageJ [146] was used further to verify the homogeneous stretching of the specimen (both tow and stitch directions show approximately the same length of 135mm, see Figure 4.24).

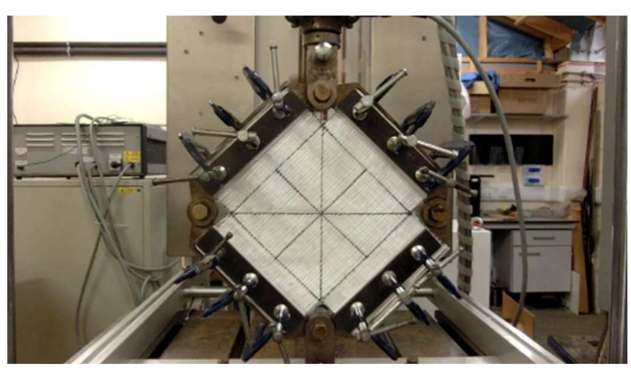

Figure 4.23: Picture frame test setup with 10% pre-stretched pure-UDNCF specimen

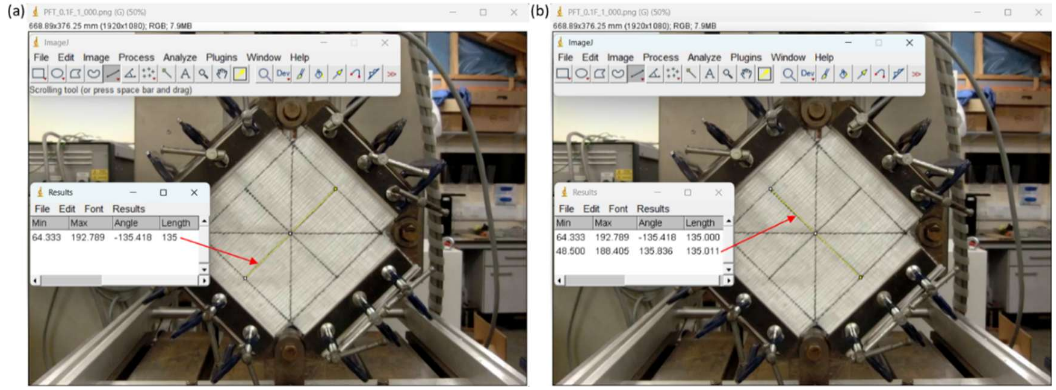

Figure 4.24: Measuring the length of the region of interest prior to performing the test (a) along the tow direction (b) along the stitch direction

4.5.3. Results and Analysis

Figure 4.25 compares all 'combined G-clamp' PF pre-stretched test results. As with the standard tightly-clamped and other modifications of the PF tests, the kinematics of all the pre-stretched PF test specimens lie close to the ideal prediction (indicating pin-joined net kinematics, see Figure 4.25a). Figure 4.25b compares normalised axial force vs measured shear angle curves of friction-modified combined G-clamp PF test (0% pre-stretched) and pre-stretched PF test specimens after setting the force of the machine to zero before performing the test. However, fabric pre-stretching adds an initial tensile force to the specimen (see Figure 4.26a), which is not recorded by the machine because it is performed manually. Therefore, using the tensile curve (see Figure 3.62), the initial tensile force of each pre-stretched specimen is calculated, i.e., for each pre-stretch, the normalised axial force of the tensile test is first multiplied by the side length of the tensile specimen to calculate the axial force. The axial force is then multiplied by cos 45 and divided by the side length of the PF rig to find the normalised initial force of the PF test.

Figure 4.26b compares normalised axial force vs measured shear angle curves of pre-stretched PF test specimens including pre-tensions. Due to the initial tensile force in the stitch direction, the axial force is higher in all the pre-stretched specimens compared to the 0% pre-stretched PF curve at low shear angles. PSS data also suggest either the tensile or shear stiffness of the specimen increases when sheared and stretched at the same time. Beyond the 25˚ shear angle, the force of 5% and 10% pre-stretched specimens is slightly reduced compared to the 0% pre-stretched specimen. The 20% pre-stretched average curve shows comparatively higher forces than 0% pre-stretched specimens at low shear angles, but at high shear angles, it approaches the 0% pre-stretched curve. The minor reduction of axial force in pre-stretched curves at high shear angles compared to the 0% pre-stretched curve could be due to less inter-tow friction or perhaps because of potential microstructural changes (such as damage in the stitches and tow waviness) induced by the pre-stretching of the specimens.

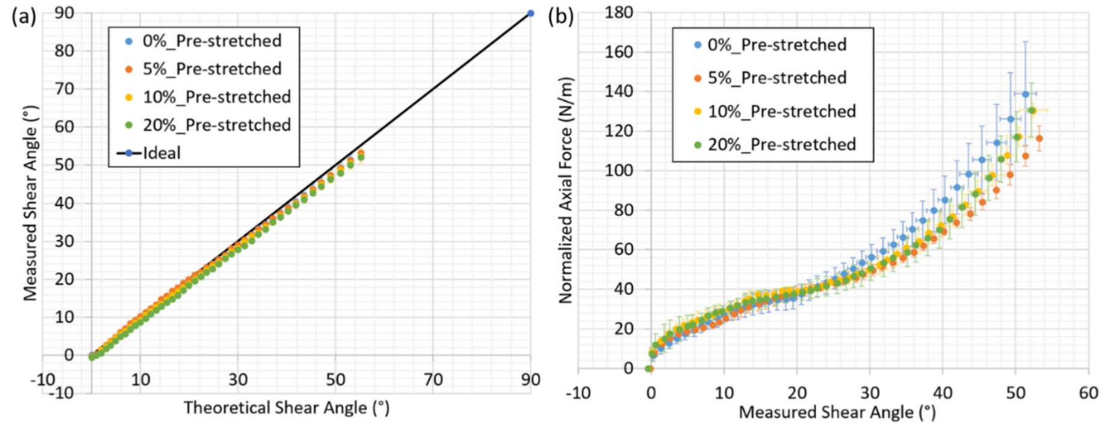

Figure 4.25: A comparison of 0%, 5%, 10% and 20% pre-stretched friction-modified PF tests (a) measured vs theoretical shear angle curves (b) normalised force vs measured shear angle curves. The error bars indicate +/- 1SD of four specimens.

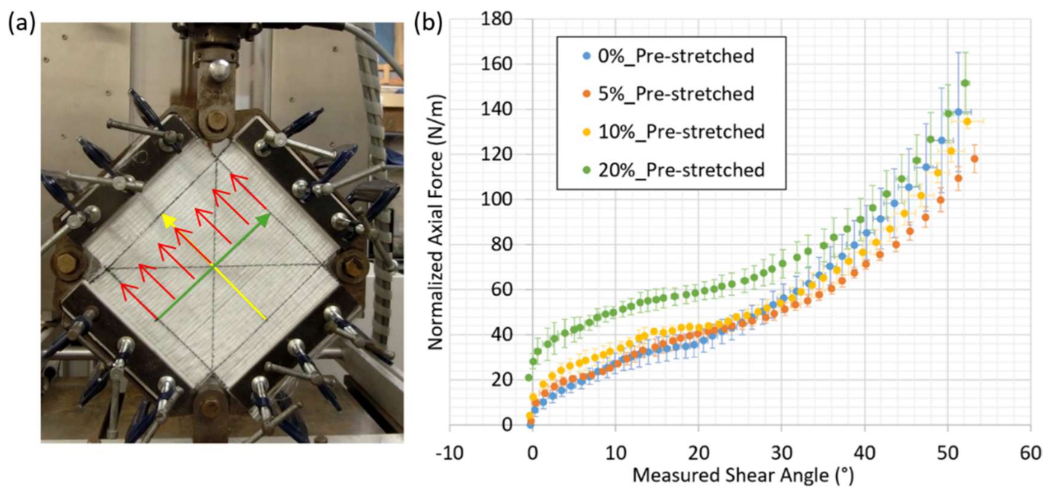

Figure 4.26: (a) A pre-stretched PF specimen, the yellow and green arrows indicate the initial chain-stitch & the tow directions, respectively. The red arrows indicate the direction of the initial force applied to stretch the fabric before shearing (b) normalised force vs measured shear angle curves of pre-stretched friction-modified PF tests including pre-tensions

As observed in the tightly-clamped PF test, the pre-stretched specimens also show pronounced in-plane bending at the end of the tows at high shear angles (see Figure 4.27). Pre-stretching the pure-UDNCF in the stitch direction may not significantly affect the in-plane bending force at low shear angles because the fabric is subjected to small deformations where the tows remain relatively aligned with minimal distortion. At high shear angles, the in-plane bending force is expected to decrease with increasing stitch stretching due to the reduction in the number of tows per unit length.

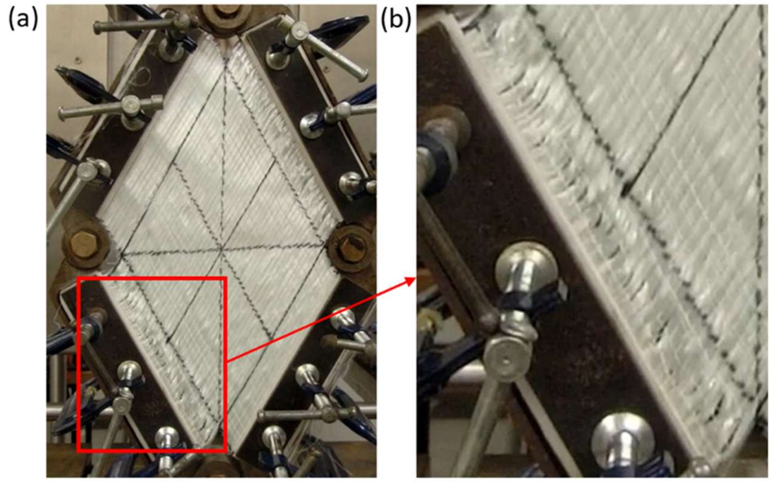

Figure 4.27: In-plane bending at the end of the tows of the pre-stretched PF test (a) G-clamped PF test specimen at 30˚of the shear angle (b) a magnified image of (a)

4.6. Summary of Force Results

According to all the experimental results discussed in Chapters 3 and 4, the standard UBE and CBE tests include three low-energy deformation modes i.e., shear, tensile strain in the stitch direction, and in-plane bending of tows, whereas the PSS and SS tests include only shear and stitch strain, and the PF test includes only shear and in-plane bending. Only the tensile test conducted in the stitch direction involves just one deformation mode, i.e., tensile stretching in the stitch direction. The 2D plot, such as normalised force vs measured shear angle, ignores tensile strain in the stitch direction. Therefore, all test results are plotted as 3D graphs (using MATLAB [222]) to illustrate them in the normalised axial force vs measured shear angle vs tensile strain in the stitch direction, parameter space (see Figure 4.28). The tensile test result lies along the YZ plane as there is no shearing during the test, while the 0% pre-stretched PF test (G-clamp combined curve) lies along the XZ plane as it does not generate stitch stretching. All the other test results are spread throughout the three-dimensional space (see Figure 4.28). The pre-stretched PF test curves (5%, 10%, and 20%) plotted in Figure 4.28 include the tensile force used to create that stretch, i.e., pre-tensions (see Figure 4.26b).

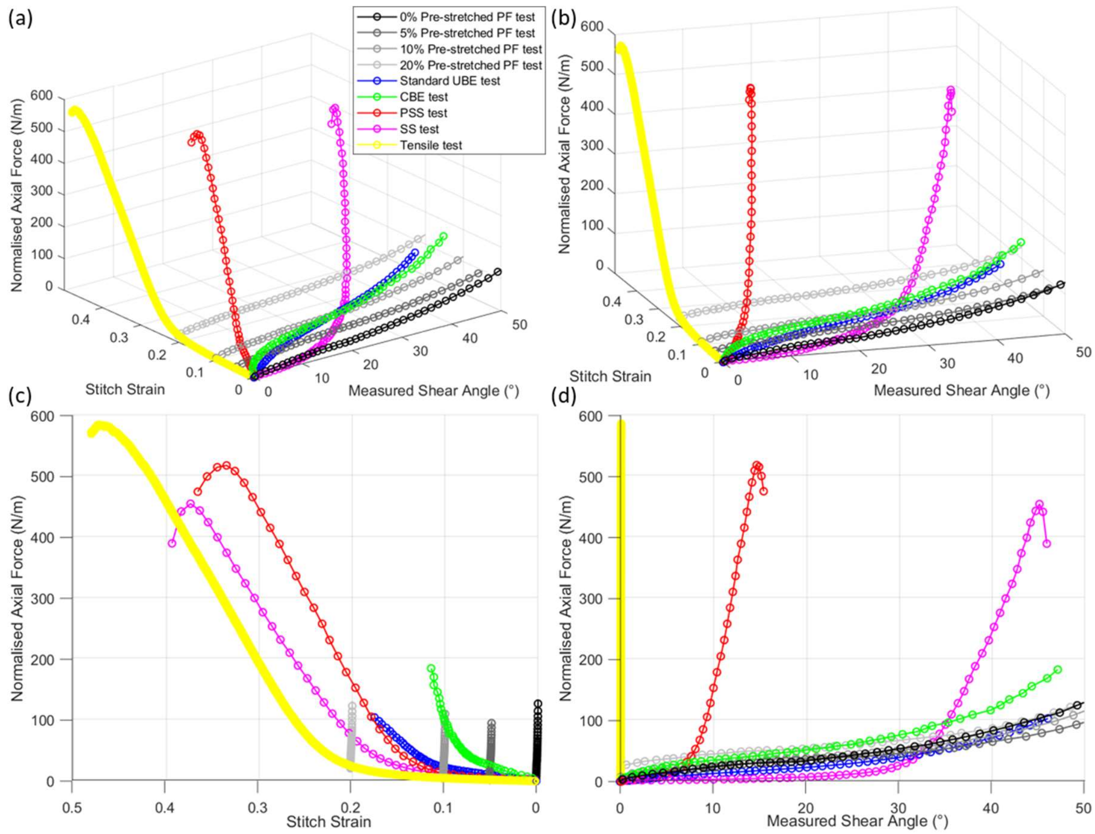

Figure 4.28: Normalised axial force vs measured shear angle and stitch strain from various shear and tensile testing data (a)&(b) The same 3D graph with different perspectives (c)&(d) 2D versions of the 3D graphs

It is worth noting that the tensile and PSS tests show a significant difference in stitch strains at a given force than the tensile and SS tests (see Figure 4.28c). This could be because the initial pre-stretching of the specimens is not considered, as the compliant nature of the fabric changes easily during handling. Section 4.7 further investigates the source of this error, i.e., pre-stretch in the stitch direction. Table 4.1 summarises all the experiments performed to characterise the pure-UDNCF based on kinematics. The test is classed as 'Well-defined' if the fabric deformation can be predicted accurately using analytical equations, it is ‘Homogeneous’ if the fabric shows the same deformation across the entire specimen, and its kinematics are considered to be 'Imposed kinematics' if the boundary conditions of the test impose the test kinematics (i.e., there is no adjustment of the kinematics to permit energy minimisation). The standard UBE test and the CBE tests are inhomogeneous and can be divided into four different areas (Regions A, B1, B2, and C) according to the nature of the deformation they experience during the test. Compared to the CBE test, the UBE test is poorly constrained and undergoes unusual deformations to minimise in-plane bending (such as out-of-plane bending in the B regions and no in-plane bending of the tows). Furthermore, neither specimen has imposed kinematics, consequently, the fabric is free to ‘choose’ kinematics associated with energy minimisation.

Table 4.1: Tests performed to characterise the pure-UDNCF and attributes of each test. The machine and the materials reference frames are shown in each figure by the red and yellow-green arrows system, respectively (yellow-stitch direction, green-tow direction)

Deformation of the specimen	Normalised axial force vs measured shear angle/ stitch strain curve	Well-defined	Homogeneous	Imposed kinematics
PF test (including different pre-stretching) 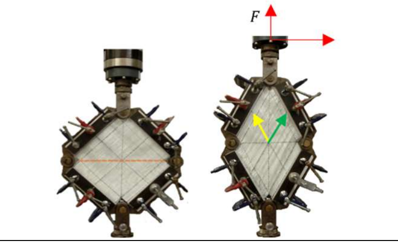	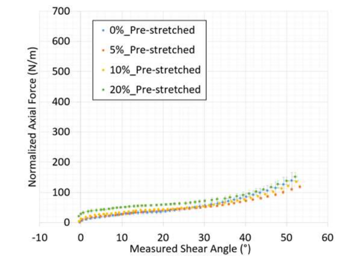	Yes	Yes (almost)	Yes
UBE test 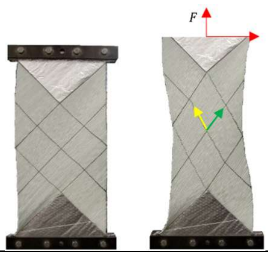	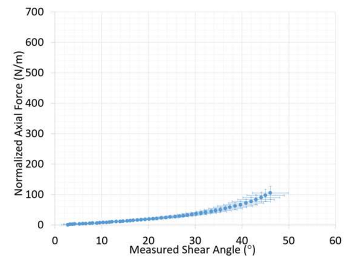	No	No	No
CBE test 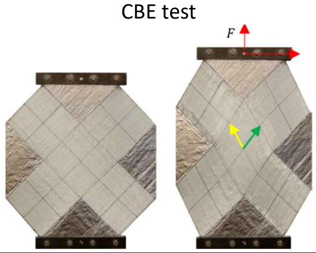	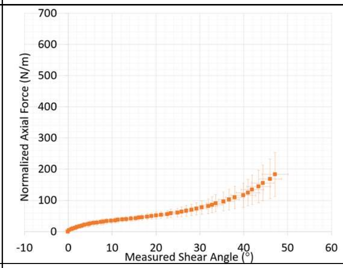	Yes	No	No
PSS test 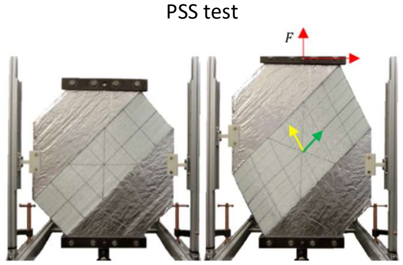	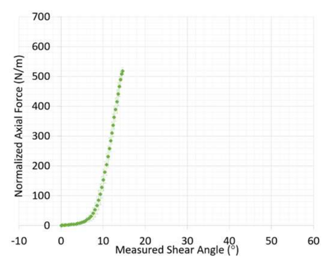	Yes	Yes	Yes
SS test 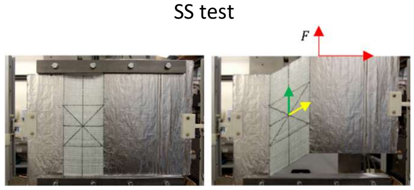	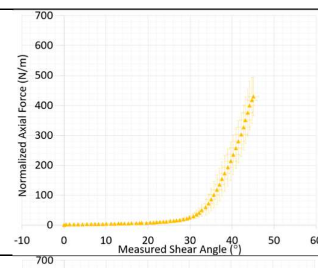	Yes	Yes	Yes
Tensile test 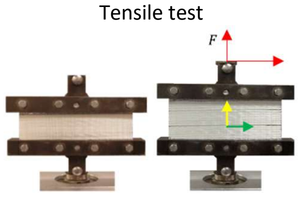	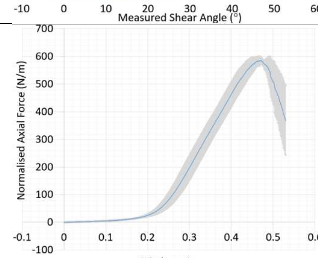	Yes	Yes	Yes

Detailed and reliable data obtained from the experiments showing well-defined and imposed kinematics, with homogeneous deformation across the specimen, can be used to develop constitutive models and simulations. Except for the standard UBE and CBE, the other tests can be used for further analysis (CBE will be useful in verifying numerical simulations. The standard UBE test is poorly constrained and is perhaps less useful for verifying numerical simulations, though it would be interesting to see if the unusual behaviour observed in this test is reproduced in simulations). As discussed, there are three potential contributions to the axial force, namely, shear, tensile stretching along the stitch direction and in-plane bending of the tows. Table 4.2 shows which of these potential contributions are present in the different tests. Only the tensile test in the stitch direction produces one contribution i.e., tensile stretching. The PSS and SS tests include two contributions i.e., tensile stretching in the stitch direction and shear. There is no contribution from the in-plane bending of the tows because they remain perfectly straight during the tests (see Table 4.1, forces due to in-plane bending of stitches are negligible). In the PF test, pure shear is imposed, however, close to the edges where the tows are clamped into the PF rig, there is a rapid change in the direction of the tows (the tows are bent in-plane). Therefore, in-plane bending contributes to the force measured in the PF test, though the size of this contribution depends to some extent on the boundary conditions applied (see Section 3.6). Note that in the literature, this contribution to the measured PF force is generally ignored.

Table 4.2: Tests performed to characterise the pure-UDNCF and the contribution of forces to the total axial force of each test

Test	Tensile stretching	Shear	In-plane bending
Tensile			
PSS			
SS			
PF			

Major Contribution   Negligible Contribution

4.7. Experimental Error in the New Tests

As shown in Figure 4.28c, pre-stretch in the stitch direction of the pure-UDNCF could significantly affect the experimental results of the new tests. The absence of stabilising fibres in the fabric may result in initial stretching during handling. This can cause significant variation in the outcome of each test, similar to the pre-shear angle error of the UBE test discussed in Section 2.5.2.1.

To determine the pre-stretching in the stitch direction of the specimens, it is necessary to define the number of tows per unit length for the undeformed material. Note that this method allows the correction of pre-stretching errors that may occur even with careful handling of the fabric, i.e., in cases where practical adjustments are not feasible during the experimental process, this approach can be employed to adjust the data, ensuring greater accuracy in the results. The initial state of the fabric was considered to be the condition after the fabric was cut from the roll and relaxed on a flat surface (with manual adjustments). Then the number of tows per 50mm width of fabric (tensile specimens had the shortest width of 50 mm of all the test specimens used to evaluate pure-UDNCF) was measured. Depending on the tow width, the number of tows per 50mm varied from 16 to 18 (see Figures 4.29 a and b). There is a significant difference between the widths of tows in the fabric at the same level (see Figure 4.29a, the widths of tows A and B are 2mm and 2.7mm, respectively) as well as the width change along the length of the individual tows (see Figure 4.29a, the width of the A tow varies from 2mm to 1.7mm and the width of the C tow varies from 2.5mm to 3mm). These differences may be caused by reasons such as tow compaction and tension variations during manufacturing, irregular distribution of glass fibres within the tow and variations in the stitch density (irregular stitch placement).

(a) (b)

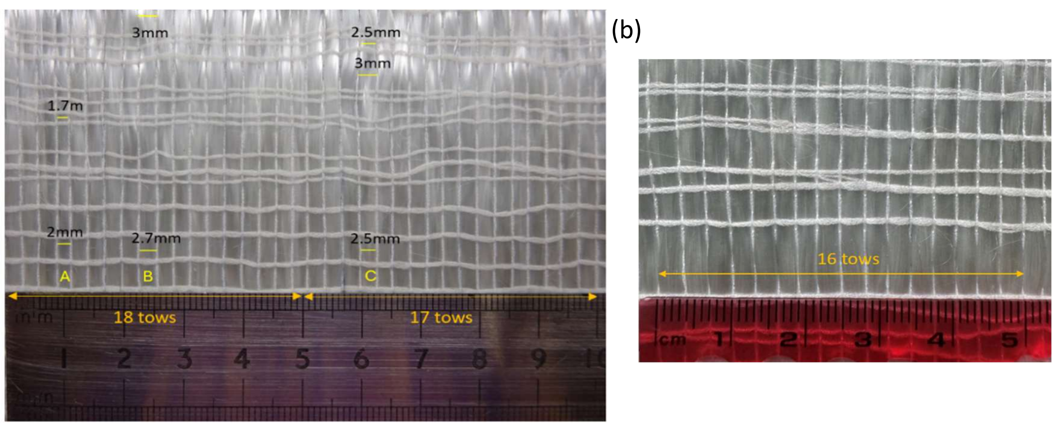

Figure 4.29: (a) and (b) Variations of the number of tows per 50mm width of fabric

To continue the analysis, 17 tows per 50mm stitch length was selected as the standard tow count in the initial state of the fabric, i.e., no pre-tension or pre-compression of the stitches. The tows in each tensile, PSS, SS and PF test specimens were then counted, and the results are summarised in Table 4.3.

Table 4.3: The number of tows per specimen to evaluate pre-stretching or -compression

<table>
<tr><th rowspan="3">Test</th><th colspan="6">Number of tows</th><th rowspan="3">The stitch length of the sample (mm)</th><th rowspan="3">Average number of tows to be in the sample</th><th colspan="3">Pre-tension (+) or compression (-) % (99% confidence level)</th></tr>
<tr><th colspan="4">Specimen</th><th rowspan="2">Avg.</th><th rowspan="2">Standard error</th><th rowspan="2">Lower margin</th><th rowspan="2">Average</th><th rowspan="2">Upper margin</th></tr>
<tr><th>1</th><th>2</th><th>3</th><th>4</th></tr>
<tr><td>Tensile test</td><td>17</td><td>16</td><td>17</td><td>18</td><td>17.0</td><td>0.41</td><td>50</td><td>17.0</td><td>-1.1</td><td>0.0</td><td>1.1</td></tr>
<tr><td>PSS test</td><td>43</td><td>43</td><td>46</td><td>45</td><td>44.3</td><td>0.75</td><td>141.4</td><td>48.1</td><td>6.0</td><td>8.0</td><td>9.9</td></tr>
<tr><td>SS test</td><td>31</td><td>32</td><td>32</td><td>33</td><td>32.0</td><td>0.41</td><td>100</td><td>34.0</td><td>4.8</td><td>5.9</td><td>6.9</td></tr>
<tr><td>0% pre-stretched PF test</td><td>43</td><td>45</td><td>46</td><td>47</td><td>45.3</td><td>0.85</td><td rowspan="4">135</td><td>45.9</td><td>-0.8</td><td>1.4</td><td>3.6</td></tr>
<tr><td>5% pre-stretched PF test</td><td>40</td><td>41</td><td>40</td><td>42</td><td>40.8</td><td>0.48</td><td>43.6</td><td>5.3</td><td>6.5</td><td>7.8</td></tr>
<tr><td>10% pre-stretched PF test</td><td>38</td><td>40</td><td>40</td><td>39</td><td>39.3</td><td>0.48</td><td>41.3</td><td>3.8</td><td>5.0</td><td>6.2</td></tr>
<tr><td>20% pre-stretched PF test</td><td>38</td><td>37</td><td>39</td><td>37</td><td>37.8</td><td>0.48</td><td>36.7</td><td>-4.0</td><td>-2.8</td><td>-1.6</td></tr>
</table>

According to the calculations, the initial number of tows in the sample defines whether it is in pre-tension or pre-compression. The average number of tows in the tensile specimens is equal to the standard tow count of the fabric i.e., 17 tows per 50mm stitch length, indicating that the tensile specimens were relaxed prior to testing (see Table 4.3). In contrast, PSS and SS specimens show approximately 8% and 6% pre-tensions, respectively. In addition, pre-stretched PF specimens show different levels of pre-stretching than the previous percentages, i.e., 0, 5, 10, and 20. The modified pre-stretched percentages are as follows (note that only 20% of the pre-stretched PF test specimens show pre-compression compared to the expected level):

- 0% pre-stretched PF test ----------------> 1% pre-stretched PF test
- 5% pre-stretched PF test ----------------> 12% pre-stretched PF test
- 10% pre-stretched PF test----------------> 15% pre-stretched PF test
- 20% pre-stretched PF test----------------> 17% pre-stretched PF test

The fabric pre-stretching adds an initial tensile force to the specimen, which is not recorded by the machine. Therefore, using the tensile curve, the initial tensile force of each pre-stretched specimen is calculated i.e., first, the normalised axial force related to each pre-stretching was determined by the tensile test and then multiplied by the side length of the tensile specimen to calculate the axial force. The axial force is then multiplied by cos 45 (only for PSS and pre-stretched PF tests because the stitch direction in these specimens is at 45˚ to the applied force) and divided by the effective length of the specimen in the tow direction to find the normalised initial force of the test. Note that the pre-tensions included in the pre-stretched friction-modified PF tests (see Figure 4.26) were further modified with this method to find the precise pre-tension in each specimen. Corrected test results are plotted as 3D graphs (see Figure 4.30). The standard error was calculated to both stitch strain and normalised force. The normalised force changes slightly in response to pre-stretching. Therefore, the error bars in the force direction are not visible on the graphs. When pre-stretching in the stitch direction is considered, the gap between the tensile, PSS, and SS graphs narrows significantly (see Figure 4.28c and 4.30c). The new PSS and SS curves fall within the stitch strain error bars of the tensile test, indicating improved data accuracy (see Figure 4.30c). Based on the overall results, it can be concluded that the novel tests developed to characterise pure-UDNCF are highly sensitive for pre-stretching in the stitch direction.

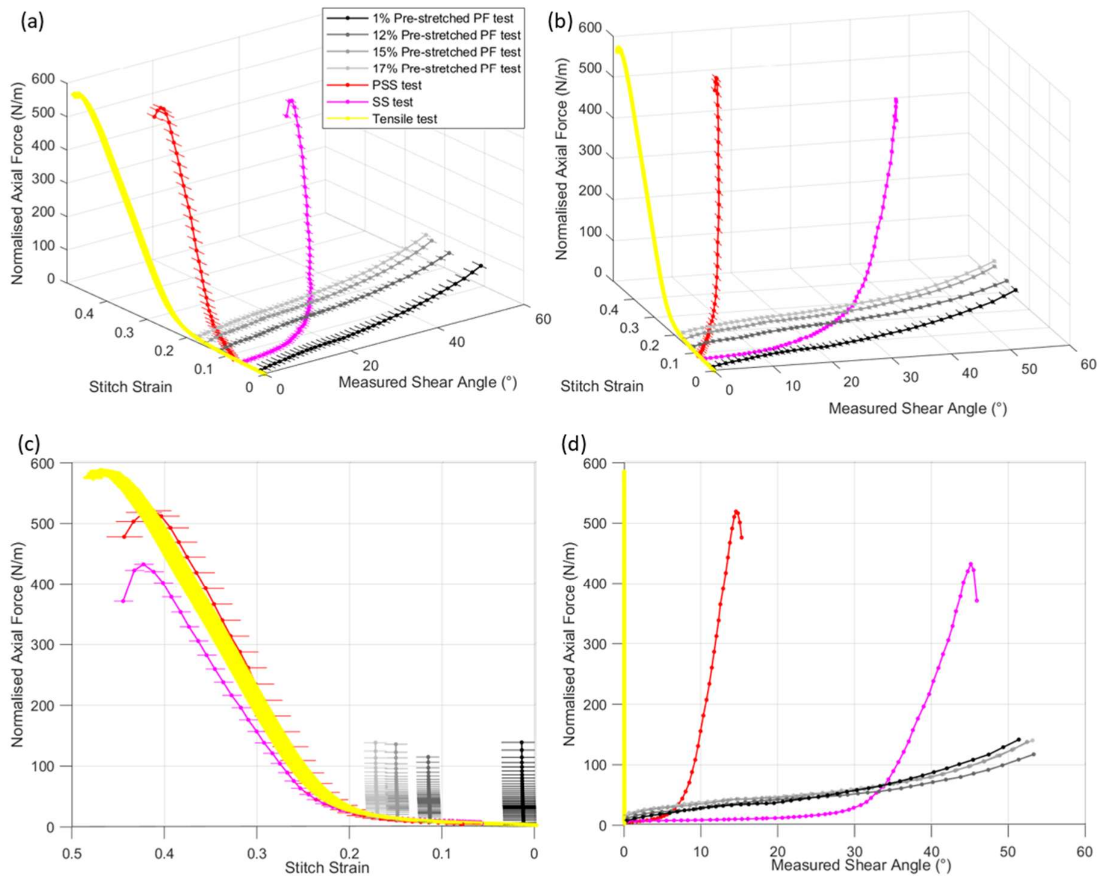

Figure 4.30: Normalised axial force vs. measured shear angle and stitch strain from tensile PSS, SS and PF testing data including pre-stretching in the stitch direction. (a)&(b) The same 3D graph is shown from different perspectives (c)&(d) 2D versions of the 3D graphs. The error bars indicate the standard error of the mean.

It is interesting to note that for a given tensile strain in the stitch direction (but different amounts of fabric shear), the PSS axial force measurement is significantly higher than the SS axial force measurement (see Figure 4.30c). This suggests either that shearing the fabric has the effect of increasing its tensile stiffness in the direction of the stitches or that stretching in the stitch direction has the effect of increasing the shear stiffness of the fabric. Note however that as the stitch direction is not aligned with the axial direction in both the PSS and SS tests, this decreases the contribution of force due to stretching of the fabric in the stitch direction, to the axial force measurement. This may explain why the SS axial force measurement is smaller than the PSS axial force measurement. Figure 4.31 compares the deformation of PSS and SS specimens. When axial displacement is imposed, the stitches in both specimens begin to stretch and shear. Note that during the deformation of both the PSS and SS specimens, the tow direction remains constant and only the stitches simultaneously stretch and shear (Figures 4.31 b&d). The stitch directions of the PSS and SS specimens are initially orientated at 45˚ and 90˚, respectively, relative to the direction of the applied axial displacement (see Figures 4.31 a&c). In terms of imposed kinematics, the PSS test is more likely to stretch in the stitch direction than shear, whereas the SS test is more likely to shear than stretch (i.e., due to the boundary conditions).

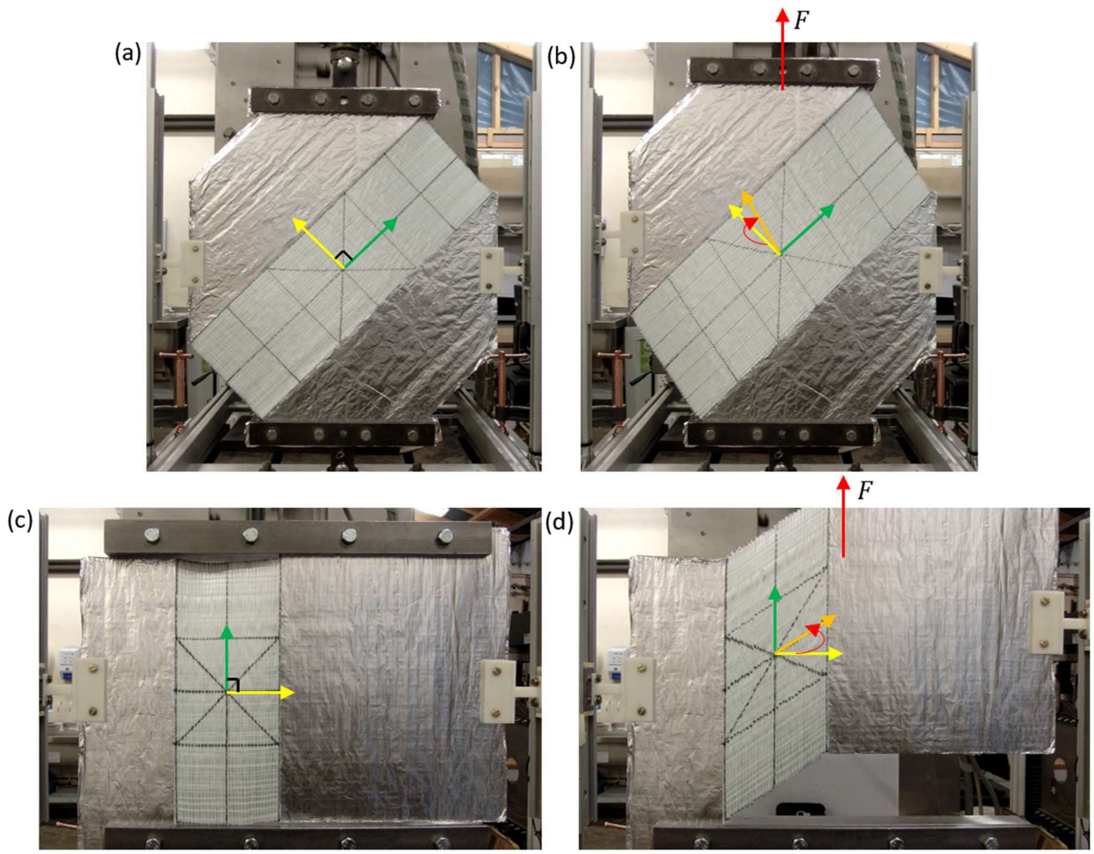

Figure 4.31: Comparison of deformation of two shear specimens (a) undeformed PSS (b) deformed PSS (c) undeformed SS (d) deformed SS, the yellow and green arrows indicate the initial chain-stitch direction and the tow direction, respectively. The orange arrow indicates the change in stitch direction due to the axial displacement

Returning to the force contributions in Table 4.2, the next step is to use the four experimental results i.e., tensile, PSS, SS, and PF tests to isolate the contribution of tensile stretching, shear, and in-plane bending to the total axial force in these tests. Section 4.8 discusses attempts to isolate the three contributions.

4.8. Isolating the Tensile, Shear and In-Plane Bending Contributions

The various tests measure different aspects of the mechanical behaviour of the fabric, as shown in Table 4.2. The challenge is to isolate the separate contributions to the measured axial machine force and estimate the behaviour of each of the various stiffnesses, as a function of both shear angle and tensile stretching in the stitch direction. Sections 4.8.1 and 4.8.2 describe different attempts to do this.

4.8.1. Power-Based Approach to Isolating the Shear Force in the PSS and SS Tests

A first attempt was made to isolate the shear signal by subtracting the known tensile test data from the PSS and SS test results (these two tests were chosen as they have no contribution to the measured axial force from the in-plane bending of the tows). To do this, a power-based approach was used to isolate the contributions to the measured axial force, due to shear and stretching in the stitch direction. This involved a rather lengthy derivation of the displacement rate in the stitch direction, as a function of the displacement rate of the machine crosshead for both the PSS (see Appendix J) and SS tests (see Appendix K). Figure 4.32 shows the theoretical and experimental (displacement rate in the stitch direction, $\dot{\mathrm{D}}_{\mathrm{S}}$)/(displacement rate of the machine crosshead, $\dot{\mathrm{D}}$) vs shear angle curves of both the PSS and SS tests. A ratio of less than one for the displacement rate in the stitch direction compared to the machine crosshead displacement rate means that the stitches are not stretching as much as the overall specimen is being displaced, which is to be expected. The initial ratio of experimental $(\dot{D}_S/\dot{D})$ values for both the PSS and SS tests provide insight into how the specimens behave at the beginning of the test. In the PSS test, the initial ratio of 0.7 indicates that the displacement rate in the stitch direction is 70% of the displacement rate of the machine crosshead. This suggests that much of the displacement of the machine is accommodated by stretching of the stitches. In the SS test, an initial ratio close to zero indicates that almost none of the displacement of the machine is initially accommodated by stretching of the stitches. In the SS test, the theoretical and experimental curves lay close to each other, though there is a drop in the experimental data relative to the theoretical prediction at high shear angles, probably due to the failures of stitches. In the PSS test, the experimental data is up to 8% lower than the theoretical prediction even at low shear angles. The reason for this discrepancy is unclear, however, it could be related to specimen sagging, visible in Figure 4.33. When the fabric is not perfectly flat at the beginning of the test, it may take some time to straighten or flatten before stretching. Hence, the experimental displacement rate in the stitch direction may be lower than predicted.

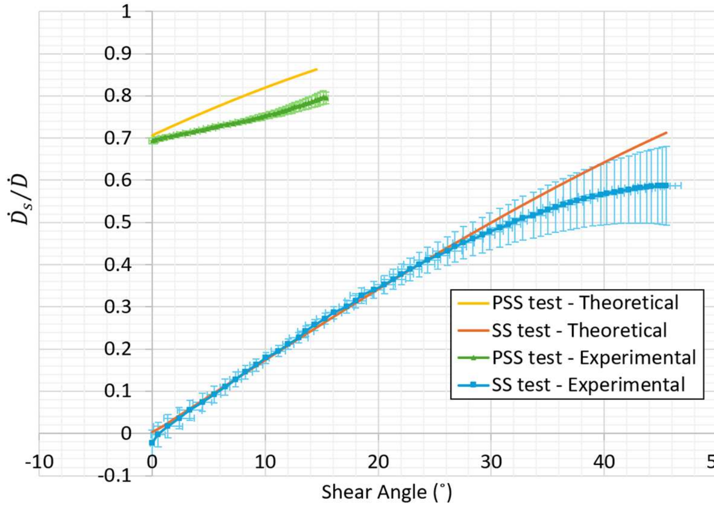

Figure 4.32: Comparison of theoretical and experimental ($\dot{D}_s/\dot{D}$) vs shear angle curves of PSS and SS tests

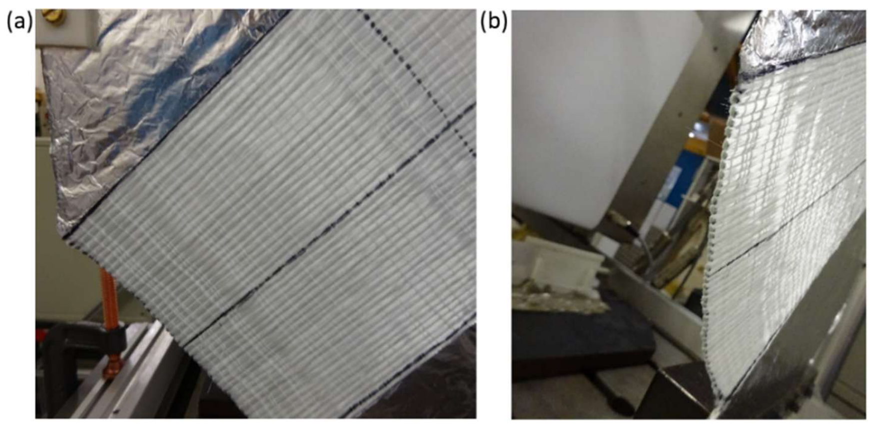

Figure 4.33: Sagging of the PSS specimen (a) front view (b) side view

An assumption in this analysis is that the normalised tensile force versus strain in the stitch direction, as measured in the tensile test (see Section 3.10), is unaffected by fabric shear. However, this approach provided limited success, resulting in unrealistic predictions of fabric shear force contributions at high shear angles (i.e., beyond a measured shear angle of 20˚ the specimens show significant deviations, either very high or negative in some cases), see for example Figure 4.34. This suggests that either: (a) the tensile force of the fabric along the stitch direction is a function of both strain in the stitch direction and fabric shear, or (b) spurious results may have been due to variability in the test data, or (c) some combination of both (a) and (b) is true. As mentioned already, judging by the results shown in Figure 4.30, point (a) seems likely. Concerning point (b), it is worth noting that at high tensile strains in the stitch direction, the force measured in the PSS and SS tests is likely to be dominated by the energy contribution from stitch stretching, as the contribution from fabric shear is relatively small. Consequently, any variability of the tensile test data makes it very difficult to extract the relatively small shear signal from the PSS and SS test results, this mismatch between the size of the two signals (tensile and shear) is quite likely to produce spurious data, making the process of subtracting the tensile signal from the total signal, very prone to error.

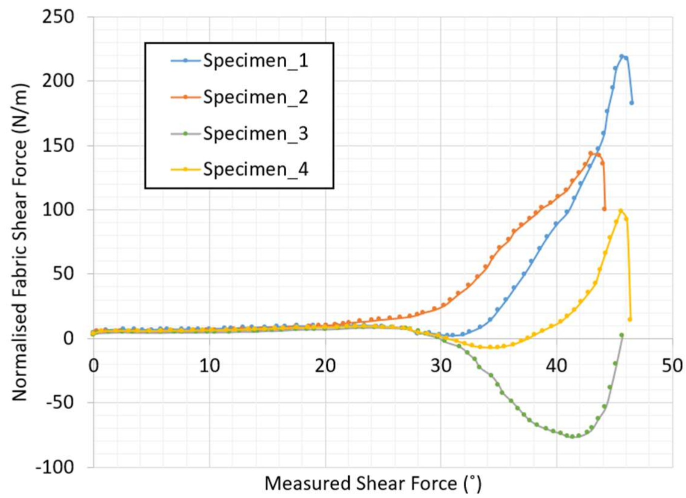

Figure 4.34: Normalised fabric shear force vs measured shear angle curves of SS specimens

4.8.2. Intuitive Approach to Isolating the Tensile, Shear & In-Plane Bending Forces

A second method to isolate the three force contributions is to use an intuitive approach; making reasonable estimates of the likely shear, stitch tensile and in-plane bending contributions to the axial force measured in the experiments, and then evaluating these estimates based on: (i) expected behaviour and (ii) their predictive capacity. For completeness, two different attempts to do this are discussed in detail in the following sections, and the second attempt (Section 4.8.2.2) proved successful results.

4.8.2.1. First Estimate: Assuming No Coupling Between Stitch Tensile and Fabric Shear

The approach of estimating the material behaviour requires understanding how each force (shear & tensile load in the stitch direction, and in-plane bending) acts along the axial direction. In the following discussion, the term 'material system' refers to the local non-orthogonal reference frame of the material, with one basis pointed along the tow direction and the other along the stitch direction. The 'machine system' refers to the reference frame of the machine (orthogonal) with one basis directed along the axial travel direction (the figures in Table 4.1 show the material and machine systems of each test). For this first estimate, a polynomial surface was created from the tensile test data (see Figure 4.35), assuming no coupling between tensile stiffness and shear i.e., the 2D curve of tensile experimental data (yellow dots shown in Figure 4.35) extends as a constant surface along the measured shear angle direction. Note the use of the term 'inherent' in the graph. This is meant to infer that this is the contribution of an isolated deformation mode, in this case, tensile stretching in the stitch direction, as measured in the 'material' system. This can then be normalised and expressed in the axial direction to determine the 'inherent normalised axial force'.

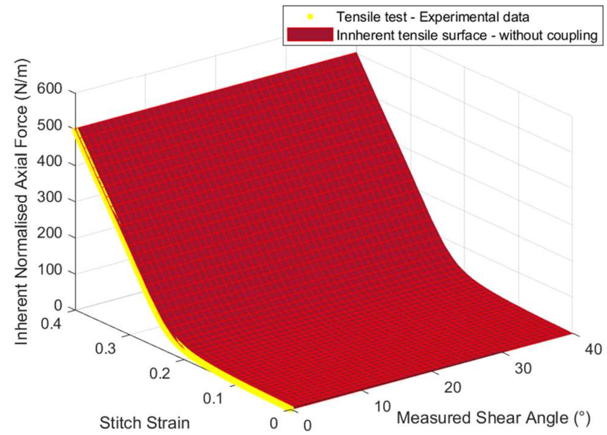

Figure 4.35: Inherent tensile surface without coupling

Using this estimate of the inherent tensile data, $F_{t\theta}$, the component of the stitch tensile force acting along the machine axial loading direction for the two tests: (i) SS (Eq. 4.9), and (ii) PSS (Eq. 4.14) was calculated and then subtracted from the measured (normalised) axial force data for each test, to obtain the shear contribution to the measured axial force (Eq. 4.11 for the SS test and Eq. 4.16 for the PSS test). The normalised axial force due to shear was then transformed back to the material system (Eq. 4.12 for the SS test and Eq. 4.18 for the PSS test).

Analysis of the SS Test

In the SS test, the material shear direction acts co-linear with the axial loading direction of the machine throughout the test, while the stitch tensile load direction acts at a changing angle, ω_A, to the axial loading direction of the machine (see Table 4.1).

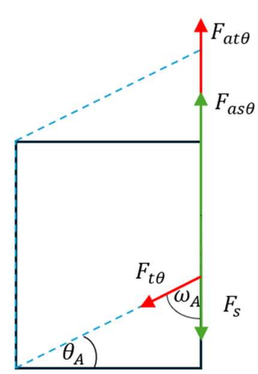

Figure 4.36: Forces acting on the SS specimen during deformation

According to Figure 4.36,

$$\omega_A = \frac{\pi}{2} - \theta_A \tag{4.8}$$

$$F_{at\theta} = F_{t\theta} \cos\left(\frac{\pi}{2} - \theta_A\right) \tag{4.9}$$

where, $F_{at\theta}$ is the axial force due to tension along the stitch direction, at a given shear angle θ_A measured in the axial loading direction of the machine and $F_{t\theta}$ is the tensile force per unit length measured in the stitch direction and is given by the polynomial shown in Figure 4.35. The total axial machine force per unit length measured in the SS test is,

$$F_{at\theta} + F_{as\theta} = \underbrace{F_{t\theta} \cos\left(\frac{\pi}{2} - \theta_A\right)}_{\text{Measured data (normalised axial force of SS test)}} + F_s \tag{4.10}$$

where for the SS test, $$F_s = F_{as\theta} \tag{4.11}$$

Here, $F_{as\theta}$ is the axial machine force attributable to fabric shear and F_s is the material shear force per unit length acting along the tow direction. Thus,

$$F_s = F_{at\theta} + F_{as\theta} - F_{t\theta} \cos\left(\frac{\pi}{2} - \theta_A\right) \tag{4.12}$$

Analysis of the PSS Test

In the PSS test, neither the material shear direction along the tows nor the tensile stretching along the stitch direction are oriented co-linear with the axial loading direction of the machine, and so both the relevant force components acting in the axial loading direction of the machine must be determined.

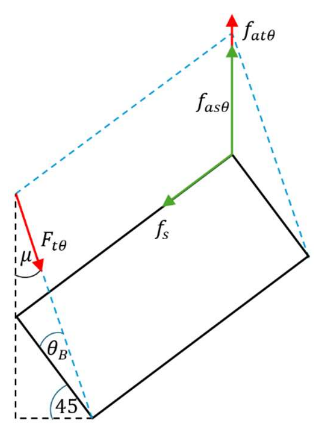

Figure 4.37: The forces acting on the PSS specimen during deformation

According to Figure 4.37,

$$\mu = \frac{\pi}{4} - \theta_B \tag{4.13}$$

$$f_{at\theta} = F_{t\theta} \cos\left(\frac{\pi}{4} - \theta_B\right) \tag{4.14}$$

Here μ is the angle between the axial loading direction of the machine and the stitch direction, $f_{at\theta}$ is the force due to tension in the stitch direction, acting along the axial loading direction of the machine at a given shear angle θ_B, and $F_{t\theta}$ is the tensile force per unit length acting along the stitch direction and is given by the polynomial shown in Figure 4.35.

The direction of the shear force due to fabric shear does not change during the test. For the PSS test,

$$f_{as\theta} = f_s \cos(\frac{\pi}{4}) \tag{4.15}$$

Therefore,

$$f_s = \sqrt{2} f_{as\theta} \tag{4.16}$$

The total axial machine force per unit length measured in the PSS test is,

$$f_{at\theta} + f_{as\theta} = \underbrace{F_{t\theta} \cos\left(\frac{\pi}{4} - \theta_B\right)}_{\text{Measured data (normalised axial force of PSS test)}} + \frac{f_s}{\sqrt{2}} \tag{4.17}$$

where, $f_{as\theta}$ is the force acting along the axial loading direction of the machine due to fabric shear and f_s is the shear force per unit length acting along the tow direction. Thus,

$$f_s = \sqrt{2}\left(f_{at\theta} + f_{as\theta} - F_{t\theta} \cos\left[\frac{\pi}{4} - \theta_B\right]\right) \tag{4.18}$$

Figure 4.38 compares projected normalised axial force due to stretching in the stitch direction ($F_{at\theta}$ and $f_{at\theta}$ for the SS and the PSS tests, respectively) vs shear angle curves of the SS and the PSS tests. The PSS test shows higher normalised axial tensile forces than the SS test at a given shear angle, demonstrating that the tensile stiffness in the stitch direction of pure-UDNCF is higher during the PSS test than the SS test. When the total normalised axial forces of the two tests are compared (Figure 4.30d), the PSS test shows a higher normalised axial force than the SS test. These findings indicate that the PSS test has a larger tensile contribution to the axial force than the SS test at a given shear angle.

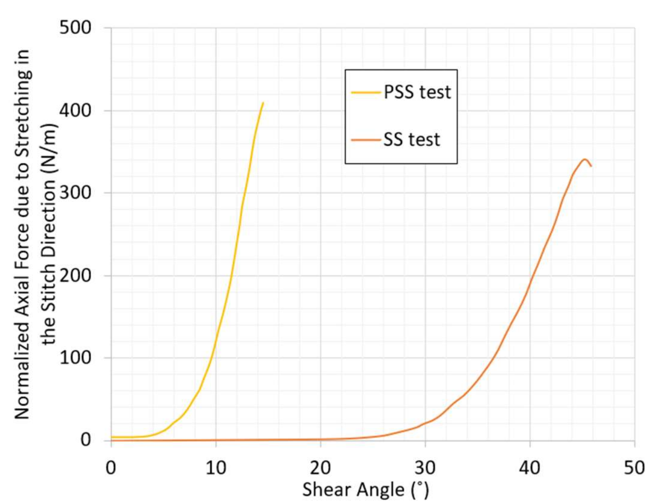

Figure 4.38: Projected normalised axial force due to stretching in the stitch direction vs shear angle curves of PSS and SS tests

Using Eq. 4.12 and Eq. 4.18, the inherent material shear force acting along the tow direction (i.e. the shear force acting in the material system), can be estimated from the two test results, these are plotted in Figure 4.39. In the tensile test, the shear force is zero and can be plotted along the stitch strain direction (red dots shown in Figure 4.39). A simple polynomial surface was then created to fit the inherent shear data from all three tests (see Figure 4.39b). Note that it is difficult to create high-degree polynomial surfaces to fit inherent shear data, as those surfaces do not predict positive data along the X-axis (the measured shear angle). Clearly, the fitted simple polynomial surface is quite poor due to the limited amount of data (R-square value = 0.3288).

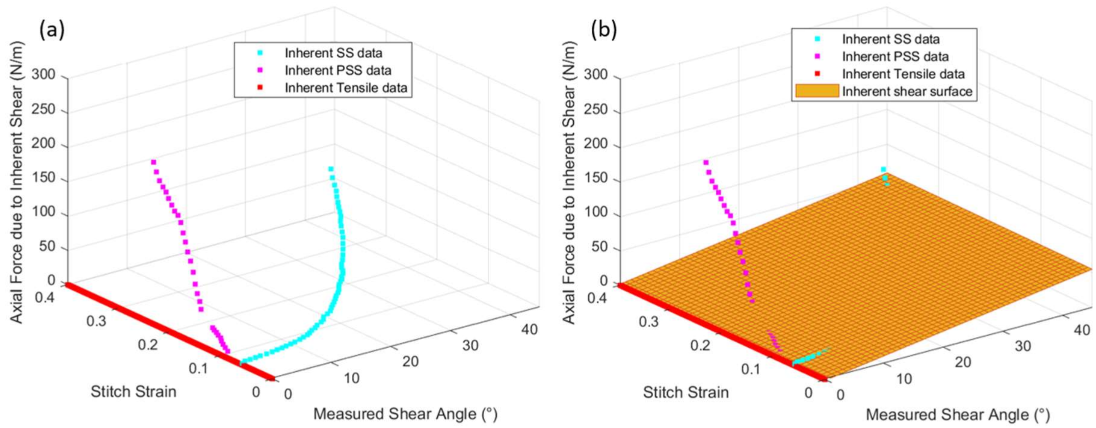

Figure 4.39: First estimate of the normalised axial force due to the inherent shear behaviour of the fabric as a function of shear angle and stitch strain (a) inherent shear data (b) fitted shear surface

The polynomial equation of the shear surface plotted in Figure 4.39b was then used to estimate the normalised shear force in the machine system of each PF test (F_{MS}, yellow dots shown in Figure 4.40) i.e., for the four pre-stretching levels of 1%, 12%, 15% and 17% using Eq. 4.19 (similar to Eq. 1.12).

$$F_{MS} = \frac{F_{IS}}{2\cos\left(\frac{\emptyset}{2}\right)} \tag{4.19}$$

where, F_{IS} and $\emptyset$ represent the normalised material shear force in the tow direction (from the polynomial equation of the shear surface plotted in Figure 4.39b), and the frame angle, respectively. The surface polynomial fitted to the shear data in the PF test and transformed to the axial loading direction is shown by the gold colour in Figure 4.40. The green surface in Figure 4.40 represents the polynomial surface created from the PF test experimental data including pre-stretching in the stitch direction (see Section 4.7) i.e., the experimental surface of the PF test shows an increase in normalised force with increasing stitch strain at 0˚ shear angle due to the inclusion of pre-stretching of the specimens calculated using the tensile curve as described in Section 4.7. The (in-plane bending + pre-stretching) surface of the PF test machine system (Figure 4.40, magenta) was obtained by subtracting the shear surface (Figure 4.40, gold) from the PF test experimental surface (Figure 4.40, green).

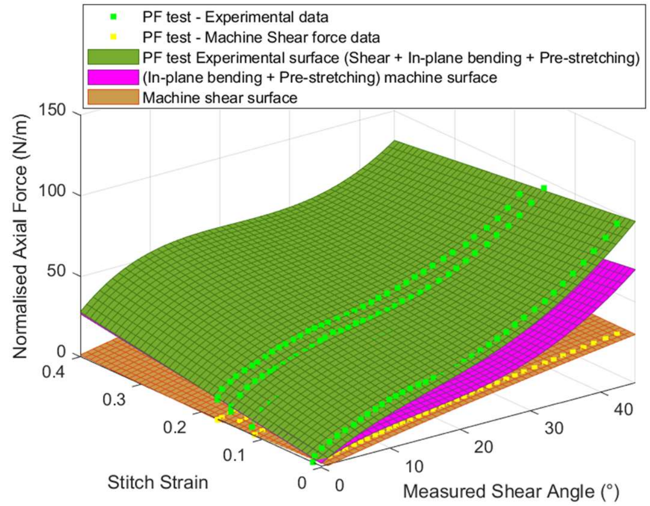

Figure 4.40: Comparison of three surfaces of the PF test machine system

The in-plane bending surface of the PF test machine system (see Figure 4.41, blue) was then created by subtracting normalised axial force related to the pre-stretching of the PF specimens from the (in-plane bending + pre-stretching) surface (Figure 4.40, magenta).

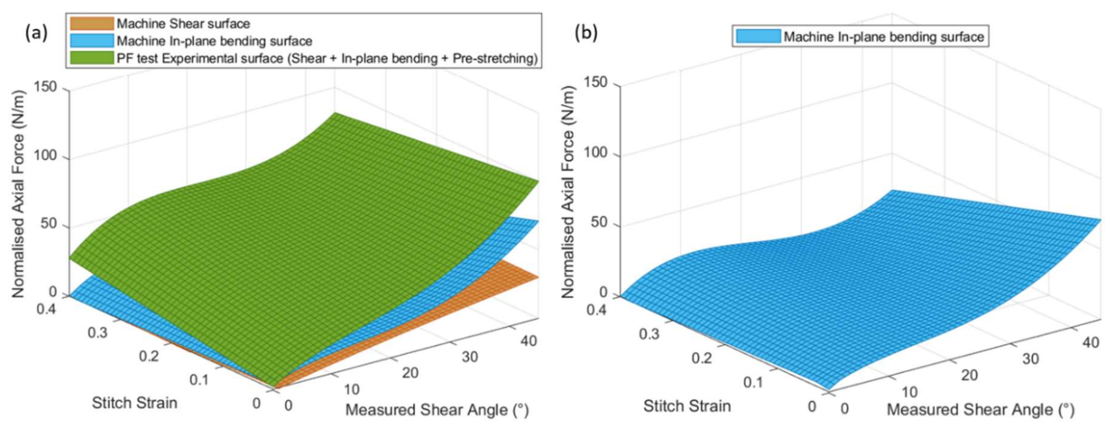

Figure 4.41: (a) Comparison of the in-plane bending surface of the machine system with PF test experimental surface and machine shear surface (b) Machine In-plane bending surface

The next step is to convert the in-plane bending surface in the machine system (F_I) into the material system (i.e. acting along the tow direction). This can be achieved by applying Eq. 4.20 and assuming that in the PF test, the in-plane bending contribution varies with the shear angle in the same way that the shear contribution.

$$F_I = \frac{F_{II}}{2\cos\left(\frac{\emptyset}{2}\right)} \tag{4.20}$$

$$F_{II} = F_I * 2\cos\left(\frac{\emptyset}{2}\right) \tag{4.21}$$

where, F_{II} and $\emptyset$ represent the normalised inherent in-plane bending force and the frame angle at a given displacement, respectively. Figure 4.42 shows the resultant in-plane bending surface in the inherent system. The polynomial coefficients of each surface created in the first estimate are given in Table 4.4.

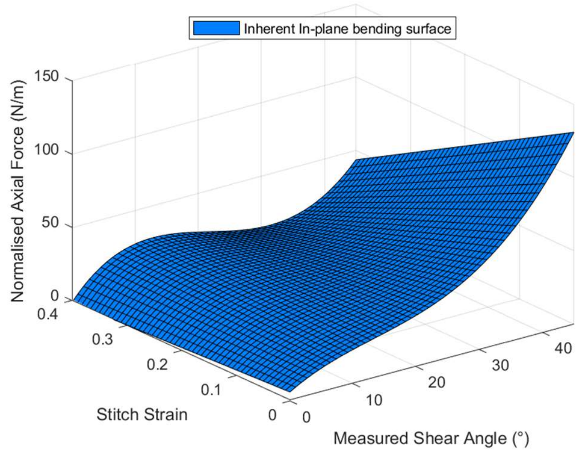

Figure 4.42: In-plane bending surface in the inherent system

Table 4.4: Polynomial coefficients of each surface created in the first estimate. Note that in these equations x and y represent measured shear angle and stitch strain, respectively.

Surface	Coefficients
Inherent tensile surface without coupling (Figure 4.35) $F(x, y)$ =	-1.0209710805646 - 1.77451394659320×10^{-14} x + 60.7440626111559 y + 4.94950938715750×10^{-13} xy + 2664.44217344838 y^2 - 4.78091532368798×10^{-12} xy^2 - 48460.1643425319 y^3 + 1.68151023064346×10^{-11} xy^3 + 254330.827984507 y^4 - 1.96390712269969 ×10^{-11} xy^4 -332058.062797372 y^5
Inherent shear surface (Figure 4.39b) $F(x, y)$ =	-1.17362358021095 + 1.25379196212327 x + 6.87870614339393 y
(Shear + In-plane bending + Pre-stretching) surface (Figure 4.40, green) $F(x, y)$ =	2.45136847337048 + 2.71969201742742 x + 63.3870919485944 y - 0.101927518330002 x^2 + 3.84956944820504 xy + 0.00270602615595376 x^3 - 0.274473930296184 x^2y - 1.58428391032865×10^{-5} x^4 + 0.00299676924308330 x^3y
The shear surface of the machine system (Figure 4.40, gold) $F(x, y)$ =	-0.801117550291480 + 0.879323883825207 x + 4.83244604515357 y - 0.00633346922991317 x^2 - 0.0356214434485306 xy + 4.32798302505990×10^{-5} x^3 + 0.000230237060843955 x^2y
In-plane bending surface of the machine system (Figure 4.41b) $F(x, y)$ =	4.10639078778193 + 1.82564292547804 x - 10.6116569879850 y - 0.0938657104137839 x^2 + 3.91254403156207 xy + 0.00259287828107317 x^3 - 0.271592681135368 x^2y - 1.49790282303571×10^{-5} x^4 + 0.00291598230681054 x^3y
In-plane bending surface of the inherent system (Figure 4.42) $F(x, y)$ =	6.06414635933933 + 2.61712200247933 x - 18.7808272952403 y - 0.120744219514451 x^2 + 6.96458304475857 xy + 0.00339523881779145 x^3 - 0.471194167050409 x^2y - 1.40852504547740×10^{-5} x^4 + 0.00483746928559456 x^3y

The next step is to compare the original machine data with the prediction of the combined contributions when converted from the material system to the machine system, i.e., using the three proposed surfaces (in the material system), see Figures 4.35, 4.39b and 4.42 from the first iteration.

According to Figures 4.43 and 4.44, machine axial force predictions (in orange) in the tensile and PF tests with different amounts of pre-stretching closely match the experimental data (in blue). The SS test indicates a significant over-prediction at moderate shear angles and stitch strains (see Figure 4.45), while the PSS shows a significant under-prediction at high shear angles and stitch strains (see Figure 4.46). To reduce the gap between the original and machine predictions of the PSS and SS test, the inherent shear (Figure 4.39b) surface should be further reduced. Therefore, in the second iteration, assume that the tensile force increases with increasing shear angle to allocate more tensile contribution at high shear angles and reduce the inherent shear for PSS and SS tests.

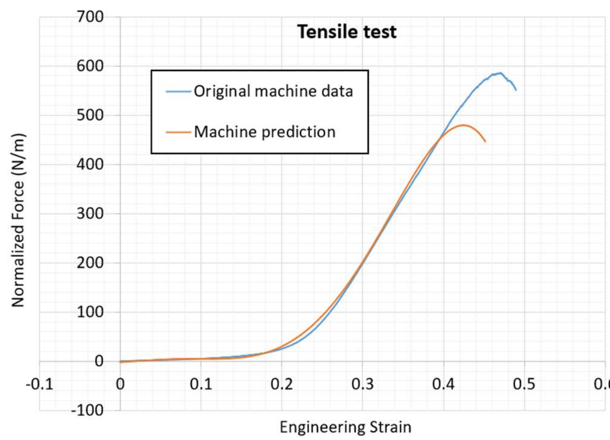

Figure 4.43: Comparison of original machine data and machine prediction of tensile test in the first estimate.

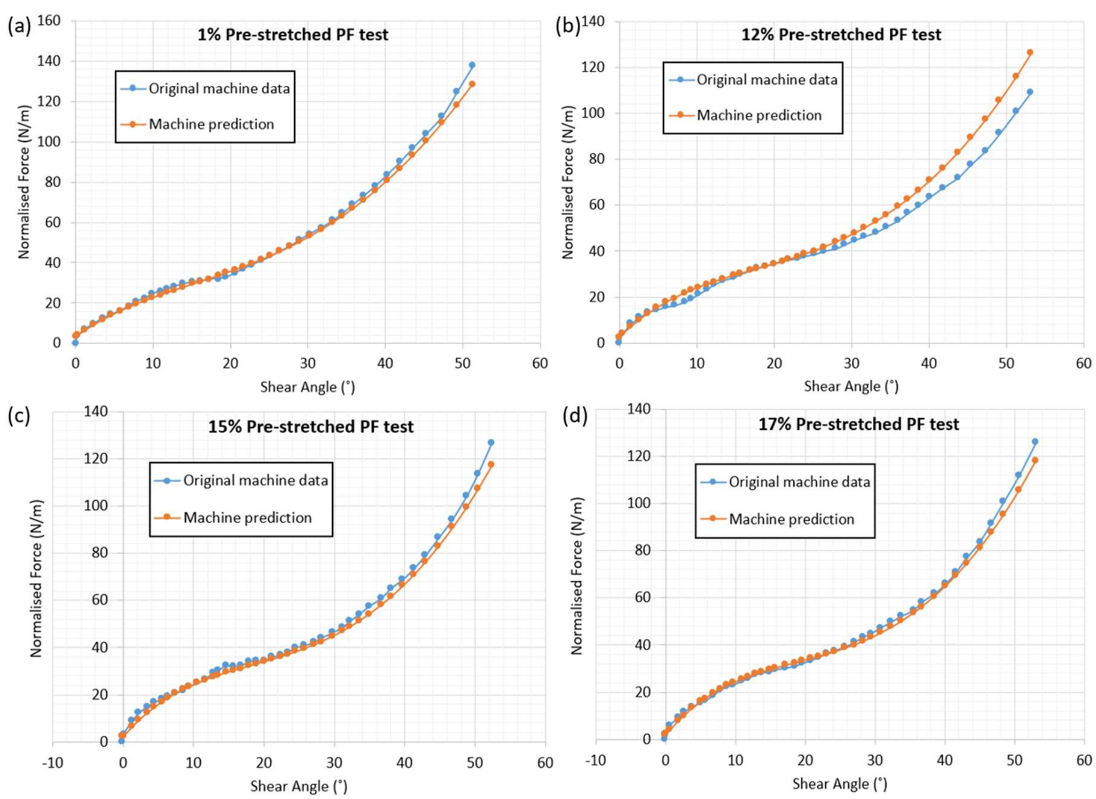

Figure 4.44: Comparison of original machine data and machine prediction in the first estimate of the picture frame test with different stretching percentages (a) 0% (b) 5% (c) 10% (d) 20%

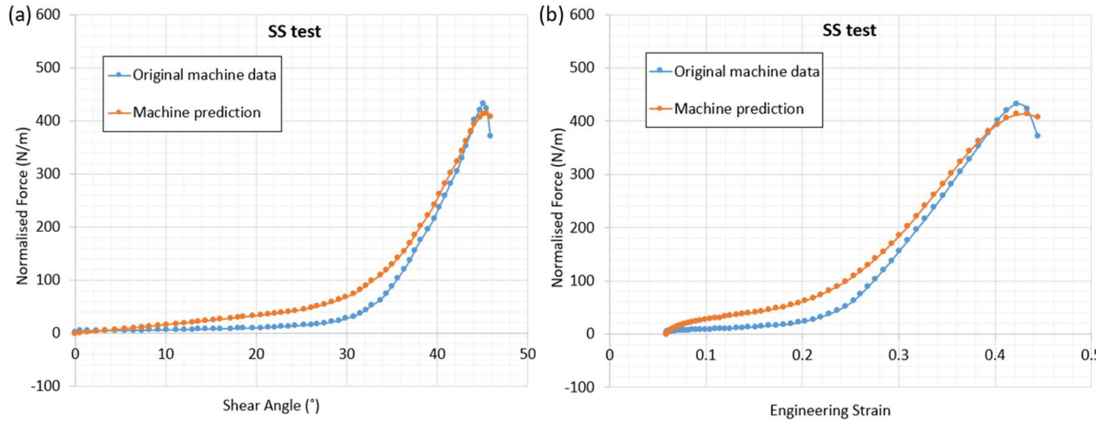

Figure 4.45: Comparison of original machine data and machine prediction of SS test in the first estimate (a) normalised axial force vs measured shear angle (b) normalised axial force vs engineering strain

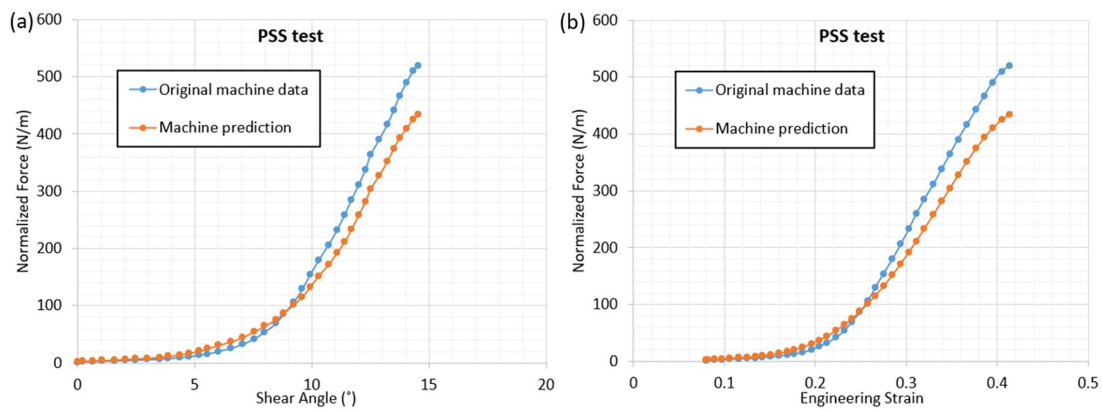

Figure 4.46: Comparison of original machine data and machine prediction of PSS test in the first estimate (a) normalised axial force vs measured shear angle (b) normalised axial force vs engineering strain

4.8.2.2. Second Estimate: Assuming a Linear Coupling Between Tensile Stiffness in the Stitch Direction and Fabric Shear

A polynomial surface was generated for the tensile test data, this time assuming that the fabric tensile and shear stiffnesses are coupled. The aim is to increase the contribution to the tensile force at high angles/tensile strains and consequently reduce the contribution assigned to the shear resistance of the fabric. Figure 4.47a shows a linear increase in tensile force with increasing shear angle. Figure 4.47b shows the modified material shear force surface, acting along the tow direction (the inherent shear surface created by following the same procedure as in Section 4.8.2.1 first iteration, Eq. 4.12 and Eq. 4.18).

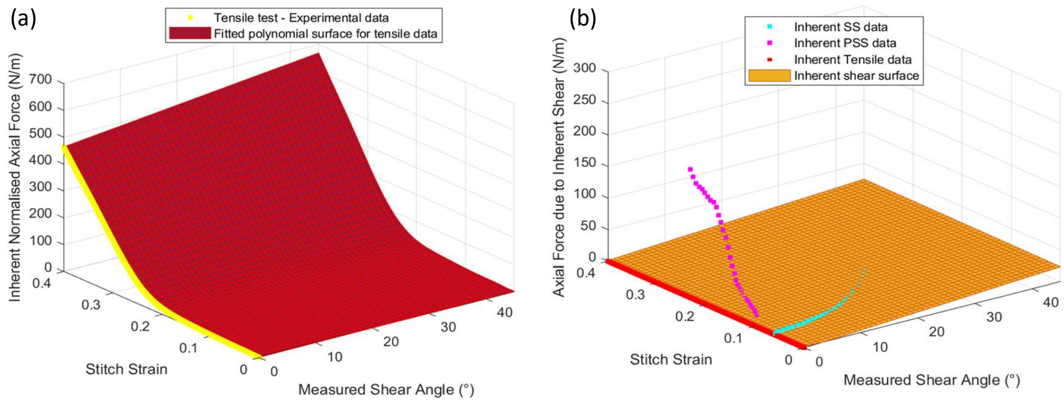

Figure 4.47: (a) Inherent tensile surface with coupling (b) Inherent shear surface

Before continuing the fitting process, Figure 4.48 compares the produced inherent shear surface (Figure 4.47b) with the experimental data from the PF test. The PF tests produce much larger forces than the inherent shear surface, i.e., inherent PSS and SS data at the same state of shear and stitch strain. There are 3 possible reasons:

1. Friction in the bearings causes higher forces during the PF test.
2. The boundary condition of the PF test induces increased force.
3. The in-plane bending stiffness explains the difference.

The friction of the bearings was reasonably modified as discussed in Section 3.8; however, friction may still be present in the PF test because the friction experienced by the rig varies with the stiffness of the material and is uncertain. The boundary conditions of the PF are also modified as discussed in Section 3.6 and Kahavita et al. [221] to achieve accurate results. In this study, the impact of the first two reasons has been carefully investigated and minimised. Thus, it is reasonable to assume that the third reason, i.e., in-plane bending stiffness, will have a considerable impact on the normalised axial force of the PF test.

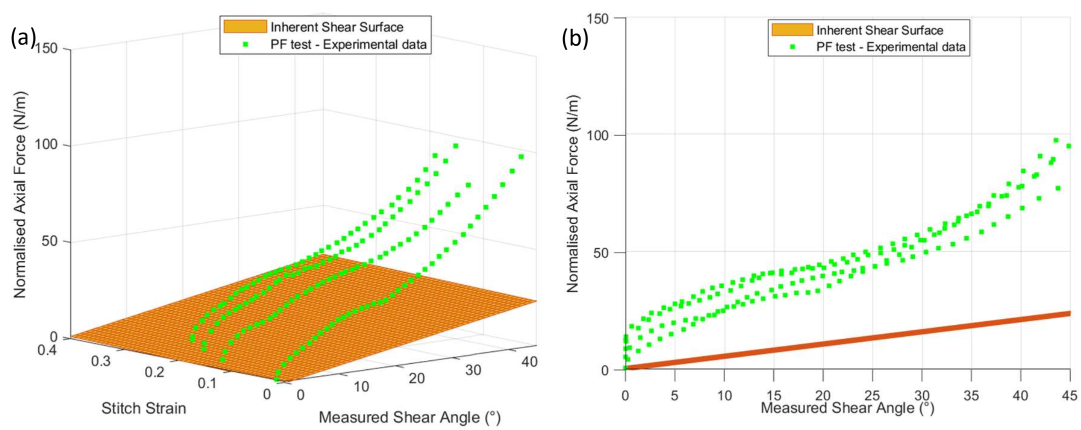

Figure 4.48: Comparison of inherent shear surface and PF test experimental data, the same graph is shown from different perspectives

Following the fitting process discussed in the first iteration, Figure 4.49 shows the resultant in-plane bending surface (blue colour). According to Figure 4.49a, the shear contribution to the machine axial load is significantly lower than the in-plane bending contribution of the 0% stitch stretched PF test. This suggests the axial force measured in the PF test is more likely contributed by the in-plane bending than shear. This may be true specifically for Pure-UDNCFs, or it may be true for all fabrics measured in the PF test, as other researchers have observed in-plane bending in the PF test (S-shaped deformation [110] [111]) however, ignored its contribution to the measured force. To the author's knowledge, no method has been developed so far to isolate the in-plane bending stiffness during the PF test. Therefore, this method provides a better solution to determine the in-plane bending stiffness of fabrics using experimental data.

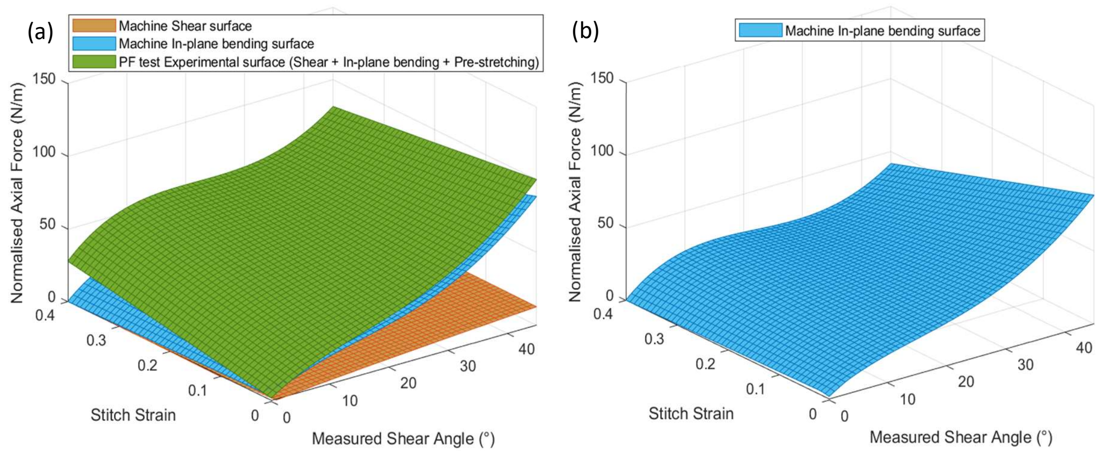

Figure 4.49: Second estimate (a) comparison of PF test experimental, shear and in-plane bending surfaces of the machine system (b) In-plane bending surface of the machine system

Figure 4.50 shows the resultant in-plane bending surface in the inherent system calculated using Eq. 4.21. Table 4.5 shows the polynomial coefficients of each surface created in the second estimate.

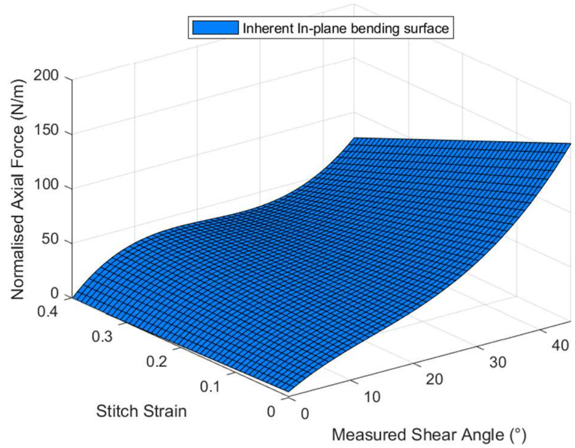

Figure 4.50: In-plane bending surface in the inherent system, according to the second estimate

Table 4.5: Polynomial coefficients of each surface created in the second estimate. Note that in these equations x and y represent measured shear angle and stitch strain, respectively.

Surface	Coefficients
Inherent tensile surface without coupling (Figure 4.47a) $F(x, y)$ =	2.21217227554466 - 0.0623886735663608 x - 238.075195972052 y + 5.21978043650349 xy + 8503.57946593765 y^2 - 74.2065948501789 xy^2 - 89989.2114133273 y^3 + 339.617068379317 xy^3 + 371678.160794590 y^4 - 372.942840325184 xy^4 - 446266.728859619 y^5
Inherent shear surface (Figure 4.47b) $F(x, y)$ =	-0.422720945299102 + 0.521840469958453 x + 3.93657539047443 y
(Shear + In-plane bending + Pre-stretching) surface (Figure 4.48a, green) $F(x, y)$ =	2.45136847337048 + 2.71969201742742 x + 63.3870919485944 y - 0.101927518330002 x^2 + 3.84956944820504 xy + 0.00270602615595376 x^3 - 0.274473930296184 x^2y - 1.58428391032865×10^{-5} x^4 + 0.00299676924308330 x^3y
The shear surface of the machine system (Figure 4.48a, gold) $F(x, y)$ =	-0.286654599109757 + 0.365524660088591 x + 2.76844386811610 y - 0.00262834751845358 x^2 - 0.0208634342480003 xy + 1.79462149482027×10^{-5} x^3 + 0.000143337612399050 x^2y
In-plane bending surface of the machine system (Figure 4.48b) $F(x, y)$ =	3.57744213388911 + 2.34613534855281 x - 8.53506647159684 y - 0.0981812512616992 x^2 + 3.89577414495472 xy + 0.00263692170772902 x^3 - 0.271450531929627 x^2y - 1.51612611650781×10^{-5} x^4 + 0.00291580750650486 x^3y
In-plane bending surface of the inherent system (Figure 4.49) $F(x, y)$ =	5.31334366347962 + 3.34900518047926 x - 15.8395034187052 y - 0.120739964621193 x^2 + 6.96493204760085 xy + 0.00339515896379840 x^3 - 0.471212658128505 x^2y - 1.40848344908908×10^{-5} x^4 + 0.00483770942404927x^3y

The comparison of the original machine data and the prediction of the combined contributions when converted from the material system to the machine system, i.e., using the three proposed surfaces (in the material system, see Figures 4.47a, 4.47b and 4.50 from the second iteration) show good fitting compared to the all four tests in the first iteration (see Figures 4.51, 4.52, 4.53 and 4.54). Especially, the gap shown in the original and machine predictions of the SS test in the first iteration (see Figure 4.45) is significantly reduced in the second iteration (see Figure 4.53). This suggests that the assumption, that most of the force in the PF test is due to in-plane bending is true. However, the PSS test still shows a significant under-prediction at high shear angles and stitch strains (see Figure 4.54). As this is a manual fitting process, it is technically challenging to match all the experimental data. Ideally, an automated genetic fitting algorithm could potentially improve the fitting process across all the experimental data by automatically adjusting the parameters of a predetermined model or function. This can result in a better fit to the experimental data, as indicated by an R-square value close to 1.

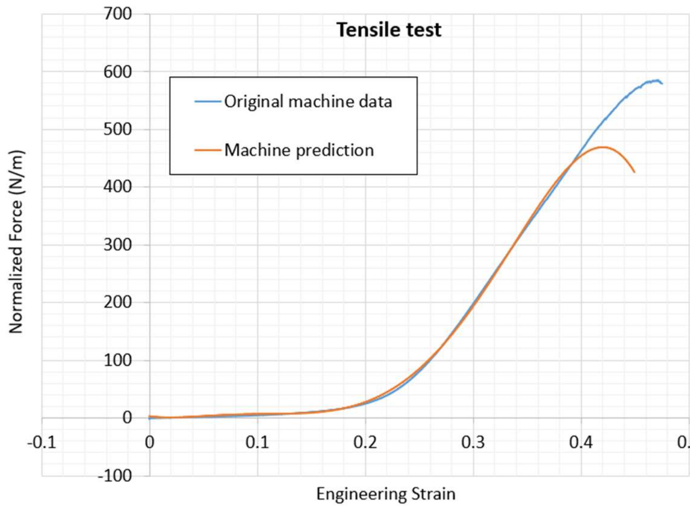

Figure 4.51: Comparison of original machine data and machine prediction of tensile test

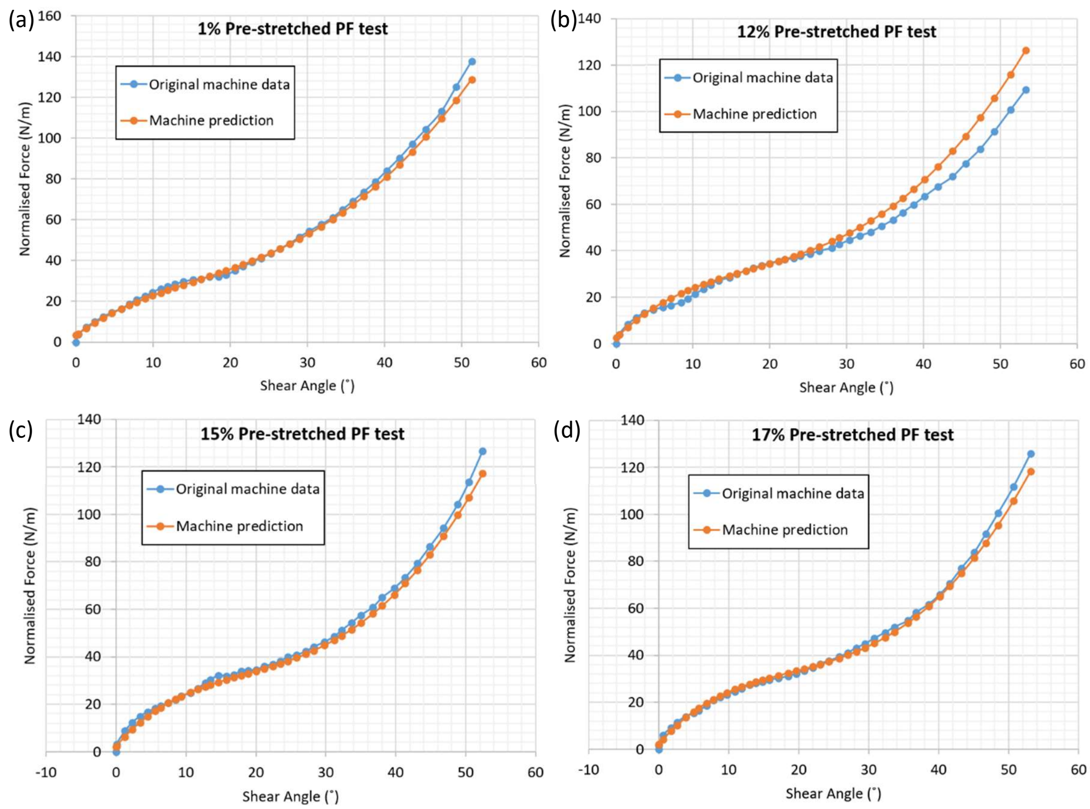

Figure 4.52: Comparison of original machine data and machine prediction of the picture frame test with different stretching percentages (a) 1% (b) 12% (c) 15% (d) 17%

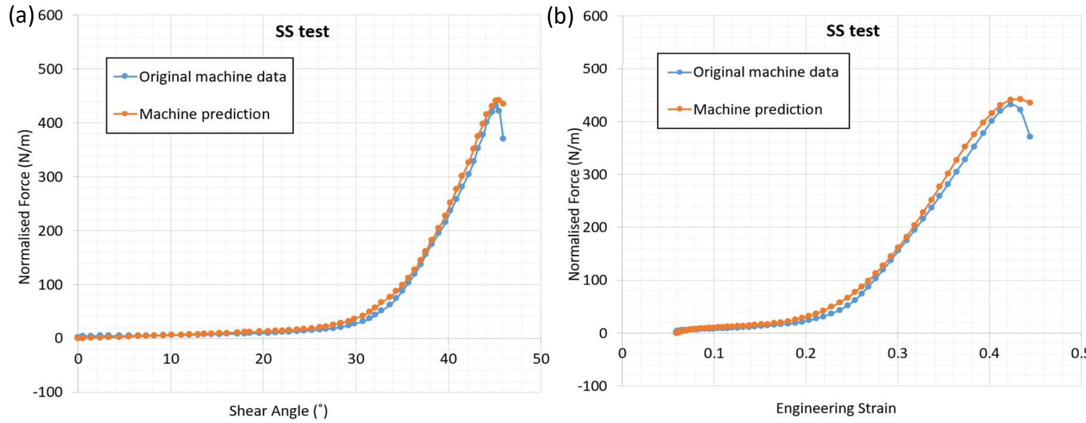

Figure 4.53: Comparison of original machine data and machine prediction of SS test (a) normalised axial force vs measured shear angle (b) normalised axial force vs engineering strain

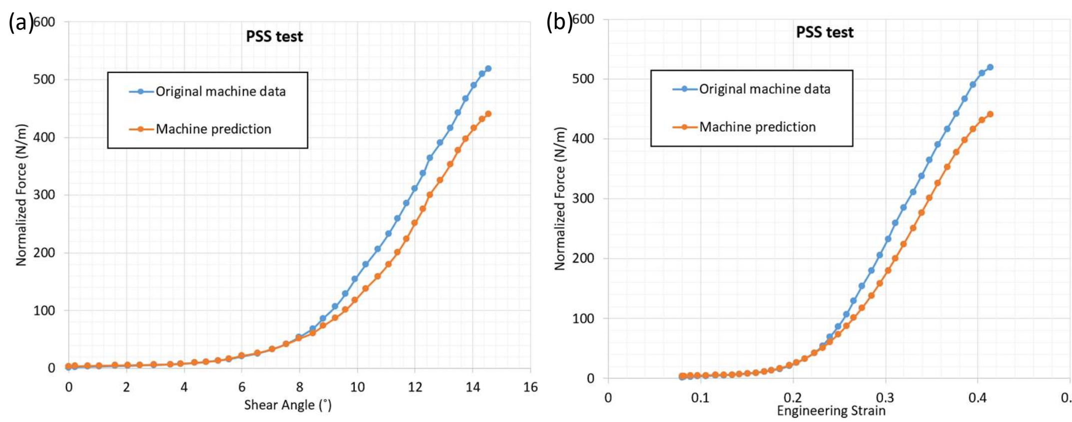

Figure 4.54: Comparison of original machine data and machine prediction of PSS test (a) normalised axial force vs measured shear angle (b) normalised axial force vs engineering strain

4.9. Chapter Summary

To isolate the contribution of each deformation mode i.e., shear, in-plane bending and tensile strain in the stitch direction, new characterisation tests have been designed to generate well-defined kinematics and different combinations of shear and tensile strain in the stitch direction.

- **Cruciform Bias Extension (CBE) Test:** This test is similar to the standard UBE test but has a wider specimen size (cruciform-shaped shear specimen), a better controlled initial shear angle and well-defined in-plane bending kinematics. However, the shear/tensile behaviour of the CBE test is challenging to extract from the test results due to the different shear/tensile strains occurring in different regions of the specimen. Nevertheless, the CBE could be very useful in evaluating numerical predictions of finite element simulations after implementing an appropriate constitutive model.

- **Parallelogram Shear-Stretch (PSS) Test:** Upon shearing the specimen becomes a parallelogram. The side clamps allow only vertical motion at the boundaries due to the linear bearings. The complexity of shear in different regions is reduced in the PSS specimen because it deforms as a single region, in contrast with the standard UBE and CBE tests.
- **Simple Shear (SS) Test:** This method is designed to generate simple shear of the pure-UDNCF and achieves higher shear angles than the PSS test and samples with a different combination of shear and tensile strain in the stitch direction.

In addition to the new shear tests, the **pre-stretched PF test** is used to explore alternative regions of the deformation space. During the analysis, it was identified that an **experimental error** in the new tests, i.e., pre-stretching in the stitch direction, can cause a significant discrepancy in the test results, especially when handling fabrics lacking stabilising fibres, such as pure-UDNCF. This chapter further discussed a method of adjusting the pre-stretching that can occur in specimens, even if the fabric is handled with care. The results implied that the novel tests developed to characterise pure-UDNCF are highly sensitive for pre-stretching in the stitch direction.

Separating the three contributions i.e., shear, stitch strain and in-plane bending is challenging. Except for the tensile test performed on the stitch direction, all the other tests generate more than one contribution from the three low-stiffness deformation modes to the axial force. A power-based analysis failed to produce accurate results for extracting the shear signal from PSS and SS tests. Consequently, alternative approaches were attempted to isolate the three stiffnesses of the pure-UDNCF, by considering the combined experimental results of the PSS, SS, tensile, PF test and pre-stretched PF tests. The second attempt to do this, which involved the use of guessed trial functions, proved to be the most effective approach. The separate contributions from shear, in-plane bending and tensile strain in the stitch direction, provide good predictions of the measured axial force of each of the experiments. In addition, this study developed a novel method to isolate the in-plane bending stiffness using experimental data. This approach suggested that most of the force in the PF test is due to the in-plane bending. This result may depend on the fabric (pure-UDNCF), or this indicates that it is important to consider in-plane bending contribution during the PF test for other fabrics as well. The separate contributions, i.e., shear, in-plane bending and tensile strain in the stitch direction, can be used to inform the development of constitutive models for pure-UDNCFs.

Chapter 5 Bending Characterisation

5.1. Introduction

Beyond tensile and shear deformations, bending, including both in-plane and out-of-plane is another critical deformation mode that significantly affects the behaviour of fabric reinforcement. Out-of-plane bending involves deformation perpendicular to the plane of the fabric, and the cantilever bending test is commonly performed to find the out-of-plane bending stiffness of fabric reinforcements. The test involves fixing one end of a fabric specimen and allowing the other end to bend freely under its weight. The out-of-plane bending stiffness, a key property that affects the overall mechanical performance of fabrics, can be calculated by measuring the deflection. This provides a critical insight into the handling characteristics of engineering fabrics. In this chapter, the cantilever bending test is performed on three engineering fabrics i.e., plain-woven, twill-woven and pure-UDNCF. The flexural rigidities of two woven fabrics are compared with the pure-UDNCF. Examining woven fabrics provides a reference for comparison and allows evaluation of how the complex architecture of non-woven fabrics influences their bending performance.

In-plane bending stiffness refers to the resistance of the fabric reinforcement to bending in its plane i.e., how the fabric behaves when bent along its surface, as opposed to out-of-plane bending (bent perpendicular to its surface). The in-plane bending stiffness of the fabric is important when conforming the material to complex shapes through forming and draping operations. It plays a key role in resisting unwanted deformation and wrinkling while maintaining the integrity of the desired shape i.e., optimal in-plane bending stiffness allows the fabric to retain its structural integrity under applied forces, resulting in a smooth and uniform fit over complex geometries. Harrison et al. [6] determined the in-plane bending stiffness of fabrics through inverse modelling of data obtained from the bias extension test. Such approaches are mainly based on assumptions and computer models, emphasising the need for an experimental approach. As an initial step to bridge this gap, a new experimental method can be developed to qualitatively analyse the in-plane bending behaviour of engineered fabrics. The ultimate goal of this new test is to provide a direct, clear method to characterise in-plane bending stiffness, laying the foundation for future quantitative analysis. The results of a well-developed in-plane bending test will provide critical data for the FEM, enabling better predictions of how the fabric will behave under various loads.

The structure of this chapter is as follows. Section 5.2 explains the experimental setups and analysis for the cantilever bending test of three different fabric reinforcements. The out-of-plane bending results of all three fabrics are compared at the end of that section (Section 5.2.3.4). A new test method developed to qualitatively determine the in-plane bending of pure-UDNCF is covered in Section 5.3 and the chapter summary is provided in Section 5.4.

5.2. Out-of-plane Bending Test

5.2.1. Sample Preparation

To perform the cantilever bending test, five samples with dimensions of 250 × 25 mm^2 were prepared in each of three key directions: warp, weft, and bias, ensuring a detailed evaluation of their out-of-plane bending behaviour across different orientations (see Figure 5.1). The study utilised three fabric types—plain-woven, twill-woven, and pure-UDNCF.

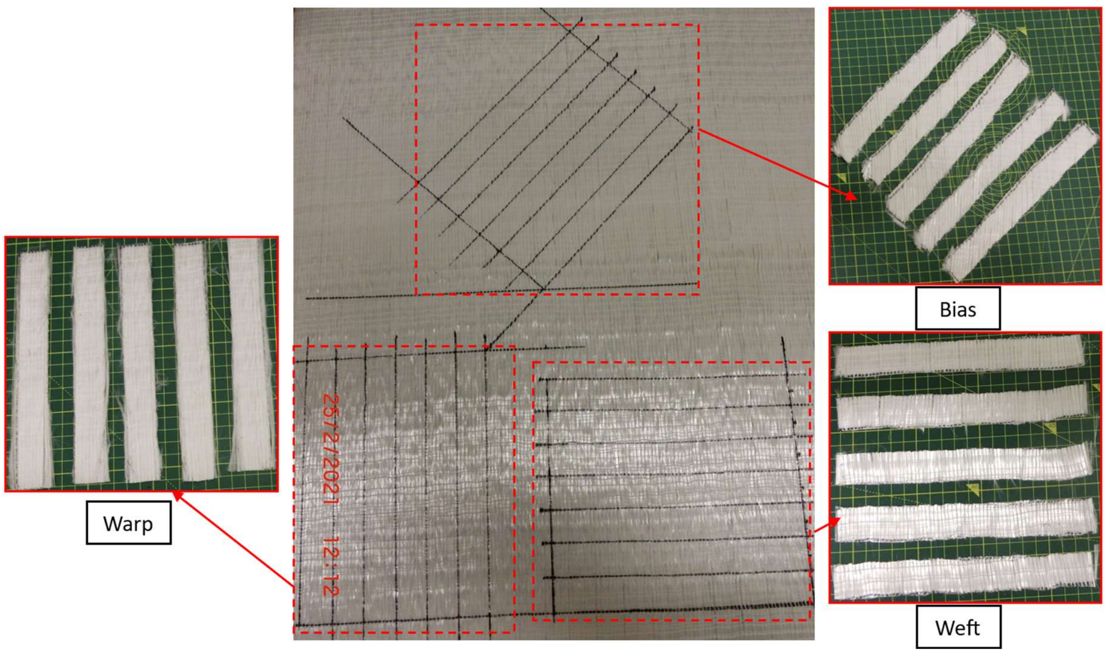

Figure 5. 1: Cantilever bending specimens of pure-UDNCF in the warp, weft, and bias directions (a) marked outlines (b) prepared specimens

5.2.2. Test Procedure

A test specimen was placed on a flexometer with platform width, height and slope of 30mm, 150mm and 133mm, respectively. A steel ruler was then placed on the top of the test specimen ensuring that the zero was aligned with the leading edge of the specimen and the flexometer platform (see Figure 5.2a). The specimen was then extended at a constant rate of $5mms^{-1}$ over the flexometer, enabling it to bend under its weight until it touched the 41.5° slope (see Figure 5.2b), as per the British Standard (BS 3356:1990). Note that the underside of the steel ruler used in this test is rubber-coated to help grip the sample and prevent slipping. The overhanging length of the fabric (l, Figure 5.2b) was measured. Both ends of the top and bottom surfaces of the specimens (4 measurements per sample, see Figure 5.3) were tested to calculate the average. The flexural rigidity of the fabric was calculated using Eq 2.4 (in Chapter 2).

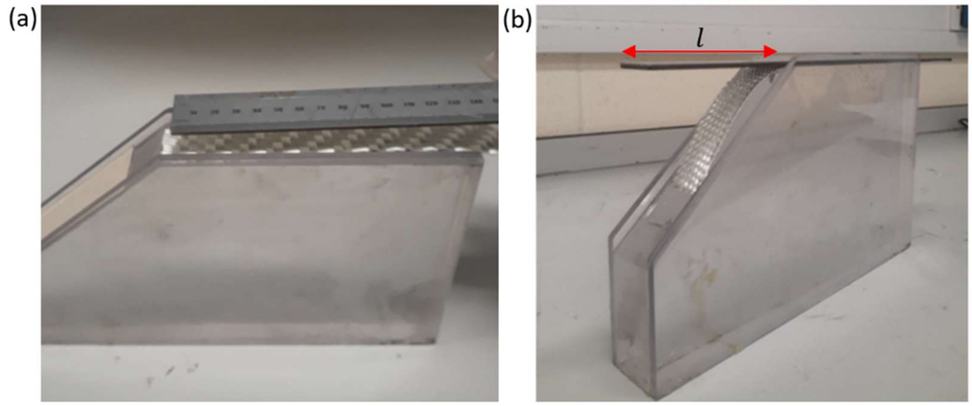

Figure 5.2: The setup of cantilever bending test (a) placing the specimen and the ruler (b) reading overhanging length

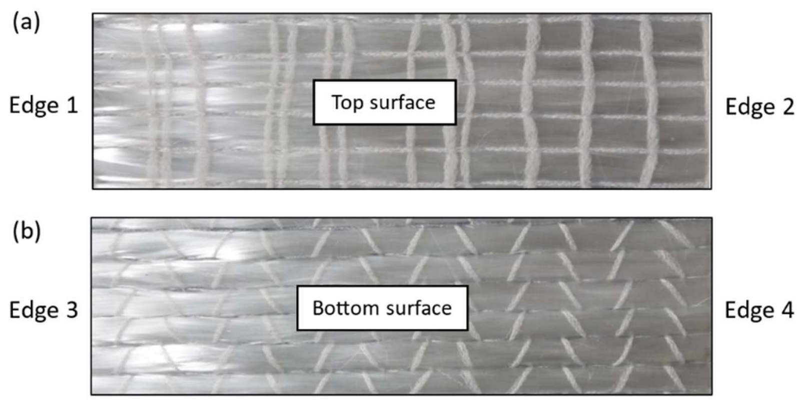

Figure 5.3: Measurements based on the specimen orientations (a) top surface (b) bottom surface

5.2.3. Results and Analysis

5.2.3.1. Plain-Woven Glass Fabric

The findings of cantilever bending tests on plain woven glass fabric (see Section 3.2 for full description) is first discussed to better comprehend the simpler and more predictable out-of-plane deformation behaviour. The test result of the plain-woven fabric is summarised in Table 5.1. A comparison of the out-of-plane bending stiffness in each direction of the fabric is shown in Figure 5.4.

Table 5.1: Cantilever bending test results of plain-woven fabric in all three directions (warp, weft, and bias)

Fibre Direction	Sample No.	Sample Mass /g	Weight per unit area/ Nm^{-2}	Average weight per unit area/ Nm^{-2}	Over hanging length/ mm				Average per Sample/ mm	SD per sample/ mm	Average/ mm	SD/ mm	Flexural Rigidity x 10^{-4} (Nm)
					1	2	3	4					
Warp	1	1.6	3.2	3.16	135	131	132	135	133	2.1	135	1.8	9.69
	2	1.5	3		136	135	133	137	135	1.7			
	3	1.6	3.2		133	136	137	135	135	1.7			
	4	1.6	3.2		135	136	134	135	135	0.8			
	5	1.6	3.2		132	135	137	138	136	2.6			
Weft	1	1.6	3.2	3.12	133	135	133	135	134	1.2	135	1.6	9.60
	2	1.5	3		135	134	135	138	136	1.7			
	3	1.5	3		132	135	134	135	134	1.4			
	4	1.6	3.2		133	133	137	137	135	2.3			
	5	1.6	3.2		136	137	135	138	137	1.3			
Bias	1	1.6	3.2	3.16	88	87	92	93	90	2.9	92	2.2	3.05
	2	1.6	3.2		87	90	90	92	90	2.1			
	3	1.6	3.2		90	87	92	87	89	2.4			
	4	1.6	3.2		93	95	94	96	95	1.3			
	5	1.5	3		96	98	93	95	96	2.1			

The plain-woven fabric shows the same bending stiffness in both warp and weft directions. In both directions, the tows are aligned directly along the direction of the applied bending forces. Besides that, the length of the fibres in both directions are assumed to be the same due to the symmetrical or balanced woven structure (see Figure 3.1). When the areal density of the cantilever bending specimens is considered, all the samples have approximately equal densities (see Table 5.1). Therefore, the flexural rigidity of the plain-woven fabric in the warp and weft directions can be approximately equal. However, the bias direction displays a bending stiffness about 68% lower than the warp or weft direction. In the bias direction, the plain-woven fabric is more flexible (i.e., do not need to follow the straight paths of tows. Therefore, have more freedom to move relative to each other) and causes less frictional forces due to the arrangement of short fibres.

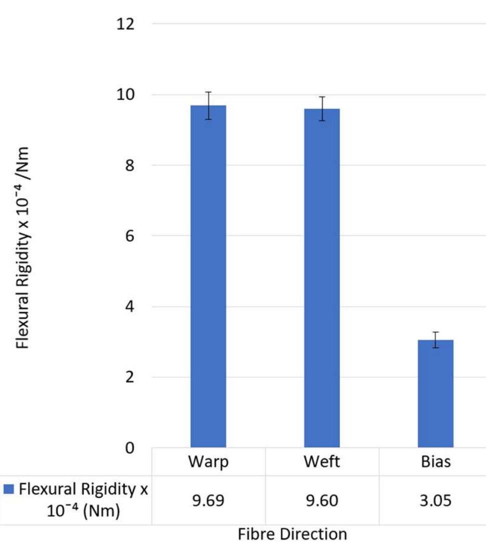

Figure 5.4: Flexural Rigidity of plain-woven fabric in all three directions (warp, weft, and bias)

5.2.3.2. Twill-Woven Glass Fabric

Apart from the plain-woven fabric, a cantilever bending test was performed on twill-woven glass fabric (see Section 3.2 for full description) to see how the woven fabric structure and fabric properties affect the out-of-plane bending stiffness. Test results are summarised in Table 5.2.

Table 5.2: Cantilever bending test results of twill-woven fabric in all three directions (warp, weft, and bias)

Fibre Direction	Sample No.	Sample Mass /g	Weight per unit area/ Nm^{-2}	Average weight per unit area/ Nm^{-2}	Over hanging length/ mm				Average per Sample/ mm	SD per sample/ mm	Average /mm	SD/ mm	Flexural Regidity x 10^{-4} (Nm)
					1	2	3	4					
Warp	1	7.3	11.68	11.90	209	213	208	210	210	2.2	209	2.5	136.33
	2	7.3	11.68		214	207	212	209	211	3.1			
	3	7.6	12.16		209	208	207	209	208	1.0			
	4	7.4	11.84		208	206	207	202	206	2.6			
	5	7.6	12.16		217	212	208	210	212	3.9			
Weft	1	7.4	11.84	11.81	207	218	213	212	213	4.5	210	4.2	136.99
	2	7.2	11.52		203	209	213	214	210	5.0			
	3	7.5	12		215	213	218	212	215	2.6			
	4	7.4	11.84		203	202	207	207	205	2.6			
	5	7.4	11.84		209	201	212	215	209	6.0			
Bias	1	7.2	11.52	11.81	114	112	109	110	111	2.2	108	2.1	18.44
	2	7.5	12		109	108	110	107	109	1.3			
	3	7.3	11.68		104	105	102	101	103	1.8			
	4	7.5	12		111	109	103	105	107	3.7			
	5	7.4	11.84		109	111	107	108	109	1.7			

The twill-woven glass fabric shows approximately the same bending stiffnesses in both warp and weft directions (see Figure 5.5). Similar to plain-woven fabric, twill-woven fabric has a balanced structure (see Figure 3.2) and areal densities of the specimen in both warp and weft directions are approximately the same (see Table 5.2). Therefore, the flexural rigidity of the twill-woven fabric in both directions can be nearly equal. However, the bias direction displays a bending stiffness about 86.5% lower than the warp or weft direction due to more flexibility and low frictional forces between the short fibres.

When comparing the two woven fabrics, the flexural rigidity of the warp or weft direction of the twill-woven fabric is almost 14 times higher than that of plain-woven fabric; however, for bias direction, this difference is low i.e., the twill-woven fabric is only 6 times higher than the plain-woven fabric. Considering the woven structure, the plain-woven fabric should show higher out-of-plain bending stiffness than the twill-woven fabric due to the dense interlacement that increases structural integrity when all other parameters remain constant [223] [224]. The difference in the bending stiffness in the plain and twill-woven fabrics used in this experiment (with the twill-woven being 14 times higher than that of the plain-woven fabric) could have been due to the differences in other parameters such as significantly higher areal density (i.e., flexural rigidity of fabric is directly proportional to areal density, see Eq. 2.4) and absence of gaps (dense and continuous distribution of fibres) in the twill woven fabric than plain-woven fabric (see Table 3.1). In the bias direction, the applied load is shared between both sets of tows (warp and weft) i.e., the tows are neither fully aligned with nor fully perpendicular to the applied force. The bias samples contain short fibres in both directions, resulting in less structural integrity than in the warp and weft directions. However, the plain weave fabric has more interlacing points than the twill weave fabric, which increases its structural integrity and lowers the difference in flexural rigidities between the two fabrics in the bias direction (twill-woven is only 6 times higher than the plain-woven fabric, see Figure 5.5).

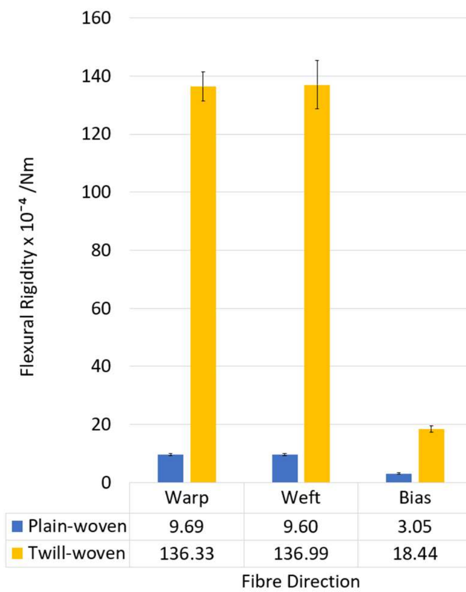

Figure 5.5: Comparison of flexural rigidities of woven fabrics in all three directions (warp, weft, and bias)

5.2.3.3. Pure-Unidirectional Non-Crimp Fabric

This section focuses on the cantilever bending test of a complex fabric, pure-UDNCF and Table 5.3 summarises the result.

Table 5.3: Cantilever bending test results of pure-UDNCF in all three directions (warp, weft, and bias)

Fibre Direction	Sample No.	Sample Mass /g	Weight per unit area/ Nm^{-2}	Average weight per unit area/ Nm^{-2}	Over hanging length/ mm								Average per Sample/ mm	SD per sample/ mm		Average /mm	SD/ mm		SD Avg/ mm	Flexural Regidity $x\ 10^{-4}$
					1		2		3		4									
					Min	Max	Min	Max	Min	Max	Min	Max		Max	Min		Min	Max		
Warp	1	8.5	13.6	13.79	240		235		237		233		236	3.0		235	3.0		3.0	209.64
	2	8.9	14.24		239		234		237		230		235	3.9						
	3	8.6	13.76		238		235		231		232		234	3.2						
	4	8.5	13.6		235		233		231		230		232	2.2						
	5	8.6	13.76		239		235		235		232		235	2.9						
Weft	1	6.8	13.6	13.68	–											–	–		–	–
	2	7.2	14.4																	
	3	6.5	13																	
	4	6.8	13.6																	
	5	6.9	13.8																	
Bias	1	7.2	14.4	13.72	34	52	33	50	35	50	32	48	42	1.3	1.6	41	1.4	2.4	1.9	1.10
	2	6.5	13		33	53	31	52	34	51	31	49	42	1.5	1.7					
	3	7	14		31	51	32	51	28	48	28	49	40	2.1	1.5					
	4	6.8	13.6		31	55	31	53	28	48	29	48	40	1.5	3.6					
	5	6.8	13.6		30	55	31	54	30	49	29	48	41	0.8	3.5					

In the pure-UDNCF, the average areal density of each direction is approximately equal (see Table 5.3). However, there are significant differences between the flexural rigidities of the three directions of the fabric. Figure 5.6 shows the flexural rigidities in all three directions of pure-UDNCF on a log scale for a clear comparison. Pure-UDNCF has high-density tows and low-density stitches perpendicular to each other, with no additional stabilising fibres (unbalanced fabric structure). Therefore, the bending direction of the specimens changes due to the cutting direction of the specimen. Based on the calculations, a notable increase in flexural rigidity was observed in the warp direction i.e., about 200 times the bending stiffness in the bias direction (see Figure 5.6). The lack of crimp in the tows allows for more direct load transfer, leading to higher rigidity. Interestingly, the flexural rigidity in the weft direction for pure-UDNCF is almost zero due to the presence of only low-tensile stitches i.e., the fabric sample moves along the slope (no overhanging, see Figure 5.7a), meaning that pure-UDNCF is highly flexible and offers no resistance to bending in weft direction. This sharp contrast with the warp direction suggests that pure-UDNCF is highly anisotropic. Thus, it is reasonable to assume that the wrinkling along the stitch direction during the picture frame (PF) test is caused by the lower out-of-plane bending stiffness in the stitch direction than the tow direction (in Chapter 3, Section 3.4.2.1). In the bias direction, the overhanging length has two values; minimum and maximum (see Table 5.3). The edge of the specimen with the short tows touches the slope first (see Figure 5.7b) and at this point, the overhanging length is considered ‘minimum’. The overhang length is considered 'maximum' when both edges touch the slope. Therefore, eight measurements were taken to calculate the average overhang length in the bias direction of pure-UDNCF.

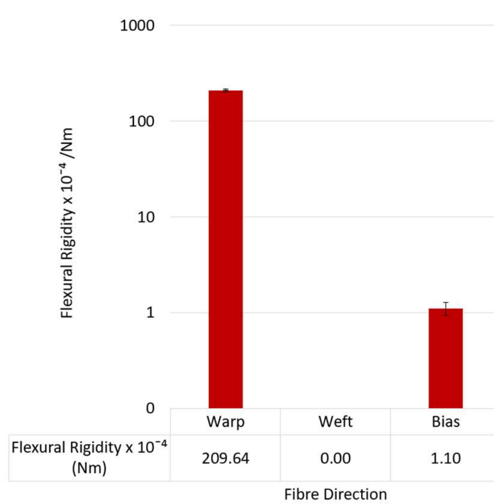

Figure 5.6: Flexural Rigidity of pure-UDNCF in all three directions (warp, weft, and bias). This graph is shown in the log scale.

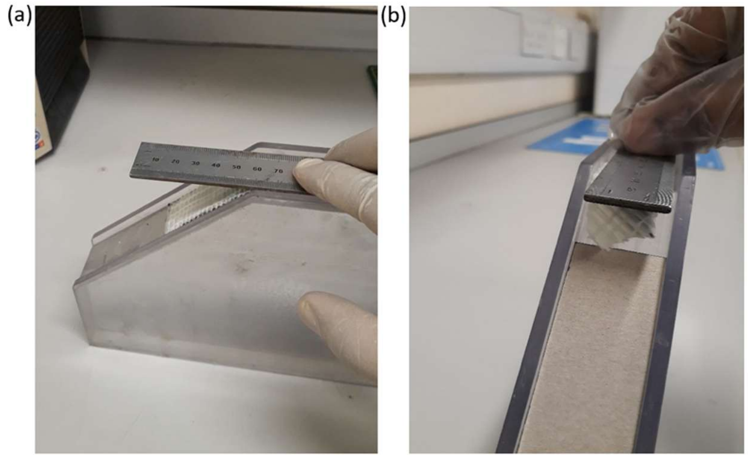

Figure 5.7: Cantilever bending test of pure-UDNCF (a) weft direction (b) bias direction

When considering the warp direction, the tows are aligned with the bending direction (see Figure 5.8a), resulting in higher bending stiffness. However, since there are only stitches without fibres in the bending direction, there is no bending stiffness in the weft direction (see Figure 5.8b), which results in better drapability. In the bias direction, short fibres and stitches are perpendicular to each other and present 45˚ to the bending direction (see Figure 5.8c). The tows at the edge of the specimen vary in length. Tow 2 in Figure 5.8c provides comparatively high flexural rigidity due to increased length than Tow 1. Therefore, stiffness improves slightly in the bias direction compared to the weft.

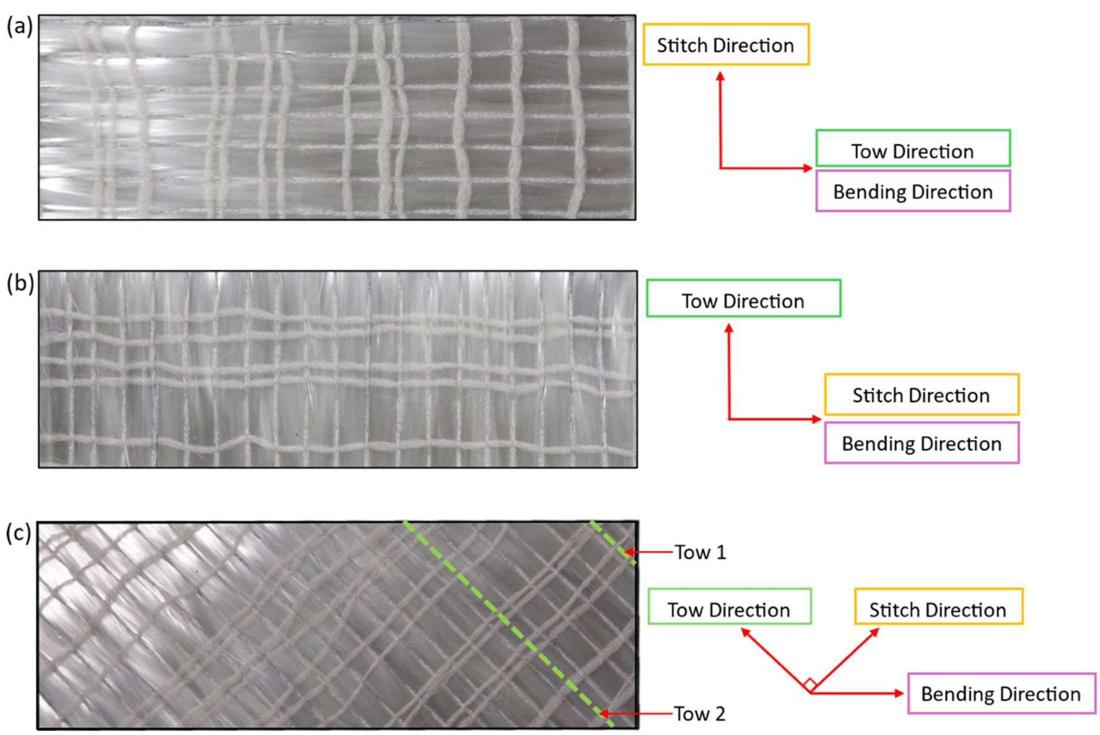

Figure 5.8: Orientation of tow, stitch, and bending directions of pure-UDNCF cantilever specimens in the (a) warp (b) weft (c) bias directions

5.2.3.4. Comparison of the Out-Of-Plain Bending Results of Three Fabrics

A comparison of the flexural rigidity of the three glass fabrics (plain-woven, twill-woven and pure-UDNCF) in the three different directions is shown in Figure 5.9 (for a better comparison the graph is shown in the log scale). The pure-UDNCF shows a significant increase in flexural rigidity in the warp direction, approximately 95.7% and 38.5% greater than that of the plain-woven and the twill-woven warp direction, respectively. Compared to woven fabrics, pure-UDNCF contain long tows aligned in a single direction i.e., the non-crimp arrangement avoids tow waviness, resulting in greater mechanical performance in this direction. Although the warp tow width of the pure-UDNCF is smaller than the twill-woven fabric, the average areal density of the pure-UDNCF is greater than that of the twill-woven fabric (see Table 3.1) which may be due to the more efficient packing of fibres in the pure-UDNCF. Increased areal density thus increases the flexural rigidity if the lengths are the same. In contrast, pure-UDNCF has no flexural rigidity in the weft direction, which is far lower than that of both woven fabrics. This indicates that pure-UDNCF offers no support or stiffness in the weft direction, while woven fabrics, particularly twill-woven, provide some degree of stiffness in this direction.

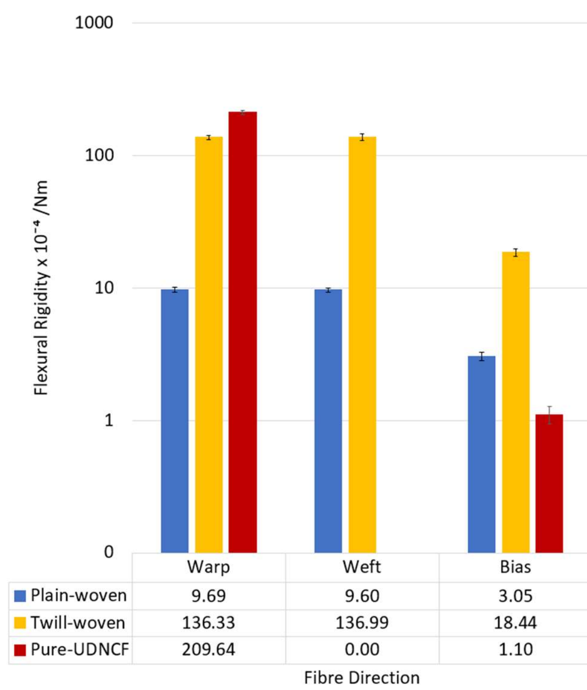

Figure 5.9: Comparison of flexural rigidities of three glass fabrics: plain-woven, twill-woven, and pure-UDNCF in warp, weft and bias directions. This graph is shown in logarithmic scale

Compared to the warp and weft, both woven fabrics have the lowest flexural stiffness in the bias direction due to their short fibre structure (Figure 5.9). The interlacing points in the woven fabrics make them more bending-resistant than pure-UDNCF. Compared to twill-woven fabric, gaps between tows and other fabric parameters such as low areal density and thickness reduce the flexural rigidity of plain-woven fabric in the bias direction. Although the fabric parameters of pure-UDNCF are better than woven fabrics, the flexural rigidity of pure-UDNCF is noticeably lower than that of woven fabrics due to the unbalanced fabric structure, i.e., the poor continuity of the sample in the bias direction due to the presence of short tows in only one direction.

5.3. In-plane Bending Test

As discussed in Chapters 3 & 4, all PF tests performed on pure-UDNCF show in-plane bending near the end of the tows at high shear angles (see Figure 5.10a). In addition, in-plane bending is visible in CBE specimens (see Figure 5.10b). Besides that, standard UBE specimens also show in-plane bending, however, it is not very significant (the tow direction remains almost straight at the transition between Regions A and B2, see Figure 5.10c). A new test method was developed to qualitatively evaluate the in-plane bending of fabric reinforcements.

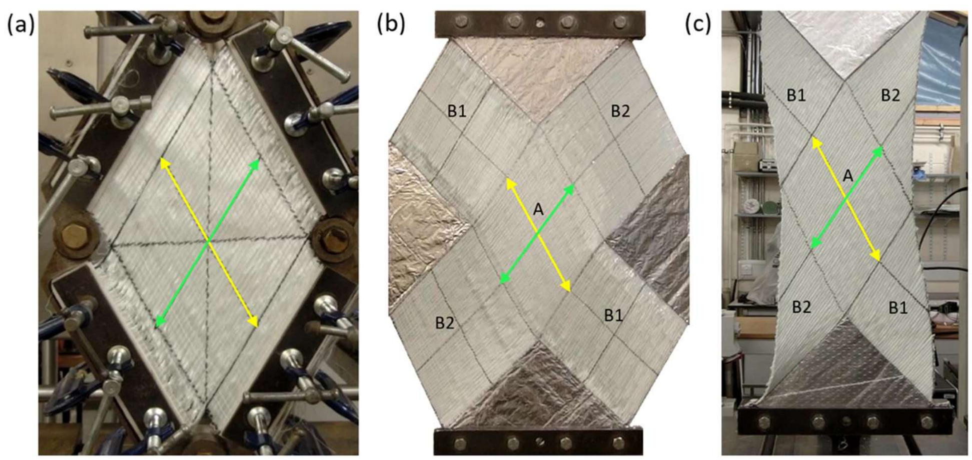

Figure 5.10: In-plane bending of tows in different tests (a) PF test (b) CBE test (c) standard UBE test, the yellow and green arrows indicate stitch direction and the tow direction, respectively

5.3.1. Theory

When one end of a fabric is fixed and the other is free, the fabric deforms vertically under its weight (M_f). When there is no in-plane bending, the fabric is deformed by pure shear, i.e., the square shape of the specimen transforms to a linear parallelogram shape. When in-plane bending occurs, the fixed ends deviate from the straight line and convert into an orange shape (see Figure 5.11). During this deformation, the width of the specimen (w_f) remains constant, but the effective length changes from to l_f to $l_f^{'}$ due to the bending of the tows under the specimen weight (M_f). d is the vertical displacement of the fabric.

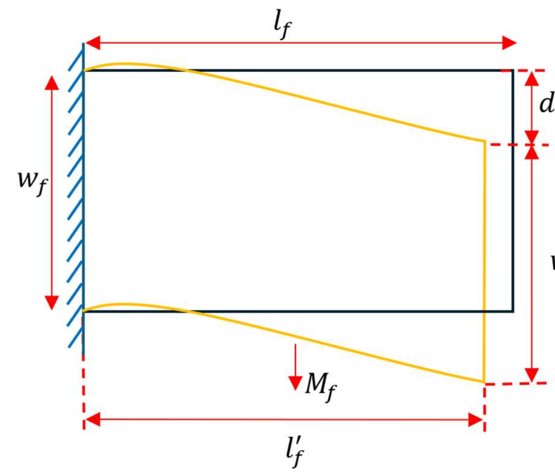

Figure 5.11: In-plane bending deformation of fabric reinforcement

5.3.2. Sample Preparation

Three samples with an initial length, l_f of 450mm and an initial width, w_f of 250mm were prepared to test the in-plane bending stiffness of the pure-UDNCF. A thin stainless-steel plate with a smooth surface (assumed to be frictionless) was selected to fix the fabric. First, a rubber strip with a thickness of 2mm was glued to one side (right) of the steel plate (see Figure 5.12a). Subsequently, a sample with dimensions of 250×450mm^2 (with a clamping region of 30×250mm^2) was placed on top of the steel plate close to the left side, as shown in Figure 5.12b. A thinner rubber strip was then placed on top of the sample on the left side (see Figure 5.12c). A Perspex plate was placed on the top of the entire setup (see Figure 5.12d). To minimise the friction between the fabric and the Perspex plate, the thickness of the rubber strip at the fabric-free edge (right side) was chosen to be 2mm because the initial thickness of a single-layer pure-UDNCF is approximately 1.1mm (see Table 3.1). The thickness of the rubber strip on the fabric fixed side (left side) was selected to be less than the other side (i.e., the total thickness of the rubber strip and the fabric should be approximately equal to 2mm) to maintain a uniform gap between the steel and Perspex plates.

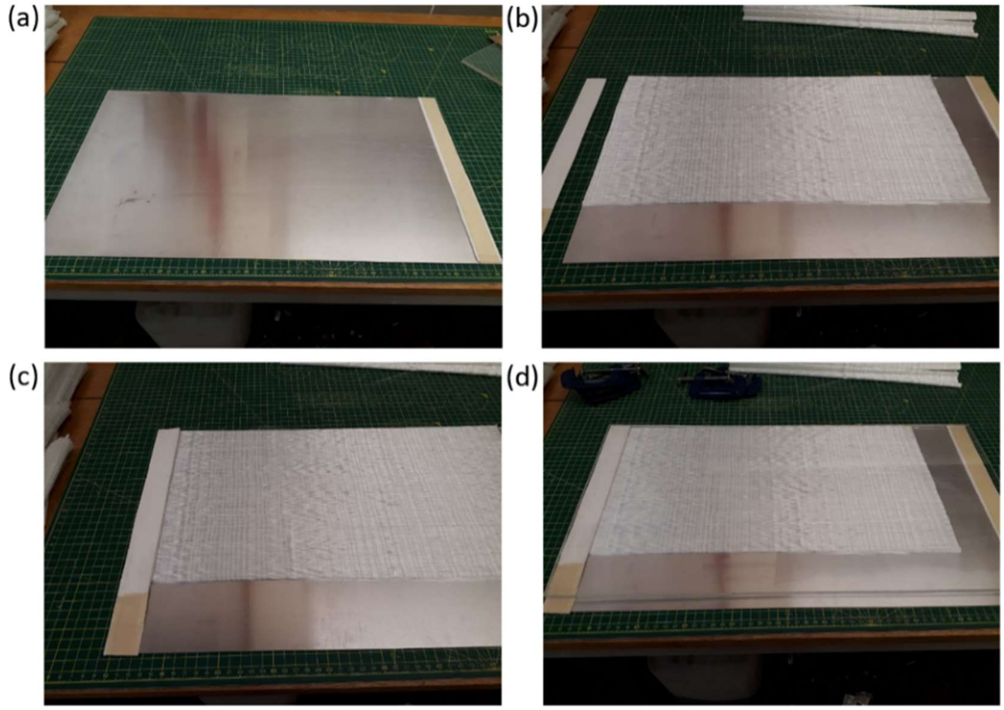

Figure 5.12: Steps to develop a setup for evaluating in-plane fabric bending of fabric reinforcements

The setup was tightened using Glamps (see Figure 5.13a). Two extra G-clamps were fixed to the middle of the setup (top and bottom) to prevent fabric movement before reaching the vertical position i.e., reduce the thickness between the stainless steel and Perspex plates. Before performing the test, the setup alignment was verified (see Figure 5.13b). To measure the vertical displacement of the fabric, a ruler was attached at the fabric-free end (see Figure 5.13a)

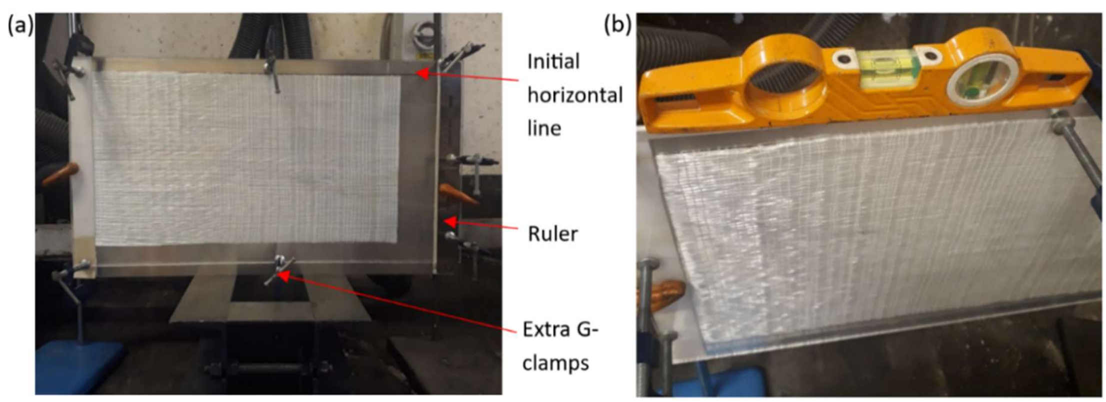

Figure 5.13: (a) Complete setup (b) Check alignment of the setup before performing the test

5.3.3. Test Procedure

After holding the setup vertically as shown in Figure 5.13a, the two extra G-clamps (top- and bottom-middle) were removed, and the sample was given some time (2 min) for vertical displacement. The vertical displacement was observed to be time-dependent; For example, at the beginning (within 10 seconds) the measurement was 30mm and after about 2 minutes, the measurement increased to 35mm. To facilitate the vertical displacement of the fabric, the setup was mounted on a vibration table. The test was conducted for one minute on a vibration table with a vibration frequency of 4 Hz and the resultant vertical displacement was measured.

5.3.4. Results and Analysis

Figure 5.14 shows a pure-UDNCF sample deformed in the in-plane bending. There is a slight curvature close to the fixed edge of the fabric; beyond that, the tows are present straight and parallel to each other. The curvature along the length of the fabric provides a qualitative insight into the bending stiffness. Figure 5.14 shows how the top and bottom tows (at the fixed ends) of the specimen deviate from a straight line due to the in-plane bending. Furthermore, the deviations in both the top and bottom tows are the same, indicating that the pure-UDNCF exhibits uniform in-plane bending throughout the specimen. In addition, the width of the specimen remains constant, confirming that there is no strain in the stitch direction. Since pure-UDNCF has no stabilising fibres, its mechanical response is highly sensitive to its construction. This test setup facilitates isolating the bending characteristics without interference from tensile behaviour.

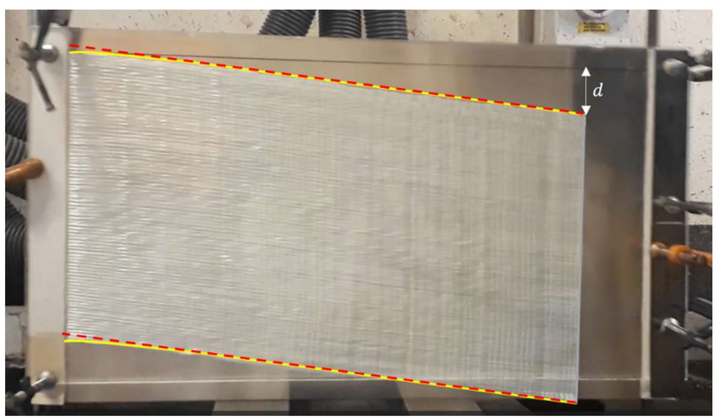

Figure 5.14: In-plane bending deformation of a pure-UDNCF specimen

Table 5.4 summarises the response of the fabric before and after introducing the oscillations. The vibration table induces a vertical displacement and helps to accelerate the settling process of the fabric, i.e., it might take longer for the fabric to fully conform to the shape. In addition, the vibration helps to minimise any friction between the fabric, the steel plate, and the Perspex plate, allowing the fabric to settle into a more relaxed and unstrained state (friction can reduce vertical displacement, resulting in an overestimation of in-plane bending stiffness). Table 5.4 shows that the vertical displacement of all three specimens improves significantly after 1 minute of vibration. This may suggest a reduction of friction between the sample/ steel plate/ Perspex plates or lower bending stiffness of the pure-UDNCF or both. However, the discrepancy between the vertical measurements after vibration indicates that friction is still present and affects the results. Suggestions for improving the reliability of novel in-plane bending test measurements are discussed in Section 5.3.4.1. The results of the improved test method can be used to quantify the in-plane bending stiffness of fabrics.

Table 5.4: In-plane bending test results of pure-UDNCF

Specimen No.	Specimen mass (g)	Vertical displacement, d (mm)		
		Within first 10s	After 2 min	After vibrating for 1 min
1	156.5	30	35	45
2	160.8	32	40	51
3	158.3	35	42	55

5.3.4.1. Suggestions for Test Improvement

To better observe the curvatures and vertical displacements, a grid can be marked on the fabric with a black Sharpie pen along with selected tows and stitches. The experiment can be recorded, and high-resolution imaging or video analysis tools can be used to trace the deflection curves. Multiple tows of the marked grid can be selected and averaged to improve the accuracy of vertical measurements. Furthermore, the experiment can be repeated with various specimen sizes to see how the vertical displacement changes with the length, width, and weight of the specimen. In addition, it is necessary to find the optimal vibration time and frequency for better in-plane bending of the fabric by minimising friction (this frequency may vary depending on the specimen size and the density of the fabric). For example, Figure 5.15 shows the in-plane bent pure-UDNCF specimen at a vibration frequency of 8Hz. The bottom edge of the specimen near the fixed end has begun to wrinkle (it is not clearly visible because the sample is in contact with the vibrating table at the bottom). These wrinkles can add error to the test by causing friction between the specimen and the Perspex plate. By considering all these factors, the experiment can be further improved. However, due to time constraints, it was unable to expand on this topic within the scope of this study. Transitioning from qualitative to quantitative assessments would be a logical next step in improving this method.

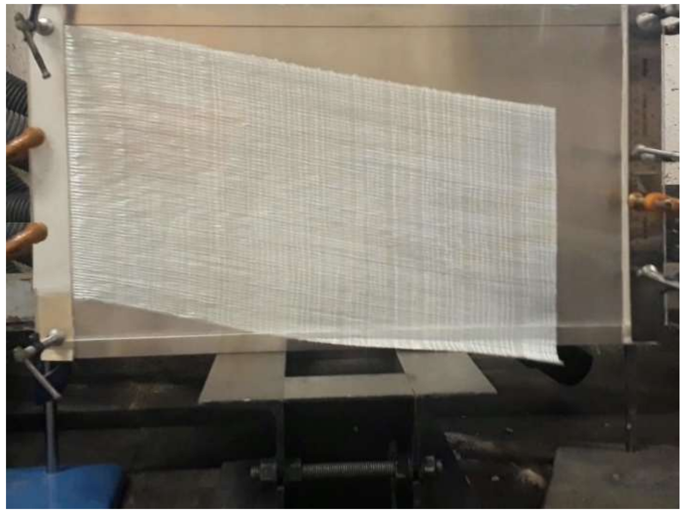

Figure 5.15: In-plane bent pure-UDNCF specimen at 8Hz vibration frequency

5.4. Chapter Summary

Out-of-plane bending test (cantilever bending test) was performed on the three fabrics i.e., plain-woven, twill-woven and pure-UDNCF. The results revealed that the pure-UDNCF has a significantly higher flexural rigidity in the warp direction than the woven fabrics (approximately 1.5 and 23 times higher than twill and plain-woven fabrics, respectively) due to the dense tow alignment with the non-crimp structure. However, the bending stiffness of pure-UDNCF in the weft and bias directions is almost negligible. Both plain-woven and twill-woven fabrics show a balanced bending stiffness in both warp and weft directions, and the flexural rigidity of twill-woven fabric is approximately 14 times that of plain-woven fabric.

The novel in-plane bending experiment is a simple and effective method to qualitatively assess the in-plane bending behaviour of pure-UDNCF. In the experiment, the curvature of the tows near the fixed edge of the fabric, i.e., deviation from the straight line, provides a qualitative measurement of in-plane bending stiffness. In addition, the consistent bending curvature of the specimen reflects the inherent uniformity of the pure-UDNCF material and the controlled boundary conditions of the experiment. This uniform curvature also validates the reliability of the experimental setup in isolating and analysing the in-plane bending properties. The in-plane bending response is essential for understanding the fabric behaviour in forming and other structural applications. Section 5.3.4.1 suggests methods to improve the in-plane bending test to obtain reliable data. This test can be used as a starting point for future comprehensive quantitative assessments of in-plane bending in engineering fabrics.

Chapter 6 Forming Experiments and Analysis

6.1. Introduction

The results of characterisation tests of engineering fabrics, such as tensile, shear, and bending tests, provide key material properties that can be input into numerical forming models. These numerical models simulate fabrics under different forming conditions, allowing researchers to predict deformation behaviour and potential defects under different fibre orientations prior to actual production. However, these numerical models need to be validated against the experimental results to ensure reliability and accuracy. Therefore, forming experiments are critical for bridging the gap between theoretical and numerical models and practical applications.

Experimental forming of engineering fabrics involves physically shaping the material into complex geometries to assess its real-world behaviour during processing. This chapter focuses on the hemisphere-forming and analysis of pure-UDNCF. During the forming process, it allows the direct observation and measurement of the fabric response to forces such as tension, compression, shear and bending. A key aspect of comparing the output of numerical models with experimental data is to examine fabric deformations such as shear angles and stretching in the stitch direction at selected locations on the pure-UDNCF. Excessive tensile or shear deformation can cause defects including wrinkling, voids and fibre misalignment. By comparing these local measurements, i.e., shear angles and stitch stretching between the numerical model and experimental data, researchers may assess the accuracy of the model and make changes to increase prediction accuracy [100] [154]. In addition to validating models, preforming experiments are necessary to achieve specific design and performance within budget constraints. Minimising defects leads to higher-quality components and efficient manufacturing processes.

The structure of the rest of this chapter is as follows: Sections 6.2 discuss the experimental method of hemisphere forming of pure-UDNCF. Post-analysis of formed hemispheres is summarised in Section 6.3, and the methods of evaluating the shear angles and stretching in the stitch direction at selected locations are detailed in Section 6.4. Section 6.5 presents the results and analysis of hemisphere forming of the pure-UDNCF and the chapter summary is provided in Section 6.6.

6.2. Experimental Method

6.2.1. Forming Set-up

The punch and die forming method was selected to form the pure-UDNCF into a hemispherical shape. Figures 6.1a&b show the 3D model (sketched using Autodesk Fusion 360 [225]) and the actual setup, respectively. The dimensions of the punch and die are given in Figures 6.1c&d. According to the University of Glasgow setup, the gap between the punch and die is 2mm (Figure 6.1d). Therefore, a maximum of two layers was selected for the forming process of the pure-UDNCF (the thickness of the fabric is around 1.1mm, see Section 3.2).

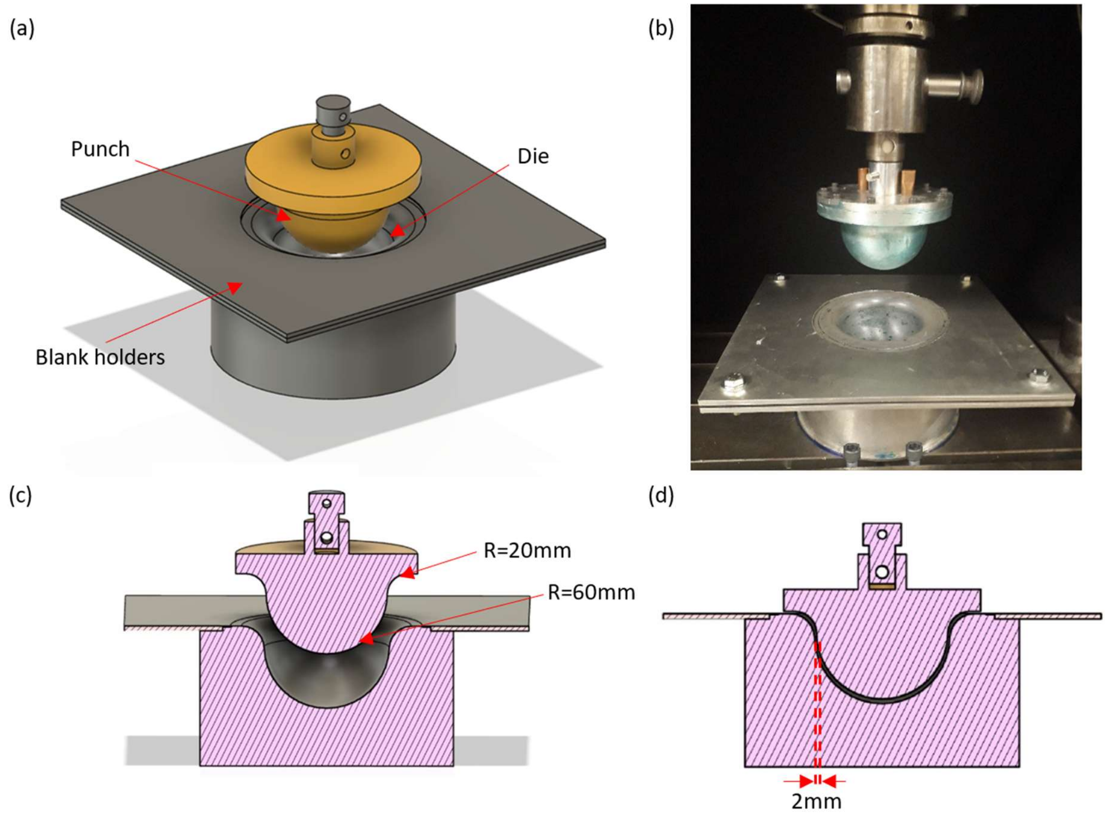

Figure 6.1: The punch and die forming setup (a) 3D model (b) actual setup (c) and (d) cross-section of the 3D model (dimensions indicated)

6.2.2. Sample Preparation and Testing

Square-shaped fabric samples of pure-UDNCF with dimensions of 320×320mm^2 were cut in the warp/weft and bias (45˚) directions (see Figure 6.2). Before placing the specimens, the surfaces in the punch and die were cleaned with acetone and double coatings of the release agent (PVA mould release agent) were applied to facilitate the removal of the specimen (see Figure 6.3). The PVA was allowed to dry completely for about 15 minutes before forming the fabric. Fabrics with different tow-stitch orientations were used to form the mono (stitch direction at 0˚ and 45˚) and bilayer (0˚/90˚, +45˚/-45˚ and 0˚/45˚) hemispherical specimens.

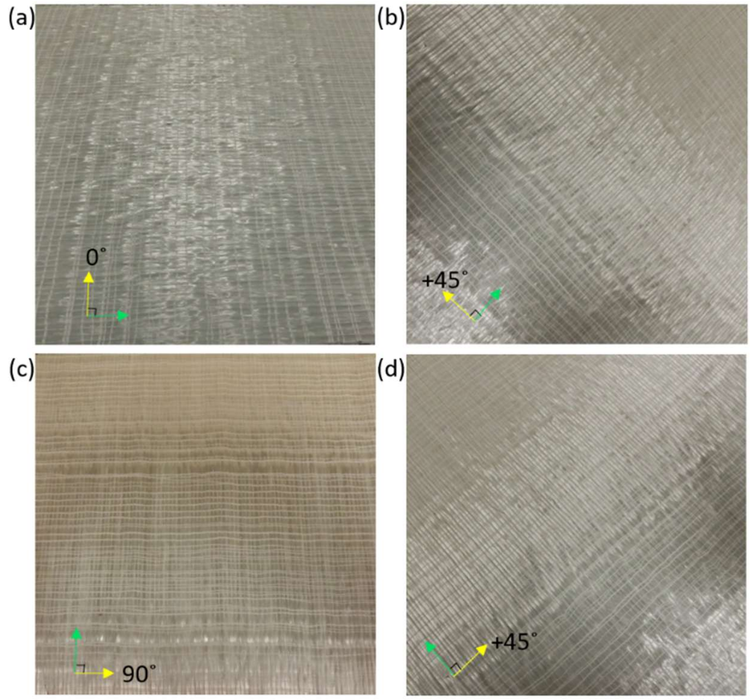

Figure 6.2: Fabric samples with different tow and stitch orientations, the yellow and green arrows indicate the initial chain-stitch and the tow directions, respectively.

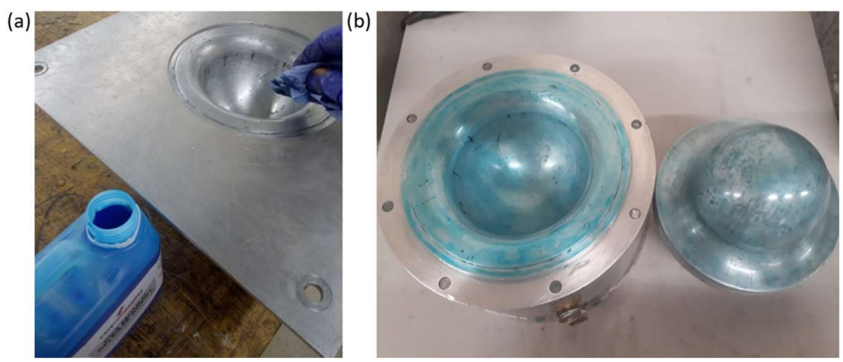

Figure 6.3: PVA release agent (a) applying (b) allowing to dry completely

A hemisphere punch tool consisting of a 60mm radius and a cavity with a 2mm edge fillet was used to form pure-UDNCF (Figure 6.1). A square-shaped blank was placed over the cavity and constrained by a blank holder weighing 2 kg, which provided 126 Pa of static pressure. Four bolts are placed on the four corners of the blank holder (see Figure 6.4). Note that these mounting bolts are not tightened and are only used to maintain the relative translational position of the two plates together. The setup was securely fixed to the test bed using bolts as visible in Figure 6.4 to prevent any movement during the forming process. The fabric was then formed on a Zwick Z250 tensile testing machine mounted with a 250kN load cell at a displacement rate of 50mm/min. The preforms were formed via two fixation methods discussed in Section 6.2.3.

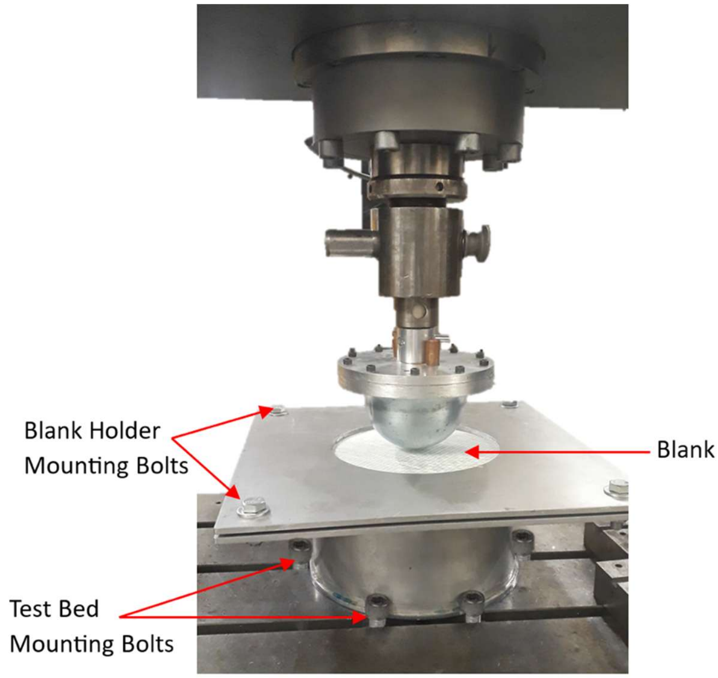

Figure 6.4: Complete fabric forming setup

6.2.3. Fixation Methods

When pressure is released after punching, the fabric tends to return to its original shape. Fixation techniques help maintain the desired shape and facilitate the handling of formed specimens during post-forming analysis. Two different fixing methods were used for pure-UDNCF after forming the hemispherical shape and are discussed in detail in the following sections.

6.2.3.1. Acetone/Epoxy Solution Method

This method involves fixing the fabric without changing its behaviour, i.e., the fabric is first formed, the male tool is removed and then the preform is fixed with an acetone/epoxy solution. This method allows the fabric layers to move freely during forming. After forming the fabric into the desired shape, the specimen is fixed by applying the solution. This creates a more stable structure that can be further handled and processed. The method is as follows.

The punch was moved upward following a few minutes of holding the formed fabric under an initial 2kN load. Note that the fabric has now formed a hemispherical shape. To fix or freeze the shape, acetone/epoxy solution (Epoxy 10% by weight) was applied using a wash bottle (see Figure 6.5). The composition of the solution is given in Table 6.1 (Note that a few specimens were examined after curing with less than 10% epoxy in acetone solutions i.e. 0.5%, 1% and 5%. Following drying, the formed specimens indicated that the amount of epoxy added was insufficient to retain the shape and bond two layers of thick fabric together). The load was again applied and allowed to cure for 24 hours (note that the punch was first moved down and a load of 2kN was applied for 30 minutes. The machine load was then released, and the punch and weight of approximately 0.2kN (see Figure 6.6) were kept on the top of the blank for 24 hours).

Figure 6.5: Appling acetone/epoxy solution using a wash bottle

Table 6.1: Composition of the Acetone/ Epoxy solution

Component	Added Amount (g)	Mixing %
Epoxy Resin (IN2 Epoxy Infusion Resin, EasyComposites EP-IN2-S-1)	5	8.8
Hardner (AT30 Slow Epoxy Hardener, EasyComposites AT30-S-0230)	1.5	2.7
Acetone (EasyComposites ACTN-05)	50	88.5

Figure 6.6: Applying 0.2kN load during curing

After 24 hours, the formed hemispheres were removed from the moulds and kept for a couple of hours for further air-drying i.e., until the acetone odour completely disappeared. The weight of each specimen was then measured, and the amount of epoxy resin absorbed was calculated by subtracting the initial weight of each fabric used for forming (discussed in Section 6.5.1). Due to time constraints, only one specimen from each mono (stitch direction at 0˚ and 45˚) and bilayer (0˚/90˚, +45˚/-45˚ and 0˚/45˚) was formed using the acetone/epoxy fixation method. Figures 6.7a&b, show a formed monolayer specimen (45˚) of pure-UDNCF and the method of storing the specimens, respectively.

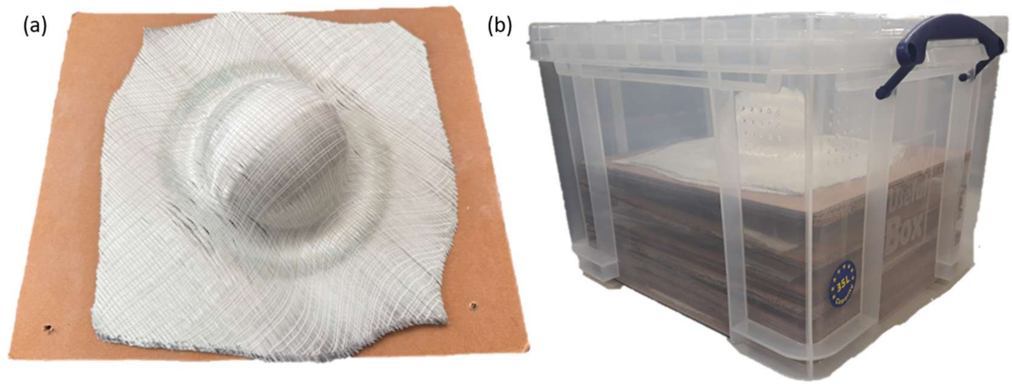

Figure 6.7: (a) Formed monolayer (45˚) specimen of the pure-UDNCF specimen using acetone-epoxy method (b) Method of storing the specimens

6.2.3.2. Adhesive Spray Method

This fixing method involves changing the behaviour of the fabric before forming i.e., applying an adhesive spray between two layers before forming the fabric. After applying the adhesive spray, pressure is applied to ensure proper contact between the adhesive and the fabric surfaces. Once the adhesive begins to cure i.e., when a chemical reaction solidifies the adhesive to form strong bonds, the applied pressure conforms the fabric to the desired shape. Therefore, the adhesive layer prevents the sliding of plies by increasing inter-ply friction from the beginning and improves the structural integrity. The method is as follows.

A thin layer of spray adhesive (3M Super 77) was applied to the surface of two fabric pieces and was allowed to dry for 30 seconds. The two fabrics were then assembled and positioned for pressing to form hemispherical specimens. This method can only be used to form multilayer specimens, in this case, bilayer specimens, as the spray is applied between two layers. Three bilayer specimens (0˚/90˚, +45˚/-45˚ and 0˚/45˚) were formed using the adhesive spray method and Figure 6.8a shows a formed hemispherical-shaped bilayer (+45˚/-45˚) pure-UDNCF sample. Selecting a suitable adhesive spray is important because some fail to retain the shape of the specimen over time. Figure

6.8 compares two specimens with the same orientation of fabrics formed using two different adhesive sprays. The 3M Super 77 applied specimen shows the desired hemispherical shape (Figure 6.8a) whereas the specimen formed with 3M Spray Mount (Figure 6.8b) shows a distorted/relaxed shape. Therefore, 3M Super 77 adhesive spray is recommended for forming bilayer pure-UDNCF specimens.

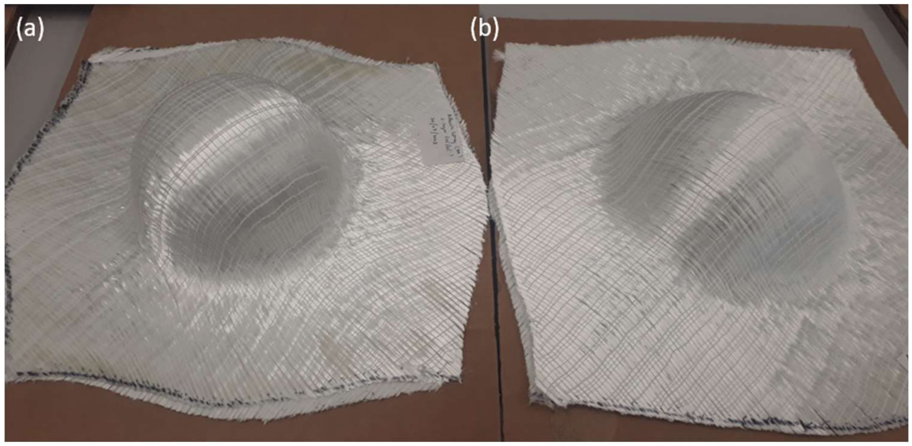

Figure 6.8: Formed bilayer specimens (+45/-45) using different adhesive sprays (a) 3M Super 77 (b) 3M Spray Mount

6.3. Post-Analysis Techniques

After forming the pure-UDNCF, the next step is to measure the fibre angles and strains in the stitch direction of the formed components. This enables the experimental forming results to be later compared with the numerical simulations, leading to the validation of the accuracy of the model. Three approaches, i.e., Manual, Structured Light Scanning (SLS) and Laser Scanning methods, were explored to evaluate stretching in the stitch direction and the fibre angle measurements of the formed hemispheres. Manual measurement methods provide simplicity and cost-effectiveness. However, the main drawbacks are limited precision, and inefficiency in handling complex hemispherical geometry (discussed in Appendix L). Therefore, this study moved to digital scanning methods that can provide higher accuracy in capturing the geometry of the formed component than manual measurements. When scanned with SLS, the formed hemispheres were not sensitive enough to accurately capture the complex pattern of the pure-UDNCF, and the texture appeared as a solid surface (see Appendix M). Therefore, the study concentrated on scanning the formed hemispheres with a 3D Laser Scanner, as detailed in Section 6.3.1.

6.3.1. Laser Scanning

Given the challenges associated with SLS for materials like pure-UDNCF, an alternative scanning method that can handle these issues more effectively is a 3D Laser Scanner with specialised equipment for complex materials. This study used an EinScan H 3D Laser Scanner at the University of Glasgow (see Figure 6.9a), which has many advantages including fast scanning, full-colour reproduction, portability and ease of use. All the hemispheres formed using the two fixation methods (8 specimens) discussed in Section 6.2.3 were scanned with an EinScan H 3D Laser Scanner (see Figure 6.9b). Appendix N describes the pre-settings and important information to be followed when scanning.

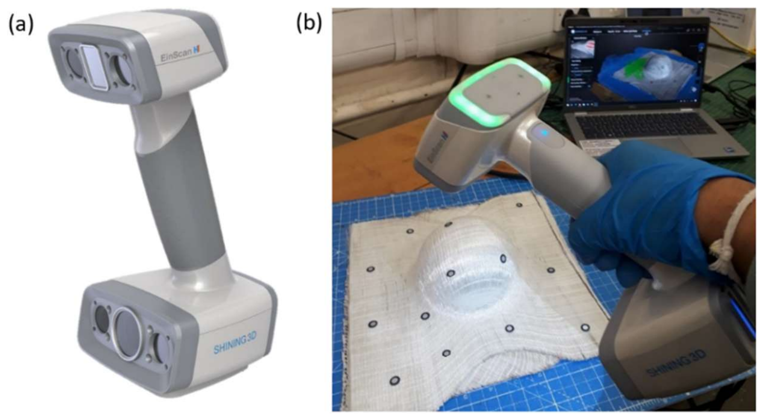

Figure 6.9: (a) EinScan H 3D laser scanner (b) Scanning the formed hemispheres

After scanning, the output (OBJ file) was uploaded to Autodesk 3ds Max [226] to measure the stretching in the stitch direction and tow-stitch angles at selected points (see Figure 6.10).

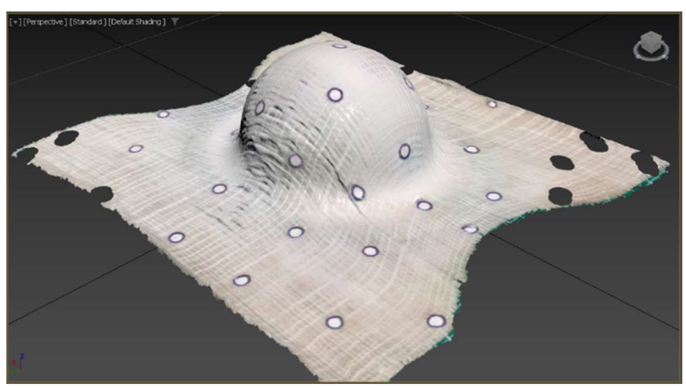

Figure 6.10: A model of a hemisphere in Autodesk 3ds Max.

6.4. Methods of Measuring Shear Angles and Stretching in the Stitch Direction

To determine the tow-stitch angle, 25 locations were selected from the total surface of the specimen along four radial lines (see Figure 6.11). Note that when these locations are marked on the 2D grid, as shown in Figure 6.11, the points inside the hemisphere deviate from the radial lines due to fundamental differences that occur when projecting through a 3D hemisphere. Table 6.2 summarises the XY coordinates of the selected points. To determine stretching in the stitch direction, 7 stitches were selected with respect to the selected locations (i.e., passing through or close). The names of the selected stitches vary depending on the initial stitch angle of the top surface of the specimen i.e., stitches at a 0˚ angle (straight-cut specimens) are marked A-G (see Figure 6.11a), whereas stitches at a 45˚ angle (bias-cut specimens) are marked P-V (see Figure 6.11b). The fibre orientation of the straight-cut and the bias-cut specimens are schematically represented in Figures 6.11c&d, respectively.

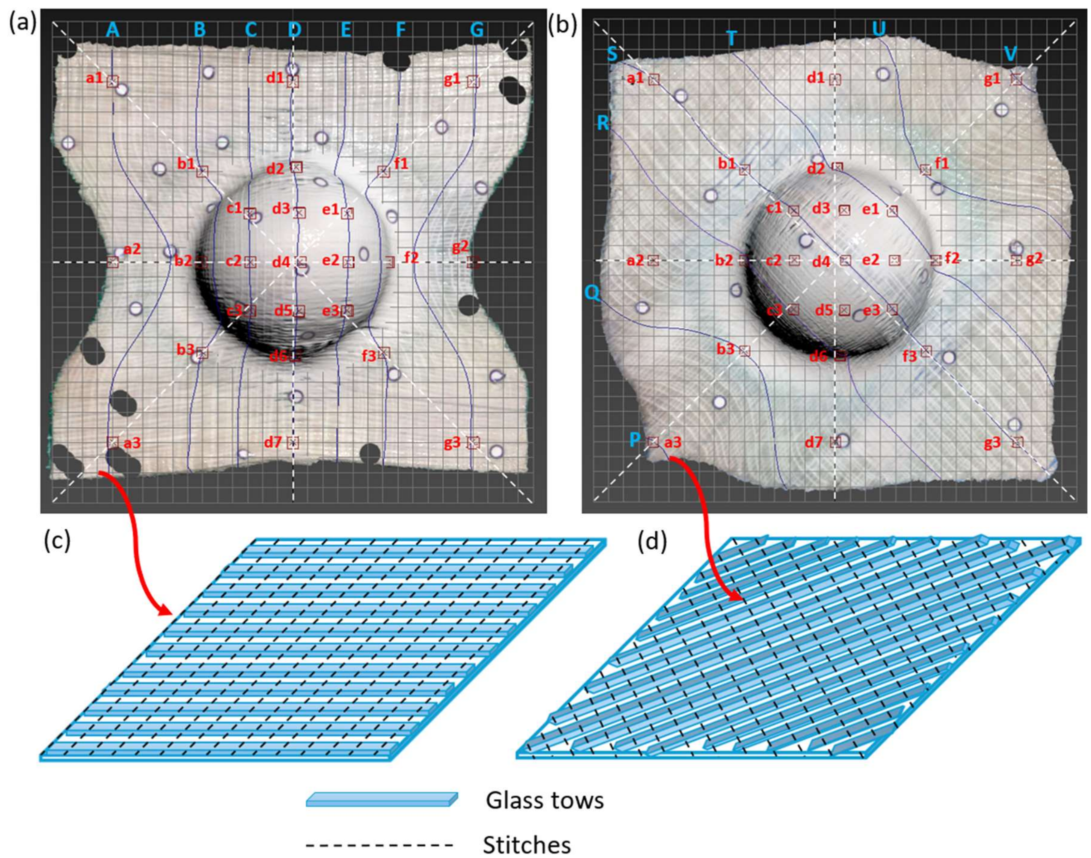

Figure 6.11: (a) & (b) Straight-cut and bias-cut specimens, respectively. Selected points and stitches are marked by the red crosses and the blue lines, respectively. The grid represents the initial dimension (320x320mm^2) of the square-shaped fabric specimen. (c) & (d) fibre orientation of specimens

Table 6.2: XY coordinates of the selected locations

	Location	Coordinate
1	a1	(-120,120)
2	a2	(-120,0)
3	a3	(-120,-120)
4	b1	(-60,60)
5	b2	(-60,0)
6	b3	(-60,-60)
7	c1	(-30,30)
8	c2	(-30,0)
9	c3	(-30,-30)
10	d1	(0,120)
11	d2	(0,60)
12	d3	(0,30)
13	d4	(0,0)
14	d5	(0,-30)
15	d6	(0,-60)
16	d7	(0,-120)
17	e1	(30,30)
18	e2	(30,0)
19	e3	(30,-30)
20	f1	(60,60)
21	f2	(60,0)
22	f3	(60,-60)
23	g1	(-120,120)
24	g2	(120,0)
25	g3	(120,-120)

All the selected stitches of the specimens with the stitches at 0˚ (A-G, see Figure 6.11a) are equal in length and their initial stitch length can be considered as 320mm. The specimens with the stitches at a 45˚ angle (see Figure 6.11b) show different initial stitch lengths and the length of the stitches depends on the location of the point. Therefore, finding the initial stitch length (to determine the strain in the stitch direction during forming) of the selected stitches is challenging. Some researchers have marked the grid using a marker pen before forming the fabric [227] [228] [229]. In this study, acetone/epoxy solution was used as the fixing method (discussed in Section 6.2.3.1), therefore, if the grid is marked using a marker pen, the marked lines may disappear due to dissolution in acetone. Marking a physical gridline is not appropriate for these specimens. The method used in this study to find the initial stitch length is as follows.

The initial length of the S stitch (diagonal stitch) can be calculated using the initial measurements of the specimen. 'd4' is the centre of the specimen and it remains in the same location before and after forming. The a3, b3, c3, e1, f1, and g1 are present on the diagonal tow and the distances between d4 and these points are constant as there is negligible stretching in the tow direction. The 3D distances (following the surface geometry) between the d4 and these points were measured using Autodesk 3ds Max [226]. Figure 6.12a shows the measuring distance between d4 and e1 points. Then, the e1' point (the initial position of the e1 point in square-shaped fabric samples before forming) was marked on the 2D grid based on the distance measured between d4 and e1 (see Figure 6.12b, highlighted in green colour). A line drawn in the bias direction on point e1' represents the initial length of the T stitch. Note that the T stitch is located along position e1, and the white-coloured straight lines marked at 45˚ on the 2D grid (P'-V') shown in Figure 6.12b represent the initial position and shape of the P-V stitches. Based on this method, the initial lengths of all the selected stitches were measured.

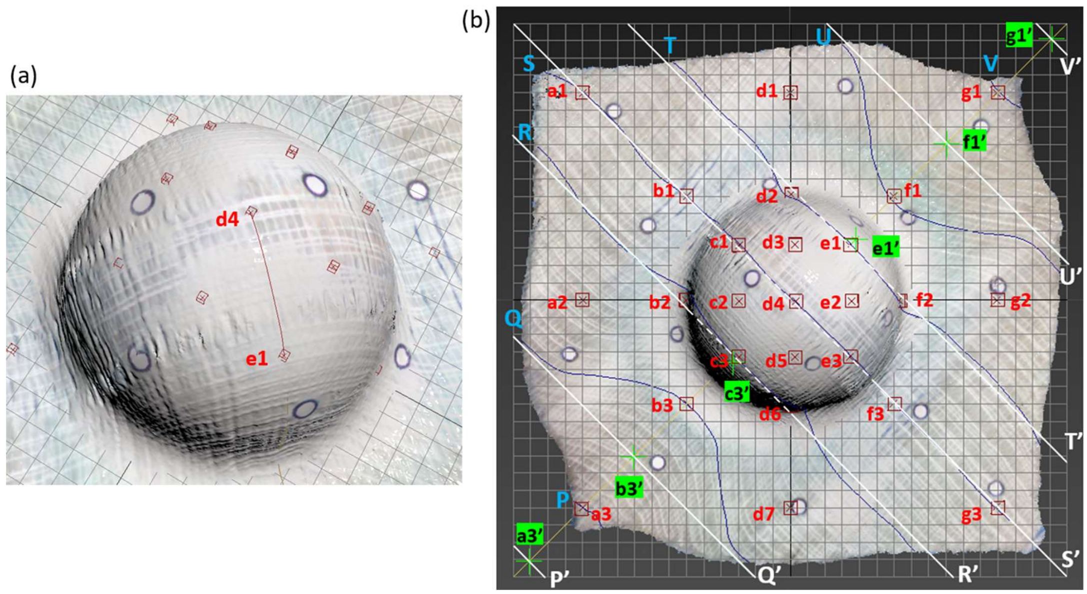

Figure 6.12: Estimation of the initial length of the selected stitches in the bias-cut specimens (a) Measuring the distance between d4 and e1 points (b) The initial positions of the selected points a3, b3, c3, e1, f1 and g1 are highlighted in green.

The initial length of the selected stitches (l') is measured using the lines drawn along the bias direction of the relocated points (P'-V', white lines in Figure 6.12b). The final lengths of the stitches (l) are determined by measuring the lengths of the curves drawn along the selected stitches after forming the fabric into a hemisphere (P-V, blue lines in Figure 6.12b). Both lengths can be measured using Autodesk 3ds Max [226]. The average engineering strain in the stitch direction after forming, γ, is calculated using Eq 6.1.

$$\gamma = \frac{l - l'}{l'} \tag{6.1}$$

In the pure-UDNCF, the initial tow-stitch angle of all points is assumed to be 90˚. The shear angle, θ, is determined by the difference between the initial tow-stitch angle ($\pi/2$), and the measured tow-stitch angle after forming, ω, as shown in Eq. 6.1.

$$\theta = \frac{\pi}{2} - \omega \tag{6.2}$$

The most significant step in the post-forming analysis is to measure the shear angle at each point (see Figure 6.11 and Table 6.2). Autodesk 3ds Max [226] facilitates measuring the shear angle of each point, including those on the surface of the hemisphere (see Figure 6.13).

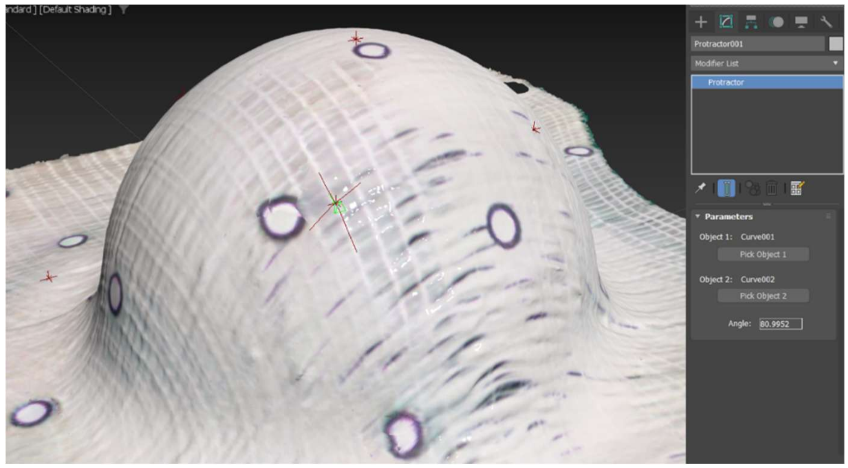

Figure 6.13: Measuring tow-stitch angle using Autodesk 3ds Max

6.5. Results and Analysis

6.5.1. Mass Comparison After Fixing

As discussed in Section 6.2.3, pure-UDNCF is fixed using two methods after forming into a hemispherical shape i.e., acetone/epoxy and adhesive spray methods. The initial weights of the fabrics were measured prior to forming and the final weight was measured after 48 hours of drying. Table 6.3 summarises the weight results of the 8 specimens. Monolayer specimens have a higher percentage of epoxy (3.3%) than bilayer samples (2.2%), even though the total absorbed epoxy is higher in the bilayer specimens. The bilayer sample has more material than the monolayer sample (twice the mass), resulting in a larger fibre volume to absorb the epoxy. In contrast, the monolayer specimens have less fibre volume, and the absorbed epoxy is concentrated in a smaller mass. As a result, a smaller amount of absorbed epoxy can cause a larger percentage increase relative to the initial weight of the monolayer sample i.e., the smaller volume of fabric results in a higher concentration of epoxy per unit mass. In addition, a weight comparison of the two fixing methods reveals that applying an adhesive layer resulted in less weight gain than using acetone/epoxy. This could be because the amount of adhesive used is less than that of the epoxy resin, or because the acetone has not fully evaporated from the specimens or both. A comparative analysis of all the data shows that the weight gain of all eight specimens was relatively low (less than 5%) for both fixing methods (i.e., acetone/epoxy and adhesive spray) when used to form a stable solid hemisphere.

Table 6.3: Percentage of epoxy or adhesive by mass of specimens after forming.

Fixation Method	No. of layers	Mass (g)			Epoxy or Adhesive %		
		Initial	After forming and 48 hours of drying	Difference	in each specimen	Average	SD
Acetone/Epoxy Solution	Single	133.4	137.8	4.4	3.3	3.3	0.1
		134.1	138.4	4.3	3.2		
	Double	269.5	275.5	6.0	2.2	2.2	0.1
		270.0	275.6	5.6	2.1		
		269.3	275.6	6.3	2.3		
Adhesive Spray		267.0	271.0	4.0	1.5	1.6	0.1
		266.1	270.3	4.2	1.6		
		268.2	272.7	4.5	1.7		

6.5.2. Acetone/Epoxy Fixing Method

6.5.2.1. Monolayer Forming

This method involves fixing the fabric after forming it into a desired shape without affecting the properties of the fabric during forming. Both the mono and bilayer specimens were formed using the acetone/epoxy (AE) fixing method. The adhesive spray method is not applicable for single-layer specimens since it only applies between the two layers. There are two forms of single-layer specimens i.e., specimens with stitches at 0˚ (referred to here as ‘ Mono/0/AE’) and 45˚ (referred to here as ‘Mono/45/AE’) orientations, and only one of each is used for the analysis.

Mono/0/AE

Figure 6.14a depicts the dimensions of the Mono/0/AE specimen, which is symmetrical in both the x and y axes i.e., two axes of symmetry. When the force is applied, the stitches, which are more flexible and aligned along the vertical direction, are drawn toward the die as the fabric curves, causing a reduction in width. According to Figure 6.14a, the initial width of the specimen decreases from 320mm to 290mm. Meanwhile, the glass tows, which are stiffer and aligned along the length of the fabric, bend to conform to the curved shape of the punch but resist stretching. A maximum of 37mm tow contraction on both sides along the diameter of the hemisphere, see the red circle area in Figure 6.14a. In the middle of the hemisphere, the total contraction along the stitch and tow directions are 13% and 23%, respectively. This difference is due to reduced contraction caused by stretching along the stitch direction in Pure-UDNCF. Therefore, a pure-UDNCF specimen with stitches at an angle of 0˚ produces a biaxially symmetric structure. In contrast, woven biaxial fabrics with 0-90° fibre orientation exhibit similar contraction along both fibre directions, resulting in four-axis symmetric structures (see Figure 6.14b [227]).

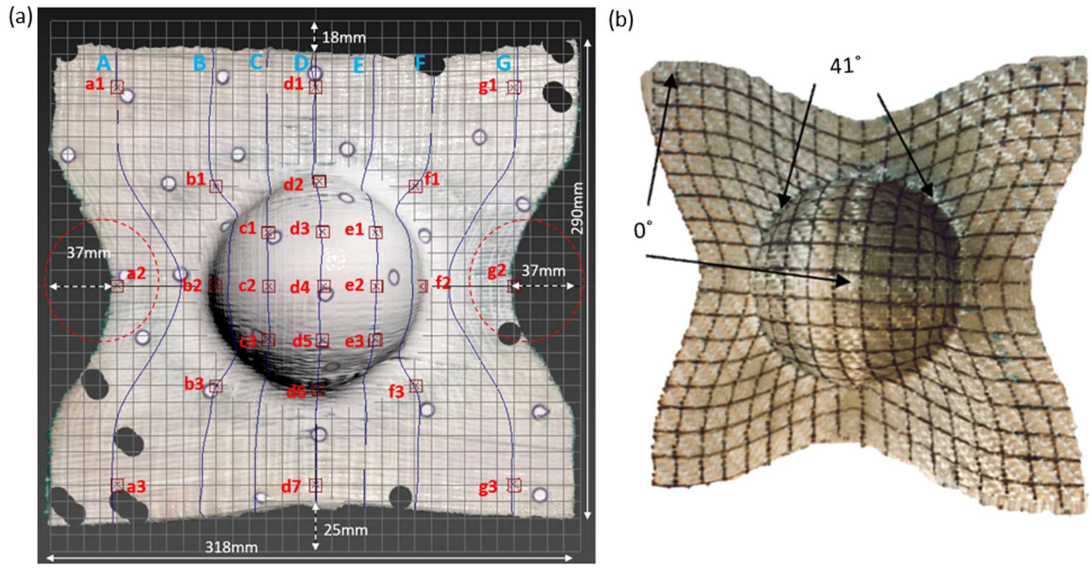

Figure 6.14: (a) Dimensions of the Mono/0/AE specimen (b) hemispherical forming of biaxial fabric with 0˚-90˚ fibre orientation [227]

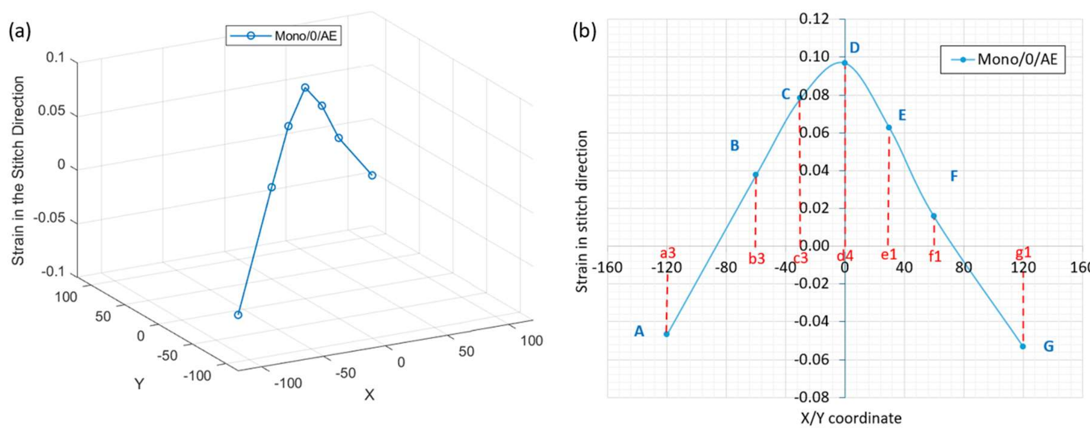

Figure 6.15: Strain in the stitch direction vs X/Y coordinates of the selected points located along the diagonal of the Mono/0/AE specimen (a) 3D and (b) 2D graphs

The average engineering strain in the stitch direction along selected lines (A-G, see Figure 6.14a) is calculated using Eq. 6.1 and summarised in Table O.1 in Appendix O. Note that this study focuses on the average strain along the stitch length i.e., the integral of all local strains combined instead of measuring the strain changes at every small point along the length of the stitch. This simplifies analysis and makes comparison easier with simulations. Figure 6.15a shows a 3D graph of strain in the stitch direction vs fabric surface (points located along the diagonal of the XY plane of the specimen, the centre of the hemisphere is considered as (0,0)) of the Mono/0/AE specimen. For a better observation, the 3D graph is shown as a 2D graph in Figure 6.15b. This graph does not include error bars because a single specimen was formed for each fabric orientation. As expected, the stitch along the centreline of the fabric (D, see Figure 6.14a) shows the maximum amount of stretch since it is located on the diameter of the hemisphere and the strain of the other stitches gradually decreases from the middle to the sides of the hemisphere. The stitches close to the edges of the specimen (i.e., A and G, see Figure 6.14a) show negative strain, implying that the tows are compressed (see Figure 6.16a). When the centre of the fabric conforms to a hemisphere, the stitches near the edges are pushed toward the centre of the fabric, causing compression, particularly if the edges do not need to stretch significantly to form the required shape. This leads to the stitches near the edges of the blank exhibiting negative (compressive) strain. Along the stitch direction, high stretching is clearly observed in the Mono/0/AE specimen (see Figure 6.16b), indicating a loss of continuity, creating gaps. Further, the compaction of glass tows is also observed perpendicular to the stitch direction close to the equator of the hemisphere i.e., generating the clustering or aggregation of tows, instead of being evenly spread out (see Figure 6.16b). This can result in regions with low fibre densities and others with high fibre densities, causing a lack of consistency. In addition, in-plain meso-scale tow wrinkling produced by excessive tension in the stitches is visible. Similar defects with different magnitudes were also observed in Schirmaier et al. [44] for quasi-UDNCFs during the hemispherical forming.

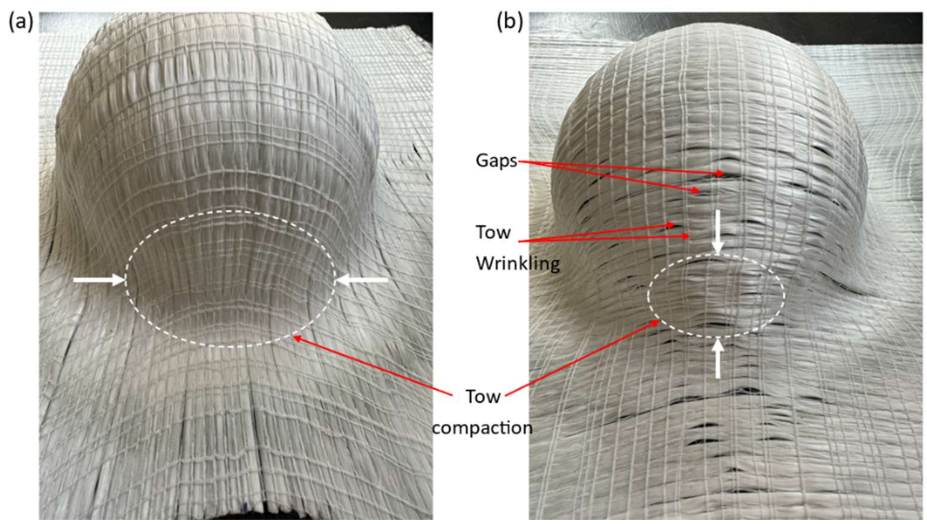

Figure 6.16: Defects of Mono/0/AE specimen along (a) tow direction (b) stitch direction

Shear angles at selected locations were measured using Autodesk 3ds Max [226] as stated in Section 6.4 and summarised in Table P.1 in Appendix P. Measuring the shear angles helps understand how the fabric deforms during forming, which is key for optimising manufacturing processes and ensuring the fabric accurately fits the desired shape. In addition, comparing the scanning results of the experimental forming i.e., shear angles and strain in the stitch direction with the numerical simulations is an important step in validating the accuracy of model predictions. Using MATLAB [230] a surface can be generated through the data points corresponding to the expected actual shear surface (interpolated surface by the ‘griddata’ using the 'cubic' method). Figure 6.17 shows the interpolated surface fitted to the shear angles of selected points (Table P.1 in Appendix P). Each red point corresponds to a specific location on the fabric, and the Z-axis indicates the measured shear angle. The purpose of fitting a surface is to obtain the overall shear behaviour across the fabric, which might not be immediately apparent from the raw data points. According to Figure 6.17, along diagonals, the shear angle increases from the edges to the equator and gradually decreases from the equator to the centre of the hemisphere. Adding more data points can improve the accuracy and smoothness of the surface.

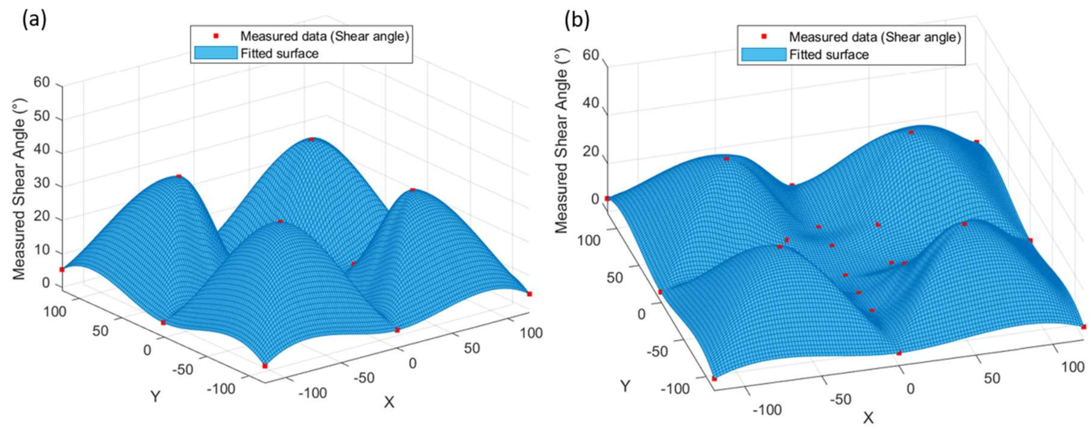

Figure 6.17: Measured shear angle at the selected locations of Mono/0/AE specimen, (a) and (b) The same 3D graph is shown from different perspectives. The red dots and the blue surface indicate the measured shear angles, and the shear surface generated using those points, respectively.

Mono/45/AE

In the Mono/45/AE specimen, the stitches and tows in the ±45˚ direction contract by 13% and 19%, respectively, and the deformation is almost symmetrical along the diagonals (see Figure 6.18). The average engineering strain along the selected lines (P-V, see Figure 6.18) is calculated using Eq. 6.1 and summarised in Table O.2 in Appendix O. These selected stitches of the bias-cut sample (P-V) are of different initial lengths. P and V stitches are the shortest because they are close to the edge of the specimen, whereas S is the longest since it runs along the diagonal of the specimen.

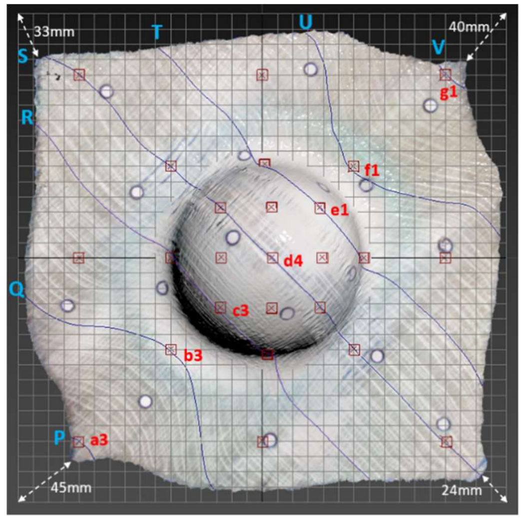

Figure 6.18: Mono/45/AE specimen

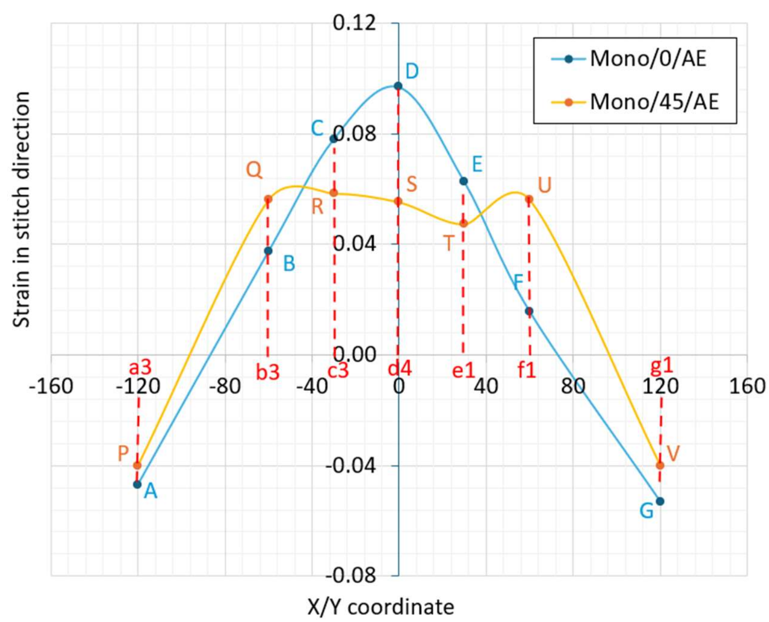

Figure 6.19: Strain in the stitch direction vs X/Y coordinates of the selected points located along the diagonal of the Mono/0/AE and Mono/45/AE specimens

Figure 6.19 shows a 2D graph of strain in the stitch direction vs X/Y coordinates of the selected points along the diagonal of the Mono/45/AE specimen. The short stitches close to the edges of the specimen (P and V) exhibit negative or compressive strain. The edges do not need to stretch as much as the rest of the fabric and may even be pushed inward as the material bends, leading to compression. Except for the stitches close to the edges, the remaining stitches are almost equal in strain because they are uniformly stretched as the fabric conforms to the shape of the hemisphere. Compared to the straight-cut specimen (Mono/0/AE), the stitches in the middle of the hemisphere of the bias-cut specimen show lower strain, however, the stitches near the equator (Q & U) of the bias-cut hemisphere show higher strain than the straight-cut specimen (see Figure 6.19). The stitches in the middle of the hemisphere of the straight-cut specimen experience high strain as the stitches are directly aligned with the principal directions (x and y) and need to stretch more to conform to the shape of the hemisphere. In addition, the difference in the initial length of selected stitches in the two specimens may also affect this. Note that at the selected points, i.e., a3, b3, c3, d4, e1, f1 and g1, all stitches in Mono/0/AE have an initial length of 320mm whereas the lengths of stitches in Mono/45/AE specimen vary from 25mm to 452mm (see Tables O.1 and O.2 in Appendix O).

Calculated shear angles at selected locations of the Mono/45/AE specimen are summarised in Table P.1 in Appendix P and the generated surface through the data points using MATLAB [230] is shown in Figure 6.20a. Along horizontal and vertical axes, the shear angle increases from the edges to the equator and then gradually decreases from the equator to the centre of the hemisphere whereas along the diagonal, the shear angle is almost negligible.

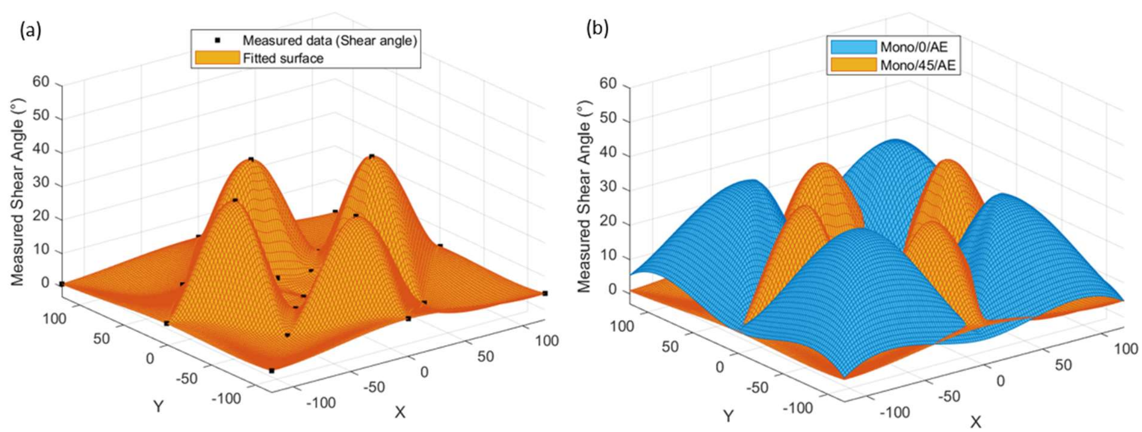

Figure 6.20: Fitted surfaces relative to the shear angle measured at selected locations (a) Mono/45/AE (b) Comparison of Mono/0/AE and Mono/45/AE specimens

The comparison of the shear angles at the selected 25 points in the two specimens shows that the straight-cut specimen (Mono/0/AE) shears along the diagonals and the bias-cut specimen (Mono/45/AE) shears along the vertical and horizontal axes (see Figure 6.20b). Figure 6.21a&b shows the dominating areas related to shear and tensile deformations of the two specimens. The regions between these two dominance areas consist of interactions of both types of deformations.

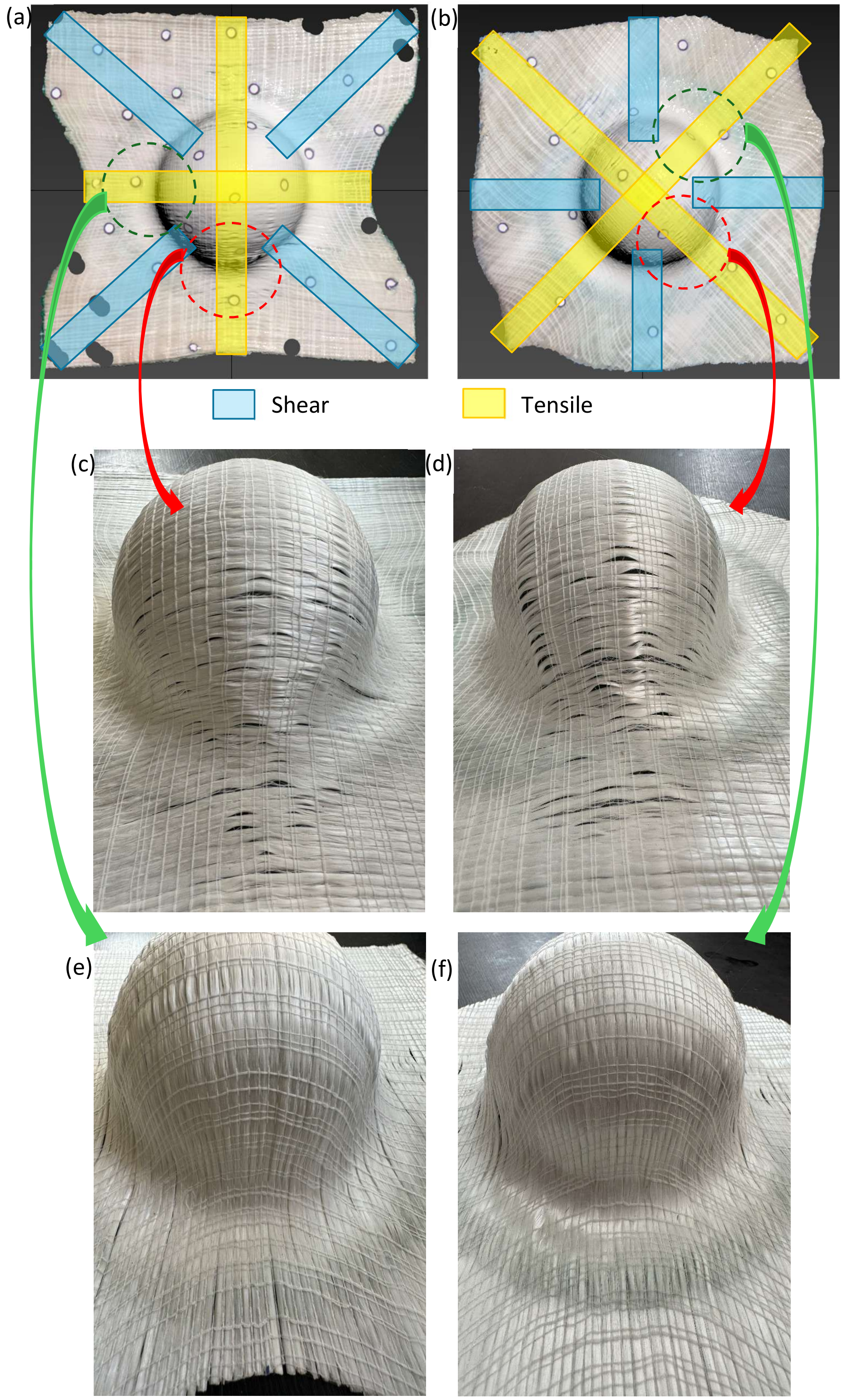

Figure 6.21: (a) & (b) dominant deformation regions (c) & (e) surface along the tensile regions of the Mono/0/AE specimen (d) & (f) surface along the tensile regions of the Mono/45/AE specimen.

Depending on the tow orientation to the applied force, the tensile and shear regions of the specimen may vary. In the Mono/0/AE specimen (see Figure 6.21a), tensile forces are primarily resisted along the horizontal (here horizontal and vertical relate to the orientation of the image on the page) axis (aligned with the tows), while shear occurs along the diagonals. The stitching stretches vertically as the tows carry the load. In contrast, the Mono/45/AE specimen (see Figure 6.21b) experiences tensile stretching along the diagonals and shear along the vertical and horizontal axes, as the tows are not aligned (45˚ angle) with the forming direction (the direction of force applied by the punch), leading to different strain distribution patterns. If further explained, in the Mono/0/AE specimen, tows and stitches are aligned along the same direction as the forming direction, i.e., parallel to the direction in which the fabric is being stretched or shaped over the tool. In contrast, the tows and stitches in the Mono/45/AE specimen are at a 45˚ angle relative to the forming direction.

Figure 6.21c&d compares the surfaces of the hemisphere in the high tensile stretching regions of the two specimens. It can be observed that variations in the stitch density affected the formation of defects in both specimens, i.e., regions with greater spacing between adjacent stitches appear to have larger gaps because there is less constraint on the motion of tows. In addition, the Mono/0/AE and Mono/45/AE specimens show similar defects, i.e., tow wrinkling and gaps, however, the size and quantity of the defects are comparatively higher in the Mono/45/AE specimen than the Mono/0/AE specimen. Even though the stretching in the stitch direction in the hemisphere region is reduced in the Mono/45/AE specimen (see Figure 6.19), the frictional forces acting on the specimen surface may be higher compared to the Mono/0/AE specimen i.e., as the fabric is formed, the tows experience friction from the contact surface (die and blank holder). This friction could be greater when the tows are not aligned with the forming direction (i.e., at 45°), as the tows are forced to slide and reorient themselves to fit the die shape. When comparing the two specimens along the other tensile axis (along the tow direction, see Figures 6.21e&f), Mono/0/AE shows higher tow compaction than the Mono/45/AE specimens. This could be because the Mono/45/AE specimen stretches more in the stitch direction than the Mono/0/AE specimen (see Figure 6.19, compare B & F stitches of the Mono/0/AE specimen with Q & U stitches of the Mono/45/AE specimen).

Figure 6.22 shows the forming force as a function of the punch displacement for monolayer straight and bias-cut specimens. The force is higher in the bias-cut specimen than the straight-cut specimen. Labanieh et al. [231] also observed an approximately 50% increase in forming force for bias-cut specimens of a woven fabric than for straight-cut specimens, during hemispherical forming with the same blank holding pressure and initial specimen dimensions and shape (see Fig. 4 in Labanieh et al. [231]). The results reveal this difference is due to the variation in tow contact lengths with the tooling surfaces for the two orientations. The radial tows in the bias-cut specimen have a longer contact length than the straight-cut (see yellow strips marked in Figure 6.21a&b). Labanieh et al. [231] further stated that the tow tension also depends on the contact angle at the holder corner i.e., the angle between the fabric tows and the corner of the curved surface they are draped over during the forming process. This angle is important because it can affect the frictional behaviour between the fabric and the tool surface, which in turn can affect the tension in the fabric. The longer contact length and high contact angle at the holder corner in bias-cut specimens cause higher friction forces, which leads to a higher forming force. As a result of the increased friction force, the bias-cut specimen may be more prone to defects, such as gap formation, than the straight-cut specimen.

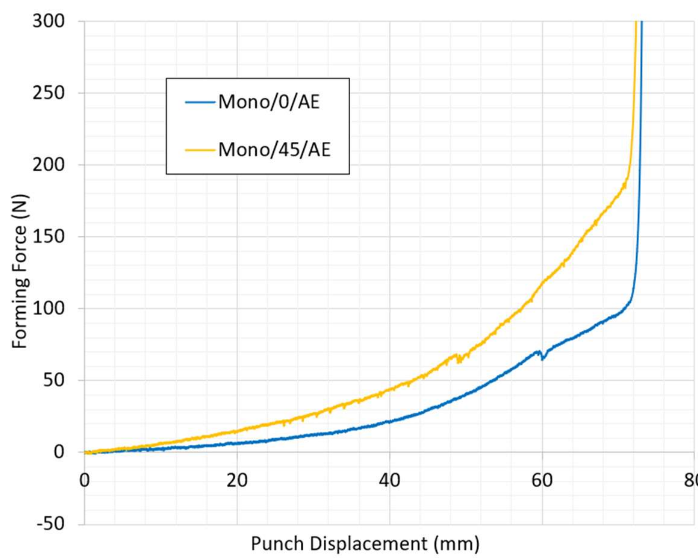

Figure 6.22: Forming force vs punch displacement of monolayer straight- and bias-cut specimens

6.5.2.2. Bilayer Forming

Bilayer specimens were formed using three different stacking sequences i.e., specimens with stitches at 0˚ & 90˚ (referred to here as ' Bi/0-90/AE'), +45˚ & -45˚ (referred to here as ' Bi/45-45/AE'), and 0˚ & 45˚ (referred to here as ' Bi/0-45/AE'). One specimen of each is used for this analysis.

Bi/0-90/AE

Figure 6.23a shows the dimensions of the Bi/0-90/AE specimen. Stitches of the top and bottom layers are present along the vertical and horizontal axes respectively (see Figure 6.23c). The specimen width close to the edges is high (i.e., 310mm) compared to the Mono/0/AE specimen (i.e., 290 mm, see Figure 6.23b). This may be due to the imposed frictional force caused by the relative drawing of the two fabric layers in opposite directions, i.e., the inter-ply friction effect. The higher formation force in the bilayer specimen than in the monolayer specimen indicates friction between the two layers due to different fibre orientations (see Figure 6.24a). Furthermore, imbalance contractions in the middle of the specimen along both the stitch and tow directions (see the red circle area in Figure 6.23a) indicate significant amounts of relative sliding between the two layers during forming. Note that in the acetone/epoxy method, fixing is applied after the fabric is formed.

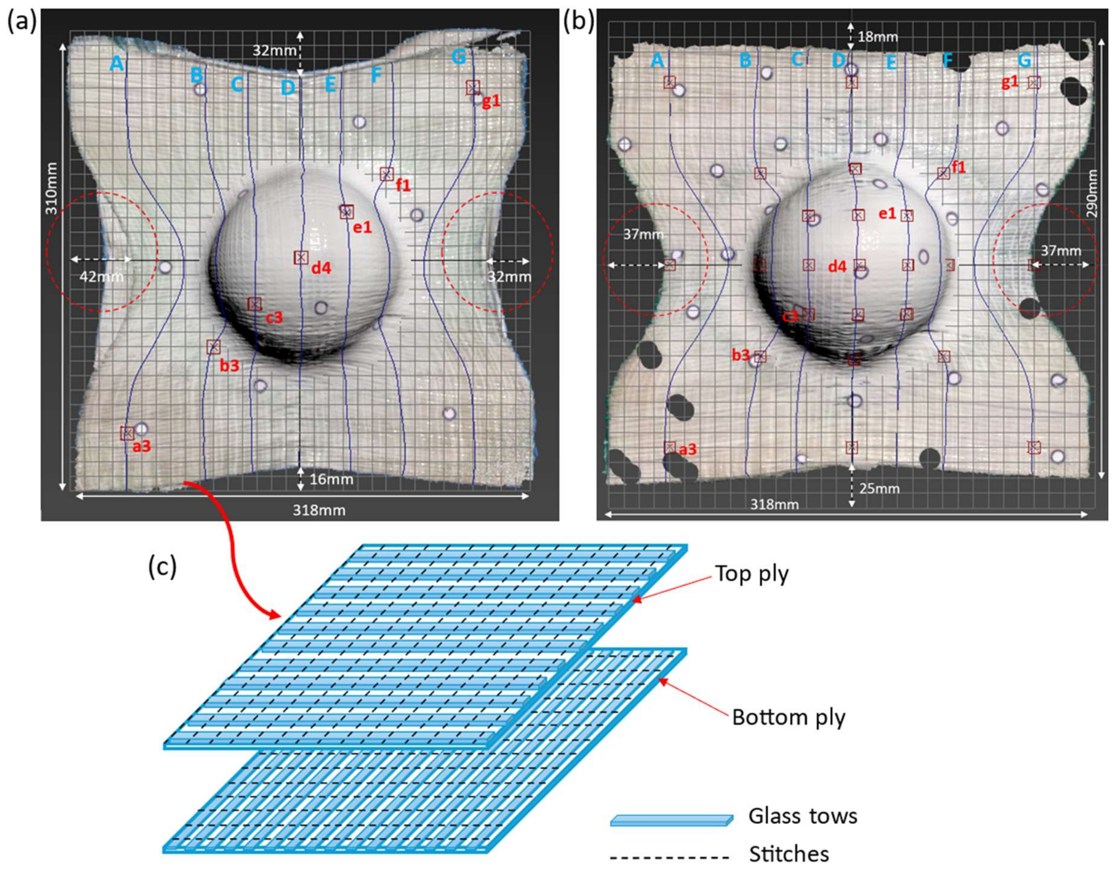

Figure 6.23: Dimensions of the specimens (a) Bi/0-90/AE (b) Mono/0/AE (c) Fibre orientation of two plies

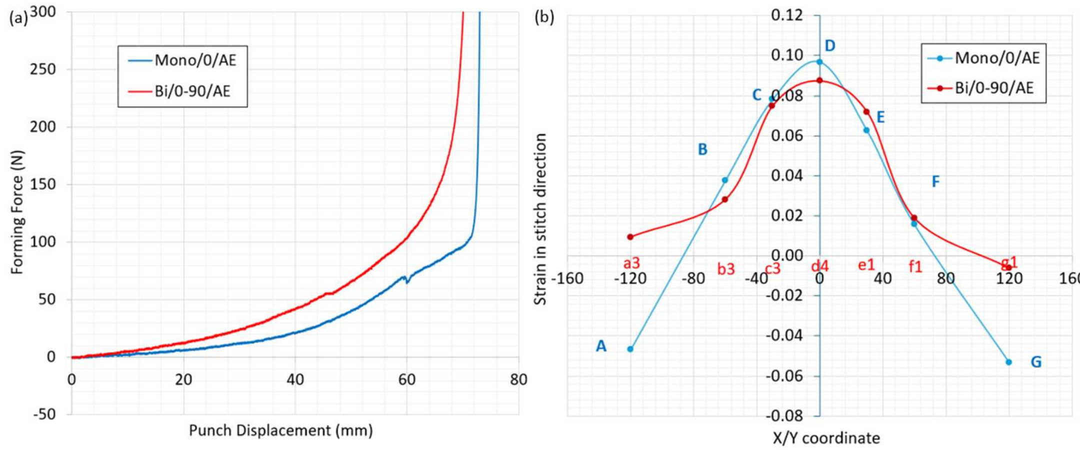

Figure 6.24: Comparison of Mono/0/AE and Bi/0-90/AE specimens (a) Forming force vs punch displacement curves (b) strain in the stitch direction vs X/Y coordinates of the selected points located along the diagonal

Calculation of engineering strains in selected stitches of Bi/0-90/AE is shown in Table O.1 in Appendix O. Figure 6.24b shows a comparison of stitch strain vs X/Y coordinates of the selected points along the diagonal of the Mono/0/AE and Bi /0-90/AE specimens. The bilayer specimen shows slightly lower stitch strain at the selected locations on the hemisphere surface than the monolayer specimen. When the two-layer specimen is deformed into a hemisphere, the layers begin to conform to the three-dimensional shape, but deform unevenly due to their different orientations, i.e., in the top layer, low-stiffness stitches are oriented in the vertical direction whereas in the bottom layer, high-stiffness tows are oriented along this same direction. As the top layer stretches, it encounters resistance from the bottom layer, which is much less compliant due to the stiff tows. The stitches close to the edges of the bilayer specimen show a strain increase compared to the monolayer specimen. This is probably due to the frictional interaction between the two layers (induced by the action of stitches in the bottom layer) reducing stitch drawing towards the die. Figure 6.25a shows the fitted surfaces for the shear angles at the selected locations of the Bi/0-90/AE specimen and Figure 6.25b compares the mono and bilayer specimens. The maximum shear angle achieved by the bilayer specimen (near the equator of the hemisphere) is lower than that of the monolayer specimen because the bottom layer oriented perpendicular to the equator can provide greater resistance to shear deformation.

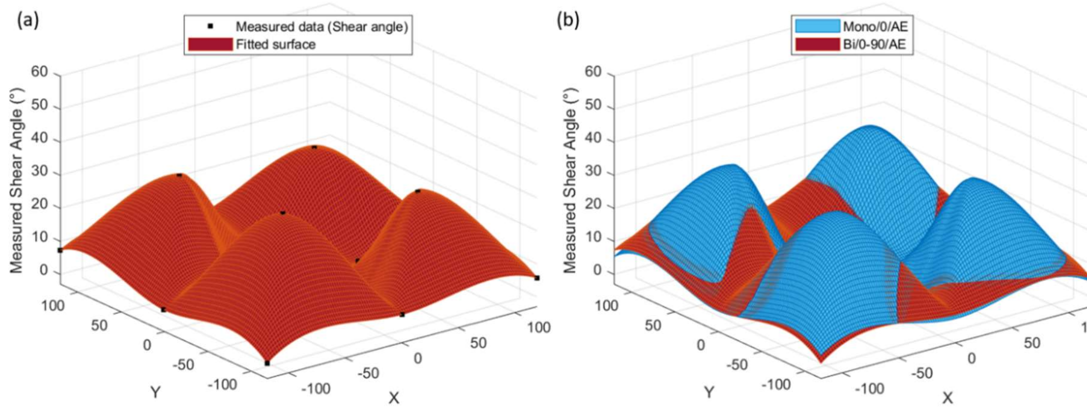

Figure 6.25: Fitted surfaces relative to the shear angle measured at selected locations (a) Bi/0-90/AE (b) Comparison of Bi/0-90/AE and Mono/0/AE specimens

Bi/45-45/AE

Figure 6.26a shows the dimensions of the Bi/45-45/AE specimen, where the stitches of the top and bottom layers are present in ±45˚ directions (Figure 6.26c shows fibre orientation of two plies). Compared to the Mono/45/AE specimen (Figure 6.26b), an increase in the perimeter shrinkage of the blank along the diagonal can be observed, i.e., in the single-layer specimen, the perimeter shrinkage along the diagonal is measured as 33mm and 24mm whereas the bilayer specimen shows 30mm and 45mm (see Figure 6.26a). This can be further observed by the strain measured in the stitch direction vs X/Y coordinates of the selected points along the diagonal of the two specimens (see Figure 6.27, the strain calculations are given in Table O.2 in Appendix O). The bilayer specimen shows lower average stitch strains than the monolayer specimen in the hemispherical surface, again implying that stitch stretching of the top layer is constrained by the high-stiffness tows of the bottom layer along the same axis. Increased stitch strain outside the hemisphere (in the flat surface) is probably a result of drawing the stitch towards the centre of the fabric due to tow bending in the opposite bias direction of the stitch. As a result of the stitch drawing (e.g. see stitch Q and U in Figure 6.26a), a significant increase in shear deformation can be observed near the edges of the vertical and horizontal directions of the bilayer (see Figure 6.28). Furthermore, as the sample moves beyond its initial dimensions (see the red circle area in Figure 6.26a, note that the grid represents the initial dimensions), a higher deformation in the vertical direction compared to the horizontal direction is observed. Therefore shear angles measured along the vertical direction are higher than in the monolayer specimen.

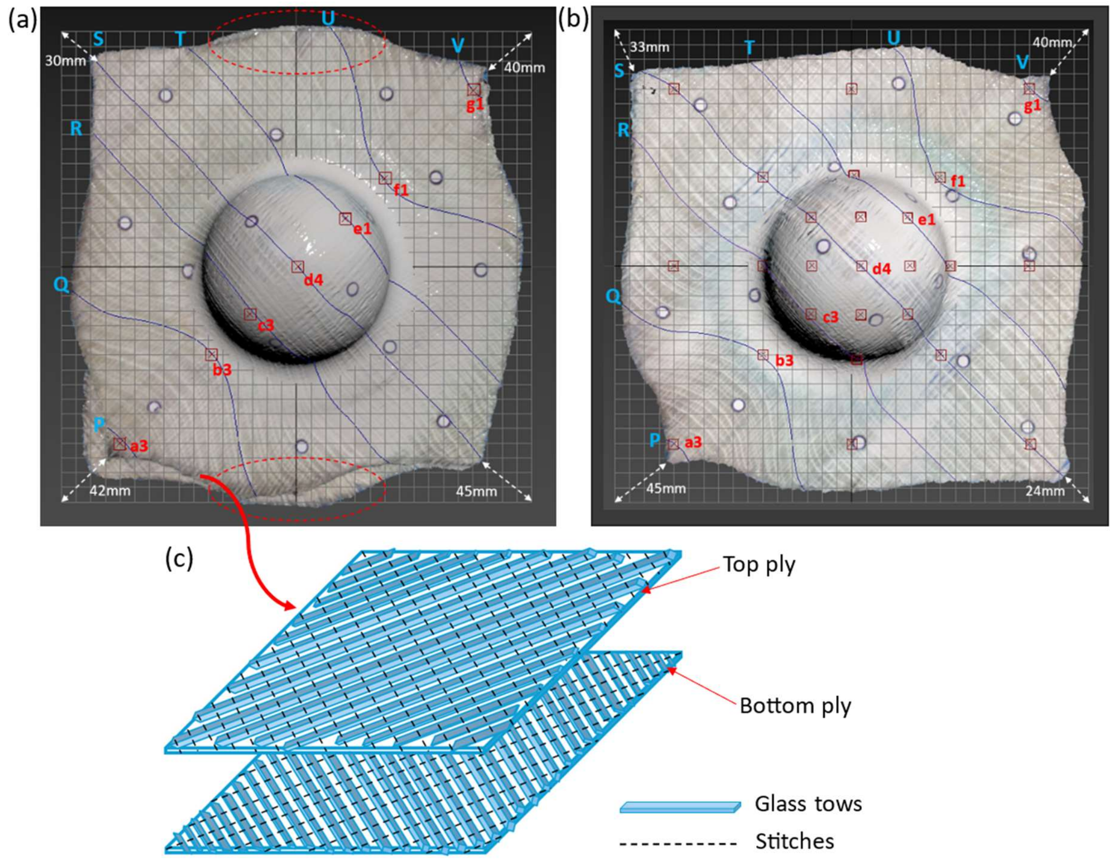

Figure 6.26: Dimensions of the specimens (a) Bi/45-45/AE (b) Mono/45/AE (c) Fibre orientation of two plies

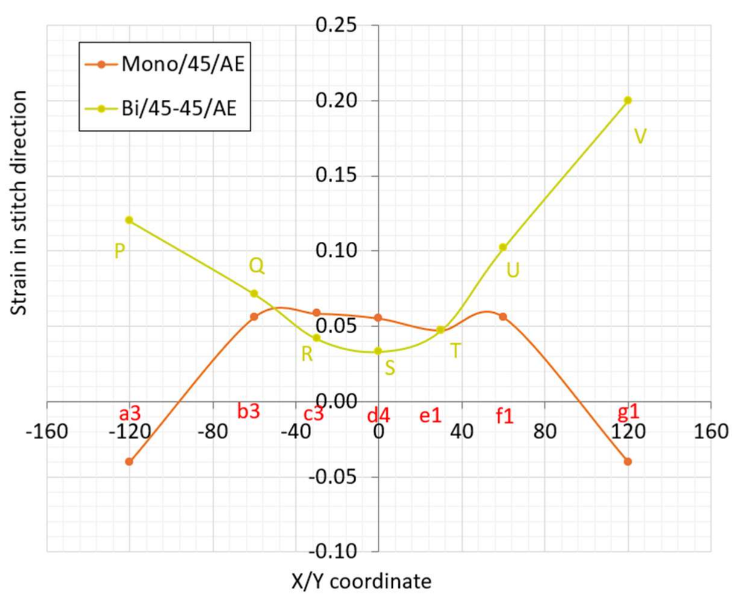

Figure 6.27: Strain in the stitch direction vs X/Y coordinates of the selected points located along the diagonal of the Mono/45/AE and Bi/45-45/AE specimens

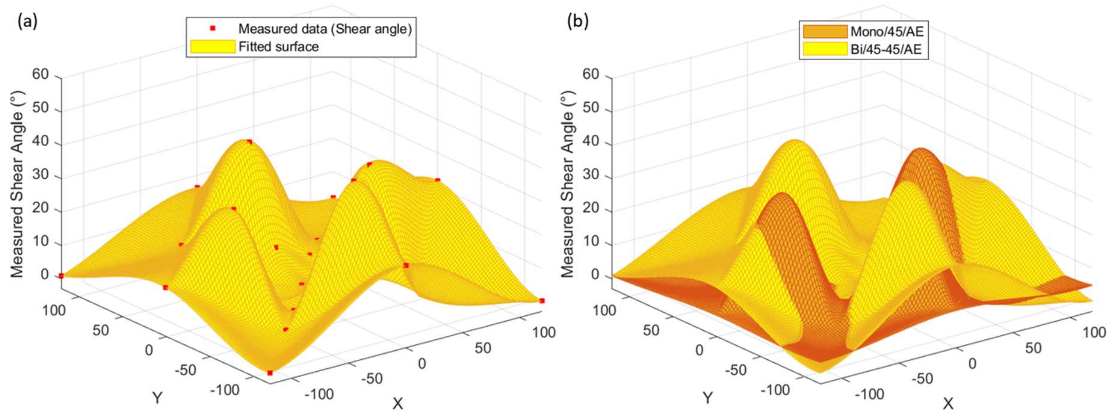

Figure 6.28: Fitted surfaces relative to the shear angle measured at selected locations (a) Bi/45-45/AE (b) Comparison of Bi/45-45/AE and Mono/45/AE specimens

Bi/0-45/AE

In the Bi/0-45/AE sample, the stitches of the top layer are orientated in the 0˚ direction and the bottom layer in the 45˚ direction (see Figures 6.29a and b). Allaoui et al. [232] formed a two-ply woven fabric in both 0˚/45˚ (i.e., the external and internal layers oriented 0˚ at 45˚, respectively) and 45˚/0˚ orientations using a prismatic punch. The same defects were observed in both specimens in the same areas; however, the amplitudes of the defects were higher in the 45˚/0˚ specimen compared with that of the 0˚/45˚ specimen (see Figs 7 and 11 in Allaoui et al. [232]). Because when a more defective ply is in the lower position, the compression exerted by the upper layer can cause a significant reduction in defect formation. In this study, a comparison of monolayer specimens shows that the amplitude and defect quantity of Mono/45/AE is higher than that of Mono/0/AE (see Figure 6.21c&d). Therefore, in the bilayer specimen of pure-UDNCF with 0˚ and 45˚ ply orientations, the 0˚ ply is stacked as the outer layer and the 45˚ ply as the inner layer was selected.

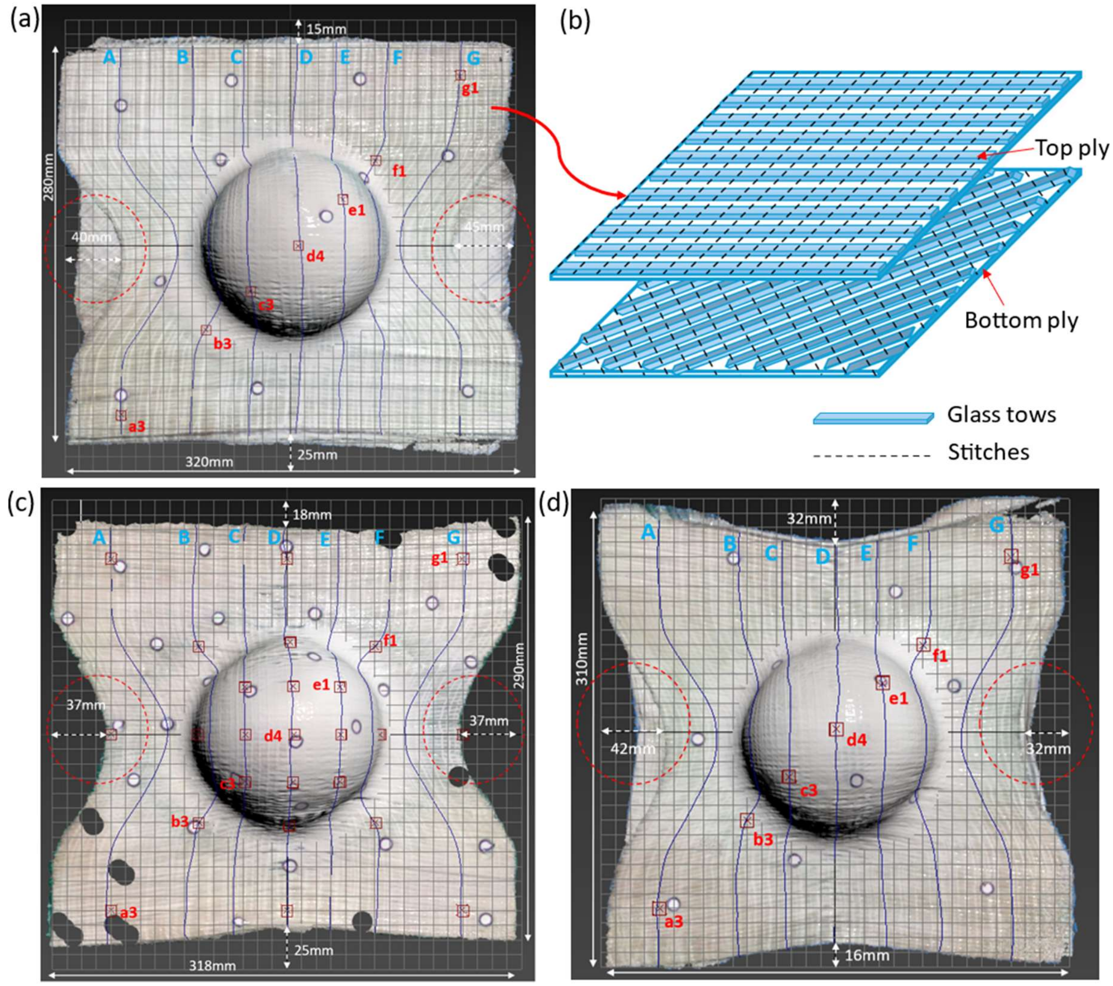

Figure 6.29: (a) Bi/0-45/AE specimen (b) Fibre orientation of two plies (c) Mono/0/AE specimen (d) Bi/0-90/AE specimen

Although the Bi/0-45/AE specimen is a bilayer, it deforms to a shape more similar to the Mono/0/AE specimen (see Figure 6.29c) than the Bi/0-90/AE (see Figure 6.29d). The initial width (horizontal direction) of the top layer of Bi/0-45/AE decreases significantly from 320mm to 280mm whereas the length of the fabric (vertical direction) sample remains the same. The 0° and 45° layers deform differently due to their fibre orientations, leading to shear imbalances that result in lateral displacement i.e., the upper layer of the sample shifts slightly to the left side at the top and the right side at the bottom (see Figure 6.29a). Due to inter-ply sliding, the overall lateral displacement is reduced by enabling the layers to adjust to the shear forces more effectively. The measured strain in the stitch direction vs X/Y coordinates at selected points along the diagonal of the Bi/0-45/AE specimen also follows a similar pattern as the Mono/0/AE specimen (see Figure 6.30, the strain calculations are given in Table O.1 in Appendix O), however, the stitch stretching in the hemisphere surface is slightly higher than the monolayer specimen as there is no contraction in the middle along the stitch direction.

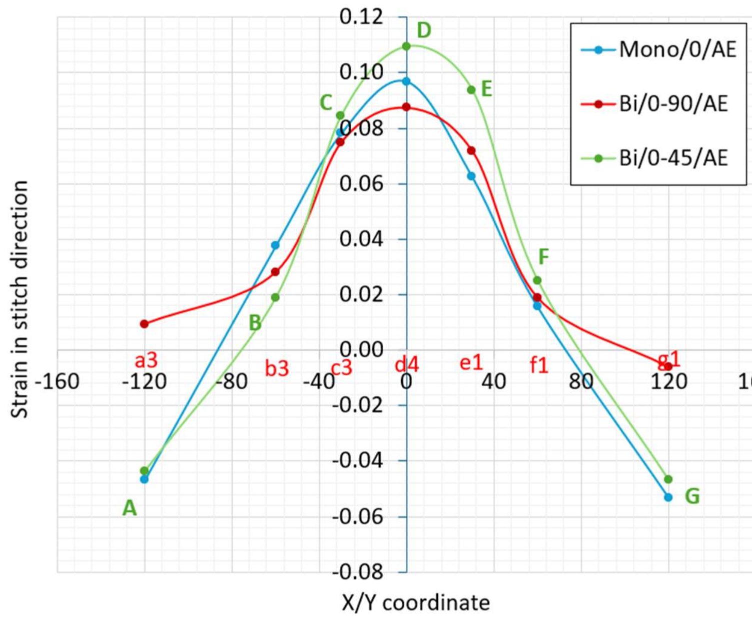

Figure 6.30: A comparison of the strain in the stitch direction vs X/Y coordinates of the selected points located along the diagonal of the Mono/0/AE, Bi/0-90/AE and Bi/0-45/AE specimens

Figure 6.31a shows the fitted surfaces for the shear angles at the selected locations of the Bi/0-45/AE specimen and Figures 6.31b&c compare the fitted surface of Bi/0-45/AE with Mono/0/AE and Bi/0-90/AE specimens' surfaces, respectively. The maximum shear angle achieved by the Mono/0/AE specimen (near the equator of the hemisphere) is higher than that of the Bi/0-45/AE specimen (see Figure 6.31b). Both specimens exhibit a reduction in width compared to length, however, the absence of contraction in the middle of the Bi/0-45/AE specimen due to the frictional force acting on the bias direction resists the shear deformation compared to a single-ply specimen. Comparing bilayer specimens (see Figure 6.31c), the Bi/0-90/AE shows less shear than the Bi/0-45/AE due to the perpendicular orientation between the two fabric layers.

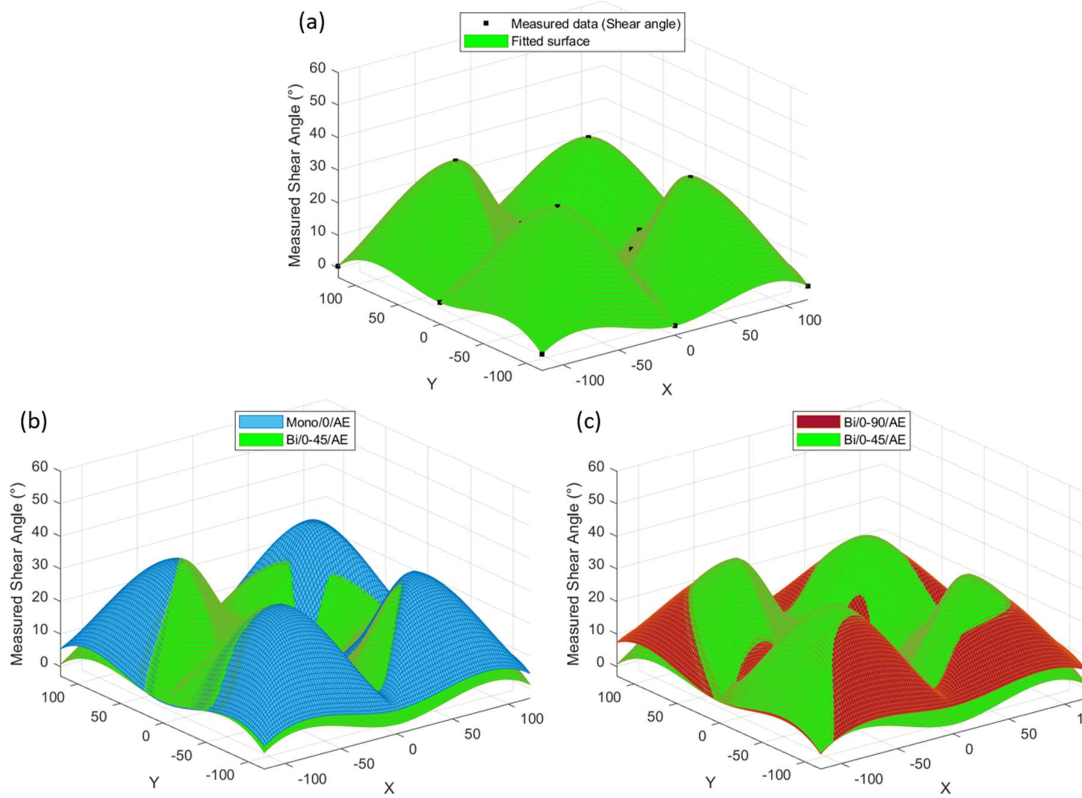

Figure 6.31: Fitted surfaces relative to the shear angle measured at selected locations (a) Bi/0-45/AE (b) Comparison of Bi/0-45/AE and Mono/0/AE specimens (c) Comparison of Bi/0-45/AE and Bi/0-90/AE specimens

Defects in Bilayer Specimens

Figure 6.32 compares the surface of the hemisphere along the stitch direction of all five specimens formed by the acetone/epoxy fixing method. Qualitatively, the amplitude of mesoscale wrinkles along the tows i.e., in-plane waviness for tows in all bilayer specimens (see Figure 6.32c,d&e) is higher than that of monolayer specimens (see Figure 6.32a&b) due to inter-ply friction. Researchers have shown that the amplitude of defects in multilayer specimens depends on several factors including orientation of the plies, inter-ply friction caused by relative sliding between layers and the relative motion between the tool and the fabric (ply-tool friction) [232] [233]. Various modifications have been used to reduce the inter-ply and ply-tool frictions such as the changes in the reinforcement (i.e., material, meso-structure and specimen dimensions [231]), process parameters (i.e., pressure and velocity [234] [235]), and use of interleaving materials (i.e., textile and metal sheets [232] [236]).

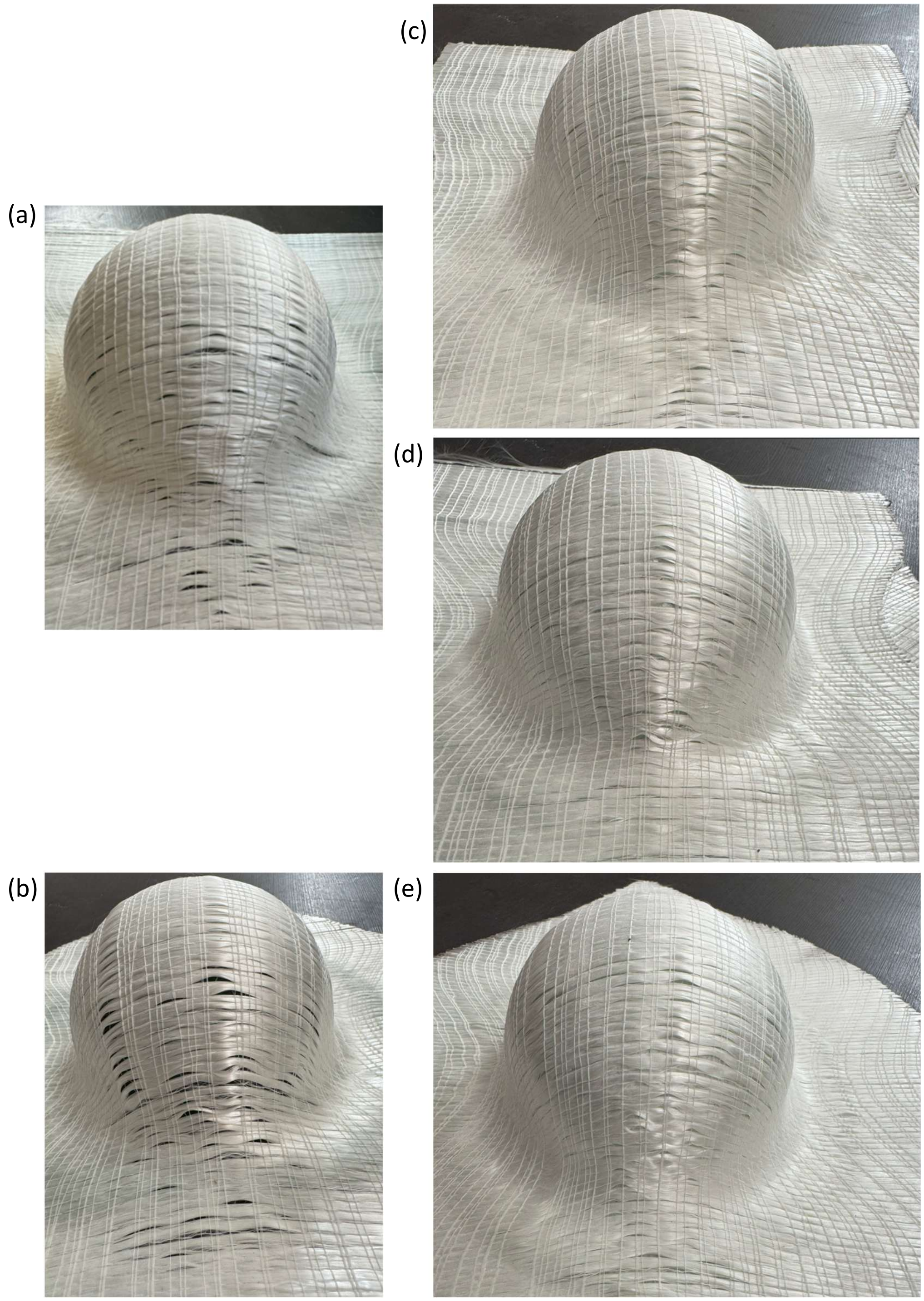

Figure 6.32: Comparison of defects in mono and bilayer specimens fixed by acetone/epoxy method (a) Mono/0/AE (b) Mono/45/AE (c) Bi/0-90/AE (d) Bi/0-45/AE (e) Bi/45-45/AE

Figure 6.33 shows the forming force of the three bilayer specimens fixed using the acetone/epoxy method as a function of the punch displacement. The forming force of the reinforcement in the ±45˚ tow orientation is larger than the 0˚/90˚ orientation. In both specimens, the tows of the two plies are present perpendicular to each other, however, ply-tool and inter-ply frictions are different due to the different tow lengths. The longer contact length of the radial tows and the high contact angle at the holder corners (the angle between the tows and the surface of the holder corner) of the Bi/45-45/AE specimen cause higher friction forces, which could lead to a higher forming force. Qu et al. [237] reported a similar result for two-layer specimens in the tetrahedral forming of a carbon-Kevlar hybrid woven fabric. Under different forming speeds, the ±45˚ initial fibre orientation exhibits a larger forming force than the 0˚/90˚ orientation (see Figure 14 in Qu et al. [237]). Therefore, the Bi/45-45/AE sample may be more prone to in-plane waviness than the Bi/0-90/AE sample (see Figure 6.32c&e). According to Figure 6.33, the forming force vs punch displacement curve of Bi/0-45/AE lies between the specimen curves with ±45˚ and 0˚/90˚ tow orientations. Due to the presence of both plies with 0˚ and 45˚ tow directions in Bi/0-45/AE, the friction contribution may be in the middle of the Bi/0-90/AE and Bi/45-45/AE samples.

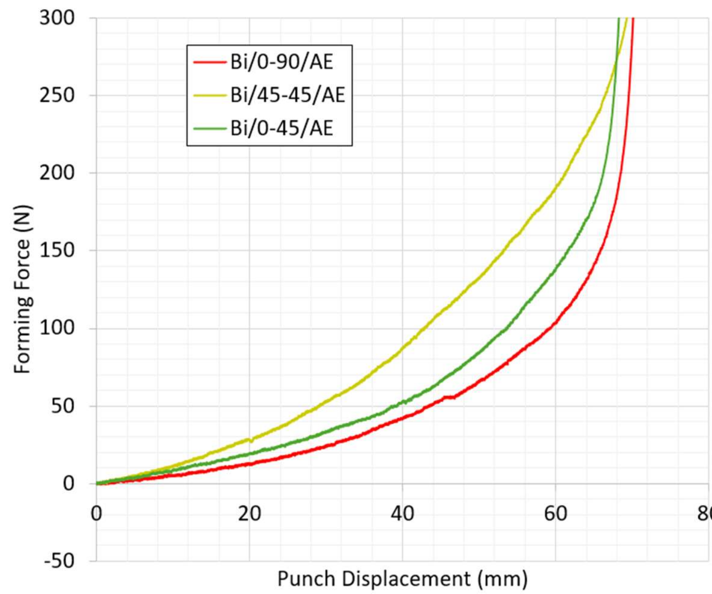

Figure 6.33: Forming force vs punch displacement of three bilayer specimens fixed with acetone/epoxy method

Furthermore, when comparing the mono and bilayer samples, the gaps in the straight-cut samples (Figure 6.32a,c&d) are not significantly different. However, in the bias-cut specimens, the bilayer specimen (see Figure 6.32e) shows a reduction in the gaps (number of gaps and amplitudes) compared to the monolayer specimen (see Figure 6.32b). This can be attributed to the reduced stretching in the stitch direction of the top layer of the bilayer specimen (see Figure 6.27) due to the high-stiffness tows in the bottom layer along the same axis.

6.5.3. Adhesive Spray Method

The acetone/epoxy method allows for relative movement of the fabric layers as it is used after the fabric is formed and consequently has no effect on interplay friction during the forming process. In contrast, the adhesive spray method (Ad) limits the relative movement due to the adhesion of the plies to each other prior to and during forming. To compare the effectiveness of these two fixing methods, bilayer specimens were formed using the adhesive spray method in three different stacking sequences similar to the acetone/epoxy method i.e., specimens with stitches at 0˚ & 90˚ (referred to here as 'Bi/0-90/Ad'), +45˚ & -45˚ (referred to here as 'Bi/45-45/Ad'), and 0˚ & 45˚ (referred to here as 'Bi/0-45/Ad'). One specimen of each is used for analysis.

6.5.3.1. Bilayer Specimens

Bi/0-90/Ad

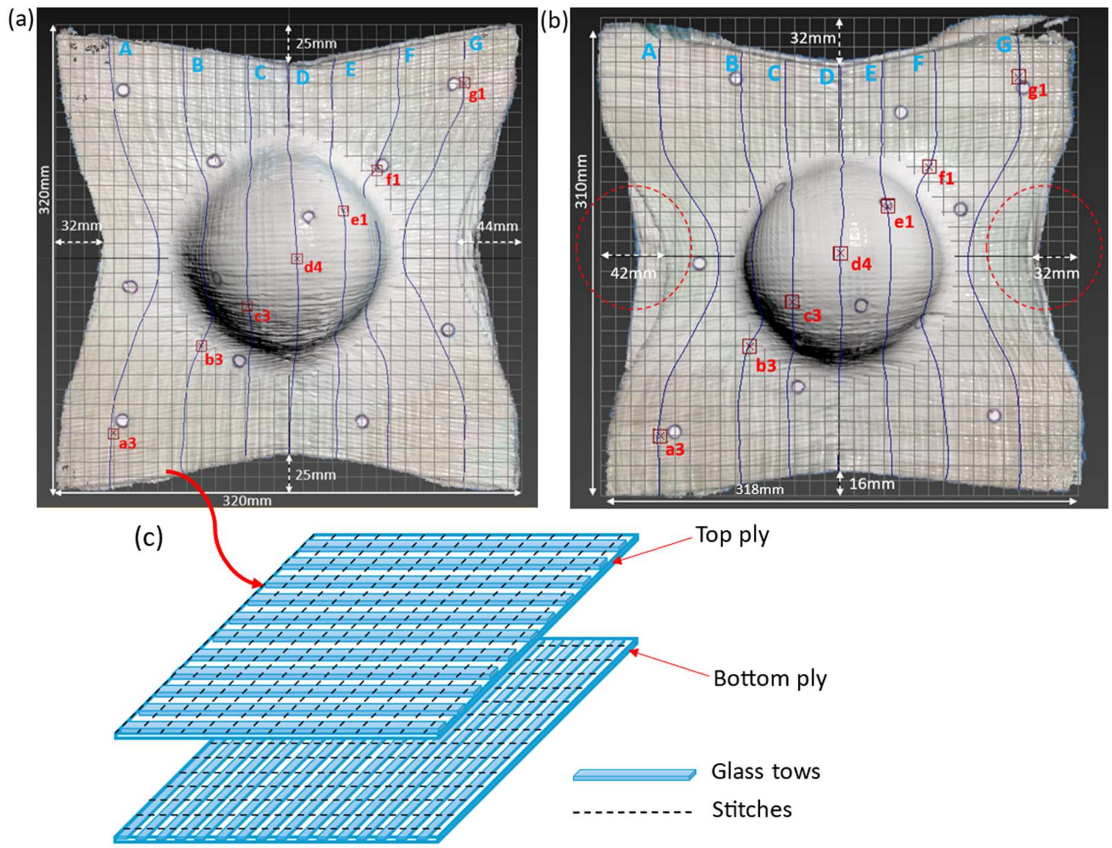

Figure 6.34: Dimensions of the specimens (a) Bi/0-90/Ad (b) Bi/0-90/AE (c) Fibre orientation of two plies

Figures 6.34a&b show 0˚/90˚ bilayer specimens fixed with adhesive spray and acetone/epoxy solution, respectively. The Bi/0-90/Ad specimen shows materials draw-in in all four sides (see Figure 6.34a) resulting in almost a four-axis symmetric structure similar to biaxial fabrics with 0-90° fibre orientation (see Figures 6.14b and 6.34c). Applying adhesive prior to forming bonds, the two plies together and minimise the inter-ply sliding. Thus, this single unit possesses tows in both the warp and weft directions and behaves similarly to biaxial fabrics. This lack of sliding forces the plies to deform together, which increases internal resistance to the forming process. The fabric layers therefore deform simultaneously i.e., the tows are drawn inward towards the centre from all four directions, leading to greater shear stresses between the tows within the layers. As a result, the forming force of Bi/0-90/Ad is higher than the Bi/0-90/AE specimen (see Figure 6.35a).

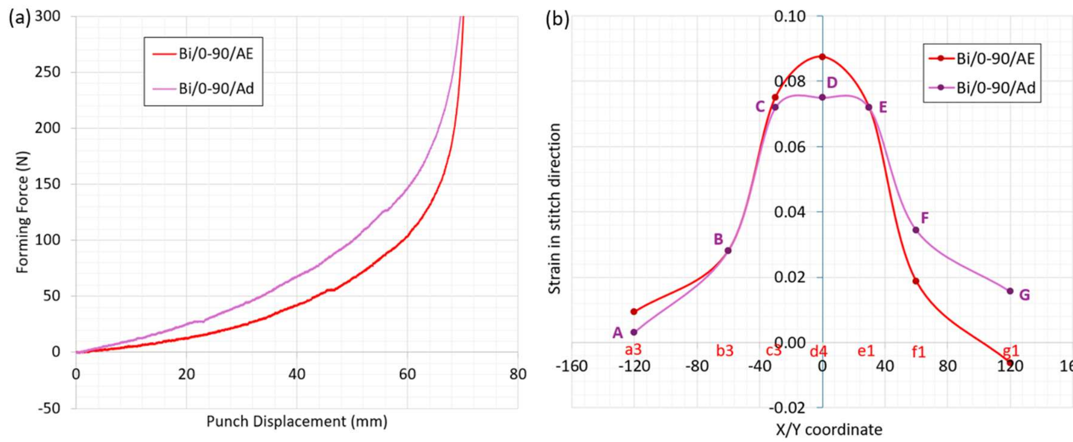

Figure 6.35: Comparison of Bi/0-90/AE and Bi/0-90/Ad specimens (a) Forming force vs punch displacement curves (b) Strain in the stitch direction vs X/Y coordinates of the selected points located along the diagonal

Figure 6.35b compares strain in the stitch direction vs X/Y coordinates of the selected points along the diagonal of the specimens prepared using the two fixation methods. The two graphs, i.e., Bi/0-90/AE and Bi/0-90/Ad, are almost identical in shape (the strain calculations are given in Table O.1 in Appendix O). However, the stitch stretching in the middle of the Bi/0-90/Ad hemisphere reaches a plateau and is slightly lower than the Bi/0-90/AE specimen, as there is a significant contraction in the middle along the stitch direction. In addition, the 'G' stitch in the Bi/0-90/Ad shows a significantly higher strain than the Bi/0-90/AE specimen. As shown in Figure 6.34a, the right edge of the top ply of the Bi/0-90/Ad specimen is not well attached to the bottom ply. Therefore, the top ply significantly draws towards the centre of the hemisphere and increases the stretching of the 'G' stitch during forming.

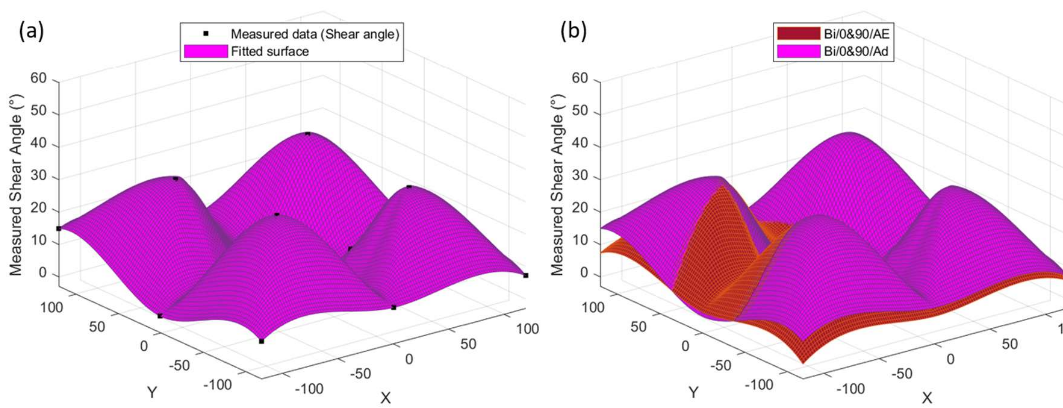

Figure 6.36: Fitted surfaces relative to the shear angle measured at selected locations (a) Bi/0-90/Ad (b) Comparison of Bi/0-90/Ad and BI/0-90/AE specimens

Figure 6.36a shows the fitted surfaces for the shear angles at the selected locations of the Bi/0-90/Ad specimen. A comparison of shear angles measured at selected locations shows higher values across the Bi/0-90/Ad specimen compared to the Bi/0-90/AE specimen (see Figure 6.36b). The adhesive bonds prevent the 0° and 90° fibres in adjacent layers from sliding relative to each other. This restriction favours more shear deformation within each layer. Since the layers cannot distribute the stress through sliding, the tows begin to bend more to accommodate the applied forming forces and form the desired shape. As a result, the shear angles within the Bi/0-90/Ad specimen increase.

Bi/45-45/Ad

Bi/45-45/Ad specimen shows material draw-in in all four sides (see Figure 6.37a) resulting in an almost four-axis symmetric structure, similar to woven biaxial fabrics with ±45° fibre orientation (see Figures 6.37d) i.e., the adhesion of two plies with tows perpendicular to each other (see Figures 6.37b) behaves more like a biaxial sheet similar to the forming of a woven biaxial fabric. Due to the significant amount of relative sliding between the two layers, the Bi/45-45/AE specimen (see Figure 6.37c) deviates from the behaviour of the woven biaxial fabrics. When comparing the forming forces using different fixing methods of samples with the same ± 45° tow orientation, the Bi/45-45/Ad sample shows a higher forming force than the Bi/45-45/AE sample due to the reduction of inter-ply sliding after adhesive spray application i.e., resistance to forming due to increased internal stress (see Figure 6.38a).

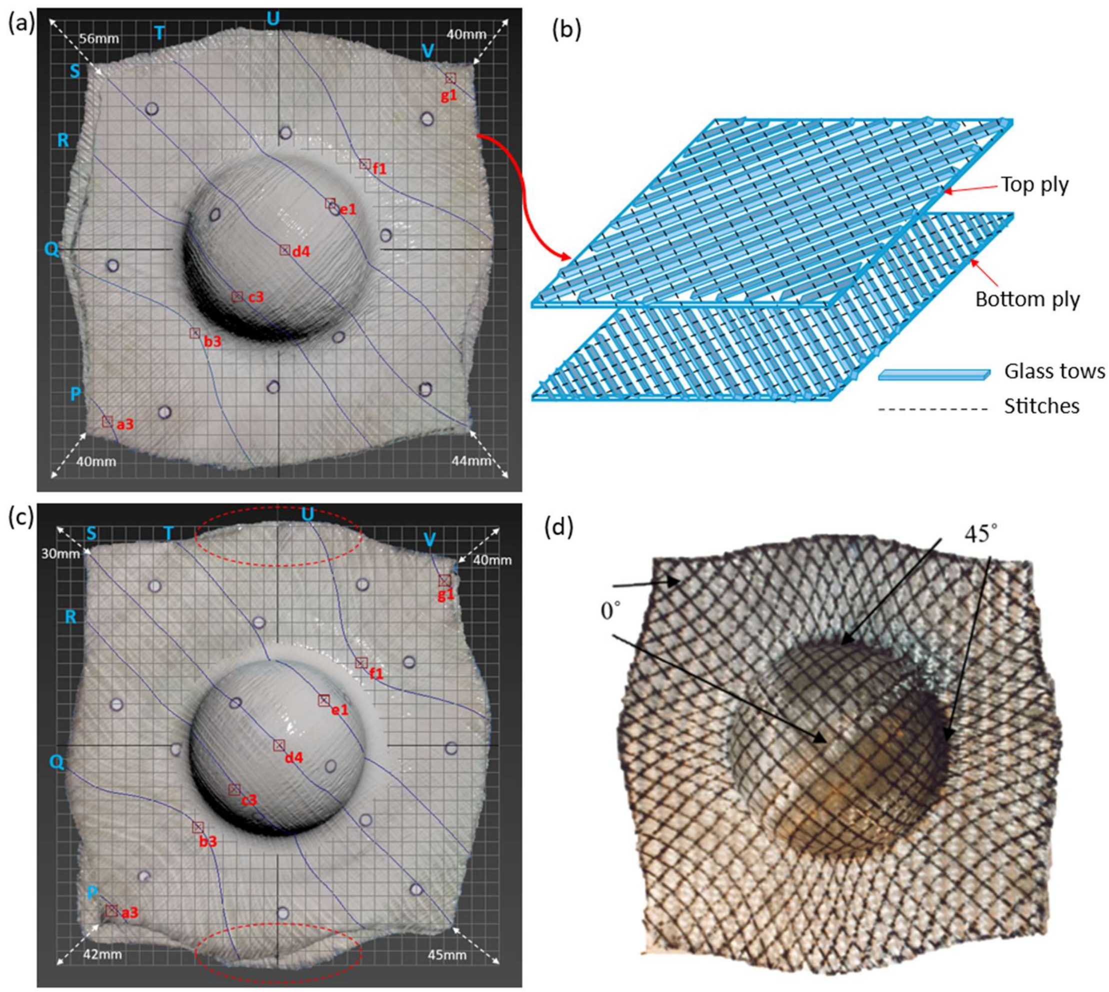

Figure 6.37: (a) Bi/45-45/Ad specimen (b) Fibre orientation of two plies (c) Bi/45-45/AE specimen (d) hemispherical forming of biaxial fabric with ±45˚ fibre orientation [227]

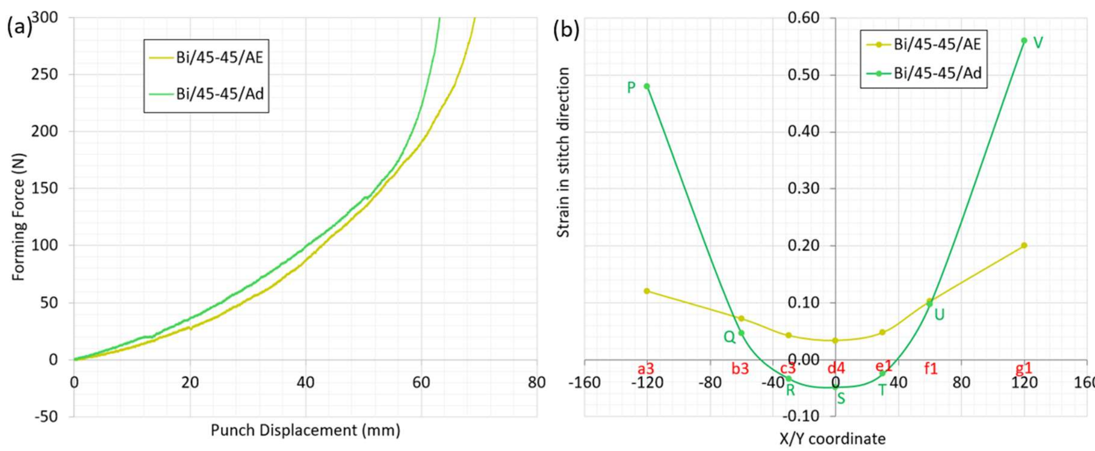

Figure 6.38: Comparison of Bi/45-45/AE and Bi/45-45/Ad specimens (a) Forming force vs punch displacement curves (b) Strain in the stitch direction vs X/Y coordinates of the selected points located along the diagonal

The strain in the stitch direction at selected locations of Bi/45-45/Ad shows a significant difference compared to the Bi/45-45/AE specimen (see Figure 6.38b), where the short stitches in the flat region show high positive strains and stitches across the hemisphere surface show negative strain. As the tows are forced to deform along the curved surface, the stitches orientated at 45° experience compression. This is because the fabric cannot move or stretch freely, leading to the shortening of the stitches, resulting in negative (compressive) stitch strains. As the movements of the hemispheric region are minimised, tension begins to build up on the adjacent flat surfaces. As a result, the stitches in the flat surface pull more, leading to significant stretching i.e., higher positive stitch strains. Figure 6.39 shows that the shear angles measured at selected locations of Bi/45-45/Ad are higher than the Bi/45-45/AE specimen. The significant stitch stretching on the flat surface pushes the tows further and increases shear in the areas that prefer to shear (see the regions marked in Figure 6.21b). In the Bi/45-45/AE specimen, the lack of bonding between the two layers allows for inter-ply sliding, resulting in a reduced shear angle (lowering the shear deformation).

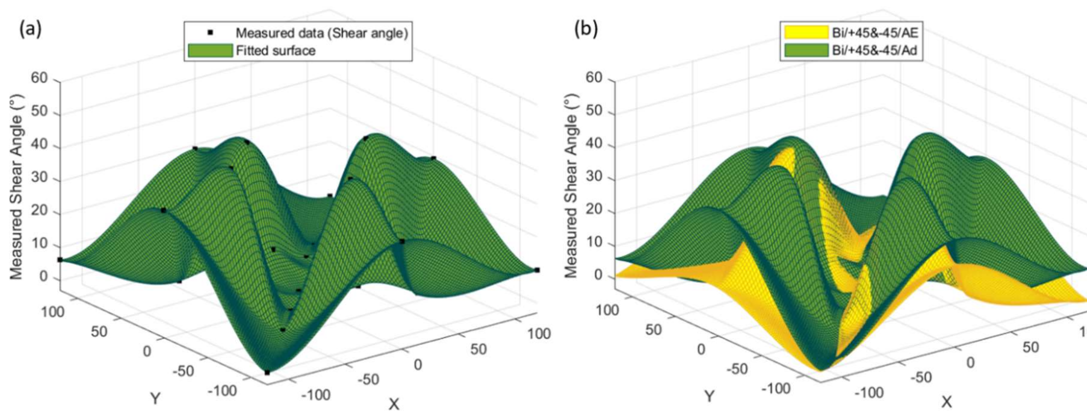

Figure 6.39: Fitted surfaces relative to the shear angle measured at selected locations (a) Bi/45-45/Ad (b) Comparison of Bi/45-45/Ad and Bi/45-45/AE specimens

Bi/0-45/Ad

In the Bi/0-45/Ad sample, the initial width of the top layer is significantly reduced from 320mm to 265mm (see Figure 6.40a) and this width reduction is more pronounced than that of the Bi/0-45/AE sample (see Figure 6.40b). As a result, the strain in the stitch in the flat region is more negative in the Bi/0-45/Ad specimen (see Figure 6.41a, the strain calculations are given in Table O.1 in Appendix O). The compressions of the adhesive-applied specimen are higher because the 0° layer cannot slide relative to the 45° layer beneath it (see Figure 6.40c), causing it to compress more to accommodate the shape i.e., the forming force of Bi/0-45/Ad is higher than the Bi/0-45/AE specimen (see Figure 6.41b). Stitch stretching in the hemisphere region is greater in the Bi/0-45/Ad specimen than in the Bi/0-45/AE specimen (Figure 6.41a), possibly due to the stronger lateral displacement (i.e., the specimen shifts to the left side at the top and the right side at the bottom) of the top layer of the adhesive-applied specimen. This can be clearly observed by stitch lines that are more inclined relative to the grid (see Figure 6.40a). Compared to the acetone/epoxy method, the adhesive spray method restricts inter-ply sliding, forcing the layers to deform together, which amplifies the lateral displacement as the fabric tries to conform to the hemisphere.

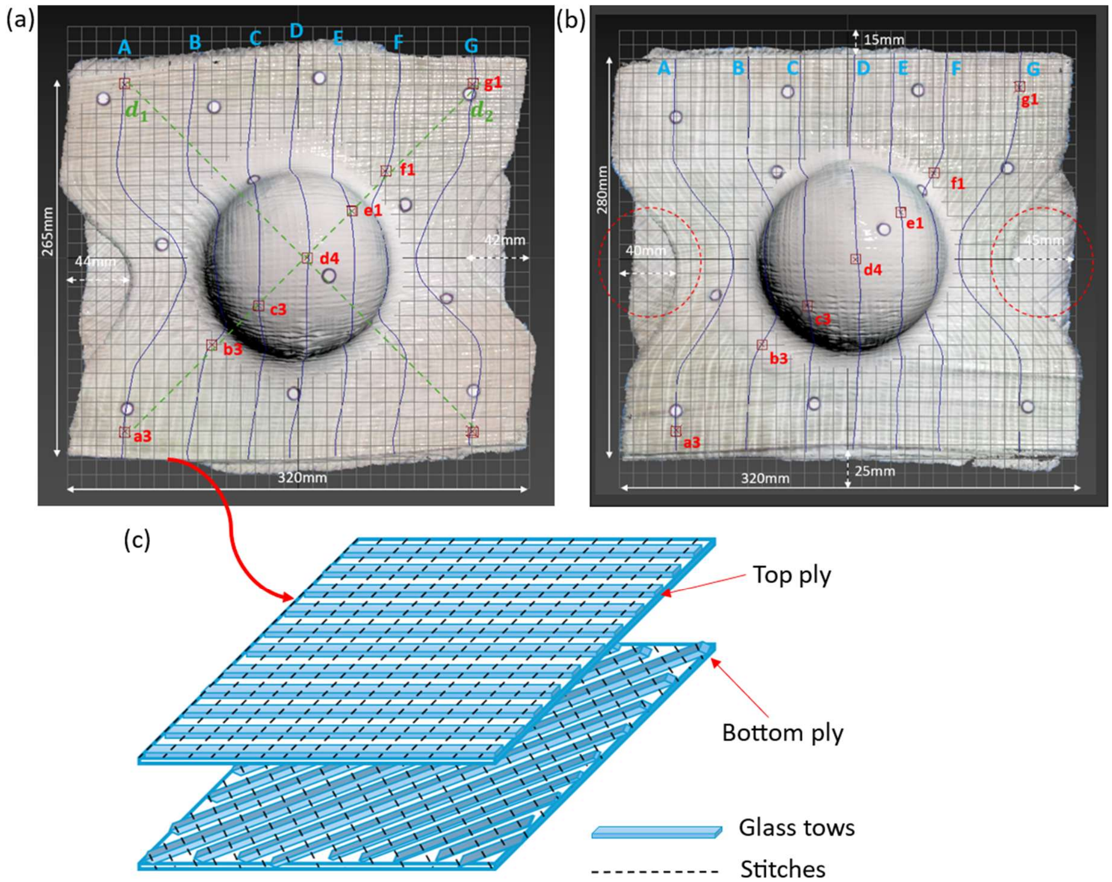

Figure 6.40: Dimensions of the specimen (a) Bi/0-45/Ad (b) Bi/0-45/AE (c) Fibre orientation of two plies

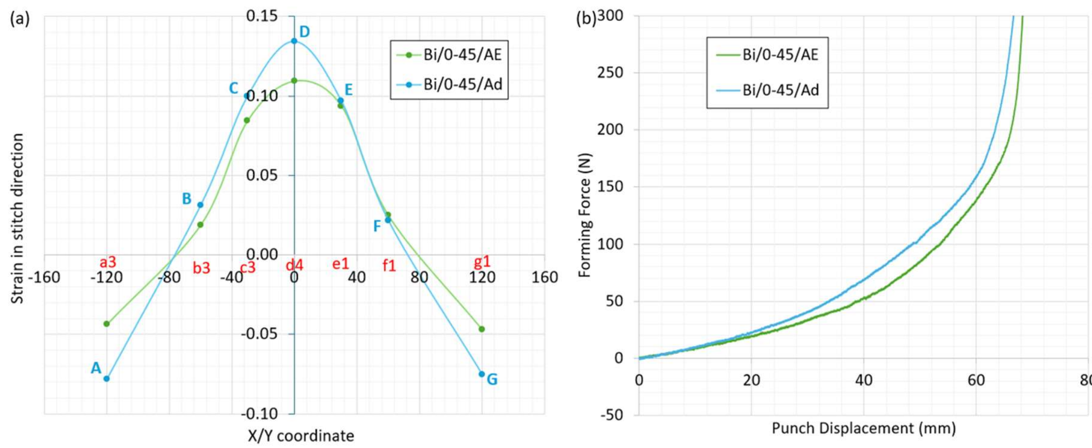

Figure 6.41: Comparison of Bi/0-45/Ad and Bi/0-45/AE (a) Strain in the stitch direction vs X/Y coordinates of the selected points located along the diagonal (b) Forming force vs punch displacement curves

Figure 6.42a shows the fitted surfaces for the shear angles at the selected locations of the Bi/0-45/Ad specimen and Figure 6.42b compares the fitted surface of Bi/0-45/Ad with Bi/0-45/AE specimen. Due to the lateral displacement, the Bi/0-45/Ad specimen significantly sheared along the d_2 diagonal (see Figure 6.40) and reduces the shear along the d_1 diagonal. Therefore, the shear surface of this specimen exhibits an unbalanced deviating nature.

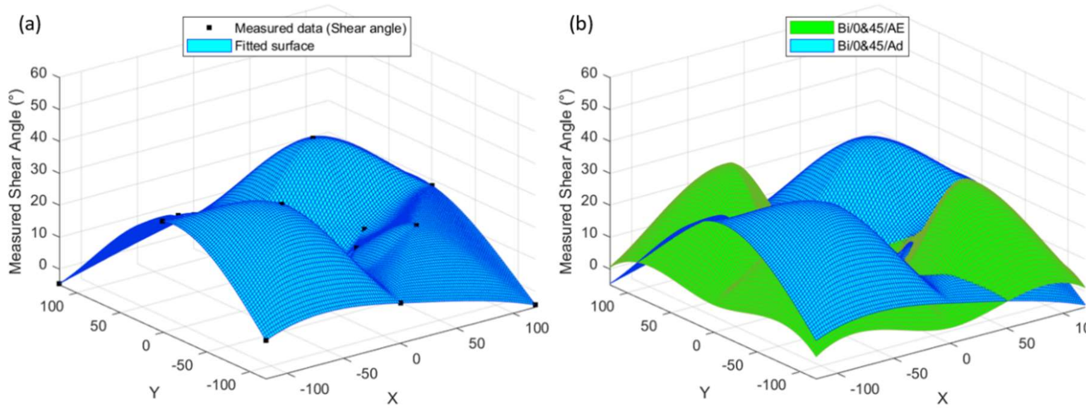

Figure 6.42: Fitted surfaces relative to the shear angle measured at selected locations (a) Bi/0-45/Ad (b) Comparison of Bi/0-45/Ad and Bi/0-45/AE specimens

Defects in Adhesive Spray Method

Figure 6.43 compares the surfaces of the hemispheres along the stitch direction of bilayer specimens formed by the adhesive spray and acetone/epoxy fixing methods.

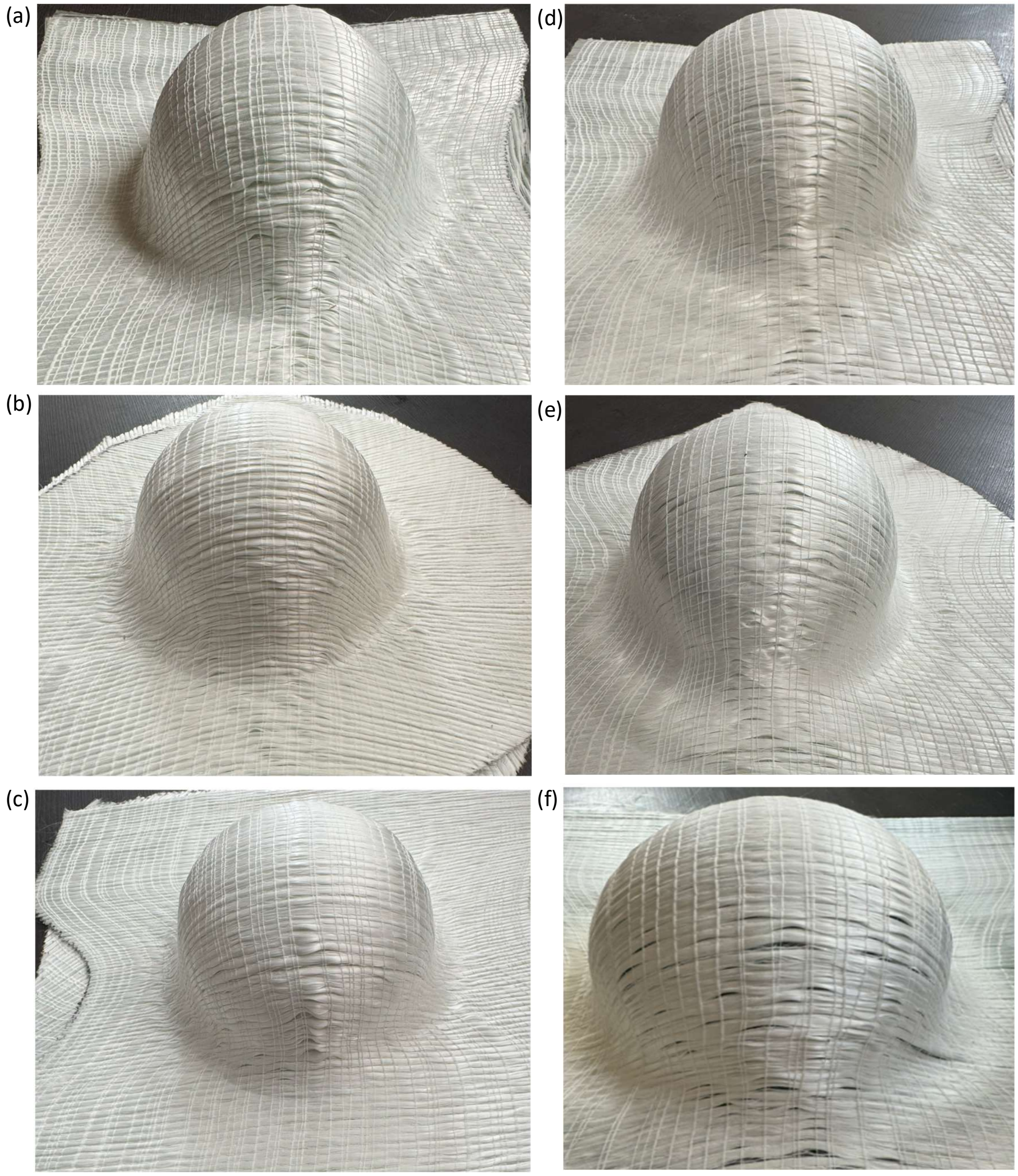

Figure 6.43: Comparison of defects in bilayer specimens fixed by adhesive spray (a-c) and acetone/epoxy (d-f) methods (a) Bi/0-90/Ad (b) Bi/45-45/Ad (c) Bi/0-45/Ad (d) Bi/0-90/AE (e) Bi/45-45/AE (f) Bi/0-45/AE

The gaps formed in the specimens of the acetone/epoxy method (Figure 6.43d-f) are reduced in the adhesive spray specimens (Figure 6.43a-c) due to the reduction of stitch stretching in the hemisphere region (this may not be clearly observed in the Figure, however, physically it is more visible). However, in-plane mesoscale wrinkles or waviness of tows are higher in specimens formed using the adhesive spray method than those fixed using the acetone/epoxy method. The application of adhesive spray restricts inter-ply sliding, forcing the fabric plies to deform as a single unit. As a result, increased internal stress creates higher forming forces in the specimen fixed with the adhesive spray than in the acetone/epoxy method (see Figures 6.35a, 6.38a and 6.41a). When forming complex geometries like a hemisphere, the fabric needs to accommodate significant shear deformation, especially around curved regions. Without the ability to slide and realign freely, the fabric layers develop localised areas of excess material, which leads to in-plane wrinkles or waviness.

Figure 6.44 shows the forming force of three bilayer specimens fixed using the adhesive spray method as a function of the punch displacement. Similar to the acetone/epoxy method (see Figure 6.32), the highest forming force is shown by the ±45˚ tow orientation. For the 0˚/45˚ and 0˚/90˚ samples, the difference between the forming forces shown in the acetone/epoxy method is further reduced and almost the same at the lower punch displacements (until 40mm) in the adhesive spray method (see Figure 6.44). The force required to form the Bi/0-45/Ad specimen beyond the 40 mm punch displacement is greater than that of the Bi/0-90/Ad specimen probably due to a significant inter-ply frictional contribution at higher punch displacements.

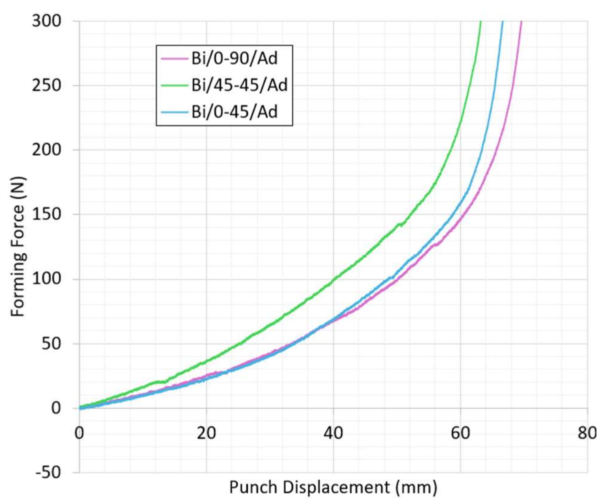

Figure 6.44: Forming force vs punch displacement of three bilayer specimens fixed with adhesive spray method

In addition to the in-plane wrinkles, the Bi/0-45/Ad specimen shows out-of-plane mesoscale tow wrinkles in the hemisphere region where the spacing of the stitches is high (see Figure 6.43c). In contrast to other bilayer specimens, the 0˚/45˚ configuration is more susceptible to lateral displacement because different fibre orientations lead to shear imbalance, and the adhesive spray prevents the layers from adjusting to relieve this shear. This may lead to the observed out-of-plane wrinkling.

6.6. Chapter Summary

The forming experiments discussed in this chapter provide a detailed investigation into the behaviour of pure-UDNCF during hemisphere forming. Two fixation methods i.e., acetone/epoxy and adhesive spray were used to maintain the desired shape and facilitate the handling of formed specimens during post-analysis. Five samples were formed using the acetone/epoxy method i.e., two monolayers (stitch direction at 0˚ and 45˚) and three bilayers (0˚/90˚, +45˚/-45˚ & 0˚/45˚) and three samples using adhesive spray method (0˚/90˚, +45˚/-45˚ & 0˚/45˚).

A comparison of the weight of the specimen after fixing with the acetone/epoxy method reveals that although the amount of weight gain after fixing is greater in bilayer specimens than in monolayer specimens, the percentage of weight gain is higher in monolayer specimens (3.3%) than in bilayer specimens (2.2%). Thus, the adsorbed epoxy dispersion relative to the initial weight of monolayer specimens is higher than that of bilayer specimens. A weight comparison of the specimens from the two fixing methods reveals that the adhesive spray method achieves a lower weight than the acetone/epoxy method, either because a thin layer of adhesive spray is applied between two plies, or because of the acetone/epoxy coated samples are not fully evaporated or a combination of both explanations. These two fixing methods formed stable and rigid hemispherical specimens with a weight gain of less than 5% relative to their initial weights.

Several critical findings were observed regarding the impact of fixing methods on pure-UDNCF deformation, wrinkling, and the overall forming force required. The results demonstrated that the adhesive spray method significantly alters the forming behaviour by restricting inter-ply sliding, thereby increasing internal resistance during deformation i.e., the adhesive sprays applied to the fabric prior to forming cause changes in the fabric behaviour. The adhesive layer forces the bilayer to act as a more cohesive unit, preventing the independent movement of individual plies and leading to high forming forces. This restriction increases the localised shear imbalances, leading to increased lateral displacement in specific orientations, such as the 0˚/45° specimen (Bi/0-45/Ad). The adhesive spray method reduced gap formation in the hemisphere region by reducing stitch stretching; however, adhering two plies together can exacerbate in-plane and out-of-plane wrinkling because the fabric plies cannot freely adjust their positions during forming.

In contrast, after obtaining the desired shape, stabilisation of the structure with an acetone/epoxy solution ensures that the behaviour of the fabric remains constant throughout the forming process. Therefore, this method facilitates inter-ply sliding and reduces the internal stresses between the two plies. As a result, the acetone/epoxy method lowers forming forces and prevents lateral displacement compared to the adhesive layer-applied specimens. Furthermore, acetone/epoxy-treated specimens show better surface quality due to reduced in-plane wrinkling. In addition, this method can produce monolayer specimens by applying a mould-release agent to the fabric-contacting surfaces, allowing for easy removal of the specimen without causing any damage. Both fixing methods used in this study show long-term post-forming stability, however, the acetone/epoxy method produces minimal defects compared to the adhesive spray method. If the shape to be formed is relatively simple (e.g., flat), the adhesive spray method could be useful. High friction will not cause significant challenges and will help maintain the alignment of the layers. For more complex shapes like hemispheres i.e., double curved surfaces (double dome), the acetone/epoxy fixing method is preferable. Allowing the plies to slide during the forming reduces the formation of wrinkles and ensures that the fabric can conform to the complex mould shape more easily. However, it is worth noting that the adhesive spray method worked well in modifying the fabric forming behaviour, offering improved control over fibre orientation and helping to reduce gaps or inconsistencies in the fabric. Therefore, the fast and simple adhesive spray method can optimise the forming behaviour and be used locally to modify the behaviour in specific locations.

Another key observation found in this study is the role of fibre orientation in determining the extent of deformation and defects. A monolayer specimen with a 45° orientation (Mono/45/AE) showed distinct differences in the stitch strain and gaps formed in the hemisphere region, compared to the monolayer specimen with a 0° orientation (Mono/0/AE). This is thought to be due to the increased frictional force caused by tow misalignment with the forming direction. Similar to the monolayer specimens, the Bilayer 0/90 specimens (Bi/0-90/AE and Bi/0-90/Ad) show a lower forming force than the +45/-45 specimens (Bi/45-45/AE and Bi/45-45/Ad) and the forming force of 0/45 specimens (Bi/0-45/AE and Bi/0-45/Ad) lies between the other two layup configurations. In addition to the tow orientations, the stacking sequence is also critical during the formation of multilayer specimens. In this study, the formed specimens are mono and bilayers. Thus, the stacking sequence is not significant, however, when forming the bilayer specimen with 0˚ and 45˚ ply orientations, 0˚/45˚ stacking sequence (i.e., the 0˚ ply is stacked as the outer layer and the 45˚ ply as the inner layer) was selected to reduce the amount of defect formation.

The experimental results presented in this chapter form a solid foundation for validating numerical models that predict the forming behaviour of pure-UDNCF. Numerical modelling can significantly benefit from the following experimental observations:

- **Shear angle distribution:** The experimental measurements of shear angles in monolayer (0˚ and 45˚) and bilayer specimens with different stacking sequences i.e., 0°/90° and +45°/-

45˚ and 0˚/45˚ can be used to verify whether numerical models accurately predict the strain distribution across the fabric during hemispherical forming.

- **Forming force predictions:** By comparing the measured forming forces of specimens fixed using both adhesive spray and acetone/epoxy methods, with simulated force values, numerical models can be validated to predict force-displacement curves more reliably.
- **Wrinkling and defect formation**: Observations of in-plane and out-of-plane mesoscale tow wrinkles, as well as stitch strain distribution, provide a direct means to test numerical models for their ability to predict wrinkle initiation and propagation. Accurate models should reflect the interaction between tow orientations, fixation methods, and shear forces that lead to these defects.
- **Lateral displacement and shear strain:** The lateral displacement observed in the 0°/45° stacking sequence due to shear strain imbalances can serve as an important metric for validating models of shear deformation and fibre sliding. Incorporating this data into simulations will improve the accuracy of predicting geometric distortions during the forming process.

The results of the forming experiments provide a critical dataset for the validation of numerical models that simulate the forming behaviour of pure-UDNCF. These models can eventually aid in optimising forming processes, reducing defects, and improving the manufacturability of complex composite structures.

Chapter 7 Conclusions

7.1. Research Summary

This thesis focuses on the experimental characterisation and forming analysis of the pure-unidirectional non-crimp fabric (pure-UDNCF). The studies presented in the previous chapters are evaluated in relation to each of the objectives outlined in the introduction (see Section 1.2). For more clarity, the complete research project is presented as a flowchart in Figure 7.1. The following sections of this chapter present a summary of recent research findings and their significance. Furthermore, the chapter concludes with a discussion of future research work.

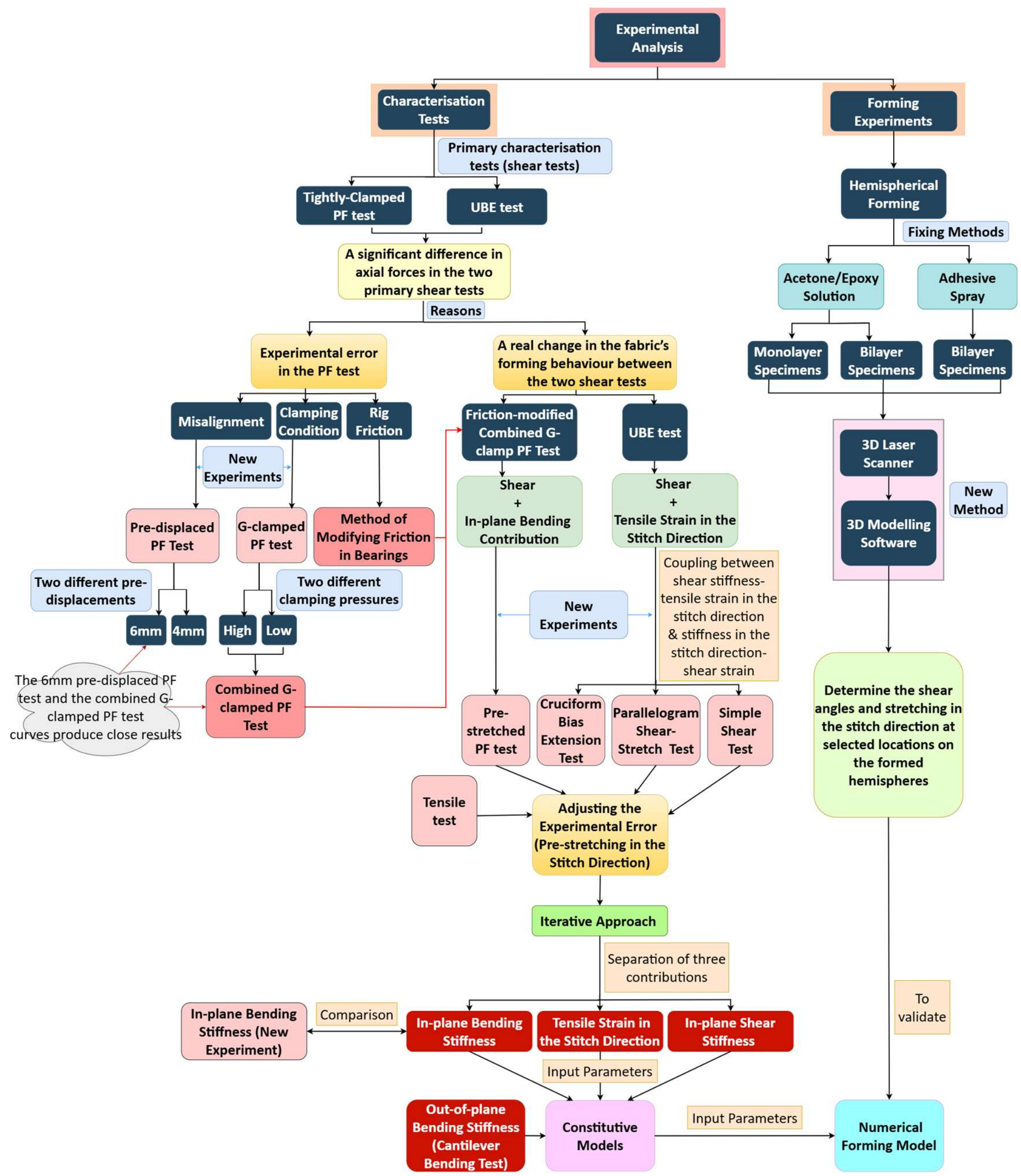

Figure 7.1: Flowchart of the Research

7.2. Characterisation Tests

7.2.1. Primary Characterisation Tests

When compared to the woven fabrics (plain and twill), pure-UDNCF shows unusual stretching behaviour during the uniaxial bias extension (UBE) test due to the presence of compliant stitches in the direction perpendicular to the main tows (and there are no additional fibres to stabilise the fabric). The in-plane shear behaviour of a pure-UDNCF was also measured using another common shear test, the tightly-clamped picture frame test and initially suggested a significant difference, with the tightly-clamped PF test result being dramatically higher than the standard UBE test result. The reason for the difference in the pure-UDNCF behaviour in these two shear tests was based on two hypotheses (a) experimental error in the PF test or (b) a real change in the shear resistance of the fabric in the two tests. Sections 7.2.2 and 7.2.3 discuss the further experiments performed on these two hypotheses and their conclusions.

7.2.2. Experimental Error in the Picture Frame Test

The experimental error in the PF test was investigated using a few modifications to address tow misalignment, clamping conditions and friction in the PF rig bearings.

- **Tow Misalignment:** Unavoidable tow misalignment in the PF test can lead to significant force overestimation (ex: 125% at 20˚ shear angle) due to the tensile strain in the fibres. A modification of the tightly-clamped PF test procedure is proposed to reduce sensitivity to sample misalignment by **positively pre-displacing the PF** rig (moving upward) before loading the undeformed sample. This experiment was performed under two different pre-displacements, i.e., 4mm and 6mm. The 6mm pre-displaced method shows a significant reduction in the normalised axial force compared to the 4mm pre-displaced and conventional tightly-clamped PF tests, by a factor of 1.9X and 2.1X, respectively at 20˚ shear angle. The pre-displaced PF test reduces misalignment error by intentionally inducing compressive stress (rather than tension) in the fibre orientations during the test. This is evidenced by the onset of wrinkling at low shear angles.
- **Clamping Condition:** In what has become the conventional PF test, the specimen is fixed to the PF rig by bolting (originally McGuiness et al. [220] used a pressure-tightening method). This tightly clamping condition was replaced by **G-clamps** under two different clamping pressures, i.e., low (1Nm) and high (5Nm), to determine how the clamping condition affects the measured force. In contrast to the tightly-clamped PF test curve, both clamping pressures resulted in reduced axial forces, i.e., by a factor of 0.3X and 0.6X, for high and low clamping pressures, respectively, at 20˚ shear angle. A gradually weighted combination of the two G-clamp PF test

results was proposed as the optimum compromise. The combined G-clamped and the 6mm pre-displaced PF test curves produced similar results, though the combined G-clamped PF test is considered to be the preferred test method due to a simpler test sample preparation, compared to the 6mm pre-displaced PF test.

- **Friction in Bearings:** The force measured in the PF test can be significantly overestimated due to the resistance to frame rotation caused by the friction in the bearings. Furthermore, using G-clamps for PF testing may cause additional load on the bearings, leading to higher friction. The proposed novel method for determining the influence of friction in the bearings when adding extra weight to the rig revealed that the initial 'jump' in the measured axial force increases with the addition of extra weight. To improve the accuracy of the PF results, the initial jump noted throughout the test results was subtracted from the test data. The friction in the PF rig also depends on the stiffness of the material. However, separating the specific friction force from the overall axial force in the PF test is challenging. This is an important finding because the presence of friction can significantly contribute to the axial force of the PF test, i.e., 15% of overestimation of axial force due to friction of the bearings. Researchers assume that the rig is frictionless based on how easily it can be pulled manually. The accuracy of the results can be improved by verifying that the rig is free of friction using a method like this before performing the PF test on fabrics.

After these modifications, the friction-modified G-clamped combined PF test curve showed a significant reduction of axial force compared to the tightly-clamped PF test curve, however, the normalised force measured in the standard UBE test remained lower. During the PF tests, in addition to shear, an in-plane bending contribution to the measured force was also identified (all PF tests of pure-UDNCF show significant in-plane bending at the ends of the tows, whereas this in-plane bending is largely absent in UBE tests on this material). Therefore, the additional deformation modes, including in-plane bending in the PF test and stitch stretching in the UBE test, may affect the measured force results. Further experiments were conducted on pure-UDNCF to determine if there was a true change in the shear resistance of the fabric between the two shear tests.

7.2.3. A Real Change in the Forming Behaviour of the Fabric

During the UBE test of pure-UDNCF, stretching in the stitch direction was quantified by measuring the increase in side-length of the central region of the specimen. It was hypothesised that there may be a coupling between shear stiffness and tensile strain in the stitch direction, as well as between tensile stiffness in the stitch direction and shear strain. In contrast to the UBE test, stretching in the stitch direction does not occur in the PF test, due to the boundary conditions of the test. Nevertheless, in-plane bending may affect the PF test results (the axial force measured during the PF test could be a combination of shear and in-plane bending). It was decided that further tests were required to better understand the true nature of the mechanical forming properties of the pure-UDNCF. To this end, research was continued by designing new experiments that imposed different but measurable amounts of shear, stretching in the stitch direction and in-plane bending, in the fabric.

- **Cruciform Bias Extension (CBE) Test:** This is an expanded version of the UBE specimen, with the rectangular shape modified to an octagonal shape and its central region kept the same size. The specimen is transformed into a cruciform shape by bonding aluminium foil in regions of the specimen where no deformation is desired. The CBE specimen experiences three low-energy deformation modes i.e., shear, tensile strain in the stitch direction, and in-plane bending. In addition, different regions of the specimen exhibit different deformations during the test, in other words, the specimen undergoes inhomogeneous deformation. Therefore, isolating the contribution of each part of the specimen to the measured axial force is extremely challenging. This test is nevertheless considered useful for future validation of numerical predictions, once an appropriate constitutive model has been implemented in an FEA code.

- **Parallelogram Shear-Stretch (PSS) Test:** The PSS specimens were created by further adhering aluminium foil to the CBE sample to convert the cruciform shape to a rectangular shape (during the deformation, the rectangular shape converts to a parallelogram), resulting in a well-defined and homogenous deformation across the sample. Due to this modification, PSS does not experience the in-plane bending deformation as CBE and undergoes only two low-energy deformation modes, i.e., shear and tensile strain in the stitch direction. At the beginning of the test, the tows and stitches of the PSS specimens are at a 45˚ angle to the axial displacement. The angle between tows and axial displacement (45˚) remains constant throughout the test, and only the angle between stitches and axial displacement varies. This test produces test data in the (shear angle) – (tensile stretch) parameter space.

- **Simple Shear (SS) Test:** Simple shear is a mixed-mode deformation that combines pure shear and tensile strain in the stitch direction. The initial angle between the stitches and axial displacement is increased to 90˚. Similar to PSS specimens, SS specimens also show well-defined kinematics with progressively increasing amounts of shear and stitch strain occurring during the test. Therefore, data from this new SS test occupies another separate curve within the (shear angle) - (tensile elongation) parameter space.

- **Pre-Stretched Picture Frame (PSPF) Test:** During the PF test, stretching in the stitch direction does not occur due to the test boundary conditions. This new method provides test data in different regions of the (shear angle) - (tensile elongation) parameter space, when compared with the PSS and SS tests, by applying a pre-stretch to the specimen in the stitch direction. The PSPF test was performed using a G-clamp boundary condition and the results were modified to account for friction (i.e., a PF test with the least experimental error). As in the other PF tests, the pre-stretched specimens also show pronounced in-plane bending at the ends of the tows, resulting in two low-energy deformation modes: shear and in-plane bending.
- **Tensile Test:** In addition to the novel shear tests, a standard tensile test along the stitch direction was performed on pure-UDNCF. This test includes only one low-energy deformation mechanism: stitch tensile strain (no contribution from shear or in-plane bending).

7.2.4. Experimental Error in New Tests

When plotting all the test results in the (shear angle) - (tensile stretch) parameter space, the PSS test shows a significant difference in stitch strains at a given force than the tensile and SS tests, motivating an investigation of the **pre-stretching error** of specimens. This can cause significant variation in each test result, similar to the pre-shear angle error of the UBE test discussed in Alsayednoor et al. [113]. The absence of stabilising fibres in the pure-UDNCF makes the specimens more prone to pre-stretching error. A new method was developed to determine the pre-stretch amount by comparing the initial number of tows per specimen with respect to an average tow count at a given stitch length, i.e., 17 tows per 50mm stitch length. Despite careful handling, negligible errors can occur due to the complexity of the fabric. This method can be used to determine the resulting error when such practical adjustments are not feasible. Plotting the modified test results in the (shear angle) - (tensile stretch) parameter space revealed a better match to the experimental data, indicating that pure-UDNCF specimens are sensitive to pre-stretching error.

7.2.5. Iterative Approach

Except for the CBE test, all the other tests discussed in this section generate one or two contributions from the three low-stiffness deformation modes to the axial force. An **iterative approach** was proposed to isolate the three stiffnesses of the pure-UDNCF i.e., stitch tensile strain, shear, and in-plane bending, by considering pre-stretching error-adjusted experimental data from PSS, SS, PSPF and tensile tests. Since the tensile test in the stitch direction produced only one contribution, i.e., tensile stretching, the inherent tensile strain surface was created from the tensile data. The PSS and SS tests include two contributions, i.e., tensile stretching in the stitch direction and shear. The inherent shear surface was created by subtracting the inherent tensile force from the total axial force of each test and converting the resultant machine shear to the inherent shear. Among the four selected experiments, the PSPF test experiences two contributions: shear and in-plane bending. The inherent in-plane bending surface was created by subtracting the inherent shear force from the total axial force of each PSPF test and converting the resultant machine in-plane bending to the inherent in-plane bending. This is a novel approach, and the results show that the contribution of in-plane bending is higher than that of shear in the PF test, although the influence of boundary conditions and friction is minimised. This finding may be unique to pure-UDNCF or common to all fabrics, as most researchers have observed in-plane bending of the tows during PF tests but have neglected its significance. In the literature, Harrison et al. [6] determined the in-plane bending stiffness of fabrics through inverse modelling of data obtained from the bias extension test. To the author's knowledge, this is the first method introduced to isolate in-plane bending stiffness from experimental data. The three independent contributions extracted from this method provided good estimates of the axial force measured in each experiment, which could be used as input parameters to develop **constitutive models** for pure-UDNCF. In addition, the **out-of-plane bending stiffness** of the pure-UCNCF obtained by the cantilever bending test can be used for constitutive modelling. Furthermore, new experiments designed to explicitly measure the in-plane bending of pure-UDNCF have been proposed and could be further developed to quantify the **in-plane bending stiffness** and employed in constitutive models.

7.3. Forming Experiments

Characterisation tests for engineering fabrics yield essential material properties that serve as input parameters for materials constitutive models which can then be used to develop numerical forming simulations. To ensure reliability and accuracy, these numerical models need to be validated against the experimental results. Therefore, hemispherical forming experiments were performed on the pure-UDNCF. Fabrics were fixed to retain their shape after forming. Two methods were used, i.e., acetone/epoxy and adhesive spray. Both methods achieved long-term stability in post-analysis and allowed the forming of monolayer and bilayer samples with different ply orientations. In the acetone/epoxy method, the fabric was fixed without changing its forming behaviour as the stabilising solution was applied after forming the fabric into a hemisphere. Conversely, the adhesive spray method modified the behaviour of the fabric in advance by applying a spray between the two layers before forming.

During the hemispherical forming, pure-UDNCF experiences both shear and stretching. The area of shearing and stretching of the sample is determined by the tow-stitch orientation of the plies to the forming direction i.e., the straight-cut specimens (e.g., Mono/0/AE) shear along the diagonals and stretch along the vertical and horizontal axes, whereas the bias-cut specimens (e.g., Mono/45/AE) experience shear and stretching in opposite areas to the straight-cut specimens. The degree to which each deformation mode dominates depends on factors such as ply orientation, forming direction, and friction behaviour between fabric layers. The adhesive application between layers increases inter-ply friction, thereby reducing the inter-ply sliding and promoting shear-dominated deformation i.e. since the layers cannot distribute the stress through sliding, the tows begin to shear more to accommodate the applied forming forces and form the desired shape similar to biaxial fabrics. Without the ability to slide and realign freely, the fabric layers develop localised areas of excess material, which leads to in-plane wrinkles or waviness. Conversely, reducing friction between plies, such as the post-forming fixation method (acetone/epoxy method), allows more inter-ply sliding and promotes stitch stretching in the hemisphere region but increases the formation of gaps. Thus, controlling friction between the plies can balance formability and defect minimisation in complex geometries. When comparing both fixing methods, the acetone/epoxy fixing method resulted in fewer defects than the adhesive spray method. However, as a fast and simple method, the adhesive spray method offers a way to optimise forming behaviour and can be selectively applied to improve fabric performance in targeted areas.

Collecting data in formed hemispheres allows a comprehensive comparison between the experimental data and model predictions. The shear angles and stretching in the stitch direction at selected locations on the formed hemispheres were employed as the key experimental measures for validating the forming simulations of pure-UDNCF. In addition, other experimental observations including formed defects such as in-plane and out-of-plane mesoscale wrinkles, forming forces, lateral displacement and shear strain can also be used as important metrics for model validation.

7.4. Potential Applications for Pure-Unidirectional Non-Crimp Fabrics

The primary goal of Jones Manville for employing pure-UDNCF may be to produce advanced composites for specific applications, including wind turbine blades, automotive, and aerospace, where optimal fibre orientation and high stiffness and strength are essential. While pure-UDNCF offers better mechanical properties along the tow direction, the significant stretching in the stitch direction presents a challenge in advanced composites. To overcome excessive stitch-stretching, stacking multiple layers of pure-UDNCF at different angles can be employed during composite forming. In addition, a surface coating such as thermoplastic binders or resin pre-impregnation can be applied to enhance the in-plane stiffness without altering the fundamental architecture of the fabric. These methods can improve handling and drapability of the fabric during advanced composite manufacturing while reducing defects such as gaps and thinning. However, this unique stretchability can be advantageous in other applications. For instance, pure-UDNCF can be used to produce flexible strain sensors for structural health monitoring, where controlled deformation enhances sensitivity. In addition, by integrating conductive coatings or nanomaterials, pure-UDNCF could serve as a multifunctional component in energy storage devices, such as flexible supercapacitors or composite battery casings. Its lightweight and flexible nature also makes it suitable for wearable electronics, enabling smart textiles with embedded circuits for health monitoring or interactive functionalities. While stretching in the stitch direction poses challenges in high-performance composites, it opens new opportunities for innovative applications in sensing, energy storage, and wearable technology.

7.5. Future Research Work

The iterative approach proposed in this study to separate the contribution of forces to the total axial force is limited to the results of four experiments, i.e., PSS, SS, PSPF and tensile tests. To improve the accuracy, more new experiments can be developed with well-defined kinematics, but with different combinations of shear and tensile strain in the stitch direction. For example, two more specimens can be created by changing the angle between the stitch direction and axial displacement to 30˚ and 60˚ (see Figure 7.2), similar to the PSS and SS tests (note that the angle between the stitch direction and axial displacement of the PSS and SS tests is 45˚ and 90˚, respectively). The results of these tests may encompass the unexplored areas in the parameter space of normalised axial force vs measured shear angle vs tensile strain in the stitch direction.

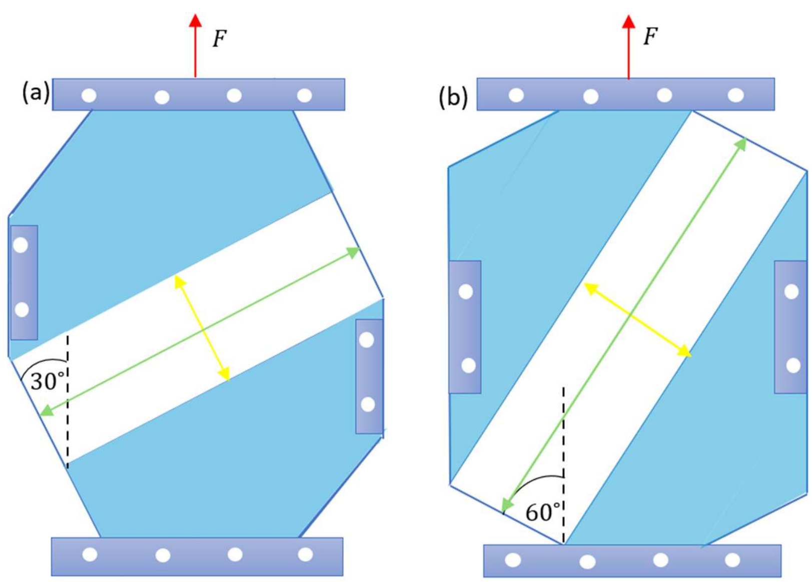

Figure 7.2: Proposed new experiments with different angles between the stitch direction and axial displacement(a) 30˚ (b) 60˚, the yellow and green arrows indicate the initial chain-stitch direction and the tow direction, respectively.

Enhanced In-Plane Bending Characterisation: Quantify the in-plane bending stiffness using the newly developed test in Chapter 5. This data could be critical in understanding how pure-UDNCF performs in high-curvature applications including its drapability, shape retention, and overall structural integrity. The quantitative measurements can be compared with the in-plane bending stiffness extracted from the interactive approach.

Development of Constitutive Models: Due to time constraints, this research concentrated on the experimental investigation of pure-UDNCF, which provided a comprehensive knowledge of its unique deformation behaviours, such as shear, tensile strain in the stitch direction, in-plane and out-of-plane bending. The following essential step is to develop material constitutive models that accurately represent these characteristics. These models can be used as essential tools for numerical forming simulations that predict the behaviour of fabrics under various forming conditions. Later, the developed numerical forming models can be evaluated using experimental forming results.

Real-Time Forming Monitoring Techniques: The forming experiment of this research consists of a three-step process that includes forming, fixing and analysing the deformation of the engineering fabric. The intermediate step of fixing is time-consuming. To avoid this step, the forming experiment can be designed with real-time monitoring techniques to analyse the fabric deformation directly during the forming process. Advanced techniques such as 3D laser scanning, digital image correlation, and fibre optic sensors could capture shear angles and stitch extension (this research also used a 3D laser scanning technique to analyse the formed specimens). Replacing the conventional mould used in this work with an open or partially open mould allows for real-time scanning during forming. Such moulds should be designed to adequately support the fabric while allowing the scanner to observe the clear deformation. This would improve accuracy by allowing immediate adjustments to the forming process as well as forming analysis efficiency by avoiding an intermediate step.

References

[1] H. Ning, N. Lub, A. A. Hassen, K. Chawla, M. Selim and S. Pillay, “A review of long fibre-reinforced thermoplastic or long fibre thermoplastic (LFT) composites,” *International Materials Reviews,* vol. 64, pp. 1-25, 2019.

[2] H. Sharma, A. Kumar, S. Rana, N. Sahoo, M. Jamil, R. Kumar, S. Sharma, C. Li, A. Kumar, S. Eldin and M. Abbas, “Critical review on advancements on the fiber-reinforced composites: Role of fiber/matrix modification on the performance of the fibrous composites,” *Journal of Materials Research and Technology,* vol. 26, pp. 2975-3002, 2023.

[3] M. S. H. Al-Furjan, L. Shan, X. Shen, M. S. Zarei, M. H. Hajmohammad and R. Kolahchi, “A review on fabrication techniques and tensile properties of glass, carbon, and Kevlar fiber reinforced rolymer composites,” *Journal of Materials Research and Technology,* vol. 19, pp. 2930-2959, 2022.

[4] S. S. P. S. Sajan and D. P. Selvaraj, “A review on polymer matrix composite materials and their applications,” *Materials Today: Proceedings,* vol. 47, pp. 5493-5498, 2021.

[5] C. J. Martín, “A Study of the Pyramid of Testing for Forming of Non-crimp Fabrics for Aerostructures (Doctoral dissertation),” University of Bristol, Bristol, 2023.

[6] P. Harrison, M. F. Alvarez and D. Anderson, “Towards comprehensive characterisation and modelling of the forming and wrinkling mechanics of engineering fabrics,” *International Journal of Solids and Structures,* vol. 154, pp. 2-18, 2018.

[7] U. Mohammed, C. Lekakou, L. Dong and M. G. Bader, “Shear deformation and micromechanics of woven fabrics,” *Composites Part A: Applied Science and Manufacturing,* vol. 31, no. 4, pp. 299-308, 2000.

[8] F. C. Campbell, “Thermoplastic Composites: An Unfulfilled Promise,” in *Manufacturing Processes for Advanced Composites*, Elsevier Science, 2004, pp. 357-397.

[9] W. D. Callister and D. G. Rethwisch, Fundamentals of materials science and engineering, London: Wiley, 2000.

[10] D. K. Rajak, D. D. Pagar, P. L. Menezes and E. Linul, "Review: Fiber-reinforced polymer composites: Manufacturing, properties, and applications," *Polymers,* vol. 11, no. 10, p. 1667, 2019.

[11] K. I. Ismail, T. C. Yap and R. Ahmed, "3D-printed fiber-reinforced polymer composites by fused deposition modelling (FDM): fiber length and fiber implementation techniques," *Polymers,* vol. 14, no. 21, p. 4659, 2022.

[12] A. K. Tanwer, "Mechanical properties testing of uni-directional and bi-directional glass fibre reinforced epoxy based composites," *International Journal of Research in Advent Technology,* vol. 2, no. 11, pp. 34-39, 2014.

[13] U. Ahmed, A. Tariq, Y. Nawab, K. Shaker, Z. Khaliq and M. Umair, "Comparison of mechanical behavior of biaxial, unidirectional and standard woven fabric reinforced composites," *Fibers and Polymers,* vol. 21, pp. 1308-1315, 2020.

[14] M. Eftekhari and A. Fatemi, "Tensile, creep and fatigue behaviours of short fibre reinforced polymer composites at elevated temperatures: a literature survey," *Fatigue & Fracture of Engineering Materials & Structures,* vol. 38, no. 12, pp. 1395-1418, 2015.

[15] S. Mortazavian and A. Fatemi, "Effects of fiber orientation and anisotropy on tensile strength and elastic modulus of short fiber reinforced polymer composites," *Composites part B: engineering,* vol. 72, pp. 116-129, 2015.

[16] K. W. Gan, Y. W. Ho, Z. Y. Ow, H. A. Israr and K. J. Wong, "Aligned discontinuous carbon fibre tows in hybrid composites and their tensile behaviour: An experimental study," *Journal of Composite Materials,* vol. 53, no. 26-27, pp. 3893-3907, 2019.

[17] H. Yu, K. D. Potter and M. R. Wisnom, "A novel manufacturing method for aligned discontinuous fibre composites (High Performance-Discontinuous Fibre method)," *Composites Part A: Applied Science and Manufacturing,* vol. 65, pp. 175-185, 2014.

[18] Y. Peng, Y. Wu, K. Wang, G. Gao and S. Ahzi, "Synergistic reinforcement of polyamide-based composites by combination of short and continuous carbon fibers via fused filament fabrication," *Composite Structures,* vol. 207, pp. 232-239, 2019.

[19] D. Yavas, Z. Zhang, Q. Liu and D. Wu, “Interlaminar shear behavior of continuous and short carbon fiber reinforced polymer composites fabricated by additive manufacturing,” *Composites Part B: Engineering,* vol. 204, p. 108460, 2021.

[20] K. Mehl, S. Schmeer, N. Motsch-Eichmann, P. Bauer, I. Müller and J. Hausmann, “Structural optimization of locally continuous fiber-reinforcements for short fiber-reinforced plastics,” *Journal of Composites Science,* vol. 5, no. 5, p. 118, 2021.

[21] T. P. Sathishkumar, J. A. Naveen and S. Satheeshkumar, “Hybrid fiber reinforced polymer composites–a review,” *Journal of Reinforced Plastics and Composites,* vol. 33, no. 5, pp. 454-471, 2014.

[22] C. Santulli, “Mechanical and impact damage analysis on carbon/natural fibers hybrid composites: A review,” *Materials,* vol. 12, no. 3, p. 517, 2019.

[23] S. A. Mirdehghan, “Fibrous polymeric composites,” in *Engineered Polymeric Fibrous Materials*, Woodhead Publishing, 2021, pp. 1-58.

[24] B. A. Newcomb and H. G. Chae, “The properties of carbon fibers,” in *Handbook of properties of textile and technical fibres*, Woodhead Publishing, 2018, pp. 841-871.

[25] R. Ghosh, S. Das, S. P. Mallick and Rajan, “Fundamentals of Carbon-Fiber-Reinforced Composite and Structures,” in *Natural and Synthetic Fiber Reinforced Composites: Synthesis, Properties and Applications*, Wiley, 2022, pp. 37-65.

[26] L. Mishnaevsky Jr, K. Branner, H. N. Petersen, J. Beauson, M. McGugan and B. F. Sørensen, “Materials for wind turbine blades: An overview,” *Materials,* vol. 10, no. 11, p. 1285, 2017.

[27] S. Prashanth, K. M. Subbaya, K. Nithin and S. Sachhidananda, “Fiber reinforced composites - A review,” *Journal of Material Sciences & Engineering ,* vol. 60, no. 3, pp. 2-6, 2017.

[28] P. Dharmavarapu and M. B. S. S. Reddy, “Aramid fibre as potential reinforcement for polymer matrix composites: a review,” *Emergent materials,* vol. 5, no. 5, pp. 1561-1578, 2022.

[29] J. W. Hearle, High-performance fibres, Woodhead Publishing, 2001.

[30] A. Knijnenberg, “Compressive failure behaviour of novel aramid fibres,” Delft University of Technology, Delft, 2009.

[31] Y. Xu, H. Zhang and G. Huang, “Review on the mechanical deterioration mechanism of aramid fabric under harsh environmental conditions,” *Polymer Testing,* vol. 128, p. 108227, 2023.

[32] J. P. Srivastava and P. Kumar, “Introduction to Glass Fiber-Based Composites and Structures,” in *Natural and Synthetic Fiber Reinforced Composites: Synthesis, Properties and Applications*, Wiley , 2022, pp. 1-16.

[33] T. Kulhan, A. Kamboj, N. K. Gupta and N. Somani, “Fabrication methods of glass fibre composites—a review,” *Functional Composites and Structures,* vol. 4, no. 2, p. 022001, 2022.

[34] N. S. Karaduman, Y. Karaduman, H. Ozdemir and G. Ozdemir, “Textile Reinforced Structural Composites for Advanced Applications,” in *Advances in Glass Science and Technology*, IntechOpen, 2017.

[35] G. A. Bibo and P. J. Hogg, “The role of reinforcement architecture on impact damage mechanisms and post-impact compression behaviour.,” *Journal of Materials Science,* vol. 31, no. 5, pp. 1115-1137, 1996.

[36] A. P. Mouritz, “Fatigue of 3D textile-reinforced composites,” in *Fatigue of Textile Composites*, Woodhead Publishing, 2015, pp. 255-274.

[37] K. Vallons, “The Behaviour of Carbon Fibre - Epoxy NCF Composites under Various,” Catholic University of Leuven, Leuven, 2009.

[38] P. Tan, L. Tong and G. P. Steven, “Modelling for predicting the mechanical properties of textile composites - A review,” *Composites Part A,* vol. 28, no. 11, pp. 903-922, 1997.

[39] A. Dixit and H. S. Mali, “Modeling Techniques for Prediction the Mechanical Properties of Woven-Fabric Textile Composite: A Review,” *Mechanics of Composite Materials,* vol. 49, no. 1, p. 1–20, 2013 .

[40] K. Bilisik, “Two-dimensional (2D) fabrics and three-dimensional (3D) preforms for ballistic and stabbing protection: A review,” *Textile Research Journal,* vol. 87, no. 18, p. 2275–2304, 2017.

[41] V. Schrank, M. Beer, M. Beckers and T. Gries, “Polymer-optical fibre (POF) integration into textile fabric structures,” in *Polymer Optical Fibres*, Woodhead Publishing, 2017, pp. 337-348.

[42] G. Jiang, Z. Gao, P. Ma, X. Miao and Y. Zhu, “Comparative study on the mechanical behavior of carbon weft-knitted biaxial fabrics stitched by polyester fibers and preoxidized polyacrylonitrile fibers,” *Journal of Industrial Textiles,* vol. 44, no. 1, pp. 5-21, 2014.

[43] M. Wouters, “Effects of fibre bundle size and stitch pattern on the static properties of unidirectional carbon-fibre non-crimp fabric composites.,” Lulea University of Technology, Lulea, 2002.

[44] F. J. Schirmaier, K. A. Weidenmann, L. Kärger and F. Henning, “Characterisation of the draping behaviour of unidirectional non-crimp fabrics (UD-NCF),” *Composites: Part A,* vol. 80, p. 28–38, 2016.

[45] P. Harrison and F. Härtel, “Evaluation of normalisation methods for uniaxial bias extension tests on engineering fabrics.,” *Composites Part A: Applied Science and Manufacturing,* vol. 67, pp. 61-69, 2014.

[46] M. Ghazimoradi, E. A. Trejo, V. Carvelli, C. Butcher and J. Montesano, “Deformation characteristics and formability of a tricot-stitched carbon fiber unidirectional non-crimp fabric,” *Composites Part A: Applied Science and Manufacturing,* vol. 145, p. 106366, 2021.

[47] S. V. Lomov, Non-crimp fabric composites: manufacturing, properties, and applications, Cambridge: Woodhead Publisher Ltd., 2011.

[48] H. Heßa and N. Himmel, “Structurally stitched NCF CFRP laminates. Part 1: Experimental characterization of in-plane and out-of-plane properties,” *Composites Science and Technology,* vol. 71, no. 5, pp. 549-568, 2011.

[49] U. Beier, F. Fischer, K. W. Sandler, V. Altstäd, C. Weimer, H. Spanner and W. Buchs, “Evaluation of preforms stitched with a low melting-temperature thermoplastic yarn in carbon fibre-reinforced composites,” *Composites Part A: Applied Science and Manufacturing,* vol. 39, no. 5, pp. 705-711, 2008.

[50] B. Schäfer, R. Zheng, N. Naouar and L. Kärger, "Membrane behavior of uni- and bidirectional non-crimp fabrics in off-axis-tension tests," *International Journal of Material Forming,* vol. 16, no. 6, p. 68, 2023.

[51] A. Shipsha, S. Hallström and M. Burman, "Effect of stacking sequence and bundle waviness in quasi-isotropic NCF composites subjected to compression," *Composites Part B: Engineering,* vol. 178, p. 107423, 2019.

[52] L. Hahn, K. Zierold, A. Golla, D. Friese and S. Rittner, "3D textiles based on warp knitted fabrics: a review," *Materials,* vol. 16, no. 10, p. 3680, 2023.

[53] F. J. Schirmaier, D. Dörr, F. Henning and L. Kärger, "A macroscopic approach to simulate the forming behaviour of stitched unidirectional non-crimp fabrics (UD-NCF)," *Composites: Part A,* vol. 102, pp. 322-335, 2017.

[54] M. Ghazimoradi, E. A. Trejo, C. Butcher and J. Montesano, "Characterizing the macroscopic response and local deformation mechanisms of a unidirectional non-crimp fabric," *Composites Part A: Applied Science and Manufacturing,* vol. 156, p. 106857, 2022.

[55] C. Krogh, J. A. Kepler and J. Jakobsen, "Pure and simple: investigating the in-plane shear kinematics of a quasi-unidirectional glass fiber non-crimp fabric using the bias-extension test.," *International Journal of Material Forming,* vol. 14, no. 6, pp. 1483-1495, 2021.

[56] E. A. Trejo, M. Ghazimoradi, C. Butcher and J. Montesano, "Assessing strain fields in unbalanced unidirectional non-crimp fabrics," *Composites Part A: Applied Science and Manufacturing,* vol. 130, p. 105758, 2020.

[57] A. Habboush, N. Sanbhal, H. Shao, J. Jiang and N. Chen, "Characterization and Analysis of In-Plane Shear Behavior of GlassWarp-Knitted Non-Crimp Fabrics Based on Picture Frame Method," *Materials,* vol. 11, p. 1550, 2018.

[58] A. Habboush, N. Sanbhal, H. Shao, J. Jiang and N. Chen, "Characterization and analysis of wrinkling behavior of glass warp knitted non-crimp fabrics based on double-dome draping geometry.," *Journal of Engineered Fibers and Fabrics,* vol. 15, pp. 1-17, 2020.

[59] K. Vallons, G. Adolphs, P. Lucas, S. V. Lomov and I. Verpoest, "Quasi-UD glass fibre NCF composites for wind energy applications: a review of requirements and existing fatigue data for blade materials," *Mechanics and Industry,* vol. 14, no. 3, pp. 175-189, 2013.

[60] T. Senner, S. Kreissl, Merklein, J. Meinhardt and A. Lipp, “A modular modeling approach for describing the in-plane forming behavior of unidirectional non-crimp-fabrics.,” *Production Engineering,* vol. 8, pp. 635-643, 2014.

[61] S. Bhat, G. Dittel, A. Knobel and T. Gries, “Investigation of the drapability of elastic-adapted textile reinforcements for double-curved concrete panels,” in *SAMPE EUROPE Conference and Exhibition 2022*, Hamburg, 2022.

[62] P. Harrison and N. Curado-Correia, “Temperature and rate dependent multi-scale shear modelling of molten thermoplastic advanced composites,” in *19th International Conference on Composite Materials*, Montreal, Canada, 2013.

[63] S. W. Hsiao and N. Kikuchi, “Numerical analysis and optimal design of composite thermoforming process,” *Computer Methods in Applied Mechanics and Engineering,* vol. 177, no. 1-2, pp. 1-34, 1999.

[64] J. Wang, P. Wang, N. Hamila and P. Boisse, “Mesoscopic analyses of the draping of 3D woven composite reinforcements based on macroscopic simulations,” *Composite Structures,* vol. 250, p. 112602, 2020.

[65] P. Potluri, D. P. Ciurezu and R. B. Ramgulam, “Measurement of meso-scale shear deformations for modelling textile composites,” *Composites Part A: Applied Science and Manufacturing,* vol. 37, no. 2, pp. 303-314, 2006.

[66] P. Harrison, F. Abdiwi, X. Z.Guo; P.Potluri; W.R.Yu, Z. Guo, P. Potluri and W. Yu, “Characterising the shear–tension coupling and wrinkling behaviour of woven engineering fabrics,” *Composites Part A: Applied Science and Manufacturing,* vol. 43, pp. 903-914, 2012.

[67] P. Harrison, “Modelling the forming mechanics of engineering fabrics using a mutually constrained pantographic beam and membrane mesh,” *Composite: Part A,* vol. 81, pp. 145-157, 2016.

[68] M. Thor, “Out-of-plane fiber waviness in composite materials: origins, detection and mechanical evaluation,” University of Augsburg, Germany, 2021.

[69] J. Hu, Structure and mechanics of woven fabrics, Cambridge: Woodhead publishing Ltd., 2004.

[70] J. Simon, "Numerical simulation and experimental investigation of the forming of tailored fibre placement preforms: a mixed embedded-ALE finite element formulation," École centrale de Nantes (Doctoral dissertation), 2022.

[71] H. A. Alshahrani, "Bending behavior of textile thermosetting composite prepregs during forming processes," Concordia University (Doctoral dissertation), 2017.

[72] Y. P. Chuves, M. Pitanga, I. Grether, M. O. Cioffi and F. Monticeli, "The influence of several carbon fiber architecture on the drapability effect," *Textiles,* vol. 2, no. 3, pp. 486-498, 2022.

[73] A. Hosseini, M. Haghi Kashani, F. Sassani, A. S. Milani and F. Ko, "A mesoscopic analytical model to predict the onset of wrinkling in plain woven preforms under bias extension shear deformation," *Materials,* vol. 10, no. 10, p. 1184, 2017.

[74] F. T. Peirce, "The "handle" of cloth as a measurable quantity," *Journal of the Textile Institute Transaction,* vol. 21, no. 9, pp. T377-T416, 1930.

[75] S. Kawabata, *The standardization and analysis of hand evaluation,* The hand evaluation and standardization committee, 1980.

[76] R. Sourki, B. Khatir, S. S. Najar, R. Vaziri and A. S. Milani, "Characterization of the dissipative large deformation bending response of dry fabric composites as occurs during forming," *Composite Structures,* vol. 310, p. 116728, 2023.

[77] *ASTM D1388: Standard Test Method for Stiffness of Fabrics,* American Society for Testing and Materials, 2002.

[78] *ISO 4604: Reinforcement fabrics — Determination of conventional flexural stiffness — Fixed-angle flexometer method,* International Organization for Standardization, 2011.

[79] *BS 3356: Method for determination of bending length and flexural rigidity of fabrics,* British Standard Institution, 1990.

[80] P. Giorgio Minazio, "FAST–fabric assurance by simple testing," *International Journal of Clothing Science and Technology,* vol. 7, no. (2/3), pp. 43-48, 1995.

[81] C. C. Chu, C. L. Cummings and N. A. Teixeira, "Mechanics of elastic performance of textile materials: Part V: A study of the factors affecting the drape of fabrics—The development of a drape meter," *Textile Research Journal,* vol. 20, no. 8, pp. 539-548, 1950.

[82] W. G. Bickley, "L. The heavy elastica," *The London, Edinburgh, and Dublin Philosophical Magazine and Journal of Science,* vol. 17, no. 113, pp. 603-622, 1934.

[83] N. J. Abbott, "Part II: A study of the peirce cantilever test for stiffness of textile fabrics," *Textile Research Journal,* vol. 21, no. 6, pp. 441-444, 1951.

[84] "Fabric Stiffness Tester TF113," Testex, 30 April 2017. [Online]. Available: https://www.testextextile.com/product/fabric-stiffness-tester-tf113/. [Accessed 03 April 2024].

[85] X. C. H. Li and Z. Gao, "Evaluation of knitted suit fabric style based on fuzzy neural network," *Journal of Engineered Fibers and Fabrics,* vol. 15, pp. 1-11, 2020.

[86] M. Seif, "Bereitstellung von Materialkennwerten für die Simulation von Bekleidungsprodukten (English: Determination of Material parameters for the simulation of clothing products)," Technical university of Dresden, Dresden, 2007.

[87] A. B. H. Musa, B. Malengier, L. Van Langenhove and C. Stevens, "The reliability of the newly developed bending tester for the measurement of flexural rigidity of textile materials," *IOP Conference Series: Materials Science and Engineering,* vol. 254, no. 14, p. 142004, 2017.

[88] M. Hübner, M. Fazeli, T. Gereke and C. Cherif, "Geometrical design and forming analysis of three-dimensional woven node structures," *Textile research journal,* vol. 88, no. 2, pp. 213-224, 2018.

[89] N. Lammens, M. Kersemans, G. Luyckx, W. Van Paepegem and J. Degrieck, "Improved accuracy in the determination of flexural rigidity of textile fabrics by the Peirce cantilever test (ASTM D1388)," *Textile Research Journal,* vol. 84, no. 12, pp. 1307-1314, 2014.

[90] E. de Bilbao, D. Soulat, G. Hivet and A. Gasser, "Experimental study of bending behaviour of reinforcements," *Experimental Mechanics,* vol. 50, pp. 333-351, 2010.

[91] B. Liang, P. Chaudet and P. Boisse, "Curvature determination in the bending test of continuous fibre reinforcements," *Strain,* vol. 53, no. 1, p. e12213, 2017.

[92] D. Soteropoulos, K. Fetfatsidis, J. A. Sherwood and J. Langworthy, "Digital method of analyzing the bending stiffness of non-crimp fabrics," in *AIP Conference Proceedings*, American Institute of Physics, 2011.

[93] L. M. Dangora, C. Mitchell, K. D. White, J. A. Sherwood and J. C. Parker, “Characterization of temperature-dependent tensile and flexural rigidities of a cross-ply thermoplastic lamina with implementation into a forming model,” *International Journal of Material Forming,* vol. 11, pp. 43-52, 2016.

[94] H. Alshahrani and M. Hojjati, “A new test method for the characterization of the bending behavior of textile prepregs,” *Composites Part A: Applied Science and Manufacturing,* vol. 97, pp. 128-140, 2017.

[95] P. Harrison, M. Fernandez Alvarez, N. Correia, P. Mimoso, C. Cristovão and R. Gomes, “Characterising the forming mechanics of pre-consolidated nylon-carbon composite,” in *ECCM 18: 18th European Conference on Composite Materials*, Athens, Greece, 2018.

[96] H. Lin, M. J. Clifford, A. C. Long, K. Lee and N. Guo, “A finite element approach to the modelling of fabric mechanics and its application to virtual fabric design and testing,” *Journal of the Textile Institute,* vol. 103, no. 10, pp. 1063-1076, 2012.

[97] Q. Nguyen-Trong, F. Ferreira and A. Gomes, “Modelling the bending behaviour of plain-woven fabric using flat shell element and strain smoothing technique.,” in *Association of Universities for Textiles (AUTEX)*, 2013.

[98] T. Lahey, “ Modelling hysteresis in the bending of fabrics,” University of Waterloo, Waterloo, 2002.

[99] “KES-FB2-S Pure Bending Tester,” Kato Tech Co.Ltd, 02 April 2016. [Online]. Available: https://english.keskato.co.jp/archives/products/kes-fb2-s. [Accessed 12 Apil 2024].

[100] S. Chen, “Fabric forming simulation and process optimisation for composites (Doctoral dissertation),” University of Nottingham, Nottingham, 2016.

[101] P. Harrison, E. Taylor and J. Alsayednoor, “Improving the accuracy of the uniaxial bias extension test on engineering fabrics using a simple wrinkle mitigation technique,” *Composites Part A,* vol. 108, p. 53–61, 2018.

[102] D. Laresser, “Investigation of the Forming Behavior of a Thermoplastic Unidirectional Tape Laminate: Forming, Experiment, Modeling, Simulation,” Johannes Kepler University, 2020.

[103] Y. Zhao, Y. Gu, T. Zhang, H. Li, B. Zhang and Z. Zhang, “Characterization of intra-ply shear behaviors of unidirectional prepregs during hot diaphragm forming process,” *Polymer Composites,* vol. 42, no. 2, pp. 1008-1020., 2021.

[104] A. Hosseini, M. H. Kashani, F. Sassani , A. S. Milani and F. K. Ko, “Identifying the distinct shear wrinkling behavior of woven composite preforms under bias extension and picture frame tests,” *Composite Structures,* vol. 185, p. 764–773, 2018.

[105] G. Hivet and A. Duong, “A contribution to the analysis of the intrinsic shear behavior of fabrics,” *Journal of Composite Materials,* vol. 45, no. 6, p. 695–716, 2011.

[106] I. Taha, Y. Abdin and S. Ebeid, “Comparison of picture frame and Bias-Extension tests for the characterization of shear behaviour in natural fibre woven fabrics,” *Fibers and Polymers,* vol. 14, pp. 338-344, 2013.

[107] A. S. Milani, J. A. Nemes, G. Lebrun and M. N. Bureau, “A Comparative Analysis of a Modified Picture Frame Test for Characterization of Woven Fabrics,” *Polymer Composites,* vol. 31, no. 4, pp. 561-568, 2010.

[108] P. Boisse, N. Hamila, E. Guzman-Maldonado, A. Madeo, G. Hivet and F. Dell’Isola, “The bias-extension test for the analysis of in-plane shear properties of textile composite reinforcements and prepregs: a review,” *International Journal of Material Forming,* vol. 10, pp. 473-492, 2017.

[109] P. Harrison, M. J. Clifford and A. C. Long, “Shear characterisation of viscous woven textile composites: a comparison between picture frame and bias extension experiments,” *Composites Science and Technology,* vol. 64, p. 1453–1465, 2004.

[110] A. Willems, S. V. Lomov, I. Verpoest and D. Vandepitte, “Optical strain fields in shear and tensile testing of textile reinforcements,” *Composites Science and Technology,* vol. 68, no. 3-4, pp. 807-819, 2008.

[111] C. Krogh, K. D. White, A. Sabato and J. A. Sherwood, “Picture-frame testing of woven prepreg fabric: an investigation of sample geometry and shear angle acquisition,” *International Journal of Material Forming,* vol. 13, pp. 341-353, 2020.

[112] F. Härtel and P. Harrison, “Evaluation of normalisation methods for uniaxial bias extension tests on engineering fabrics,” *Composites Part A: Applied Science and Manufacturing,* vol. 67, pp. Volum61-69, 2014.

[113] J. Alsayednoor J, P. Harrison and W. R. Yu, “Influence of specimen pre-shear and wrinkling on the accuracy of uniaxial bias extension test results,” *Composites Part A: Applied Science and Manufacturing,* vol. 101, p. 81–97, 2017.

[114] P. Harrison, J. Wiggers and A. Long, “Normalisation of shear test data for rate-independent compressible fabrics,” *Journal of Composite Materials,* vol. 42, no. 22, pp. 2315-2344, 2008.

[115] I. Giorgio, P. Harrison, F. Dell'Isola, J. Alsayed and E. Turco, “Wrinkling in engineering fabrics: a comparison between two different comprehensive modelling approaches,” *proceedings of the royal society A,* vol. 474, pp. 1-20, 2018.

[116] S. V. Lomov, P. Boisse, E. Deluycker, F. Morestin, K. Vanclooster, D. Vandepitte, I. Verpoest and A. Willems, “Full-field strain measurements in textile deformability studies,” *Composites Part A: Applied Science and Manufacturing,* vol. 39, no. 8, pp. 1232-1244, 2008.

[117] P. Harrison and F. Härtel, “Corrigendum to ‘Evaluation of normalisation methods for uniaxial bias extension tests on engineering fabrics’,” *Composites: Part A,* vol. 80, p. 104–106, 2016.

[118] J. Pourtier, B. Duchamp, M. Kowalski, P. Wang, X. Legrand and D. Soulat, “Two-way approach for deformation analysis of non-crimp fabrics in uniaxial bias extension tests based on pure and simple shear assumption,” *International Journal of Material Forming,* vol. 12, no. 6, pp. 995-1008, 2019.

[119] M. J. Clifford, A. C. Long and P. De Luca, “Forming of engineered prepregs and reinforced thermoplastics,” in *The Second Global Symposium on Innovations in Materials Processing and Manufacturing: Sheet Materials*, 303-316, 2001.

[120] J. Cao, R. Akkerman, P. Boisse, J. Chen, H. S. Cheng, E. F. de Graaf, J. L. Gorczyca, P. Harrison, G. Hivet, J. Launay, W. Lee, L. Liu, S. V. Lomov, A. Long, E. de Luycker, F. Morestin, J. Padvoiskis, X. Q. Peng, J. Sherwood, T. Stoilova, X. M. Tao, I. Verpoest, A. Willems, J. Wiggers, T. X. Yu and B. Zhu, “Characterization of mechanical behavior of woven fabrics: Experimental methods and benchmark results,” *Composites: Part A,* vol. 39, p. 1037–1053, 2008.

[121] K. D. H. N. Kahavita, P. Harrison, E. D. McCarthy, M. Zhang and C. M. Ó Brádaigh, “Investigation of the In-Plane Deformation Kinematics of a Unidirectional Non-Crimp Glass Fabric,” in *International Conference on Manufacturing of Advanced Composites*, Sheffield, 2022.

[122] J. Launay, G. Hivet, A. V. Duong and P. Boisse, “Experimental analysis of the influence of tensions on in plane shear behaviour of woven composite reinforcements,” *Composites Science and Technology,* vol. 68, p. 506–515, 2008.

[123] H. Montazerian, A. Rashidi, M. Hoorfar and A. S. Milani, “A frameless picture frame test with embedded sensor: Mitigation of imperfections in shear characterization of woven fabrics,” *Composite Structures,* vol. 211, p. 112–124, 2019.

[124] A. K. Pickett, “Draping, forming and consolidation,” in *Introduction to Process and Mechanical Modelling of Engineering Composites*, Germany, IFB, University Stuttgart, 2021, pp. 284-334.

[125] L. Krishnappa, J. H. Ohlendorf, M. Brink and K. D. Thoben, “Investigating the factors influencing the shear behaviour of 0/90 non-crimp fabrics to form a reference shear test,” *Journal of Composite Materials,* 2021.

[126] Z. Ahmad and B. K. Sirkova, “Tensile behavior of Basalt/Glass single and multilayer-woven fabrics,” *The journal of the textile institute,* vol. 109, no. 5, pp. 686-694, 2018.

[127] P. Quenzel, H. Kröger, B. Manin, K. Ngoc Vu, T. X. Duong, T. Gries, M. Itskov and R. A. Sauer, “Material characterisation of biaxial glass-fibre non-crimp fabrics as a function of ply orientation, stitch pattern, stitch length and stitch tension,” *Journal of Composite Materials,* vol. 56, no. 26, pp. 3971-3991, 2022.

[128] H. Nakatani, K. Nakaya, A. Matsuba, Y. Kouno and S. Ogihara, “Effect of prepreg cut on the mechanical properties in CFRP laminates,” *Journal of Solid Mechanics and Materials Engineering,* vol. 5, no. 12, pp. 742-752, 2011.

[129] T. Muttaqie, A. Hidayat, I. R. A. Fikri, J. Purwon, A. Aribowo, F. A. Wandono and A. R. Prabowo, “Analysis of prepreg carbon fibre laminates base on tensile test and FEM for UAV applications,” in *AIP Conference Proceedings*, 2023.

[130] J. M. F. D. Paiva, S. Mayer and M. C. Rezende, “Comparison of tensile strength of different carbon fabric reinforced epoxy composites,” *Materials Research,* vol. 9, pp. 83-90, 2006.

[131] *ASTM D885: Standard Test Methods For Tire Cords, Tire Cord Fabrics, And Industrial Filament Yarns Made From Manufactured Organic-Base Fibers,* American Society for Testing and Materials, 2007.

[132] Y. Yang, W. Cao, Z. Wang, J. Li and Y. Zhang, “Variation of mechanical properties and ballistic performance of fabric prepreg after resin coating processing,” *Composite Structures,* vol. 321, p. 117232, 2023.

[133] D. Zhang, L. Chen, Y. Wang, Y. Sun, N. Jia and K. Qian, “Bias tensile strength behaviors of woven fabric: theoretical and experimental,” *The Journal of The Textile Institute,* vol. 108, no. 10, pp. 1753-1761, 2017.

[134] C. Y. Yue, G. X. Sui and H. C. Looi, “Effects of heat treatment on the mechanical properties of Kevlar-29 fibre,” *Composites Science and Technology,* vol. 60, no. 3, pp. 421-427, 2000.

[135] *ASTM D3379: Standard test method for tensile strength and Young's modulus for high modulus single filament materials,* American Society for Testing and Materials, 1989.

[136] “ASTM D885/D885M-10A(2014)e1 - Standard Test Methods for Tire Cords, Tire Cord Fabrics, and Industrial Filament Yarns Made from Manufactured Organic-Base Fibers (Withdrawn 2023),” ASTM International, 10 January 2023. [Online]. Available: https://www.astm.org/d0885_d0885m-10ar14e01.html. [Accessed 06 April 2024].

[137] *ASTM D2256-02: Standard Test Method for Tensile Properties of Yarns by the Single-Strand Method,* American Society for Testing and Materials, 2008.

[138] E. Selver, H. K. Dalfi and P. Potluri, “Enhancing the mechanical performance of notched glass/epoxy composite laminates via hybridisation with thermoplastic fibres,” *Journal of Composite Materials,* vol. 57, no. 23, pp. 3703-3721, 2023.

[139] E. Omrani, H. Hasani and F. Esmaeili, “Mechanical performance of tubular composites reinforced by innovative 3D integrated knitted spacer fabrics,” *Journal of Applied Polymer Science,* vol. 135, no. 14, p. 46074, 2018.

[140] *ISO 3341: Textile glass — Yarns — Determination of breaking force and breaking elongation,* International Organization for Standardization, 2000.

[141] *ISO 2062: Textiles — Yarns from packages — Determination of single-end breaking force and elongation at break using constant rate of extension (CRE) tester,* International Organization for Standardization, 2009.

[142] M. Manins, A. Bernava and G. Strazds, "Study of Performance of Hybrid yarns (Hemp/Polypropylene/Glass) Woven Reinforcements. Int. Journal of Engineering Research and Applications," *Journal of Engineering Research and Applications,* vol. 5, no. 6, pp. 43-47, 2015.

[143] *ISO 13934-1: Textiles — Tensile properties of fabrics — Part 1: Determination of maximum force and elongation at maximum force using the strip method,* International Organization for Standardization, 2013.

[144] V. N. Khiêm, H. Krieger, M. Itskov, T. Gries and S. E. Stapleton, "An averaging based hyperelastic modeling and experimental analysis of non-crimp fabrics," *International Journal of Solids and Structures,* vol. 154, pp. 43-54, 2018.

[145] A. G. Prodromou and J. Chen, "On the relationship between shear angle and wrinkling of textile composite preforms," *Composites Part A: Applied Science and Manufacturing,* vol. 28, no. 5, pp. 491-503, 1997.

[146] C. Rueden, C. Dietz, M. Horn, J. Schindelin, B. Northan, M. Berthold and K. Eliceiri, "ImageJ Ops [Software]," 2016. [Online]. Available: https://imagej.net/Ops..

[147] V. Arumugam, R. Mishra, J. Militky and M. Tunak, "In-plane shear behavior of 3D spacer knitted fabrics," *Journal of Industrial Textiles,* vol. 46, no. 3, pp. 868-886, 2016.

[148] N. Jariyapunya and S. Baheti, "Application of image analysis method for measurement of fabric stretch deformation," *IOP Conference Series: Materials Science and Engineering,* vol. 254, no. 14, p. 142010, 2017.

[149] D. Zhu, B. Mobasher and S. D. Rajan, "Dynamic tensile testing of Kevlar 49 fabrics," *Journal of materials in civil engineering,* vol. 23, no. 3, pp. 230-239, 2011.

[150] B. Pan, K. Qian, H. Xie and A. Asundi, "Two-dimensional digital image correlation for in-plane displacement and strain measurement: a review," *Measurement science and technology,* vol. 20, no. 6, p. 062001, 2009.

[151] B. Pan, "Digital image correlation for surface deformation measurement: historical developments, recent advances and future goals," *Measurement Science and Technology,* vol. 29, no. 8, p. 082001, 2018.

[152] S. V. Lomov, A. Willems, I. Verpoest, Y. Zhu, M. Barburski and T. Stoilova, "Picture frame test of woven composite reinforcements with a full-field strain registration," *Textile Research Journal,* vol. 76, no. 3, pp. 243-252, 2006.

[153] H. Krieger, D. Kaufmann and T. Gries, "Kinematic drape algorithm and experimental approach for the design of tailored non-crimp fabrics," *Key Engineering Materials,* vol. 651, pp. 393-398, 2015.

[154] A. O. Gibbs, "Orientation control during 2D-3D composite preforming (Doctoral dissertation)," University of Nottingham, Nottingham, 2023.

[155] S. Allaoui, P. Boisse, S. Chatel, N. Hamila, G. Hivet, D. Soulat and E. Vidal-Salle, "Experimental and numerical analyses of textile reinforcement forming of a tetrahedral shape," *Composites Part A: Applied Science and Manufacturing,* vol. 42, no. 6, pp. 612-622, 2011.

[156] E. Owlia, S. Shaikhzadeh Najar and R. Tavana, "Experimental and macro finite element modeling studies on conformability behavior of woven nylon 66 composite reinforcement," *The Journal of the Textile Institute,* vol. 111, no. 6, pp. 874-881, 2020.

[157] X. K. Li and S. L. Bai, "Sheet forming of the multi-layered biaxial weft knitted fabric reinforcement. Part I: On hemispherical surfaces," *Composites Part A: Applied Science and Manufacturing,* vol. 40, no. 6-7, pp. 766-777, 2009.

[158] J. S. Lee, S. J. Hong, W. R. Yu and T. J. Kang, "The effect of blank holder force on the stamp forming behavior of non-crimp fabric with a chain stitch," *Composites science and technology,* vol. 67, no. 3-4, pp. 357-366, 2007.

[159] M. A. Khan, T. Mabrouki, E. Vidal-Sallé and P. Boisse, "Numerical and experimental analyses of woven composite reinforcement forming using a hypoelastic behaviour. Application to

the double dome benchmark," *Journal of materials processing technology,* vol. 210, no. 2, pp. 378-388, 2010.

[160] J. Pazmino, V. Carvelli and S. V. Lomov, "Formability of a non-crimp 3D orthogonal weave E-glass composite reinforcement," *Composites Part A: Applied Science and Manufacturing,* vol. 61, pp. 76-83, 2014.

[161] S. Allaoui, G. Hivet, D. Soulat, A. Wendling, P. Ouagne and S. Chatel, "Experimental preforming of highly double curved shapes with a case corner using an interlock reinforcement," *International Journal of Material Forming,* vol. 7, pp. 155-165, 2014.

[162] P. Wang, X. Legrand, P. Boisse, N. Hamila and D. Soulat, "Experimental and numerical analyses of manufacturing process of a composite square box part: Comparison between textile reinforcement forming and surface 3D weaving," *Composites Part B: Engineering,* vol. 78, pp. 26-34, 2015.

[163] P. Boisse, B. Zouari and A. Gasser, "A mesoscopic approach for the simulation of woven fibre composite forming," *Composites science and technology,* vol. 65, no. 3-4, pp. 429-436, 2005.

[164] F. Yu, "The prediction of wrinkle formation in non-crimp fabrics during double diaphragm forming (Doctoral dissertation).," University of Nottingham, Nottingham, 2022.

[165] A. C. Ackermann, "Low-cost manufacture of an advanced composite steered-fibre laminate (final year project thesis)," University of Glasgow, Glasgow, 2013.

[166] Z. Xiao and P. Harrison, "Fabric steering technology for variable stiffness panels: Manufacture and mechanical testing," *Composites Part B: Engineering,* vol. 223, p. 109105, 2021.

[167] B. Liang and P. Boisse, "A review of numerical analyses and experimental characterization methods for forming of textile reinforcements," *Chinese Journal of Aeronautics,* vol. 34, no. 8, pp. 143-163, 2021.

[168] T. Gereke, O. Döbrich, M. Hübner and C. Cherif, "Experimental and computational composite textile reinforcement forming: A review," *Composites Part A: Applied Science and Manufacturing,* vol. 46, pp. 1-10, 2013.

[169] L. P. Brown, "TexGen," in *Advanced Weaving Technology.*, Springer International Publishing, 2022, pp. 253-291.

[170] S. V. Lomov and I. Verpoest, "WiseTex–Virtual Textile software," *Fibres and Textiles,* vol. 8, no. 2, pp. 135-140, 2001.

[171] I. Verpoest and S. V. Lomov, "Virtual textile composites software WiseTex: Integration with micro-mechanical, permeability and structural analysis," *Composites Science and Technology,* vol. 65, no. 15-16, pp. 2563-2574, 2005.

[172] S. V. Lomov, E. B. Belov, T. Bischoff, S. B. Ghosh, T. T. Chi and I. Verpoest, "Carbon composites based on multiaxial multiply stitched preforms. Part 1. Geometry of the preform," *Composites Part A: Applied science and manufacturing,* vol. 33, no. 9, pp. 1171-1183, 2002.

[173] C. D. Rudd, A. C. Long, K. N. Kendall and C. Mangin, "Preform design and manufacture," in *Liquid moulding technologies: Resin transfer moulding, structural reaction injection moulding and related processing techniques*, Woodhead Publishing, 1997, pp. 151-202.

[174] S. G. Hancock and K. D. Potter, "The use of kinematic drape modelling to inform the hand lay-up of complex composite components using woven reinforcements," *Composites Part A: Applied Science and Manufacturing,* vol. 37, no. 3, pp. 413-422, 2006.

[175] K. Vanclooster, "Forming of multilayered fabric reinforced thermoplastic composites (PhD thesis)," KU Leuven, Leuven, 2009.

[176] S. G. Hancock and K. D. Potter, "Inverse drape modelling—an investigation of the set of shapes that can be formed from continuous aligned woven fibre reinforcements," *Composites Part A: applied science and manufacturing,* vol. 36, no. 7, pp. 947-953, 2005.

[177] A. S. Tam and T. G. Gutowski, "The kinematics for forming ideal aligned fibre composites into complex shapes," *Composites Manufacturing,* vol. 1, no. 4, pp. 219-228, 1990.

[178] O. Rozant, P. E. Bourban and J. Månson, "Drapability of dry textile fabrics for stampable thermoplastic preforms," *Composites Part A: Applied Science and Manufacturing,* vol. 31, no. 11, pp. 1167-1177, 2000.

[179] K. Vanclooster, S. V. Lomov and I. Verpoest, "Experimental validation of forming simulations of fabric reinforced polymers using an unsymmetrical mould configuration," *Composites Part A: Applied Science and Manufacturing,* vol. 40, no. 4, pp. 530-539, 2009.

[180] H. Lin, J. Wang, A. C. Long, M. J. Clifford and P. Harrison, "Predictive modelling for optimization of textile composite forming," *Composites Science and Technology,* vol. 67, no. 15-16, pp. 3242-3252, 2007.

[181] L. F. M. da Silva, A. Öchsner and R. D. Adams, "Numerical Approach: Finite Element Analysis," in *Handbook of Adhesion Technology*, Heidelberg, Springer, 2011, pp. 629-660.

[182] P. Boisse, Y. Aimène, A. Dogui, S. Dridi, S. Gatouillat, N. Hamila, M. Aurangzeb Khan, T. Mabrouki, F. Morestin and E. Vidal-Sallé, "Hypoelastic, hyperelastic, discrete and semi-discrete approaches for textile composite reinforcement forming," *International journal of material forming,* vol. 3, pp. 1229-1240, 2010.

[183] A. De Vaucorbeil, V. P. Nguyen, S. Sinaie and J. Y. Wu, "Material point method after 25 years: theory, implementation, and applications," in *Advances in applied mechanics*, vol. 53, Elsevier, 2020, pp. 185-398.

[184] A. Lv, Y. Zhu and C. Xian, "Efficient cloth simulation based on the material point method," *Computer Animation and Virtual Worlds,* vol. 33, no. 3-4, p. e2073, 2022.

[185] A. Nazemi and A. S. Milani, "A comparative study of emerging material point method and FEM for forming simulation of textile reinforcements," *Composites Part A: Applied Science and Manufacturing,* vol. 185, p. 108284, 2024.

[186] S. D. Müzel, E. P. Bonhin, N. M. Guimarães and E. S. Guidi, "Application of the finite element method in the analysis of composite materials: A review," *Polymers,* vol. 12, no. 4, p. 818, 2020.

[187] W. R. Yu, P. Harrison and A. Long, "Finite element forming simulation for non-crimp fabrics using a non-orthogonal constitutive equation," *Composites Part A: Applied Science and Manufacturing,* vol. 36, no. 8, pp. 1079-1093, 2005.

[188] P. Harrison, W. R. Yu and A. C. Long, "Rate dependent modelling of the forming behaviour of viscous textile composites," *Composites Part A: Applied Science and Manufacturing,* vol. 42, no. 11, pp. 1719-1726, 2011.

[189] M. A. Khan, W. Saleem, M. Asad and H. Ijaz, “A parametric sensitivity study on preforming simulations of woven composites using a hypoelastic computational model,” *Journal of Reinforced Plastics and Composites,* vol. 35, no. 3, pp. 243-257, 2016.

[190] L. Kärger, S. Florian and H. Werner, “Modeling multiaxial stress states in forming simulation of woven fabrics,” in *Material Forming 26th International ESAFORM Conference on Material Forming (ESAFORM 2023)*, Kraków, 2023.

[191] P. Badel, S. Gauthier, E. Vidal-Sallé and P. Boisse, “Rate constitutive equations for computational analyses of textile composite reinforcement mechanical behaviour during forming,” *Composites Part A: Applied Science and Manufacturing,* vol. 40, no. 8, pp. 997-1007, 2009.

[192] S. Kulkarni, K. A. Khan, K. Alhammadi, W. J. Cantwell and R. Umer, “A visco-hyperelastic approach to model rate dependent compaction response of a 3D woven fabric,” *Composites Part A: Applied Science and Manufacturing,* vol. 163, p. 107229, 2022.

[193] P. Boisse, N. Hamila and A. Madeo, “The difficulties in modeling the mechanical behavior of textile composite reinforcements with standard continuum mechanics of Cauchy. Some possible remedies,” *International Journal of Solids and Structures,* vol. 154, pp. 55-65, 2018.

[194] P. Boisse, N. Hamila, F. Helenon, B. Hagège and J. Cao, “Different approaches for woven composite reinforcement forming simulation,” *International journal of material forming,* vol. 1, pp. 21-29, 2008.

[195] P. Bussetta and N. Correia, “Numerical forming of continuous fibre reinforced composite material: A review,” *Composites Part A: Applied Science and Manufacturing,* vol. 113, pp. 12-31, 2018.

[196] G. Barbagallo, A. Madeo, F. Morestin and P. Boisse, “Modelling the deep drawing of a 3D woven fabric with a second gradient model,” *Mathematics and Mechanics of Solids,* vol. 22, no. 11, pp. 2165-2179, 2017.

[197] G. Barbagallo, A. Madeo, I. Azehaf, I. Giorgio, F. Morestin and P. Boisse, “Bias extension test on an unbalanced woven composite reinforcement: Experiments and modeling via a second-gradient continuum approach,” *Journal of Composite Materials,* vol. 51, no. 2, pp. 153-170, 2017.

[198] B. B. Boubaker, B. Haussy and J. F. Ganghoffer, “Discrete models of woven structures. Macroscopic approach,” *Composites Part B: Engineering,* vol. 38, no. 4, pp. 498-505, 2007.

[199] J. V. Viisainen and M. P. F. Sutcliffe, “Characterising the variability in wrinkling during the preforming of non-crimp fabrics,” *Composites Part A: Applied Science and Manufacturing,* vol. 149, p. 106536, 2021.

[200] G. Creech and A. K. Pickett, “Meso-modelling of non-crimp fabric composites for coupled drape and failure analysis,” *Journal of materials science,* vol. 41, pp. 6725-6736, 2006.

[201] J. Sirtautas, A. K. Pickett and P. Lépicier, “A mesoscopic model for coupled drape-infusion simulation of biaxial Non-Crimp Fabric,” *Composites Part B: Engineering,* vol. 47, pp. 48-57, 2013.

[202] M. Q. Pham, O. Döbrich, W. Trümper, T. Gereke and C. Cherif, “Numerical modelling of the mechanical behaviour of biaxial weft-knitted fabrics on different length scales,” *Materials,* vol. 12, no. 22, p. 3693, 2019.

[203] S. Bel, P. Boisse and F. Dumont, “Analyses of the deformation mechanisms of non-crimp fabric composite reinforcements during preforming,” *Applied Composite Materials,* vol. 19, pp. 513-528, 2012.

[204] S. Bel, N. Hamila, P. Boisse and F. Dumont, “Finite element model for NCF composite reinforcement preforming: Importance of inter-ply sliding,” *Composites Part A: Applied science and manufacturing,* vol. 43, no. 12, pp. 2269-2277, 2012.

[205] S. Chen, O. P. L. McGregor, L. T. Harper, A. Endruwei and N. A. Warrior, “Defect formation during preforming of a bi-axial non-crimp fabric with a pillar stitch pattern,” *Composites Part A: Applied Science and Manufacturing,* vol. 91, pp. 156-167, 2016.

[206] L. Kärger, S. Galkin, E. Kunze, M. Gude and B. Schäfer, “Prediction of forming effects in UD-NCF by macroscopic forming simulation–Capabilities and limitations,” in *ESAFORM 2021 - 24th International Conference on Material Forming*, Liege, Belgium, 2021.

[207] F. Härtel, P. Böhler and P. Middendorf, “An integral mesoscopic material characterization approach,” *Key Engineering Materials,* vol. 611, pp. 280-291, 2014.

[208] L. Kärger, A. Bernath, F. Fritz, S. Galkin, D. Magagnato, A. Oeckerath, A. Schön and F. Henning, “Development and validation of a CAE chain for unidirectional fibre reinforced composite components,” *Composite Structures,* vol. 132, pp. 350-358, 2015.

[209] L. Kärger, A. Schön, F. Fritz, P. Böhler, D. Maganato, S. Fischer and F. Henning, “Virtual Process Chain for an integrated assessment of high-performance composite structures,” in *NAFEMS World Congress*, Salzburg, 2013.

[210] B. Schäfer, S. Haas, P. Boisse and L. Kärger, “Investigation of the membrane behavior of UD-NCF in macroscopic forming simulations,” *Key Engineering Materials,* vol. 926, pp. 1413-1422, 2022.

[211] M. Ghazimoradi and J. Montesano, “Macroscopic forming simulation for a unidirectional non-crimp fabric using an anisotropic hyperelastic material model,” *Applied Composite Materials,* vol. 30, no. 6, pp. 2001-2023, 2023.

[212] B. Schäfer, D. Dörr, R. Zheng, N. Naouar and L. Kärger, “A hyperelastic approach for modeling the membrane behavior in finite element forming simulation of unidirectional non-crimp fabrics (UD-NCF),” *Composites Part A: Applied Science and Manufacturing,* vol. 185, p. 108359, 2024.

[213] L. P. Brown and A. C. Long, “Modelling the geometry of textile reinforcements for composites: TexGen,” in *Composite reinforcements for optimum performance (Second Edition)*, Woodhead Publishing Ltd, 2021.

[214] N. Kahavita and P. Harrison, “Protocols.io,” 02 July 2024. [Online]. Available: dx.doi.org/10.17504/protocols.io.81wgbyy93vpk/v1.

[215] “support@123apps.com,” 16 May 2022. [Online]. Available: https://online-video-cutter.com/. [Accessed January 2023].

[216] A. Lee, “VitualDub 1.10.4.0. [software],” 2013. [Online]. Available: http://www.virtualdub.org.

[217] A. C. Long, Composites forming technologies, Elsevier, 2014.

[218] P. Harrison, J. Wiggers, A. C. Long and C. D. Rudd, “A Constitutive Model Based on Meso and Micro Kinematics for Woven and Stitched Dry Fabrics,” in *14th International Conference on Composite Materials*, San Diego, USA, 2003.

[219] J. Wiggers, A. C. Long, P. Harrison and C. D. Rudd, “The effects of stitch architecture on the shear compliance of non-crimp fabrics,” in *Proceedings of ESAFORM*, 2003.

[220] G. B. McGuinness and C. M. ÓBrádaigh, “Characterisation of thermoplastic composite melts in rhombus-shear: the picture-frame experiment,” *Composites Part A: Applied Science and Manufacturing,* vol. 29, pp. 115-132, 1998.

[221] K. D. H. N. Kahavita, E. D. McCarthy, M. Zhang, C. M. Ó Brádaigh and P. Harrison, “Characterising the shear resistance of a unidirectional non-crimp glass fabric using modified picture frame and uniaxial bias extension test methods,” *International Journal of Material Forming,* vol. 16, no. 5, 2023.

[222] MATLAB, *R2021b (9.11.0.1769968),* The MathWorks Inc., 2021.

[223] A. Patti and D. Acierno, “Materials, weaving parameters, and tensile responses of woven textiles,” *Macromol,* vol. 3, no. 3, pp. 665-680, 2023.

[224] I. Jahan, “Effect of fabric structure on the mechanical properties of woven fabrics,” *Advance Research in Textile Engineering,* vol. 2, no. 2, p. 1018, 2017.

[225] Autodesk, “Autodesk Fusion 360,” Autodesk, Inc., California, 2024.

[226] Autodesk, “Autodesk 3ds Max,” Autodesk, Inc., California, 2024.

[227] N. Hamila and P. Boisse, “Simulations of textile composite reinforcement draping using a new semi-discrete three node finite element,” *Composites Part B: Engineering,* vol. 36, no. 6, pp. 999-1010, 2008.

[228] A. Iwata, T. Inoue, N. Naouar, P. Boisse and S. V. Lomov, “Coupled meso-macro simulation of woven fabric local deformation during draping,” *Composites Part A: Applied science and manufacturing,* vol. 118, pp. 267-280, 2019.

[229] I. Gnaba, D. Soulat, X. Legrand and P. Wang, “Investigation of the formability behaviour during stamping of tufted and un-tufted carbon preforms: Towards localized reinforcement technologies,” *International Journal of Material Forming,* pp. 1-18, 2021.

[230] MATLAB, *9.14.0 (R2023b),* Natick, Massachusetts: The MathWorks Inc., 2023.

[231] A. R. Labanieh, C. Garnier, P. Ouagne, O. Dalverny and D. Soulat, “Intra-ply yarn sliding defect in hemisphere preforming of a woven preform,” *Composites Part A: Applied Science and Manufacturing,* vol. 107, pp. 432-446, 2018.

[232] S. Allaoui, C. Cellard and G. Hivet, “Effect of inter-ply sliding on the quality of multilayer interlock dry fabric preforms,” *Composites Part A: Applied Science and Manufacturing,* vol. 68, pp. 336-345, 2015.

[233] F. N. Nezami, T. Gereke and C. Cherif, “Analyses of interaction mechanisms during forming of multilayer carbon woven fabrics for composite applications,” *Composites Part A: Applied Science and Manufacturing,* vol. 84, pp. 406-416, 2016.

[234] K. A. Fetfatsidis, D. Jauffrès, J. A. Sherwood and J. Chen, “Characterization of the tool/fabric and fabric/fabric friction for woven-fabric composites during the thermostamping process,” *International journal of material forming,* vol. 6, pp. 209-221, 2013.

[235] W. Najjar, C. Pupin, X. Legrand, S. Boude, D. Soulat and P. Dal Santo, “Analysis of frictional behaviour of carbon dry woven reinforcement,” *Journal of Reinforced Plastics and Composites,* vol. 33, no. 11, pp. 1037-1047, 2014.

[236] G. D. Lawrence, S. Chen, N. A. Warrior and L. T. Harper, “The influence of inter-ply friction during double-diaphragm forming of biaxial NCFs,” *Composites Part A: Applied Science and Manufacturing,* vol. 167, p. 107426, 2023.

[237] Z. Qu, S. Gao, Y. Zhang and J. Jia, “Analysis of the mechanical and preforming behaviors of carbon-kevlar hybrid woven reinforcement,” *Polymers,* vol. 13, no. 23, p. 4088, 2021.

Appendices

Appendix A: Derivation of engineering strain along the fibre direction in the positive pre-displaced PF rig test

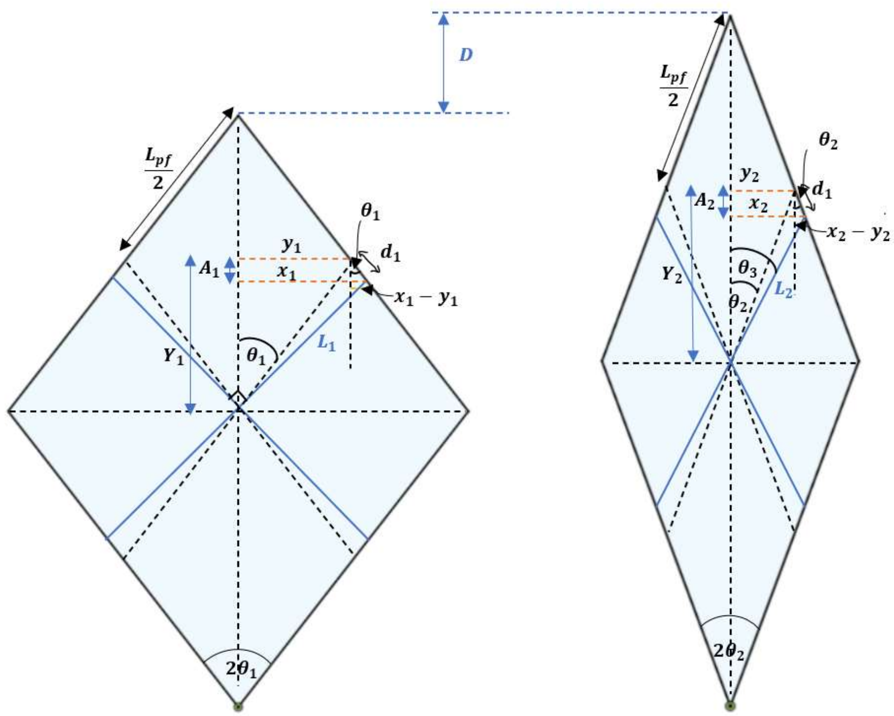

Figure A.1: Positive pre-displaced of the PF rig (a) Loaded specimen to the positive pre-displaced rig (b) The PF rig after crosshead displacement, D.

Based on the test geometry change, the fabric shear angle (θ) of the tightly-clamped PF test was derived by directly relating it to the displacement of the crosshead, d_{pf}. L_{pf} is the side length of the PF rig (see Figure 2.17 & Eq.2.10).

$$\theta = \frac{\pi}{2} - 2acos\left[\frac{1}{\sqrt{2}} + \frac{d_{pf}}{2L_{pf}}\right] \tag{A1}$$

The tow-stitch angle of the tightly-clamped PF test is related to the frame angle of the positive pre-displaced PF test. For a 4mm pre-displaced PF rig, the initial frame angle θ_1 (see Figure A.1a) can be calculated as,

$$\theta_1 = acos\left[\frac{1}{\sqrt{2}} + \frac{0.004}{2L_{pf}}\right] \tag{A2}$$

Using Figure A.1a, the initial length of the tows (L_1) can be estimated as,

$$L_1 = \sqrt{2}\,(Y_1 - A_1) \tag{A3}$$

where, $$Y_1 = \left[\frac{L_{pf}}{2}\right]\cos\theta_1 \tag{A4}$$

$$A_1 = \frac{\left[\frac{L_{pf}}{2}\right]\cos\theta_1\,(\cos\theta_1 - \sin\theta_1)}{\cos\theta_1 + \sin\theta_1} \tag{A5}$$

$$\therefore L_1 = \sqrt{2}\left\{\left(\left[\frac{L_{pf}}{2}\right]\cos\theta_1\right) - \left(\frac{\left[\frac{L_{pf}}{2}\right]\cos\theta_1\,(\cos\theta_1 - \sin\theta_1)}{\cos\theta_1 + \sin\theta_1}\right)\right\} \tag{A6}$$

The frame angle at a given displacement θ_2 (see Figure A.1b) can be calculated as,

$$\theta_2 = acos\left[\frac{1}{\sqrt{2}} + \frac{D}{2L_{pf}}\right] \tag{A7}$$

Using trigonometry,

$$Y_2 = \left[\frac{L_{pf}}{2}\right]\cos\theta_2 \tag{A8}$$

$$A_2 = d_1\cos\theta_2 \tag{A9}$$

$$x_2 = d_1\sin\theta_2 + \left[\frac{L_{pf}}{2}\right]\sin\theta_2 \tag{A10}$$

where

$$d_1 = \frac{A_1}{\cos\theta_1} \tag{A11}$$

$$\tan\theta_3 = \frac{x_2}{Y_2 - A_2} \tag{A12}$$

By applying Eqs.A8, A9 and A10 to Eq.A12 the tow-stitch angle, θ_3, at a given displacement can be calculated as

$$\theta_3 = \tan^{-1}\left[\frac{(\tan\theta_2)\,(2d_1 + L_{pf})}{L_{pf} - 2d_1}\right] \tag{A13}$$

Therefore, the theoretical length of the tows at a given displacement, L_2, can be estimated as,

$$L_2 = \frac{x_2}{sin\,\theta_3} \tag{A14}$$

Apply Eqs.A10 and A13 to Eq.A14

$$L_2 = \frac{\left(d_1\sin\theta_2 + \left[\frac{L_{pf}}{2}\right]\sin\theta_2\right)}{sin\left(\tan^{-1}\left[\frac{(\tan\theta_2)\,(2d_1 + L_{pf})}{L_{pf} - 2d_1}\right]\right)} \tag{A15}$$

The engineering strain of the tows (ε_p) in the positive pre-displaced PF rig test is given in Eq.A16

$$\varepsilon_p = \frac{L_2 - L_1}{L_1} \tag{A16}$$

By applying Eqs.A6 and A15 to Eq.A16, the theoretical engineering strain of the tows in the positive pre-displaced PF rig test at a given displacement can be calculated as,

$$\varepsilon_p = \frac{\left\{\frac{d_1\sin\theta_2 + \left[\frac{L_{pf}}{2}\right]\sin\theta_2}{sin\left(\tan^{-1}\left[\frac{(\tan\theta_2)\,(2d_1 + L_{pf})}{L_{pf} - 2d_1}\right]\right)}\right\} - \left\{\sqrt{2}\left(\left[\frac{L_{pf}}{2}\right]\cos\theta_1 - \frac{\left[\frac{L_{pf}}{2}\right]\cos\theta_1\,(\cos\theta_1 - \sin\theta_1)}{\cos\theta_1 + \sin\theta_1}\right)\right\}}{\left\{\sqrt{2}\left(\left[\frac{L_{pf}}{2}\right]\cos\theta_1 - \frac{\left[\frac{L_{pf}}{2}\right]\cos\theta_1\,(\cos\theta_1 - \sin\theta_1)}{\cos\theta_1 + \sin\theta_1}\right)\right\}} \tag{A17}$$

Appendix B: Derivation of the theoretical shear angle in the positive pre-displaced PF rig test

Substituting Eq.A7 in Eq.A13

$$\theta_3 = \tan^{-1}\left\{\frac{tan\left(acos\left[\frac{1}{\sqrt{2}}+\frac{D}{2L_{pf}}\right]\right)(2d_1+L_{pf})}{L_{pf}-2d_1}\right\} \tag{B1}$$

θ_3 represents half of the tow-stitch angle at a given displacement. The theoretical shear angle of the positive pre-displaced PF test (δ_p) can be calculated by applying Eq.B1 to Eq.A1.

$$\theta = \frac{\pi}{2} - \underbrace{2acos\left[\frac{1}{\sqrt{2}}+\frac{D}{2L_{pf}}\right]}_{\boxed{\text{Tow-stitch angle}}}$$

$$\delta_p = \frac{\pi}{2} - 2\tan^{-1}\left\{\frac{tan\left(acos\left[\frac{1}{\sqrt{2}}+\frac{D}{2L_{pf}}\right]\right)(2d_1+L_{pf})}{L_{pf}-2d_1}\right\} \tag{B2}$$

Appendix C: Derivation of engineering strain along fibre direction of the negative pre-displaced PF rig test

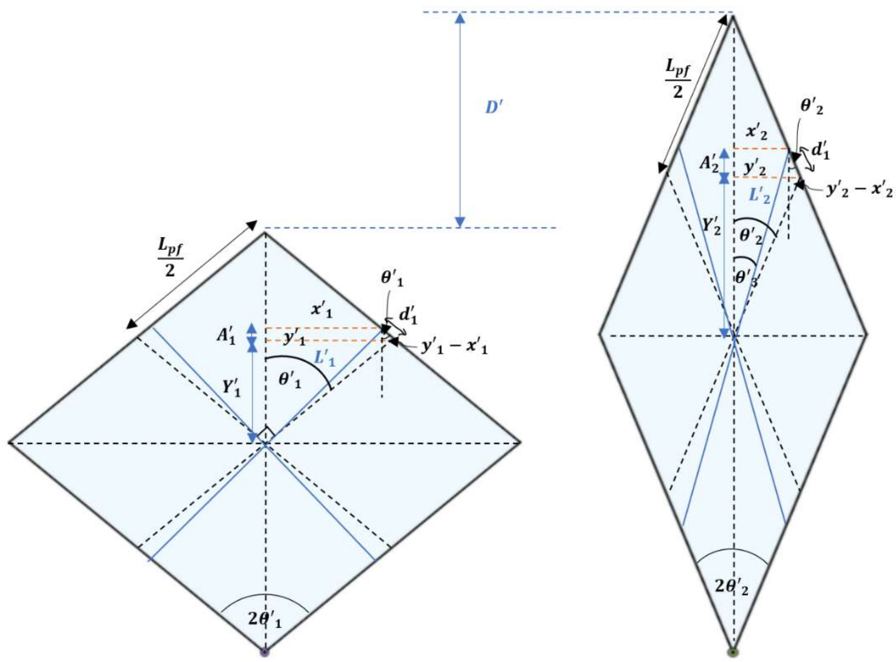

Figure C.1: Negative pre-displaced of the PF rig (a) Loaded specimen to the negative pre-displaced rig (b) The PF rig after crosshead displacement, D'.

The tow-stitch angle of the tightly-clamped PF test is related to the frame angle of the negative pre-displaced PF test.

$$\theta = \frac{\pi}{2} - 2acos\left[\frac{1}{\sqrt{2}} - \frac{D}{2L_{pf}}\right] \tag{C1}$$

For a 4mm negative pre-displaced PF rig, the initial frame angle θ_1 (see Figure C.1a) can be calculated as,

$$\therefore \theta_1' = acos\left[\frac{1}{\sqrt{2}} - \frac{0.004}{2L_{pf}}\right] \tag{C2}$$

Using Figure C.1a, the initial length of the tows (L_1') can be estimated as,

$$L_1' = \sqrt{2}\,(Y_1' + A_1') \tag{C3}$$

where
$$Y_1' = \left[\frac{L_{pf}}{2}\right]\cos\theta_1' \tag{C4}$$

$$A_1' = \frac{\left[\frac{L_{pf}}{2}\right]\cos\theta_1'\,(\sin\theta_1' - \cos\theta_1')}{\sin\theta_1' + \cos\theta_1'} \tag{C5}$$

$$\therefore L_1' = \sqrt{2}\left\{\left(\left[\frac{L_{pf}}{2}\right]\cos\theta_1'\right) + \left(\frac{\left[\frac{L_{pf}}{2}\right]\cos\theta_1'\,(\sin\theta_1' - \cos\theta_1')}{\sin\theta_1' + \cos\theta_1'}\right)\right\} \tag{C6}$$

The frame angle at a given displacement θ_2' (see Figure C.1b) can be calculated as,

$$\theta_2' = acos\left[\frac{1}{\sqrt{2}} + \frac{D'}{2L_{pf}}\right] \tag{C7}$$

Using trigonometry,

$$Y_2' = \left[\frac{L_{pf}}{2}\right]\cos\theta_2' \tag{C8}$$

$$A_2' = d_1'\cos\theta_2' \tag{C9}$$

$$x_2' = \left[\frac{L_{pf}}{2}\right]\sin\theta_2' - \ d_1'\sin\theta_2' \tag{C10}$$

where $$d_1' = \frac{A_2'}{\cos\theta_2'} \tag{C11}$$

$$\tan\theta_3' = \frac{x_2'}{Y_2' + A_2'} \tag{C12}$$

By applying Eqs.C8, C9 and C10 to Eq.C12 the tow-stitch angle, θ_3', at a given displacement can be calculated as,

$$\theta_3' = \tan^{-1}\left[\frac{(\tan\theta_2')\,(L_{pf} - 2d_1')}{L_{pf} + 2d_1'}\right] \tag{C13}$$

Therefore, the theoretical length of the tows at a given displacement, L_2' can be estimated as,

$$L_2' = \frac{x_2'}{sin\,\theta_3'} \tag{C14}$$

Apply Eqs.C10 and C13 to Eq.C14

$$L_2' = \frac{\left(\left[\frac{L_{pf}}{2}\right]\sin\theta_2' - d_1'\,\mathrm{si}\quad {}_2'\right)}{sin\left(\tan^{-1}\left[\frac{(\tan\theta_2')\,(L_{pf} - 2d_1')}{L_{pf} + 2d_1'}\right]\right)} \tag{C15}$$

The engineering strain of the tows (ε_n) in the negative pre-displaced PF rig test is given in Eq.C16

$$\varepsilon_n = \frac{L_2' - L_1'}{L_1'} \tag{C16}$$

By applying Eqs.C6 and C15 to Eq.C16, the theoretical engineering strain of the tows in the negative pre-displaced PF rig test at a given displacement can be calculated as,

$$\varepsilon_n = \frac{\left\{\frac{\left(\left[\frac{L_{pf}}{2}\right]\sin\theta_2' - d_1'\sin\theta_2'\right)}{sin\left(\tan^{-1}\left[\frac{(\tan\theta_2')\,(L_{pf} - 2d_1')}{L_{pf} + 2d_1'}\right]\right)}\right\} - \left\{\sqrt{2}\left(\left[\frac{L_{pf}}{2}\right]\cos\theta_1' + \frac{\left[\frac{L_{pf}}{2}\right]\cos\theta_1'\,(\sin\theta_1' - \cos\theta_1')}{\sin\theta_1' + \cos\theta_1'}\right)\right\}}{\left(\sqrt{2}\left(\left[\frac{L_{pf}}{2}\right]\cos\theta_1 - \frac{\left[\frac{L_{pf}}{2}\right]\cos\theta_1\,(\cos\theta_1 - \sin\theta_1)}{\cos\theta_1 + \sin\theta_1}\right)\right)} \tag{C17}$$

Appendix D: Derivation of the theoretical shear angle of the negative pre-displaced PF test

Substituting Eq.C7 in Eq.C13

$$\theta_3' = \tan^{-1}\left\{\frac{tan\left(acos\left[\frac{1}{\sqrt{2}}+\frac{D'}{2L_{pf}}\right]\right)(L_{pf} - 2d_1')}{L_{pf} + 2d_1'}\right\} \tag{D1}$$

θ_3' represents half of the tow-stitch angle at a given displacement. The theoretical shear angle of the negative pre-displaced PF test (δ_n) can be calculated as,

$$\delta_n = \frac{\pi}{2} - 2\tan^{-1}\left\{\frac{tan\left(acos\left[\frac{1}{\sqrt{2}}+\frac{D'}{2L_{pf}}\right]\right)(L_{pf} - 2d_1')}{L_{pf} + 2d_1'}\right\} \tag{D2}$$

Appendix E: Static analysis on the picture frame rig

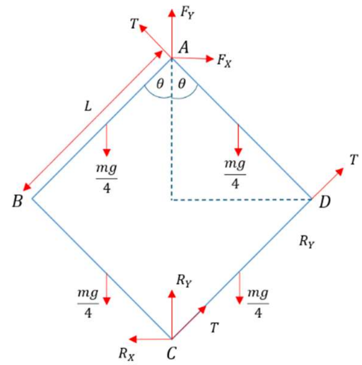

Figure E.1: Forces acting on a picture frame rig

Figure E.1 shows the forces acting on a PF rig when the system is at equilibrium and there is no friction in the bearings.

Consider force in AD beam; moment about point A to find T (tension along a bar), where L, and mg are the side length and weight of the rig, respectively.

$$LT = \frac{mg}{4} . \frac{L\, sin\theta}{2} \quad \text{(E1)}$$

Conder BC beam, moment about B to find R_x (R_x and R_y are the horizontal and vertical components of the reaction force exerted by the testbed on a rig)

$$\frac{mg}{4} . \frac{L\, sin\theta}{2} + R_x . L\cos\theta = LT + R_y . L\sin\theta \quad \text{(E2)}$$

Apply Eq.E1 to Eq.E2 $\quad R_x = \frac{R_y . \sin\theta}{\cos\theta}$ (E3)

Translational equilibrium in the vertical direction is zero. (F_x and F_y are the horizontal and vertical components of the force exerted by the rig on the loadcell)

$$\therefore F_x = R_x = \frac{R_y . \sin\theta}{\cos\theta} \quad \text{(E4)}$$

Conder AB beam, moment about point B to find F_y

$$\frac{mg}{4} . \frac{L\, sin\theta}{2} + F_x . L\cos\theta = LT + F_y . L\sin\theta \quad \text{(E5)}$$

Apply Eq.E1 and Eq.E4 to Eq.E5 $\quad \therefore F_y = R_y$ (E6)

Translational equilibrium in the horizontal direction is zero.

$$F_y + R_y = mg \quad \text{(E7)}$$

$$\therefore F_y = \frac{mg}{2} \quad \text{(E8)}$$

If there is no friction in the bearings, the loadcell measures exactly half of the weight of the rig. Friction on bearings introduces frictional resistance, which resists the motion of the frame. This frictional force must be resisted by the applied load, which affects the force measured by the load cell. As a result, when friction acts on the bearings, the loadcell measures the total force, including the force required to shear the fabric and the force to overcome the friction of the bearings.

Appendix F: Cruciform Bias Extension (CBE) Test - with Lateral Clamping

To change the kinematics with a stable setup, the CBE specimens were modified by clamping lateral C Regions with linear bearings. The frame required to fix the linear bearings was sketched using Autodesk Fusion 360 [225] (see Figure F.1a) and the prepared frame is shown in Figure F.1b. Figures F.1c&d show the 3D printed side clamps and how these clamps are mounted with the linear bearings. The front and back views of the sample after loading into the test frame are shown in Figures F.2a&b, respectively. Two methods were used to keep the vertical beams of the frame rigid and aligned. Two rubber suction cups were attached to the top of the vertical beams of the frame to fix the machine crosshead (see Figure F.1b). Besides that, the two vertical beams of the frame were tightened with the vertical poles of the machine using strong cable ties (see Figure F.2). The frame was tightly fixed to the machine test bed using G-clamps.

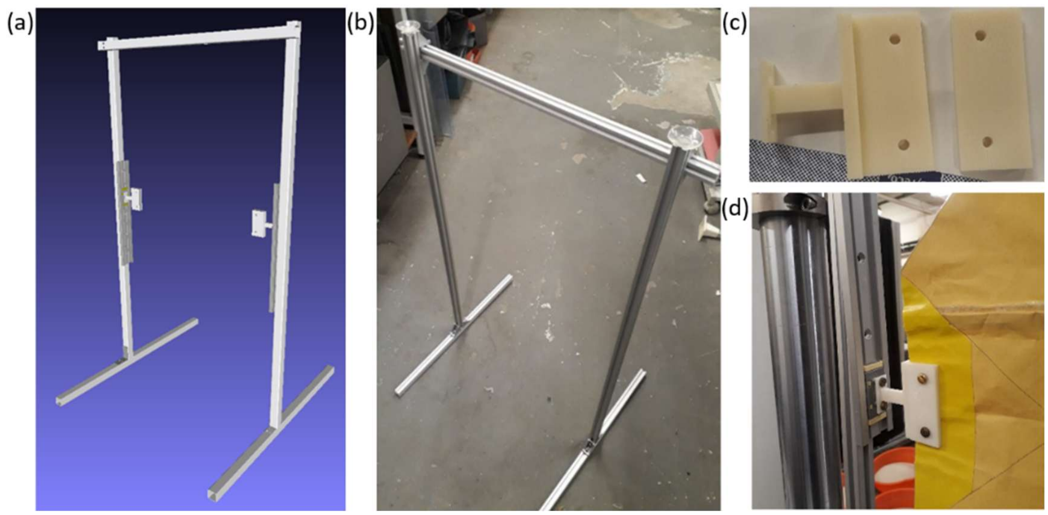

Figure F.1: Test setup of the CBE specimen with linear bearings (a) 3D model of the frame (b) Prepared test frame (c) 3D printed side clamps (d) the way that side clamps fix with the linear bearings

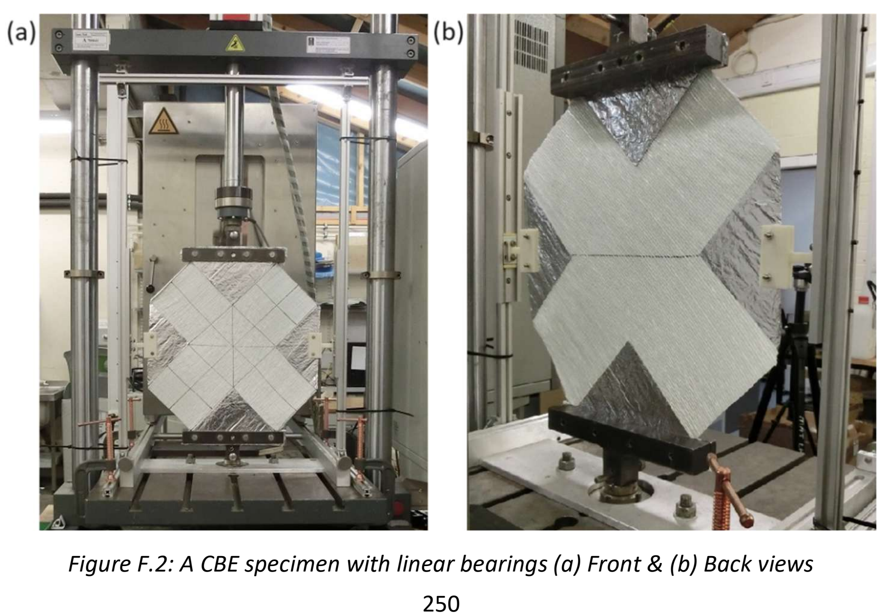

Figure F.2: A CBE specimen with linear bearings (a) Front & (b) Back views

During this test, B1 Regions shear differently due to the linear motion of the lateral C Regions and formed double curvatures in Region A (see Figure F.3). Therefore, the deformation is not homogeneous in each region. To address the complexity of shear in different B regions, the CBE specimen was further modified by glueing two large Al foils to cover all C Regions and two B1 Regions (see Section 4.3, Figure 4.9, referred to as 'PSS').

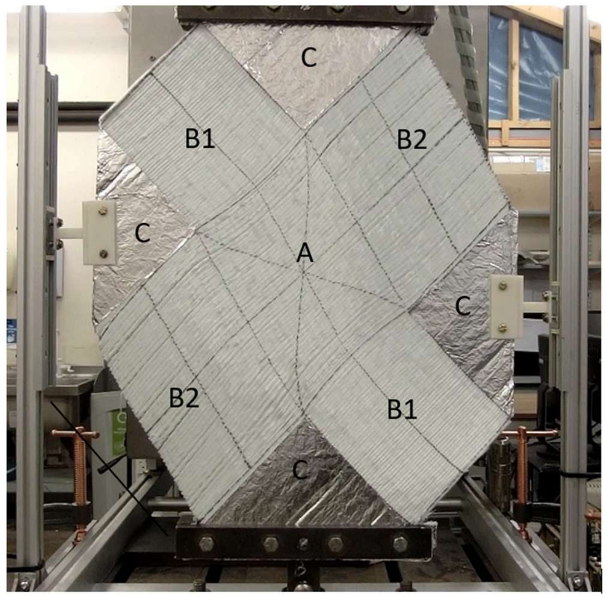

Figure F.3: Deformed CBE specimen with linear bearings

Appendix G: Derivation of the Theoretical Shear Angle and Engineering Strain in the Stitch Direction of the PSS Test

During the PSS test with linear bearings, the shape of Region A shifts from square (blue) to parallelogram (orange), as shown in Figure G.1. The change in the inter-fibre angle due to the tension can be determined by the dimensional changes in the geometry of the specimen.

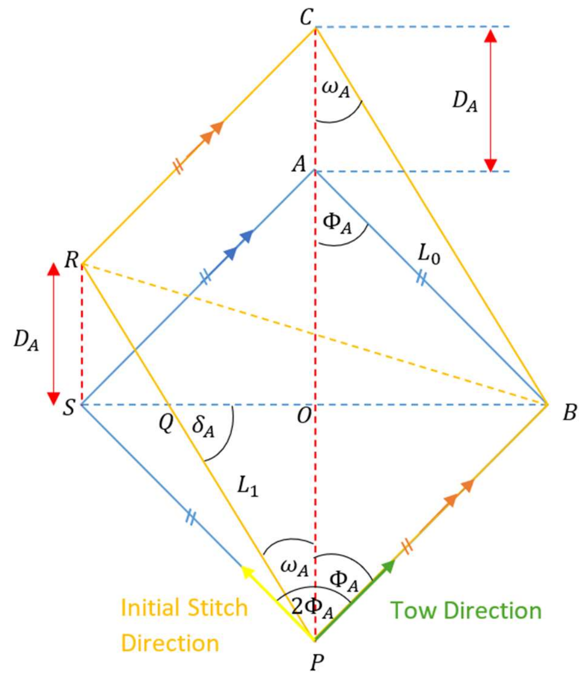

Figure G.1: Shear deformation of Region A of PSS specimen with linear bearings

The initial tow-stitch angle, $2\Phi_A = \frac{\pi}{2}$ (G1)

Considering the △ OAB,

$$OB = OA = L_0/\sqrt{2} \quad \text{(G2)}$$

$$\therefore OC = L_0/\sqrt{2} + D_A \quad \text{(G3)}$$

Considering the △ OCB,

$$\omega_A = atan\left(\frac{L_0}{L_0+\sqrt{2}D_A}\right) \quad \text{(G4)}$$

The inter-fibre angle at a given displacement = $\Phi_A + \omega_A$

The theoretical shear angle (θ_A) can then be determined by the difference between the initial inter-fibre angle and the inter-fibre angle at a given displacement

$$\theta_A = \frac{\pi}{2} - \left[\frac{\pi}{4} + atan\left(\frac{L_0}{L_0+\sqrt{2}D_A}\right)\right] \quad \text{(G5)}$$

Considering the △ OPQ

$$PQ = \frac{L_0}{\sqrt{2}\cos\omega_A} \quad \text{(G6)}$$

$$\sin\delta_A = \cos\omega_A \tag{G7}$$

Considering the △ QRS

$$\sin\delta_A = \frac{D_A}{QR} \tag{G8}$$

Apply Eq.G7 to Eq.G8

$$\therefore QR = \frac{D_A}{\cos\omega_A} \tag{G9}$$

L_1 can be calculated as a function of the displacement using Eq.G6 and Eq.G9

$$L_1 = PQ + QR = \frac{L_0}{\sqrt{2}\cos\omega_A} + \frac{D_A}{\cos\omega_A} \tag{G10}$$

Therefore, the displacement in the stitch direction during the PSS test (D_s) can be calculated as,

$$D_s = \left[\frac{L_0}{\sqrt{2}\cos\omega_A} + \frac{D_A}{\cos\ {}_A}\right] - L_0 \tag{G11}$$

The theoretical engineering strain in the stitch direction during the PSS test, α_A, is calculated as a function of the displacement

$$\alpha_A = \frac{D_S - L_0}{L_0} \tag{G12}$$

$$\alpha_A = \left[\frac{1}{\sqrt{2}\ cos\ \omega_A} + \frac{D_A}{L_0 cos\ \omega_A}\right] - 1 \tag{G13}$$

where,

$$\omega_A = \left(\frac{\pi}{4} - \theta_A\right) \tag{G14}$$

Appendix H: Investigation of the Effect of Friction in Linear Bearings on Increasing Normalised Force in the PSS Test

Figure H.1a compares the normalised force vs measured shear angle curves of the PSS specimen with and without linear bearings. The increase in the normalised force is also visible in the sample without the linear bearings. However, the absence of side clamps causes sample buckling (see Figure H.2) and makes shear angle and stitch strain measurements inaccurate. As a result, the measured vs theoretical shear angle curve shows a data deviation beyond 11° of the measured shear angles (see Figure H.1b), reducing the reliability of the experiment by denying more data points than the samples with lateral clamps. Therefore, the linear bearings are beneficial in improving the reliability of the test.

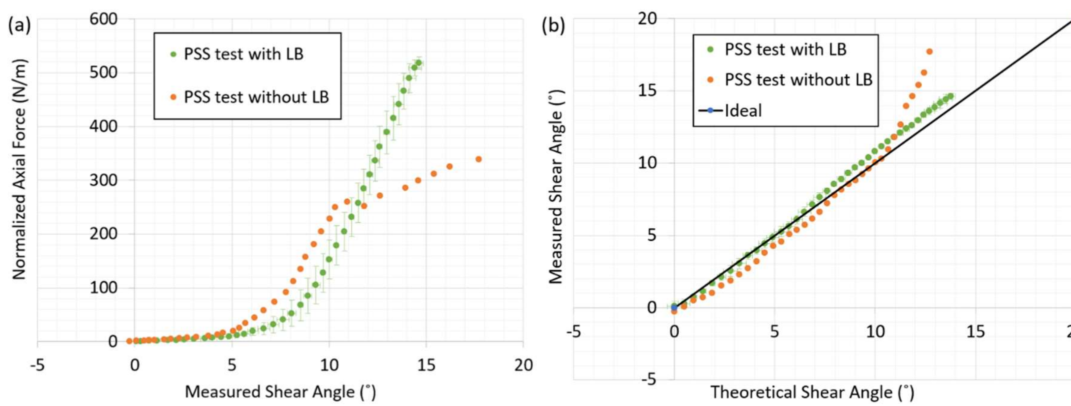

Figure H.1: Comparison of the PSS test with and without linear bearings (LB) (a) normalised force vs measured shear angle curves (b) measured vs theoretical shear angle curves

Figure H.2: Deformed PSS specimen without linear bearings

Appendix I: Derivation of the Theoretical Shear Angle and Engineering Strain in the Stitch Direction of the SS Test

During the SS test, the shape of Region A shifts from square (black) to parallelogram (orange), as shown in Figure I.1. The change in the inter-fibre angle due to the tension can be determined by the dimensional changes in the geometry of the specimen.

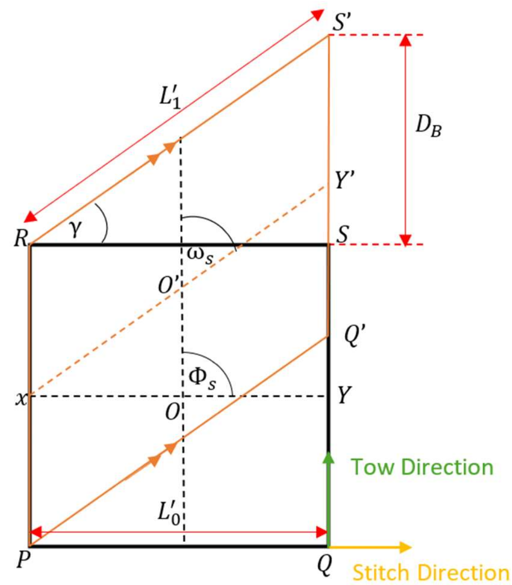

Figure I.1: Region A shear deformation of a SS test sample

The initial tow-stitch angle, $\Phi_s = \frac{\pi}{2}$ (I1)

Considering the △ SRS',

$$\gamma = tan^{-1}\left(\frac{D_B}{L_0'}\right) \quad \text{(I2)}$$

Considering the △ OXO',

$$\omega_s = 2\pi - (\gamma + (2\pi - \Phi_s)$$

$$\omega_s = \Phi_s - \gamma \quad \text{(I3)}$$

The theoretical shear angle (θ_s) can then be determined by the difference between the initial inter-fibre angle and the inter-fibre angle at a given displacement

$$\theta_s = \Phi_s - \omega_s \quad \text{(I4)}$$

Apply Eqs.I2 and I3 to Eq.I4

$$\theta_s = \Phi_s - (\Phi_s - \gamma)$$

$$\theta_s = \gamma$$

$$\theta_s = tan^{-1}\left(\frac{D_B}{L_0'}\right) \quad \text{(I5)}$$

Considering the △ SRS',

$$(L_1')^2 = (L_0')^2 + D_B^2$$

$$\therefore L_1' = \sqrt{(L_0')^2 + D_B^2} \tag{I6}$$

Therefore, the displacement in the stitch direction (D_s) can be calculated as,

$$D_s = L_1' - L_0'$$

$$D_s = \left(\sqrt{(L_0')^2 + D_B^2}\right) - L_0' \tag{I7}$$

The theoretical engineering strain in the stitch direction during the SS test, α_s, is calculated as a function of the displacement

$$\alpha_s = \frac{\left(\sqrt{(L_0')^2 + D_B^2}\right) - L_0'}{L_0'} \tag{I8}$$

Appendix J: Power-based Analysis to Separate Tensile and Shear Contributions of PSS Test

The total power (P_T) produced by the PSS specimen is the sum of the stitch stretching (P_{st}) and the fabric shear (P_{fab}).

$$P_T = P_s + P_{fab} = \left[F_{st}(D) + F_{fab}(D)\right]\dot{D} \tag{J1}$$

where $F_{st}(D)$ and $F_{fab}(D)$ are the contributions to the measured axial force from the stitch stretching and the shearing of the fabric measured by the test machine, respectively. $\dot{D}$ is the rate of displacement of the machine.

The power required to stretch the fabric at a given strain, $P(D_{ten}/L_T)$ can be calculated from the tensile test.

$$P_{ten}(D_{ten}/L_T) = F_{stitchten}(D_{ten}/L_T)\dot{D}_{ten} = F_{stitchwte}\ (D_{ten}/L_T)\cdot W_T \cdot \dot{D}_{ten} = F_{stitchwte}\ (\varepsilon)\cdot W_T \cdot\ \dot{D}_{ten} \tag{J2}$$

where,

D_{ten}	- Displacement of the tensile test
L_T	- Initial length of the tensile specimen
$F_{stitchten}(D_{ten}/L_T)$	- Force at a given strain (tensile test)
$\dot{D}_{ten}$	- Rate of displacement of the machine during the tensile test
$F_{stitchwten}$	- Tensile force per unit width
W_T	- The width of the tensile specimen

The power contribution due to stitch stretching was assumed to be independent of the fact that the sample was sheared in the PSS test. The power garnered from stretching the stitch during the PSS test can then be calculated as,

$$P_{st} = F_{stitchwten}\left(\frac{D_{stitc}}{L_0}\right)\cdot L_N \cdot \dot{D}_{stitc}\ \ (D) = F_{stitchwten}(\varepsilon)\cdot L_N \cdot \dot{D}_s(D) \tag{J3}$$

where,

D_{stitch}	- The displacement in the stitch direction during the PSS test
L_0	- The original length of the specimen in the stitch direction
L_N	- Effective length of the PSS specimen in the tow direction
$\dot{D}_s(D)$	- The rate of the displacements in the stitch direction

Assume that the measured line force, $F_{stitchwten}$, is the same function of the measured tensile strain as measured in the tensile test. Therefore, combining Eqs. J1 & J3

$$F_{st}(D) = F_{stitchwte}\ \ (\varepsilon)\cdot L_N \cdot \frac{\dot{D_s}\,(D)}{\dot{D}} \tag{J4}$$

$$F_{fab}(D) = F_{total}(D) - F_{st}(D) = F_{total}(D) - F_{stitchwten}(\varepsilon)\cdot L_N \cdot \frac{\dot{D_s}\,(D)}{\dot{D}} \tag{J5}$$

$\dot{D_s}\,(D)$ needs to be calculated to find the $F_{fab}(D)$. It has already been proved using trigonometry (see Appendix G) that the displacement in the stitch direction D_s is,

$$D_s = \left[\frac{L_0}{\sqrt{2}\cos\omega_A} + \frac{D_A}{\cos\omega_A}\right] - L_0 \quad \text{(J6)}$$

Therefore, the time derivative of the stitch stretching displacement

$$\dot{D_s} = \frac{dD_s}{dt} = \frac{\partial D_s}{\partial \omega_A} \cdot \frac{d\omega_A}{dt} + \frac{\partial D_s}{\partial D_A} \cdot \frac{dD_A}{dt} \quad \text{(J7)}$$

Considering Eq. J6,

$$\frac{L_0}{\sqrt{2}} = Constant\ (k) \left[\frac{L_0}{\sqrt{2}\cos\omega_A} + \frac{D_A}{\cos\omega_A}\right] = A$$

$$\therefore A = \left(\frac{k+D_A}{\cos\omega_A}\right)$$

$$A(\omega) = (\cos\omega_A)^{-1}(k + D_A) \quad \text{(J8)}$$

Differentiate Eq. J8

$$A'(\omega) = -(\cos\omega_A)^{-2} . -\sin\omega_A\ .(k + D_A)$$

$$= \frac{\sin\omega_A\,(k+D_A)}{(\cos\omega_A)^2}$$

$$= \frac{1}{\cos\omega_A} . \frac{\sin\omega_A}{\cos\omega_A} . (k + D_A)$$

$$= \sec\omega_A . \tan\omega_A . (k + D_A)$$

$$= \sec\omega_A . \tan\omega_A . (\frac{L_0}{\sqrt{2}} + D_A)$$

$$\therefore \frac{\partial D_s}{\partial \omega_A} = \sec\omega_A . \tan\omega_A . (\frac{L_0}{\sqrt{2}} + D_A) \quad \text{(J9)}$$

$$A'(D) = \frac{1}{\cos\omega_A} = \sec\omega_A$$

$$\therefore \frac{\partial D_s}{\partial D_A} = \sec\omega_A \quad \text{(J10)}$$

$$\omega_A = atan\left(\frac{L_0}{L_0+\sqrt{2}D_A}\right) \quad \text{(J11)}$$

Eq. J11 was already derived using trigonometry (see Appendix G).

$$D_A = \dot{D}t \quad \text{(J12)}$$

Apply Eq. J12 to Eq. J11

$$\omega_A = atan\left(\frac{L_0}{L_0+\sqrt{2}\dot{D}t}\right)$$

$$\omega_A = atan\left(\frac{L_{0/\sqrt{2}}}{L_{0/\sqrt{2}}+\dot{D}t}\right) \quad \text{(J13)}$$

Considering Eq. J13,

$$L_{0/\sqrt{2}} = constant\ (p)$$

$$\left(\frac{L_{0/\sqrt{2}}}{L_{0/\sqrt{2}}+\dot{D}t}\right) = B$$

$$\therefore B = \frac{p}{p+\dot{D}t}$$

$$f(x) = tan^{-1}x$$

$$f'(x) = \frac{1}{1+x^2}$$

$$B'(t) = \frac{1}{1+(\frac{p}{p+\dot{D}t})^2} \quad . \quad -p\dot{D}\,(p+\dot{D}t)^{-2}$$

$$= -\frac{(p+\dot{D}t)^2}{p^2+(p+\dot{D}t)^2} \cdot \frac{P\dot{D}}{(p+\dot{D}t)^2}$$

$$= -\frac{p\dot{D}}{p^2+(p+\dot{D}t)^2}$$

$$= -\frac{L_{0/\sqrt{2}} \cdot \dot{D}}{(L_{0/\sqrt{2}})^2+(L_{0/\sqrt{2}}+\dot{D}t)^2}$$

$$\therefore \frac{d\omega_A}{dt} = -\frac{L_{0/\sqrt{2}} \cdot \dot{D}}{(L_{0/\sqrt{2}})^2+(L_{0/\sqrt{2}}+\dot{D}t)^2} \qquad \text{(J14)}$$

The time derivative of the machine displacement can be calculated by applying Eqs. J9, J10, and J14 to Eq. J7. $\frac{dD_A}{dt}$ is the rate of displacement of the machine (3.33 mm/s).

The derived equation to find $\dot{D_S}$ is thus given as,

$$\dot{D_S} = \frac{dD_S}{dt} = \left(\sec\omega_A \,.\, \tan\omega_A \,.\left(\frac{L_0}{\sqrt{2}} + D_A\right).\left[-\frac{L_{0/\sqrt{2}} \cdot \dot{D}}{(L_{0/\sqrt{2}})^2+(L_{0/\sqrt{2}}+\dot{D}t)^2}\right]\right) + \left(\sec\omega_A \,.\frac{dD_A}{dt}\right) \qquad \text{(J15)}$$

Therefore, Eq. J15 can be applied to Eq. J3 to find the power garnered from stretching the stitch during the PSS test. Eventually, the contribution to the measured axial force from the shearing of the fabric can be calculated.

Appendix K: Power-based Analysis to Separate Tensile and Shear Contributions of SS Test

The power-based analysis (as stated in Appendix J) is also used to determine the exact axial force of fabric shear in the SS test. To determine the shearing of the fabric measured by the test machine, $F_{fab}(D)$, the rate of the displacements in the stitch direction, $\dot{D_s}\,(D)$ should be calculated for the SS test. It has already been demonstrated using trigonometry (see Appendix I) that the displacement in the stitch direction D_s is,

$$D_s = \left(\sqrt{(L'_0)^2 + D_B^2}\right) - L'_0 \tag{K1}$$

where, L'_0 and D_B are initial specimen length and machine displacement, respectively.

Considering Eq. K1,

$$\frac{\partial D_s}{\partial D_B} = \frac{1}{2}\,[(L'_0)^2 + D_B^2]^{-1/2}\,.\,2D_B$$

$$\frac{\partial D_s}{\partial D_B} = \frac{D_B}{\sqrt{(L'_0)^2 + D_B^2}} \tag{K2}$$

The relationship between θ_s & D_B is already derived using trigonometry (see Eq. I5 in Appendix I).

$$\theta_s = tan^{-1}\left(\frac{D_B}{L'_0}\right) \tag{K3}$$

$$D_B = \dot{D}t$$

Where, $\dot{D}$ is the rate of displacement of the machine

$$\therefore\ \theta_s = \tan^{-1}\left(\frac{\dot{D}t}{L'_0}\right) \tag{K4}$$

$$\frac{\partial \theta_s}{\partial t} = \frac{1}{1+\left(\frac{\dot{D}t}{L'_0}\right)^2}\ \cdot\ \frac{\dot{D}}{L'_0}$$

$$\frac{\partial \theta}{\partial t} = \frac{\dot{D}L'_0}{(L'_0)^2+\dot{D}^2t^2} \tag{K5}$$

Rearrange the Eq. K3

$$D_B = L'_0 \tan\theta_s \tag{K6}$$

Apply Eq. K6 to Eq. K1

$$D_s = \left(\sqrt{(L'_0)^2 + (L'_0\tan\theta_s)^2}\right) - L'_0 \tag{K7}$$

$$(D_s + L'_0)^2 = (L'_0)^2 + (L'_0)^2\tan^2(\theta_s)$$

$$(D_s + L'_0)^2 = (L'_0)^2\underbrace{(1 + \tan^2\theta_s)}_{\sec^2\theta}$$

$$(D_s + L'_0)^2 = (L'_0)^2\sec^2(\theta_s)$$

$$\therefore\ D_s = L'_0\sec(\theta_s) - L'_0 \tag{K8}$$

$$\frac{\partial D_s}{\partial \theta_s} = L'_0\sec(\theta_s).\tan(\theta_s) \tag{K9}$$

Need to find the time derivative of the machine displacement, $\dot{D_s}$

$$\dot{D_s} = \frac{dD_s}{dt} = \frac{\partial D_s}{\partial \theta_s} \cdot \frac{d\theta_s}{dt} + \frac{\partial D_s}{\partial D_B} \cdot \frac{dD_B}{dt} \tag{K10}$$

$\frac{dD_B}{dt}$ is the rate of displacement of the machine (3.33 mm/s). The time derivative of the machine displacement can be calculated by applying Eqs K2, K5, and K9 to Eq. K10.

$$\dot{D_s} = \frac{dD_s}{dt} = \left[L_0' \sec(\theta_s).\tan(\theta_s).\left(\frac{\dot{D}L_0'}{(L_0')^2+\dot{D}^2t^2}\right)\right] + \left[\left(\frac{D_B}{\sqrt{(L_0')^2+D_B^2}}\right).\left(\frac{dD_B}{dt}\right)\right] \tag{K11}$$

Therefore, Eq K11 can be applied to Eq J3 (see Appendix J) to find the power garnered from stretching the stitch during the SS test. Eventually, the contribution to the measured axial force from the shearing of the fabric can be calculated.

Appendix L: Manual Methods of Measuring Fibre Angles and Stretching in the Stitch Direction

Shear Angle Measurements

An attempt was made to develop a method for manually measuring tow-stitch angles. First, flexible wires were placed in a selected direction i.e., warp, weft, and +/- bias directions. The tow-stitch angle was then measured by placing another wire along the stitch direction and leaving the protractor along the tow direction, as shown in Figure L.1. In practice, determining the two-stitch angle in this method is quite difficult especially around the equator of the hemisphere due to the curved shape of both tows and stitches.

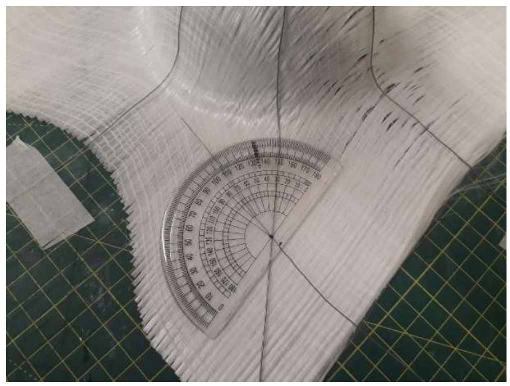

Figure L.1: Manually measuring the tow-stitch angle at a selected location

Stitch Strain Measurements

The measurements were taken with (a) a paper tape (see Figure L.2a) and (b) a flexible wire (see Figure L.2b). In practice, it is preferable to measure with flexible wires since it is easier to fold along the stitch direction and does not cause wrinkles.

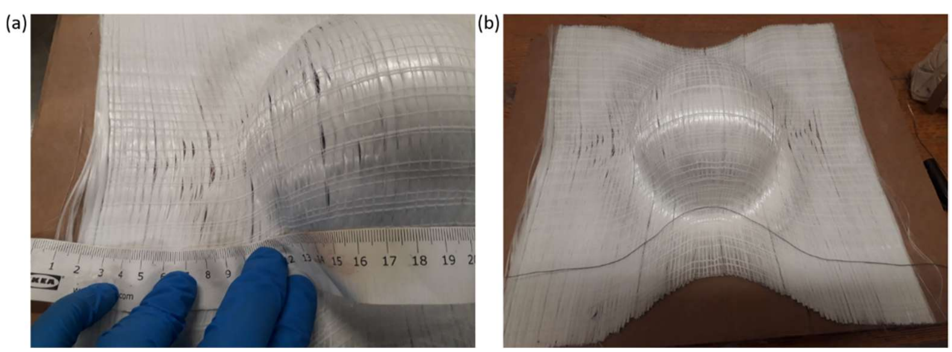

Figure L.2: Manually measuring stitch direction using (a) a paper tape (b) a flexible wire

3D coordinates of selected locations are difficult to measure manually, especially in the hemisphere area (it is necessary for comparison to numerical simulations). Therefore the study focused on the 3D scanning methods.

Appendix M: Structured Light Scanning (SLS) Method

A DAVID structured light scanner was used to perform a digital quantitative analysis of pure-UDNCF hemispheres. Figure M.1a shows the setup for scanning a formed monolayer specimen using SLS. It was initially difficult to obtain clear information about the specimen due to the bright surface of the glass fabric (see Figure M.1b). Therefore, a thin even layer of talcum powder was carefully applied with a brush (see Figure M.2). Figure M.3 shows the captured scans following the application of talcum powder.

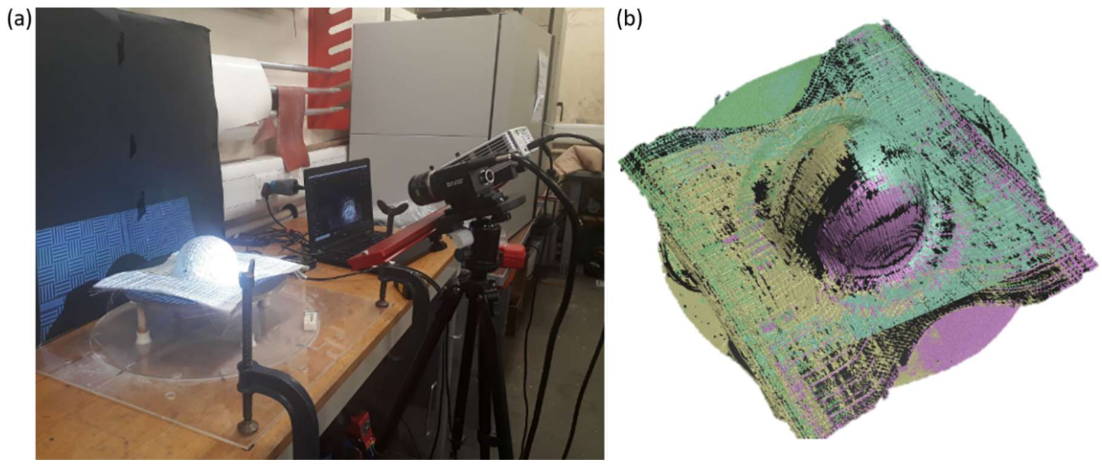

Figure M.1: Structure light scanning setup (b) Initial scanning results

Figure M.2: Application of talcum powder to the pure-UDNCF specimen

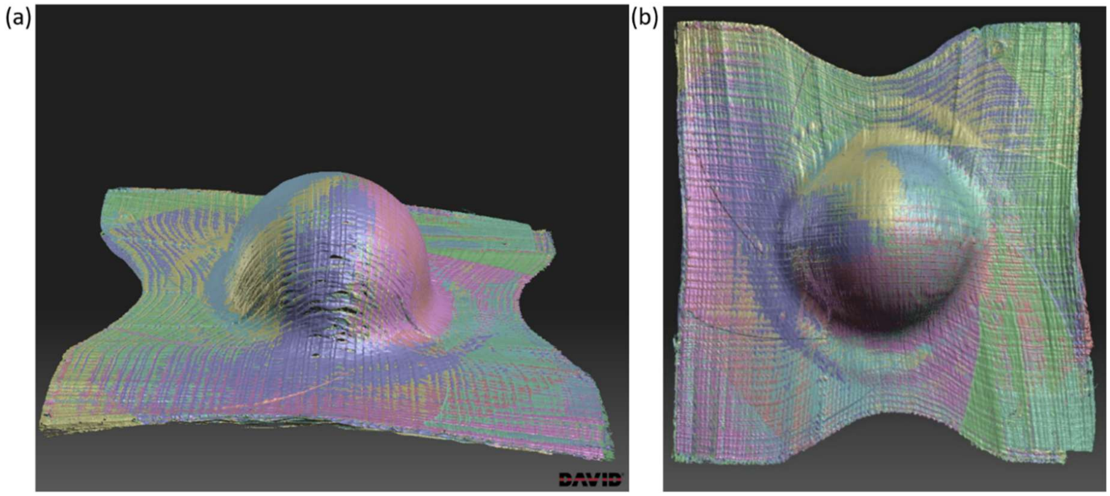

Figure M.3: Captured scans following the application of talcum powder

After scanning the hemispheres using the SLS, a fusion file was generated to integrate all the aligned scans into a single file. A common bug in this software is that the textural surface completely transforms into a solid surface after 'fusing'. Therefore, regardless of the format chosen to save the file, it appears as a solid surface (David supports three file types for import: obj, stl, and ply). Even after loading these files into different software i.e., MeshLab, Autodesk Meshmixer, and Rhino, the outcome remained the same (see Figure M.4). Therefore, the SLS method is not useful for further analysis as it is less capable of providing reliable information (fibre angles and stretching in the stitch direction) about the pure-UDNCF sample.

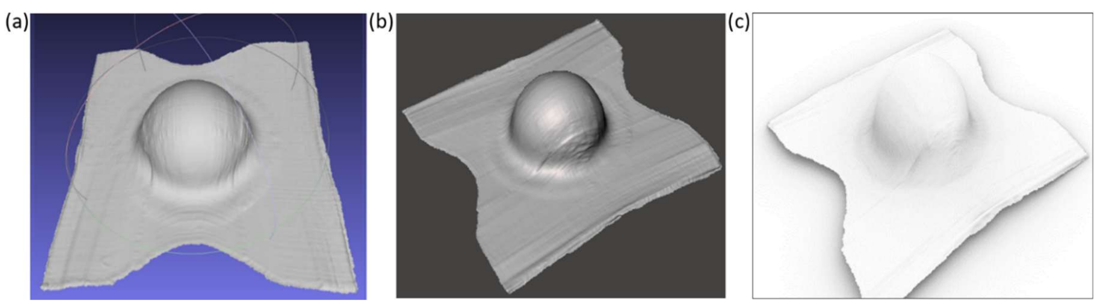

Figure M.4: Solid surfaces generated by (a) MeshLab (b) Meshmixer (c) Rhino

Appendix N: Pre-setting of the EinScan H 3D Laser Scanner to achieve the best scanning results for complex engineering fabrics (pure-UDNCF)

Before scanning a glass fabric specimen, a thin layer of talcum powder should be applied to reduce the surface brightness. The red path marked in Figure N.1 shows the steps to be followed to obtain optimal scanning results of pure-UDNCF hemispheres with the EinScan H 3D Laser Scanner.

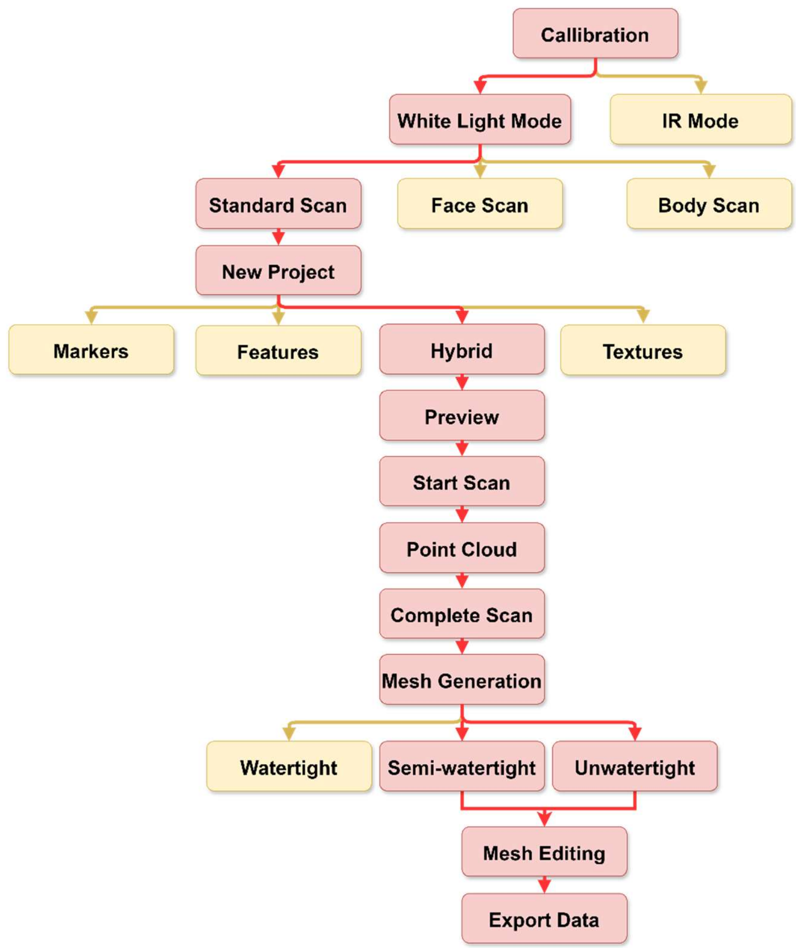

Figure N.1: Flowchart of scanning pure-UDNCF hemispheres with the EinScan H 3D laser scanner

Pure-UDNCF hemispheres comprise non-feature regions such as flat and spherical surfaces. Therefore, acquiring proper features and alignment with the scanner is challenging. Sticking the markers on the object before scanning in a random, non-linear pattern helps to track the non-feature regions (see Figure N.2a, make sure at least 4 markers are in each scanning frame). The 'Hybrid' scan option in the standard scan mode uses both features and markers to align the scans. To generate the mesh (see Figure N.2b), either 'unwatertight' or 'semi-watertight' methods can be selected (selecting watertight will result in a solid surface similar to the SLS output (see Figure N.2c)). Note that before generating the mesh of the object, **untick** the 'fill small holes' option.

Otherwise, key features such as the gaps caused by stitch stretching of the fabric during sample formation are not visible in the scanning results. Figure N.2d shows the scanning outcome of the formed pure-UDNCF hemisphere using the EinScan H 3D Laser Scanner.

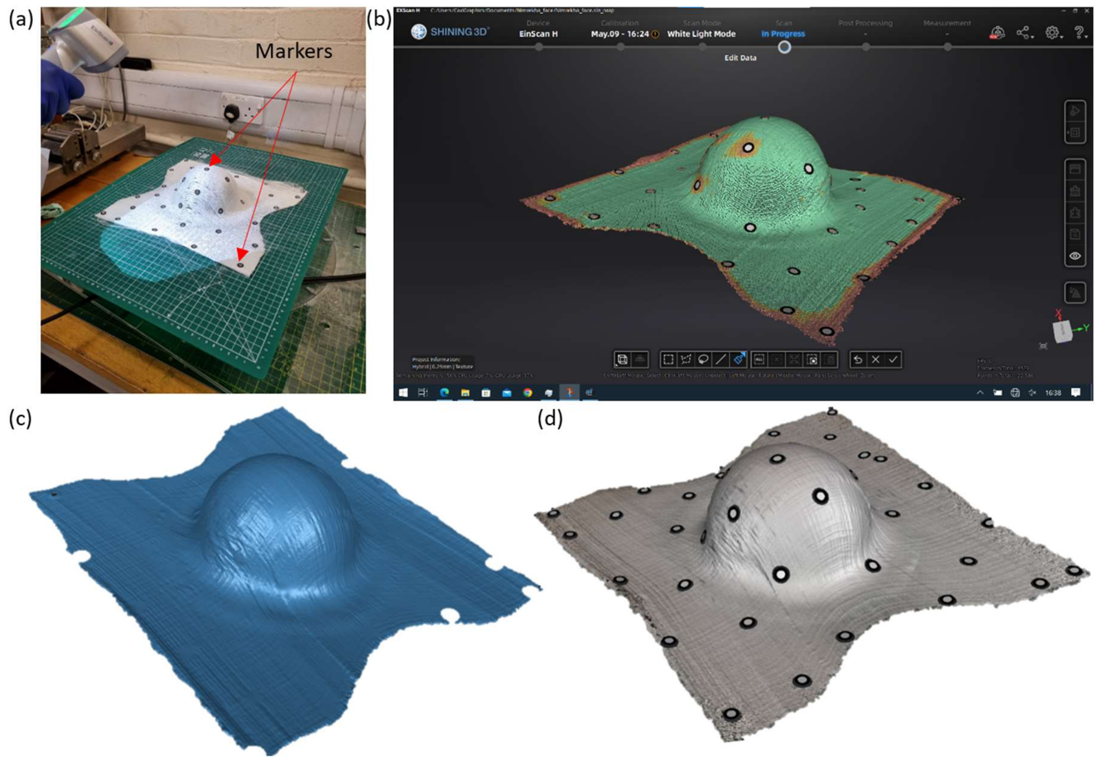

Figure N.2: (a) Marks stuck to the surface of the hemisphere (b) generated mesh (c) scanned hemisphere with the watertight option (d) The result of the hemisphere scanned using the EinScan H 3D laser scanner (with unwatertight or semi-watertight option)

Appendix O: Engineering strain in the stitch direction of formed hemispherical specimens using pure-UDNCF

Table O.1: Engineering strain in the stitch direction of the straight-cut specimens

Stitch No.	Initial Length (mm)	Mono/0/AE		Bi/0-90/AE		Bi/0-45/AE		Bi/0-90/Ad		Bi/0-45/Ad	
		Length after formin g (mm)	Stitch strain	Length after formin g (mm)	Stitch strain	Length after formin g (mm)	Stitch strain	Length after formin g (mm)	Stitch strain	Length after formin g (mm)	Stitch strain
A	320	305	-0.047	323	0.009	306	-0.044	321	0.003	295	-0.078
B		332	0.038	329	0.028	326	0.019	329	0.028	330	0.031
C		345	0.078	344	0.075	347	0.084	343	0.072	352	0.100
D		351	0.097	348	0.088	355	0.109	344	0.075	363	0.134
E		340	0.063	343	0.072	350	0.094	343	0.072	351	0.097
F		325	0.016	326	0.019	328	0.025	331	0.034	327	0.022
G		303	-0.053	318	-0.006	305	-0.047	325	0.016	296	-0.075

Table O.2: Engineering strain in the stitch direction of the bias-cut specimens

Stitch No.	Initial Length (mm)	Mono/45/AE		Bi/45-45/AE		Bi/45-45/Ad	
		Length after forming (mm)	Stitch strain	Length after forming (mm)	Stitch strain	Length after forming (mm)	Stitch strain
P	25	24	-0.040	28	0.120	37	0.480
Q	196	207	0.056	210	0.071	205	0.046
R	359	380	0.058	374	0.042	347	-0.033
S	452	477	0.055	467	0.033	430	-0.049
T	359	376	0.047	376	0.047	350	-0.025
U	196	207	0.056	216	0.102	215	0.097
V	25	24	-0.040	30	0.200	39	0.560

Appendix P: Measured shear angles at selected locations of formed hemispherical specimens using pure-UDNCF

Table P. 1: Measured shear angles at selected locations of all the hemispherical specimens

Number of points	Location	Coordinate	Measured Shear Angle (˚)							
			Mono/ 0/AE	Mono/ 45/AE	Bi/0- 90/AE	Bi/45- 45/AE	Bi/0- 45/AE	Bi/0- 90/Ad	Bi/45- 45/Ad	Bi/0- 45/Ad
1	a1	(-120,120)	5.3	0.9	7.3	0.9	0.5	14.9	6.3	-4.6
2	a2	(-120,0)	3.4	3.5	3.7	11.8	3.8	3.9	35.7	29.9
3	a3	(-120,-120)	4.4	3.8	1.9	0.6	2.3	8.9	1.0	7.4
4	b1	(-60,60)	34.6	2.3	31.4	11.7	33.5	31.7	1.6	18.5
5	b2	(-60,0)	2.0	34.6	9.9	29.7	8.5	6.1	42.8	12.2
6	b3	(-60,-60)	35.1	1.5	34.4	0.7	34.9	35.1	0.9	36.9
7	c1	(-30,30)	7.8	6.4	4.9	3.2	8.5	8.7	6.6	16.9
8	c2	(-30,0)	0.3	2.6	5.6	0.9	5.2	0.5	5.8	2.7
9	c3	(-30,-30)	10.1	3.2	6.1	0.2	8.6	9	0.5	12.0
10	d1	(0,120)	-0.1	3.8	6.6	16.3	1.1	7.6	28.8	5.6
11	d2	(0,60)	0.9	34.2	7.4	37.2	9.8	6.3	37.9	11.6
12	d3	(0,30)	2.4	2.4	3.5	9.1	3.8	1	9.1	0.2
13	d4	(0,0)	-0.6	0.3	-0.4	1.5	0.2	-0.1	0.1	0.9
14	d5	(0,-30)	1.3	4.3	2.7	9.0	1.7	1.3	6.7	2.1
15	d6	(0,-60)	3.1	31.7	3.2	39.9	10.2	6.6	41.2	9.6
16	d7	(0,-120)	4.4	8.3	5.6	21.8	0	8.3	29.7	7.7
17	e1	(30,30)	9.0	1.6	9.7	4.1	8.5	8.7	3.9	10.5
18	e2	(30,0)	1.9	1.9	2.2	1.1	2.4	1.3	3.6	1.2
19	e3	(30,-30)	11.0	0.8	8.2	3.7	9.9	12.8	2.6	10.9
20	f1	(60,60)	34.9	1.1	28.8	2.1	27.6	30.6	1.2	31.3
21	f2	(60,0)	3.6	36.8	2.5	32.0	9.4	5.3	40.8	10.2
22	f3	(60,-60)	33.8	0.2	29.9	0.3	32.8	32.6	1.3	18.8
23	g1	(-120,120)	7.2	0.2	5.4	2.8	3.9	5.4	3.4	4.9
24	g2	(120,0)	3.3	4.4	8.8	21.7	1.2	6.6	29.2	18.2
25	g3	(120,-120)	4.5	4.8	5.6	0.1	1.1	7.1	9.9	-4.3